UNIVERSIDADE FEDERAL DO PARANÁ (UFPR)

ANA LÚCIA LINDROTH DAUNER

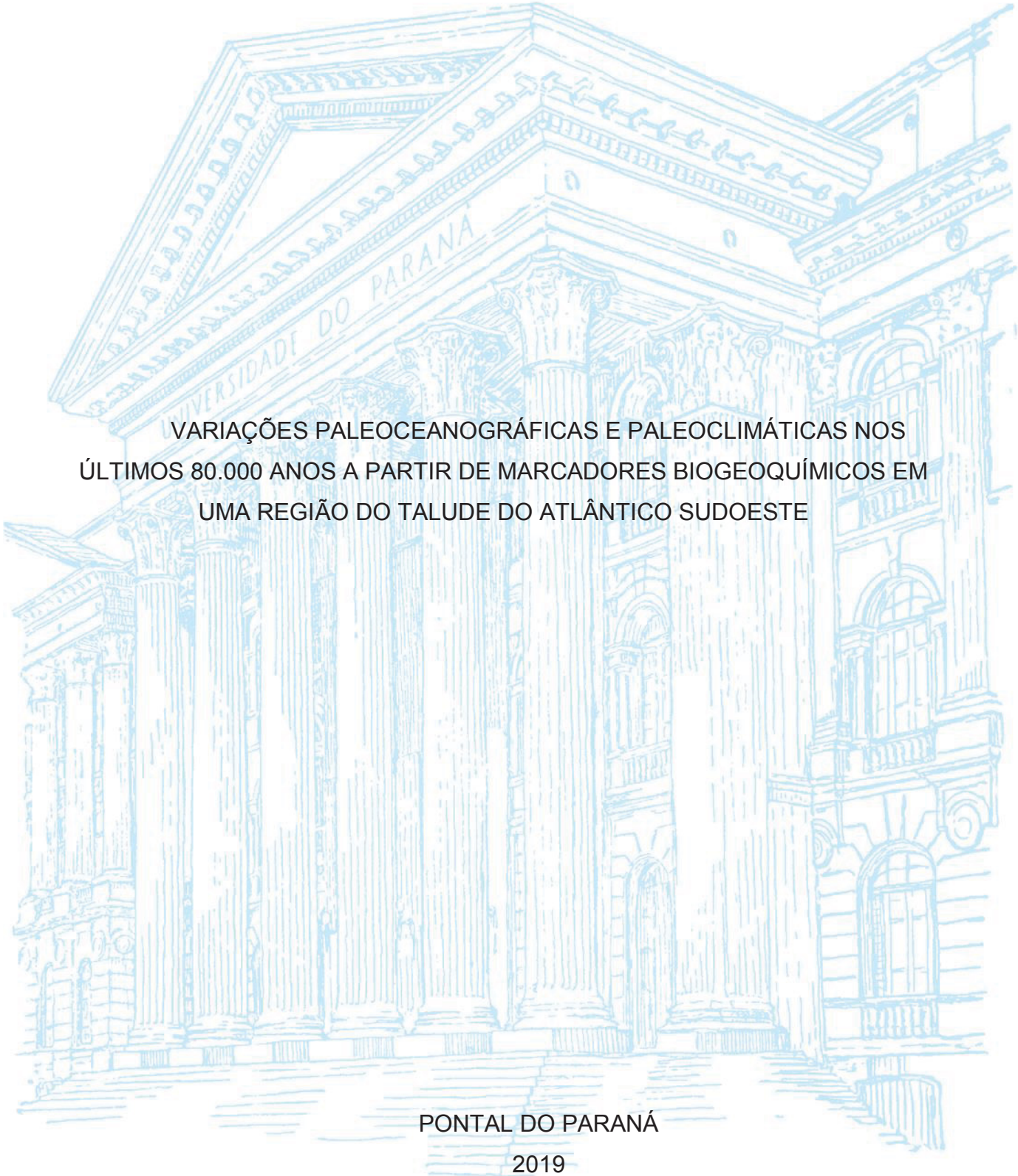

VARIAÇÕES PALEOCEANOGRÁFICAS E PALEOCLIMÁTICAS NOS ÚLTIMOS 80.000 ANOS A PARTIR DE MARCADORES BIOGEOQUÍMICOS EM UMA REGIÃO DO TALUDE DO ATLÂNTICO SUDOESTE

PONTAL DO PARANÁ

2019

ANA LÚCIA LINDROTH DAUNER

VARIAÇÕES PALEOCEANOGRÁFICAS E PALEOCLIMÁTICAS NOS ÚLTIMOS 80.000 ANOS A PARTIR DE MARCADORES BIOGEOQUÍMICOS EM UMA REGIÃO DO TALUDE DO ATLÂNTICO SUDOESTE

Tese apresentada ao Programa de Pós-Graduação em Sistemas Costeiros e Oceânicos, Setor de Ciências da Terra, Universidade Federal do Paraná, como requisito parcial para obtenção de grau de Doutor.

Orientadores: Dr. César de Castro Martins, Dr. rer. nat. Gesine Mollenhauer e Dra. Márcia Caruso Bícego

PONTAL DO PARANÁ

2019

CATALOGAÇÃO NA FONTE:
UFPR / SiBi - Biblioteca do Centro de Estudos do Mar
Fernanda Pigozzi - CRB-9/1151

Dauner, Ana Lúcia Lindroth
D242v Variações paleocenográficas e paleoclimáticas nos últimos 80.000 anos a partir de marcadores biogeoquímicos em uma região do talude do Atlântico Sudoeste. / Ana Lúcia Lindroth Dauner. – Pontal do Paraná, 2019.
165 f.: il.; color.; 29 cm.

Orientadores: Prof. Dr. César de Castro Martins, Prof. Dr. rer.nat. Gesine Mollenhauer e Profª. Dra. Márcia Caruso Bícego

Tese (Doutorado) – Programa de Pós-Graduação em Sistemas Costeiros e Oceânicos, Centro de Estudos do Mar, Setor Reitoria, Universidade Federal do Paraná.

1. Oceano - temperatura. 2. Holoceno. 3. Paleocenografia. 4. Paleoclimatologia. Título. II. Martins, Cesar de Castro. III. Mollenhauer, Gesine. IV. Bícego, Márcia Caruso. V. Universidade Federal do Paraná.

CDD 551.4601

MINISTÉRIO DA EDUCAÇÃO
SETOR REITORIA
UNIVERSIDADE FEDERAL DO PARANÁ
PRÓ-REITORIA DE PESQUISA E PÓS-GRADUAÇÃO
PROGRAMA DE PÓS-GRADUAÇÃO SISTEMAS COSTEIROS E OCEÂNICOS - 40001016054P6

TERMO DE APROVAÇÃO

Os membros da Banca Examinadora designada pelo Colegiado do Programa de Pós-Graduação em SISTEMAS COSTEIROS E OCEÂNICOS da Universidade Federal do Paraná foram convocados para realizar a arguição da Tese de Doutorado de **ANA LUCIA LINDROTH DAUNER**, intitulada: ***VARIAÇÕES PALEOCEANOGRÁFICAS E PALEOCLIMÁTICAS NOS ÚLTIMOS 80.000 ANOS A PARTIR DE MARCADORES BIOGEOQUÍMICOS EM UMA REGIÃO DO TALUDE DO ATLÂNTICO SUDOESTE***, após terem inquirido a aluna e realizado a avaliação do trabalho, são de parecer pela sua APROVAÇÃO no rito de defesa.

A outorga do título de Doutor está sujeita à homologação pelo colegiado, ao atendimento de todas as indicações e correções solicitadas pela banca e ao pleno atendimento das demandas regimentais do Programa de Pós-Graduação.

Curitiba, 29 de Maio de 2019.

CÉSAR DE CASTRO MARTINS
Presidente da Banca Examinadora

RENATA HANAE NAGAI
Avaliador Interno (UFPR)

MARCIA CARUSO BICEGO
Avaliador Externo (IO/USP)

CARLOS CONFORTI FERREIRA GUEDES
Avaliador Externo (UFPR)

RENATO DA SILVA CARREIRA
Avaliador Externo (PUC-RIO)

ANA CECILIA RIZZATTI DE ALBERGARIA BARBOSA
Avaliador Externo (UFBA)

DECLARAÇÃO

Declaro para os devidos fins que o **título correto** da tese de doutorado de autoria de **ANA LUCIA LINDROTH DAUNER** aprovada em 29 de maio de 2019 é **"Variações paleoceanográficas e paleoclimáticas nos últimos 80.000 anos a partir de marcadores biogeoquímicos em uma região do talude do Atlântico Sudoeste"** e não "Variações paleoceanográficas e paleoclimáticas nos últimos 80.000 anos a partir de marcadores biogeoquímicos em uma região do talude do Atlântico Sudoeste" como consta de ata de aprovação. A diferença entre os títulos se dá pela inserção de " ", provavelmente um erro do Sistema de Gestão Acadêmica no momento de gerar a ata. Por ser verdade, firmo a presente declaração.

Pontal do Paraná, PR, 09 de agosto de 2019.

Renata H. Nagai

Profa. Dra. Renata Hanae Nagai
Coordenadora da Pós-Graduação em Sistemas Costeiros e Oceânicos

PÓS-GRADUAÇÃO EM SISTEMAS COSTEIROS E OCEÂNICOS
UNIVERSIDADE FEDERAL DO PARANÁ

O dia em que eu entendi que a vida acadêmica é composta por trabalho duro,
e não genialidade, eu tirei um peso imenso de mim.

Rosana Pinheiro-Machado

AGRADECIMENTOS

À Coordenação de Aperfeiçoamento de Pessoal de Ensino Superior (CAPES) pela bolsa de Doutorado, e ao Conselho Nacional de Desenvolvimento Científico e Tecnológico (CNPq) e à Fundação de Amparo à Pesquisa do Estado de São Paulo (FAPESP) pelos recursos financeiros (CNPq: 305763/2011-3; FAPESP: 2015/21834-2). Agradeço também à tripulação e aos pesquisadores que participaram do cruzeiro 07/02 do Alpha-Crucis.

Aos avaliadores das semanas acadêmicas e da presente tese (Dra. Ana Cecília Rizzatti de Albergaria-Barbosa, Dr. Carlos Conforti Ferreira Guedes, Dr. Luiz Augusto dos Santos Madureira, Dra. Renata Hanae Nagai e Dr. Renato da Silva Carreira), e da revista científica em que o primeiro artigo foi submetido. À Márcia Caruso Bícego, que quando a ideia do primeiro projeto não deu tão certo, me recebeu em São Paulo e se prontificou a oferecer as amostras do NAP 63-1. As críticas e sugestões contribuíram muito para o aperfeiçoamento deste trabalho.

Aos professores e funcionários da PGSISCO e do CEM. Pelas lições aprendidas e pelos “Bom Dia!” trocados no corredor. Cada cumprimento e sorriso trocado em um dia cinzento e chuvoso em Pontal ajuda a colorir o dia!

Aos amigos!

Bia, Nati e toda a mulherada do jump; sem esse escape semanal, esses quatro anos teriam sido bem mais estressantes. Compartilhar essa uma hora de música alta, cansaço físico e brincadeiras ajudaram (e muito!) a aliviar o cansaço mental.

Mulherada do LaGPoM – Aline, Amanda, Carol, Ana Carolina, Ana Cláudia, Camila, Dóris, Fernanda Dittmar, Fernanda Ishii, Helô, Karina, Marina, Marininha, Marines e Tati, vocês são simplesmente demais! Cada frio compartilhado no laboratório, cada mistério e fantasma nos cromatógrafos, cada café, cada confabulação, cada mensagem trocada fizeram com que o doutorado ficasse um pouco mais fácil, um pouco mais divertido. Tenho muito orgulho de fazer parte desse time!

Fer, Maia e Tássia, vocês são minha inspiração e a minha certeza de que a amizade ultrapassa a distância e os anos! Não tenho palavras para descrever o quanto isso é importante.

To the new friends I made at AWI! Bingbing, Célia, Eunmi, Julian, Hendrik, Laura, Liz, Shuwen, Torben and Vera. You accepted me in your group and helped me, especially with the details and difficulties of living in a different country. Thank you so much for welcoming me! And also, to Thomas, Basit, Zhang and Wenguo. Chatting is always nice, no matter the language.

Speaking of AWI, a special thanks to Gesine and Jens! I literally wrote her an e-mail one day, and a few weeks later, I knocked on the door of her office, saying "Hi, my name is Ana Lúcia!". Gesine, your acceptance in co-advising and receiving me to work in your laboratory, as well as the conversations with you, made me evolve a lot as a researcher! Jens, you were incredibly patient with me, both responding to my long e-mails and answering to my many questions in the lab. Thank you both very much!!!

Tão importante quanto as pessoas com quem dividimos os sorrisos, são as pessoas que nos escutam chorar, que nos servem de apoio.

Ao César, que não poderia ter sido um orientador melhor. Que ao longo desses 10 anos, muitas vezes, foi quase um pai. Um orientador que me ensinou a trabalhar em equipe, que me direcionou a leitura, que corrigiu com dedicação (mesmo em meio a inúmeras outras funções) todos os meus textos. Que esteve sempre presente, mesmo à distância, para ouvir (e, principalmente, para me incentivar a falar sobre) as minhas inseguranças. Que confiou no meu trabalho, e que sempre me incentivou a ir atrás de mais. Acima de tudo, um orientador que me deu espaço pra tentar, mesmo que isso significasse errar. Muita da autoconfiança que eu tenho hoje se deve a você, César. Muito obrigada!

À minha família, de sangue e de coração! Pai, mãe, Fernando e Cindy (quase de sangue ☺). O apoio e a confiança de vocês sempre foram, e sempre serão, essenciais para mim. E à minha família agregada, que também é de coração: Mariana, Carlinhos, Meire, Andrei, Adlaise, Luna e Sol. Cada conversa, cada risada juntos é um peso a menos na alma.

E ao Mihael, o que eu posso falar? Meu companheiro, meu porto seguro, meu Grilo Falante, meu ombro amigo (que vem preparado com 10 kg de lenços de papel), meu incentivador. Você fez e faz parte do meu crescimento profissional tanto quanto do pessoal. Muito obrigada, meu amor!

RESUMO

O Oceano Atlântico Sul apresenta um papel fundamental no transporte de calor entre as diversas bacias oceânicas, assim como na transformação de massas d'água. Por esta razão, entender as oscilações climáticas naturais ocorridas nele permite compreender melhor as mudanças climáticas recentes. Além disso, compreender como essas oscilações climáticas afetaram a produção da matéria orgânica provê uma base para prever como a teia trófica marinha poderá reagir às mudanças recentes. Para estudar as mudanças ambientais ocorridas na região central do Embaiamento Sul do Brasil, foi coletado um testemunho sedimentar no talude (24,8°S; 44,3°W) a aproximadamente 840 m de profundidade. Com base em diversos marcadores geoquímicos (*n*-alcanos, alquenonas, glicerol dialquil-glicerol tetraéteres, diols, esteróis e *n*-alcanóis), foi possível estimar as variações das temperaturas da superfície e da subsuperfície do mar (capítulo 2), assim como entender a evolução da produção de matéria orgânica autóctone e do aporte de matéria orgânica alóctone nesta região (capítulo 3). A temperatura do mar apresentou duas escalas de oscilação. Na escala orbital, as variações de temperatura estão associadas à variação climática da Antártica, especialmente relacionadas à radiação solar incidente. Já na escala milenar, a temperatura de superfície do mar variou em função da formação da Água Profunda do Atlântico Norte. Assim, em períodos de maior formação de águas profundas no Hemisfério Norte, o calor do Atlântico Sul é transportado através das correntes superficiais para o Hemisfério Norte, causando um relativo resfriamento no oeste do Atlântico Sul. Em relação à produção e ao aporte de matéria orgânica, a principal contribuição encontrada foi de origem autóctone, controlada por fatores hidrodinâmicos. Essa produção marinha esteve relacionada a eventos de ressurgência da Água Central do Atlântico Sul durante os períodos de maior produtividade marinha, e ao aporte continental de nutrientes. Além disso, o aquecimento da última deglaciação promoveu a produção marinha procarionte. O aporte de material terrígeno, por sua vez, foi controlado por variações no nível do mar e na pluviosidade na região continental adjacente ao local amostrado.

Palavras-chave: Holoceno. Pleistoceno. Embaiamento Sul do Brasil. Temperatura da Superfície do Mar. Matéria Orgânica.

ABSTRACT

The South Atlantic Ocean plays a key role in the transport of heat between the world's major ocean basins, as well as in the transformation of the water masses. For this reason, the understanding of the natural climatic oscillations that occur in it allows a better understanding of the recent climate changes. In addition, the understanding of how these climatic oscillations affected the production of organic matter provides a basis for predicting how the marine trophic web could react to the recent climate changes. In order to study the environmental changes in the central region of the South Brazil Bight, a sediment core was retrieved from the continental slope (24.8° S, 44.3° W, approximately 840 m depth). Based on several geochemical markers (*n*-alkanes, alkenones, glycerol dialkyl glycerol tetraethers, long-chain diols, sterols and *n*-alkanols), it was possible to estimate the variations in sea surface and subsurface temperatures (Chapter 2), as well as to understand the evolution of the autochthonous organic matter production and the input of allochthonous organic matter in this region (Chapter 3). The sea surface temperature presented two oscillation scales. In the orbital scale, the temperature variations were associated to the Antarctic climate variations, especially the incident solar radiation. Regarding the millennial scale, the sea surface temperature varied as a result of the formation of the North Atlantic Deep Water. In periods of increased deep-water formation in the Northern Hemisphere, the heat of the South Atlantic is transported through surface currents to the Northern Hemisphere, causing a relative cooling in the western South Atlantic. In relation to the production and input of organic matter, the autochthonous organic matter was the main contributor, being controlled by hydrodynamic forcings. The marine production was related to upwelling events of the South Atlantic Central Water during periods of highest marine productivity, and to the continental nutrient input. In addition, the warming of the last deglaciation promoted the prokaryotic marine production. The contribution of terrigenous material was, in turn, controlled by variations in sea level and in pluviosity in the continental region adjacent to the sampling site.

Keywords: Holocene. Pleistocene. South Brazil Bight. Sea surface temperature. Organic Matter.

LISTA DE FIGURAS

Fig. 2.1. Map of the study area with the location of the NAP 63-1 sediment core as well as the main currents and water masses in the region (based on Biastoch et al., 2008; Campos et al., 1995; Castellanos et al., 2017; Peterson and Stramma, 1991; Piola and Matano, 2001; Schmid, 2014; Schmid et al., 2000 and Silveira et al., 2000). The indicated cores are used in discussion of the climate evaluation of the SW Atlantic. ……..…….……42

Fig. 2.2. Reference curves and age–depth model of NAP 63-1sediment core. A: benthic foraminifera $\delta^{18}O$ of LR04 stack (Lisiecki and Raymo, 2005). B: benthic foraminifera $\delta^{18}O$ of Intermediate South Atlantic (ISA) stack (Lisiecki and Stern, 2016). C: benthic foraminifera $\delta^{18}O$ of NAP 63-1 core, with the indication of the calibrated ^{14}C ages (red triangles). D: Age-depth model based on Bacon v. 2.3.5 (Blaauw and Christen, 2011). Symbols in panel D represent the positions of calibrated ^{14}C ages and benthic $\delta^{18}O$ tie-points. ……..……..48

Fig. 2.3. Evolution of $U^{K'}_{37}$ (a), TEX_{86} (b) and LDI (c) indexes in the core NAP 63-1. Grey bars indicate MIS 2 and MIS 4 duration, the orange bars indicate the AIM events and the purple bar indicates the Last Glacial Maximum (LGM). Horizontal brown lines and indicate Heinrich Stadials (HS). Black symbols at the top of the panel depict age model tie points. ……..……...49

Fig. 2.4. Temperature reconstructions for the SW Atlantic. Black symbols at the top of the panel depict age model tie points. (a) $U^{K'}_{37}$-based temperature of 30m water depth, (b) TEX_{86}-based SST and (c) LDI-based SST; all for the NAP 63-1 sediment core. They include the standard errors and the present observed temperatures. (d) $U^{K'}_{37}$-based SST for the #7485 sediment core (Lourenço et al., 2016). (e) SIMMAX-based summer SST for the SAN-76 sediment core (Toledo et al., 2007). (f) Mg/Ca-based SST for the GI-1090 sediment core (Santos et al., 2017). (g) Vertical temperature difference between LDI-based SST and $U^{K'}_{37}$-based subT (red squares) and between TEX_{86}^{H}-based SST and $U^{K'}_{37}$-based subT (blue triangles), calculated for the NAP 63-1 sediment core. The dashed lines indicate the accumulated error of the indexes (red = LDI + $U^{K'}_{37}$ errors; blue = TEX_{86}^{H} + $U^{K'}_{37}$ errors). All the temperature

records are presented using a 4-pt running average (continuous bold line). The black dashed line (20°C) represents the South Atlantic Central Water (SACW) delimitation. Grey bars indicate MIS 2 and MIS 4 duration, the orange bars indicate the AIM events and the purple bar indicates the Last Glacial Maximum (LGM). Horizontal brown lines indicate Heinrich Stadials (HS). ……..…….54

Fig. 2.5. Orbital-scale (> 10 kyr) and millennial-scale (< 10 kyr) records based on the ice cores EDML ($\delta^{18}O_{ice}$; EPICA Community Members 2010) and NGRIP $\delta^{18}O_{ice}$; Andersen et al. 2004), and on the sediment core NAP 63 -1 (TEX_{86}-based SST; LDI-based SST and $U^{K'}_{37}$-based subT; this study). Grey bars indicate MIS 2 and MIS 4 duration, the orange bars indicate the AIM events and the purple bar indicates the Last Glacial Maximum (LGM). Horizontal brown lines indicate Heinrich Stadials (HS). ……..……..56

Fig. 2.6. At the top of each panel, normalized time series of sea surface temperatures at the NAP 63-1 core. At the bottom, the wavelet power spectrum (left) and global wavelet (black line) and Fourier spectrum (gray line) of the normalized signal on the time-frequency domain. Marked regions on the wavelet spectrum indicate significant power to a 95% confidence interval. The areas under the gray cone of influence show where edge effects are important. The sequence of the panels: (top) LDI-based SST and (bottom) TEX_{86}-based SST. ……..…..61

Fig. 2.7. Cross-wavelet and wavelet coherence between the Nd excess from NW Atlantic (εNd; OCE326-GGC6 and ODP 1063 cores; Böhm et al., 2015; Roberts et al., 2010) and TEX_{86}-based annual SST. At the top, the normalized time series. The phase arrows in the cross-wavelet power spectrum rotate clockwise with 'north' origin. The vectors indicate the phase relationship, where in phase signals point upwards (N), anti-phase signals point downwards (S). If X (εNd) leads Y, arrows point to the right (E) and if X lags Y, arrow points to the left (W). Marked regions on the wavelet spectrum indicate significant power to a 95% confidence interval, and areas under the gray cone of influence show where edge effects are important and the analysis unreliable. ……..…...62

Fig. 2.8. Cross-wavelet and wavelet coherence between the local $\delta^{18}O_{sw}$ anomaly from the SE Atlantic (MD 02-2594 core; Dyez et al. 2014) and TEX_{86}-based annual SST. At the top, the normalized time series. The phase arrows in the cross-wavelet power spectrum rotate clockwise with 'north' origin. The vectors indicate the phase relationship, where in phase signals point upwards (N), anti-phase signals point downwards (S). If X ($\delta^{18}O_{sw}$ anomaly) leads Y, arrows point to the right (E) and if X lags Y, arrow points to the left (W). Marked regions on the wavelet spectrum indicate significant power to a 95% confidence interval, and areas under the gray cone of influence show where edge effects are important and the analysis unreliable. 63

Fig. 3.1. Map of the study area with the location of sediment core NAP 63-1 (yellow star) as well as the main currents and water masses in the region (based on Campos et al., 2001, 1995; Piola et al., 2008; Schmid, 2014; Schmid et al., 2000; Silveira et al., 2015, 2000). The core sites indicated by colored dots are used in the discussion of the terrestrial and marine OM evaluation. 83

Fig. 3.2. Mass accumulation rates (in ng cm^{-2} yr^{-1}) profiles of the organic molecular markers analysed in NAP 63-1 sediment core. 92

Fig. 3.3. Cluster analysis based on the temporal evolution of each organic compound group, using the SAX representation as the dissimilarity measure. The green rectangle indicates the “terrestrial-source” group and the blue rectangle indicates the “marine-source” group. 94

Fig. 3.4. Terrestrial (left) and marine (right) organic matter (OM) dendrograms (top) and wavelets (bottom) for core NAP 63-1. The terrestrial OM evolution is represented by the C_{19}-C_{23} and C_{25}-C_{39} *n*-alkanes, and marine OM evolution is represented by brassicasterol ($28\Delta^{5,22E}$) accumulation rates (ng cm^{-2} yr^{-1}). 96

Fig. 3.5. Records of the terrestrial and marine OM proxies (mass accumulation rates of C_{19}-C_{23} and C_{25}-C_{39} *n*-alkanes and $28\Delta^{5,22E}$, respectively), elemental and isotopic composition, and BIT values for core NAP 63-1. 97

Fig. 3.6. Dendrograms and terrestrial proxies for cores NAP 63-1, GeoB 2107-3 and Colônia cores, with the global sea level evolution, the anomalies (in 10^3) of Mg/Ca and Sr/Ca in the Botuverá Cave and the *n*-alkane P_{aq} index calculated for the NAP 63-1 sediment core. 99

Fig. 3.7. Temporal evolution regarding the marine organic matter in the sediment core NAP 63-1: dendrogram; brassicasterol ($28\Delta^{5,22E}$) accumulation rates; $U^{K'}_{37}$-based sea subsurface temperature (subT); mean and standard deviations of the 5α(H)-stanol/Δ^5-stenol ratio; and the contents of dinosterol ($30\Delta^{22E}$), long-chain alkenones (LCA) and crenarchaeol normalised by the brassicasterol ($28\Delta^{5,22E}$) content. The % *Globigerina bulloides*, a planktonic foraminiferal species typically associated with upwelling waters, from the sediment core GL-74 and the anomalies (in 10^3) of Mg/Ca and Sr/Ca in the Botuverá Cave are also shown. 102

Fig. 3.8. Cross-wavelet and wavelet coherence between the subsurface temperature ($U^{K'}_{37}$-based subT) (Dauner et al., 2019), and brassicasterol ($28\Delta^{5,22E}$) accumulation rates (ng cm^{-2} yr^{-1}). At the top, the normalized time series. The phase arrows in the cross-wavelet power spectrum rotate clockwise with 'north' origin. The vectors indicate the phase relationship, where in phase signals point upwards (N), anti-phase signals point downwards (S). If X (subT) leads Y (brassicasterol), arrows point to the right (E) and if X lags Y, arrow points to the left (W). Marked regions on the wavelet spectrum indicate significant power to a 95% confidence interval, and areas under the gray cone of influence show where edge effects are important and the analysis unreliable. 104

Fig. SM 1. Example of chromatogram (sample “34-36 cm”) of the first apolar fraction (recovered with *n*-hexane), containing the *n*-alkanes. ……..…..151

Fig. SM 2. Example of chromatogram (sample “34-36 cm”) of the second apolar fraction (recovered with *n*-hexane:DCM (1:2 v:v)), containing the long-chain alkenones. ……..152

Fig. SM 3. Example of chromatogram (sample “34-36 cm”) of the polar fraction (recovered with DCM:MeOH (1:1; v:v) and analysed via GC-MS), containing the *n*-alkanols, the steroids and the long-chain diols. Identification of compounds: 1 = $27\Delta^{5,22E}$; 2 = $27\Delta^{22E}$; 3 = $27\Delta^{5}$; 4 = $27\Delta^{0}$; 5 = $28\Delta^{5,22E}$; 6 = $28\Delta^{22E}$; 7 = $28\Delta^{5}$; 8 = $28\Delta^{0}$; 9 = $29\Delta^{5,22E}$; 10 = $29\Delta^{22E}$; 11 = $29\Delta^{5}$; 12 = $29\Delta^{0}$; 13 = $30\Delta^{22E}$; A = C_{28}-diols; B = C_{30}-diols; C = C_{32}-diols. ……...153

Fig. SM 4. Example of chromatogram (sample “34-36 cm”) of the polar fraction (recovered with DCM:MeOH (1:1; v:v) and analysed via HPLC-MS), containing the GDGTs. ……...154

Fig. SM 5. Principal Component Analysis performed to select the organic proxy that best illustrates the organic matter (terrestrial = top; marine = bottom) variability. ...155

Fig. SM 6. Scatter plots of $\delta^{13}C$ versus $\delta^{15}N$, considering the ranges stablished by Bianchi and Canuel (2011) and the NAP 63-1 samples. 156

LISTA DE TABELAS

Table 2.1. Age control points for the core NAP 63-1. 48

Table 2.2. Pearson correlation (R) between the TEX_{86}-based and the LDI-based SST from NAP 63-1 and other Atlantic SST reconstructions. Underlined *R* values: *p*-value < 0.05. ……...59

Table A-1. Ions used to identify GDGTs. ……137

Table A-2. Ion fragments used to identify diols. ……....138

Table A-3. $U^{K'}_{37}$-based temperature (°C) estimates minus instrumental temperatures (°C) from the WOA13, based on Ceccopieri et al. (2018). ……..138

Table A-4. Pearson correlation (R) between the TEX_{86}-based and the LDI-based SST from NAP 63-1 and other Atlantic SST reconstructions, considering only the orbital trend (periodicity > 10 kyr). Underlined R values: *p*-value > 0.05. ……..……..139

Table A-5. Pearson correlation (R) between the TEX_{86}-based and the LDI-based SST from NAP 63-1 and other Atlantic SST reconstructions, considering only the millennial oscillations (periodicity < 10 kyr). Underlined R values: *p*-value > 0.05. ……..……...139

Table B-1. $U^{K'}_{37}$, TEX_{86} and LDI indices, and temperature estimates for NAP 63-1 sediment core. ……..……140

Table SM 1. Ion fragments used to identify *n*-alkanols. ……..147

Table SM 2. Ion fragments used to identify sterols. ……..……..147

Table SM 3. Ion fragments used to identify diols. ……..……..148

Table SM 4. Molecular ions used to identify GDGTs. ……..……..148

Table SM 5. 5α(H)-stanol/Δ^5-stenol ratios calculated for core NAP 63-1. …….. 148

Table D 1. Dataset of bulk parameters, sedimentation rates (cm kyr^{-1}) and accumulation rates (ng cm^{-2} kyr^{-1}) of the apolar organic geochemical markers for core NAP 63-1: percentage of Total Organic Carbon (% TOC), percentage of Total Nitrogen (%TN), TOC/TN ratio, carbon isotope composition ($\delta^{13}C$), nitrogen isotope composition ($\delta^{15}N$) values, odd-numbered *n*-alkanes *n*-C_{15} to *n*-C_{17}, odd-numbered *n*-alkanes *n*-C_{19} to *n*-C_{23}, odd-numbered *n*-alkanes *n*-C_{25} to *n*-C_{39}, and long-chain alkenones (LCA). ……..157

Table D 2. Dataset of the accumulation rates (ng cm^{-2} kyr^{-1}) of the polar organic geochemical markers for core NAP 63-1: crenarchaeol, branched GDGTs (brGDGTs), even-numbered *n*-alkanols *n*-C_{12}-OH to *n*-C_{18}-OH, even-numbered *n*-alkanols *n*-C_{20}-OH to *n*-C_{34}-OH, phytol, dehydrocholesterol ($27\Delta^{5,22E}$), cholesterol ($27\Delta^5$), brassicasterol ($28\Delta^{5,22E}$), campesterol ($28\Delta^5$), stigmasterol ($29\Delta^{5,22E}$), sitosterol ($29\Delta^5$), dinosterol ($30\Delta^{22E}$), and long-chain diols (C_{28}1,14 + C_{30}1,14). ….162

LISTA DE ABREVIATURAS

AABW: Água Antártica de Fundo ("*Antarctic Bottom Water*")
AAIW: Água Intermediária Antártica ("*Antarctic Intermediate Water*")
ACC: Corrente Circumpolar Antártica ("*Antarctic Circumpolar Current*")
ACR: Reversão Fria da Antártica ("*Antarctic Cold Reversal*")
AIM: Máximos Isotópicos Antárticos ("*Antarctic Isotope Maximum*")
AMOC: Circulação Meridional do Atlântico ("*Atlantic Meridional Overturning Circulation*")
BC: Corrente do Brasil ("*Brazil Current*")
BCC: Corrente Costeira do Brasil ("*Brazilian Coastal Current*")
BECE: Extensão da Corrente de Benguela ("*Benguela Current Extension*")
BIT: Razão entre GDGTs Ramificados e Isoprenoides ("*Branched and Isoprenoid Tetraether Index*")
BMC: Confluência Brasil-Malvinas ("*Brazil-Malvinas Confluence*")
BP: antes do presente, ou seja, antes de 1950 ("*Before Present*")
brGDGTs: GDGTs com cadeia carbônica ramificada ("*branched GDGTs*")
BSTFA: N,O-bis(trimetil-silil-triflúor-acetamida) ("*N,O-bis (trimethylsilyltrifluoroacetamide)*")
DCM: diclorometano ("*dichloromethane*")
D-O: Oscilações Dansgaard-Oeschger ("*Dansgaard-Oeschger oscillations*")
DWBC: Corrente Profunda de Contorno Oeste ("*Deep Western Boundary Current*")
EA: Analisador Elementar ("*Elemental Analyser*")
EDML: EPICA Dronning Maud Land
EPICA: Projeto europeu de perfuração de gelo na Antártica ("*European Project for Ice Coring in Antarctica*")
Gb/Gr: *Globigerina bulloides* / *Globigerinoides ruber* (white)
GC: Cromatógrafo Gasoso ("*Gas Chromatograph*")
GDGTs: Glicerol Dialquil – Glicerol Tetraéteres ("*Glycerol Dialkyl-Glycerol Tetraethers*")
HPLC: Cromatógrafo Líquido de Alta Performance ("*High-Performance Liquid Chromatograph*")
HS: período de resfriamento que segue um evento Heinrich ("*Heinrich Stadial*")

IAEA: Agência Internacional de energia Atômica ("*International Atomic Energy Agency*")
IPCC: Painel Intergovernamental de Mudanças Climáticas ("*Intergovernmental Panel on Climate Change*")
IRMS: Espectrômetro de Massas de Razão Isotópica ("*Isotope Ratio Mass Spectrometer*")
isoGDGTs: GDGTs com cadeia carbônica isoprenoide ("*isoprenoid GDGTs*")
ITCZ: Zona de Convergência Intertropical ("*Intertropical Convergence Zone*")
IWBC: Corrente Intermediária de Contorno Oeste ("*Intermediate Western Boundary Current*")
kyr: mil anos ("*thousand years*")
LDI: Índice baseado em diols de cadeia longa ("*Long chain Diol Index*")
LGM: Último Máximo Glacial ("*Last Glacial Maximum*")
MAR: Taxas de acumulação de massa ("*Mass Accumulation Rates*")
MC: Corrente das Malvinas ("*Malvinas Current*")
MeOH: metanol ("*methanol*")
MIS: Estágio Isotópico Marinho ("*Marine Isotope Stage*")
MO: Matéria Orgânica
MS: Espectrômetro de Massas ("*Mass Spectrometer*")
MZ: Zona Marinha ("*Marine Zone*")
NADW: Água Profunda do Atlântico Norte ("*North Atlantic Deep Water*")
NBC: Corrente Norte do Brasil ("*North Brazil Current*")
OM: Matéria Orgânica ("*Organic Matter*")
PBMC: Painel Brasileiro sobre Mudanças Climáticas
RdlP: Rio da Prata ("*La Plata River*")
RSL: Nível Relativo do Mar ("*Relative Sea Level*")
SAC: Corrente do Atlântico Sul ("*South Atlantic Current*")
SACW: Água Central do Atlântico Sul ("*South Atlantic Central Water*")
SACZ: Zona de Convergência do Atlântico Sul ("*South Atlantic Convergence Zone*")
SBB: Embaiamento Sul do Brasil ("*South Brazil Bight*")
SEC: Corrente Equatorial Sul ("*South Equatorial Current*")
SIM: Monitoramento de Íons Selecionados ("*Selected Ion Monitoring*")
SST: Temperatura de Superfície do Mar ("*Sea Surface Temperature*")
subT: Temperatura da Água de Subsuperfície ("*Subsurface Temperature*")

TEX_{86}: Índice baseado em GDGTs contendo 86 átomos de carbono ("*TetraEther Index*")

TLE: Extrato de Lipídeos Totais ("*Total Lipid Extract*")

TMCS: trimetil-cloro- silano ("*trimethylchlorosilane*")

TN: Nitrogênio Total ("*Total Nitrogen*")

TOC: Carbono Orgânico Total ("*Total Organic Carbon*")

TW: Água Tropical ("*Tropical Water*")

TZ: Zona Terrestre ("*Terrestrial Zone*")

UCDW: Água Circumpolar Superior ("*Upper Circumpolar Deep Water*")

USGS: Serviço Geológico dos Estados Unidos ("*United States Geological Survey*")

$U^{K'}_{37}$: Índice de insaturação das alquenonas ("C_{37} *alkenone unsaturation index*")

WAIS: Plataforma de Gelo da Antártica Ocidental ("*West Antarctic Ice Sheet*")

YD: Dryas recente ("*Younger Dryas*")

LISTA DE SIGLAS

$\delta^{13}C$: Composição isotópica do Carbono ("*Carbon isotope composition*")

$\delta^{15}N$: Composição isotópica do Nitrogênio ("*Nitrogen isotope composition*")

$\delta^{18}O$: Composição isotópica do Oxigênio ("*Oxygen isotope composition*")

$\delta^{18}O_{sw}$: Composição isotópica do Oxigênio na água do mar ("*seawater Oxygen isotope composition*")

εNd: Excesso de Neodímio ("*Nd excess*")

SUMÁRIO

Capítulo 1 – Introdução 22

1. Justificativa 23

2. Objetivo e Hipóteses 24

3. Revisão Bibliográfica 25

3.1. Oscilações e Eventos Climáticos 25

3.2. Forçantes Ambientais 27

3.3. Marcadores Orgânicos Geoquímicos 31

Capítulo 2 36

Research Highlights 37

Abstract 38

Resumo 39

1. Introduction 40

2. Oceanographic Setting 41

3. Material and Methods 43

3.1. Sampling 43

3.2. Age Model 44

3.3. Lipid extraction and purification 44

3.4. Analytical methods 45

3.5. Data analysis 46

4. Results 47

5. Discussion 50

5.1. Temperature calibrations 50

5.2. Comparison of SST proxy records 53

5.3. Orbital- and Millennial-scale influences 58

6. Conclusions 63

Acknowledgments 64

Supplementary Data 64

Data Availability 64

References 65

Capítulo 3 ..... **76**

Research Highlights 77

Abstract 78

Resumo 79

1. Introduction 80

2. Study Area 82

3. Material and Methods 85

3.1. Sampling and Age Model 85

3.2. Bulk Parameters 86

3.3. Lipid extraction and purification 86

3.4. Analytical Methods 87

3.5. Data Processing 89

4. Results and Discussion 91

4.1. Grouping the proxies according to their temporal evolutions 93

4.2. Predominance of sources 97

4.3. Terrestrial OM 98

4.4. Marine OM 101

5. Summary and Conclusions 106

Acknowledgements 107

References 107

Capítulo 4 – Considerações Finais **122**

Referências Bibliográficas **125**

Apêndice 1 – Material Suplementar "A" do Capítulo 2 ..... **137**

Apêndice 2 – Material Suplementar “B” do Capítulo 2 140

Apêndice 3 – Material Suplementar do Capítulo 3 144

Apêndice 4 – Dados Brutos do Capítulo 3 157

CAPÍTULO 1 – INTRODUÇÃO

As mudanças climáticas em escala global e regional são assuntos muito debatidos na comunidade científica devido às suas implicações nas condições atuais e futuras do planeta. O clima da Terra muda em diferentes escalas de tempo (Crowley & Hyde, 2008; Zachos et al., 2001). Essas variações têm como base fatores naturais, como por exemplo, os ciclos de Milankovitch (Covey, 1984; Lisiecki et al., 2008) e os modos de variabilidades, como os fenômenos de Oscilação Sul (El Niño e La Niña) (Chavez et al., 2003; Lynam et al., 2004).

Dentre as diversas frequências de ciclicidades ambientais, os ciclos climáticos mais longos são os que tendem a apresentar um maior número de evidências geológicas, uma vez que a maior escala temporal faz com que as alterações ambientais sejam transmitidas e os seus efeitos, espalhados, pelo planeta através de conexões tanto atmosféricas quanto oceânicas (Clark et al., 2007; WAIS Divide Project Members, 2015). No entanto, ciclos e mudanças ambientais de menor escala temporal, como as variações na escala milenar, podem nem sempre ser bem registrados em todos os lugares do globo, dependendo da localização de onde estão sendo estudados. Um dos exemplos de ciclos ambientais que afetam o planeta Terra de forma diferente dependendo da região são os ciclos de precessão dos equinócios (de aproximadamente 26.000 anos). Neles, ocorre a intensificação das estações do ano em um hemisfério e o enfraquecimento do gradiente térmico no outro (Covey, 1984). A diferença de respostas a um mesmo fenômeno em diferentes regiões do planeta evidencia a importância de se estudar o clima em diversos ambientes e latitudes.

A identificação de alterações ambientais em diferentes escalas de tempo pode ser realizada através da aplicação de ferramentas biogeoquímicas, nas quais se encaixam os marcadores orgânicos geoquímicos. Eles têm sido utilizados para estudar processos naturais em diversos ecossistemas, incluindo o ambiente marinho, uma vez que tendem a manter a estrutura básica e até mesmo detalhes do grupo funcional da fonte original, resistindo às alterações diagenéticas (Derrien et al., 2017; Eglinton & Eglinton, 2008; Laureillard et al., 1997; Venkatesan & Kaplan, 1987).

1. Justificativa

A temática de mudanças climáticas assume posição cada vez mais relevante na vida moderna, com reflexos diretos sobre questões sociais, ambientais e econômicas. Não só o Painel Intergovernamental de Mudanças Climáticas (IPCC, 2014), mas também o Painel Brasileiro sobre Mudanças Climáticas (PBMC, 2014) destaca essa importância. No entanto, ambos também ressaltam que ainda há carência de dados e de pesquisadores/grupos de pesquisa atuantes em paleoceanografia no sudoeste do Atlântico.

Em função da complexidade das oscilações ambientais e do cenário de aquecimento global, predições climatológicas globais e regionais vêm recebendo atenção crescente (IPCC, 2014; Marengo et al., 2012) com o intuito de tentar prever quais as consequências da intervenção antrópica recente em cenários ambientais futuros. No entanto, trabalhos de predição climática esbarram na escassez de séries temporais de dados (PBMC, 2014). Nesse contexto, estudos de reconstrução climática e ambiental são importantes, uma vez que conseguem fornecer séries temporais que ultrapassam o limite das séries instrumentais, mostrando como mudanças climáticas naturais afetaram determinadas variáveis, como a temperatura do ar, e da superfície do mar ou os padrões de circulação oceânicas. O estudo desses parâmetros permite entender como as forçantes ambientais (principalmente internas) afetaram o clima durante o passado.

Assim, apesar de existirem diversas pesquisas realizadas recentemente em diferentes regiões do planeta buscando compreender o cenário climático atual e passado do clima, ainda há a necessidade de estudos adicionais sobre as mudanças ambientais em regiões específicas ainda pouco exploradas, como o Atlântico Sul. O Oceano Atlântico Sul apresenta um papel fundamental no transporte de calor entre as diversas bacias oceânicas (Clauzet et al., 2007), além de participar ativamente na formação de massas d'água (Garzoli & Matano, 2011). O entedimento das alterações climáticas ocorridas no Atlântico Sul permite melhorar a precisão das ferramentas empregadas na reconstrução das condições paleoambientais e na compreensão das oscilações ambientais recentes (Bechtel et al., 2007; Chiessi et al., 2014). Assim, se faz necessário primeiramente entender as oscilações naturais que afetam o clima no Atlântico Sul, para que seja possível distinguir entre efeitos naturais e a contribuição antropogênica nas mudanças climáticas atuais.

2. Objetivo e Hipóteses

O objetivo principal dessa tese é caracterizar as variações ambientais do Oceano Atlântico Sudoeste ocorridas nos últimos 70.000 anos (Pleistoceno Superior e Holoceno). A fim de atingir esse objetivo, as seguintes hipóteses foram testadas:

(i) Assumindo que diferentes *proxies* geoquímicos indicam a temperatura do mar em diferentes profundidades, será possível estimar variações na estratificação da coluna da água no Embaiamento Sul do Brasil a partir do Pleistoceno Superior.

(ii) Tendo em vista o padrão climático de gangorra ("*seesaw*") entre os hemisférios, espera-se que a temperatura da superfície do mar na porção oeste do Atlântico Sul responda mais a variações térmicas na Antártica do que a variações térmicas na Groelândia.

(iii) Estudos paleoambientais prévios na porção norte do Embaiamento Sul do Brasil observaram que a produtividade marinha foi governada pela ressurgência da Água Central do Atlântico Sul. No entanto, na porção sul do Embaiamento Sul do Brasil, outros autores observaram que produtividade primária respondeu ao aporte continental de nutrientes. Como a região estudada está localizada no talude e, portanto, afastada de ressurgências costeiras, assume-se que as mesmas forçantes governaram a produtividade marinha e a exportação de matéria orgânica terrestre desde o Pleistoceno Superior. Assim, tendo em vista o que foi observado nas regiões sul e norte do Embaiamento, espera-se que tenha ocorrido um maior aporte de ambas as fontes durante os períodos glaciais na região central.

Para testar essas hipóteses, foi utilizada uma abordagem *multiproxy* em um testemunho sedimentar coletado no talude da margem sudeste brasileira. Em relação às duas primeiras hipóteses, as temperaturas da superfície e subsuperfície do mar foram estimadas, utilizando como indicadores as razões $U^{K'}_{37}$, TEX_{86} e LDI. Já para testar a terceira hipótese, foram avaliadas variações do aporte e das fontes de matéria orgânica que alcançam o talude, utilizando como marcadores os *n*-alcanos, as alquenonas, os GDGTs, os *n*-alcanóis, os esteróis e os diols. Assim, as hipóteses foram abordadas no formato de artigos científicos. O primeiro artigo, referente às reconstruções de temperatura, foi publicado na revista "*Quaternary Science Reviews*". O segundo artigo, referente às variações no aporte de matéria

orgânica, está formatado de acordo com a revista "*Earth and Planetary Science Letters*".

3. Revisão Bibliográfica

3.1. Oscilações e Eventos Climáticos

O clima no planeta Terra é afetado por forçantes externas (como a variação da insolação no planeta Terra) e internas (como mudanças nas circulações atmosférica e oceânica), em diversas escalas temporais. Além da escala orbital (Covey, 1984), a comunidade científica tem reportado mudanças climáticas também na escala milenar (Barrows et al., 2007) dentro do Último Período Glacial (115.000 a 11.700 anos atrás; Bereiter et al., 2012).

Na escala orbital (Covey, 1984), são observados três ciclos com distintas periodicidades. O ciclo mais longo deles é relacionado à excentricidade da órbita terrestre (de 100.000 anos), que descreve a distância entre a Terra e o Sol (órbita circular ou elíptica) e afeta a quantidade de radiação solar que chega à Terra. O segundo ciclo é relacionado à inclinação (ou obliquidade) do eixo terrestre (de 41.000 anos). Ele descreve o ângulo do eixo de rotação da Terra em relação à órbita ao redor do sol e afeta a distribuição da radiação solar na Terra, causando invernos mais frios e verões mais quentes em ambos os hemisférios. Este ciclo também está relacionado com a mudança no volume de gelo das calotas polares (Schmidt et al., 2006). O ciclo orbital mais curto é o da precessão dos equinócios (que varia entre 22.000 e 26.000 anos), que descreve o "giro" do planeta ao redor do seu eixo. Ele afeta a distribuição sazonal da radiação solar na Terra, intensificando as estações em um hemisfério e amenizando no outro (Schmidt et al., 2006).

Ainda na escala orbital, os ciclos mais reconhecidos são os ciclos glaciais e interglaciais representados pelos Estágios Isotópicos Marinhos (MIS – "*Marine Isotope Stages"*, "*Marine Oxygen-Isotope Stages"* ou "*Oxygen Isotope Stages"*) (Emiliani, 1955; Lisiecki & Raymo, 2005; Railsback et al., 2015). Esses estágios foram deduzidos a partir da composição isotópica de oxigênio ($\delta^{18}O$) em testas de foraminíferos bentônicos obtidas em testemunhos sedimentares coletados em oceano profundo, os quais refletem mudanças na temperatura das águas oceânicas e mudanças no volume de gelo global. Considerando a partir do presente, que é o MIS 1 na escala, os estágios com números pares têm altos níveis de ^{18}O na água do mar (e alta razão isotópica $\delta^{18}O$) e representam períodos glaciais frios, enquanto as

fases ímpares apresentam baixos valores de ^{18}O na água do mar (e baixa razão isotópica $\delta^{18}O$), representando intervalos interglaciais quentes (Emiliani, 1955).

Na escala milenar, os eventos climáticos mais bem descritos são os eventos Heinrich (Hemming, 2004) e as oscilações Dansgaard-Oeschger (D-O) (Voelker, 2013) no Hemisfério Norte, e os Máximos Isotópicos Antárticos (AIM – "*Antarctic Isotope Maximum*") (EPICA Community Members, 2006) no Hemisfério Sul. Os eventos Heinrich são momentos quando ocorreram enormes liberações de *icebergs* no Atlântico Norte a partir da calota de gelo Laurenciano, em decorrência de uma instabilidade nas calotas polares (Delworth et al., 2008). Esse imenso aporte de água doce no norte do Oceano Atlântico fez com que a água superficial ficasse menos densa (apesar de fria) e não afundasse. Isso causou uma diminuição na formação da Água Profunda do Atlântico Norte (NADW – "*North Atlantic Deep Water*"). Além disso, os eventos Heinrich foram seguidos por períodos de resfriamento na região do Atlântico Norte, conhecidos como "*Heinrich stadial*" (HS) (Hemming, 2004).

Ainda considerando a escala milenar, a ocorrência dos períodos HS coincide com alguns estágios frios ("*stadial*") das oscilações D-O (Lynch-Stieglitz, 2017). Segundo Bond et al. (1993), durante o Último Período Glacial, períodos longos de resfriamento gradual ("*stadial*") foram seguidos por períodos de aquecimento abrupto ("*interstadial*"). Essas oscilações apresentam uma frequência de ocorrência na média de 10.000 a 15.000 anos, e ocorreram 25 vezes ao longo dos últimos 80 mil anos (Bond et al., 1993).

Tanto os eventos Heinrich quanto as oscilações D-O são mais perceptíveis no Hemisfério Norte e nem sempre são registradas da mesma forma no Hemisfério Sul (Delworth et al., 2008). Analisando a composição isotópica de oxigênio em testemunhos de gelo coletados na Antártica, foi possível identificar diversos períodos de aquecimento que coincidem com os períodos de resfriamento (HS) no Hemisfério Norte. Esses eventos foram nomeados de Máximos Isotópicos Antárticos (AIM) e evidenciam um padrão climático de gangorra entre os hemisférios (EPICA Community Members et al., 2006).

Além dos eventos cíclicos, alguns eventos extremos foram registrados a partir do final do Último Período Glacial: o Último Máximo Glacial (LGM – "*Last Glacial Maximum*"), o evento Bølling-Allerød, a Reversão Fria da Antártica (ACR – *"Antarctic Cold Reversal"*) e o *Younger Dryas* (YD). O LGM ocorreu entre 23.000 e 19.000

anos atrás, e foi um período com baixas concentrações de CO_2 atmosférico (Jaccard et al., 2016) e baixas temperaturas do ar, especialmente no Hemisfério Norte (Broccoli et al., 2006). O nível médio do mar estava aproximadamente 120 m abaixo do atual, com cerca de 30% dos continentes cobertos por gelo (Delworth et al., 2008). O oceano profundo passou por um resfriamento (Clark et al., 2009), causado principalmente pelo avanço da Água Antártica de Fundo (AABW – "*Antarctic Bottom Water*") em detrimento da Água Profunda do Atlântico Norte (NADW – "*North Atlantic Deep Water*") (Marchitto & Broecker, 2006). Já as temperaturas de superfície do mar apresentaram variações regionais em vez de uma tendência global de resfriamento (Mix et al., 2001). Enquanto a superfície dos oceanos resfriou em altas latitudes e em regiões subtropicais influenciados por ressurgências costeiras (Clauzet et al., 2007; Kim & Schneider, 2003; Mix et al., 2001), as regiões dos giros subtropicais, especialmente no Oceano Pacífico, passaram por um leve aquecimento (Mix et al., 2001; Pereira et al., 2018). O evento denominado de Bølling-Allerød foi um período de aquecimento abrupto registrado no Hemisfério Norte, por volta de 14.600 anos atrás, no qual o calor do Hemisfério Sul foi transportado para o Hemisfério Norte (Thiagarajan et al., 2014). Nesse mesmo período (entre 14.700 e 13.000 anos atrás), no Hemisfério Sul, ocorreu a ACR, um importante evento de resfriamento durante a deglaciação (Graham et al., 2017). Por fim, o YD foi um período de resfriamento abrupto no Hemisfério Norte, entre 12.900 e 11.700 anos atrás, quando a circulação oceânica no Atlântico (principalmente Norte) apresentava características similares às do LGM (Alley, 2000).

3.2. Forçantes Ambientais

Oscilações climáticas são moduladas por variações no padrão de circulação atmosférica e oceânica (Böhm et al., 2015; Hemming, 2004). Vários autores utilizam o atual padrão sazonal das circulações atmosférica e oceânica superficial para exemplificar os períodos glaciais e interglaciais (Arz et al., 1999; Hessler et al., 2010; Toledo et al., 2008; Venancio et al., 2018). Isso porque o padrão sazonal de insolação afeta os dois hemisférios de forma diferente. Assim, os períodos glaciais são relacionados ao atual inverno boreal, enquanto os períodos interglaciais são relacionados ao atual inverno austral.

No início dos períodos glaciais, ocorreu uma diminuição da insolação no Hemisfério Norte e um aumento no Hemisfério Sul (Berger & Loutre, 1991). Esse

aquecimento diferenciado da superfície do mar entre os hemisférios promoveu um aquecimento do ar no Hemisfério Sul em relação ao Hemisfério Norte. Essa diferença térmica, por sua vez, gerou um gradiente de pressão atmosférico que promoveu o fortalecimento dos ventos alísios de nordeste (Venancio et al., 2018). Essa disposição dos alísios migrou a Zona de Convergência Intertropical (ITCZ – "*Intertropical Convergence Zone*") para sul (Clark et al., 2007). Essa migração ao sul permitiu que a umidade do Oceano Atlântico fosse transportada para a América do Sul (Hessler et al., 2010), promovendo o fortalecimento da Zona de Convergência do Atlântico Sul (SACZ – "*South Atlantic Convergence Zone*") (Carvalho et al., 2004; Chiessi et al., 2014). Ainda, é provável que o fortalecimento dos alísios de nordeste na costa brasileira promoveu uma circulação anticiclônica na região, gerando um avanço para o norte do giro subtropical do Atlântico Sul (Rodrigues et al., 2007). Esse avanço provavelmente causou a migração da bifurcação da Corrente Equatorial Sul (SEC – "*South Equatorial Current*") para norte, o que por sua vez fortaleceu a Corrente do Brasil (BC – "*Brazil Current*"), diminuindo assim o transporte de calor para o Hemisfério Norte (Rodrigues et al., 2007; Toledo et al., 2008).

Ainda durante os períodos glaciais, também foi observada uma migração para sul dos ventos de deriva oeste e, portanto, da frente subtropical (De Deckker et al., 2012). Essa mudança no padrão de ventos empurrou a Corrente Circumpolar Antártica (ACC – "*Antarctic Circumpolar Current*") para perto do continente Antártico e promoveu a intrusão no Atlântico Sul de águas quentes e salinas provenientes do Oceano Índico, através do vazamento da Corrente das Agulhas (Clauzet et al., 2007; De Deckker et al., 2012).

Já durante intervalos interglaciais, a maior incidência solar no Hemisfério Norte aqueceu a superfície do mar, que transferiu calor para a atmosfera e baixou a pressão atmosférica no Hemisfério Norte (Berger & Loutre, 1991). Esse gradiente de pressão, por sua vez, fortaleceu os ventos alísios de sudeste (Kim & Schneider, 2003), que migraram a ITCZ para norte (Clark et al., 2007). Isso resultou em um padrão de chuvas que promove um clima mais úmido no norte da África e menos úmido na América do Sul (Hessler et al., 2010). Essa intensificação dos ventos alísios de sudeste provavelmente fortaleceu o giro ciclônico que existe na porção leste do Atlântico Sul, estendendo-o até a costa brasileira. Essa expansão do giro tropical ciclônico pode ter causado uma migração para sul do giro subtropical anticiclônico (Rodrigues et al., 2007). Isso provavelmente fez com que a bifurcação

da SEC provavelmente migrasse para sul, fortalecendo a Corrente Norte do Brasil (NBC – "*North Brazil Current*") e intensificando o transporte superficial de calor para o Hemisfério Norte (Arz et al., 1999; Rodrigues et al., 2007; Venancio et al., 2018).

Por fim, similarmente ao que aconteceu durante os períodos glacias, a distribuição dos ventos de deriva oeste acompanhou a migração da ITCZ (De Deckker et al., 2012). Essa migração ao norte enfraqueceu a ACC (Buizert & Schmittner, 2015) e diminuiu o volume de águas quentes transportado pelo vazamento da Corrente das Agulhas (De Deckker et al., 2012).

Além da circulação oceânica superficial, a circulação termohalina também apresenta um papel fundamental no sistema climático da Terra (Delworth et al., 2008; McManus et al., 2004). A Circulação Meridional do Atlântico (AMOC – "*Atlantic Meridional Overturning Circulation*") consiste em um fluxo superficial para norte de águas quentes equilibrado por um fluxo para sul de águas frias, através da formação da NADW (Buizert & Schmittner, 2015; Lynch-Stieglitz, 2017; Stocker & Johnsen, 2003). Segundo Böhm et al. (2015), a AMOC pode apresentar três modos distintos: o modo quente, o modo frio, ou o modo colapsado ("*off*").

O modo quente está relacionado às variações da radiação solar na escala orbital. O aquecimento da superfície do Oceano Austral leva a um inicial derretimento das calotas polares e diminuição da densidade da camada superficial do mar. Essa mudança na densidade gera um rápido decréscimo na formação da AABW. Essa gera um aumento no gradiente de densidades entre o Oceano Austral e o Atlântico Norte, promovendo lentamente a formação da NADW (Buizert & Schmittner, 2015). Nesse modo, a NADW ocupa uma grande porção da bacia Atlântica até os 5.000 m de profundidade (Böhm et al., 2015). Esse grande volume de água afundado é reposto pelas águas superficiais tropicais, o que mantém o Hemisfério Norte aquecido (Böhm et al., 2015). Assim, em seu modo quente, a AMOC está estável e pouco suscetível a perturbações originadas no Hemisfério Norte, como os eventos Heinrich (Buizert & Schmittner, 2015).

O modo frio está relacionado a uma AMOC menos estável e mais suscetível a eventos extremos no Hemisfério Norte (Buizert & Schmittner, 2015). Quando o Oceano Austral é resfriado, a densidade da água superficial aumenta e promove a formação da AABW. Essa, então, passa a preencher boa parte da bacia Atlântica (Buizert & Schmittner, 2015). A água formada na região da Groelândia passa a ocupar profundidades mais rasas, passando a ser chamada de Água Intermediária

Glacial do Atlântico Norte (GNAIW – "*Glacial North Atlantic Intermediate Water*") (Böhm et al., 2015).

Durante os períodos em que a AMOC se encontra no modo frio, liberações maciças de *icebergs* no Hemisfério Norte (eventos Heinrich) podem levar ao seu colapso (AMOC modo "*off*") (Böhm et al., 2015; Buizert & Schmittner, 2015). Durante esses eventos, o aporte de água doce causa uma diminuição drástica da densidade da água do mar na região da Groelândia e, portanto, da formação de águas profundas (McManus et al., 2004). Nesses cenários, a AABW acaba ocupando toda a bacia Atlântica abaixo dos 1.000 m de profundidade (Böhm et al., 2015; Buizert & Schmittner, 2015; Lynch-Stieglitz, 2017).

Apesar de o fortalecimento e/ou enfraquecimento da AMOC ser muitas vezes definido pela maior e/ou menos formação da NADW (Lynch-Stieglitz, 2017), a bacia do Atlântico Sul apresenta um papel fundamental no balanço de massa e de calor da AMOC. Garzoli e Matano (2011) fizeram uma revisão sobre a importância dos processos de formação de massas d'água no Atlântico Sul e do transporte entre bacias oceânicas para esse balanço. De modo geral, águas intermediárias e frias são importadas do Oceano Pacífico pelo estreito de Drake, enquanto águas superficiais quentes são importadas do Oceano Índico através da retroflexão da Corrente das Agulhas (Dong et al., 2011; Stramma & England, 1999). Dessa forma, embora a força do AMOC seja determinada pela convecção no Atlântico Norte, essa convecção é altamente sensível às propriedades do fluxo de retorno, especificamente se é dominada por contribuições dos oceanos Índico ou Pacífico. Assim, a convecção no Atlântico Norte é, em grande medida, dependente do tipo de massa de água que o Atlântico Sul exporta (Garzoli & Matano, 2011; Kuhlbrodt et al., 2007).

Além disso, algumas regiões do Atlântico Sul são mais sensíveis às variações na AMOC. Durante períodos de AMOC enfraquecida, ocorre um decréscimo no gradiente de densidade entre as regiões equatorial e subtropicais. Esse decréscimo afeta os padrões de circulação superficial, governada pelos ventos, o que acarreta o aprofundamento da termoclina na região da corrente de Benguela, diminuindo a ressurgência na região e aumentando a temperatura superficial (Rahmstorf et al., 2015; Venancio et al., 2018). Ainda, em função da menor exportação de águas superficiais quentes durante períodos de AMOC enfraquecida, estudos sugerem que ocorra um acúmulo de calor na margem oeste do Atlântico Sul (Rahmstorf et al.,

2015; Santos et al., 2017; Srokosz et al., 2012). No entanto, devido à grande variabilidade dos processos de troca de massa e de calor em mesoescala, a resposta do Atlântico Sul às variações da AMOC nem sempre são uniformes entre diferentes estudos (Muir & Fedorov, 2015; Srokosz et al., 2012).

Sendo assim, sobrepostas às variações climáticas e oceanográficas na escala orbital, as oscilações climáticas de escala milenar podem ser entendidas como amortecedores climáticos (Buizert & Schmittner, 2015). Durante períodos quentes/interglaciais da AMOC estável, ocorre um aquecimento do Oceano Austral devido a forçantes externas. No entanto, esse aquecimento do Hemisfério Sul é contrabalanceado pela exportação de calor para o Hemisfério Norte através das correntes superficiais durante as fases quentes das oscilações D-O (Buizert & Schmittner, 2015; Delworth et al., 2008). O aquecimento do Hemisfério Norte leva ao degelo das calotas polares e ao consequente aumento no aporte de água doce (eventos Heinrich) (Hemming, 2004). Isso diminui a densidade superficial no Atlântico Norte, restringe temporariamente a formação de NADW e promove um acúmulo de calor no Hemisfério Sul (Delworth et al., 2008; Hemming, 2004). A sucessão de fases quentes e frias das oscilações D-O gera condições progressivamente mais frias no Hemisfério Sul, caracterizando assim o cenário climático do MIS 3 (Buizert & Schmittner, 2015). Isso acaba desestabilizando a AMOC, que entra no seu modo frio/glacial, com menos formação de águas profundas na região da Groelândia. Nesse estágio, a AMOC fica mais susceptível a eventos extremos de degelo no Hemisfério Norte, que podem acabar colapsando o transporte meridional de calor no Oceano Atlântico. Como consequência, existe uma tendência de acúmulo de calor no Hemisfério Sul (Stocker & Johnsen, 2003).

3.3. Marcadores Orgânicos Geoquímicos

Devido à inexistência de dados medidos de parâmetros ambientais (tais como temperatura do ar, temperatura do mar, salinidade, ...) em períodos anteriores ao ser humano, as ciências paleoambientais utilizam *proxies* para estimar tais parâmetros. Os *proxies* paleoclimáticos são materiais físicos, químicos e biológicos preservados dentro do registro geológico que podem ser analisados e correlacionados com parâmetros climáticos ou ambientais no mundo moderno. Assim, é possível estimar indiretamente esses parâmetros.

Existem diversas classes lipídicas que podem ser utilizadas como *proxies* para avaliar alterações climáticas e de fontes de matéria orgânica no ambiente marinho (Eglinton & Eglinton, 2008). Dentre elas, as classes que são abordadas neste estudo são os hidrocarbonetos alifáticos (AHs – "*Aliphatic Hydrocarbons*"), as alquenonas, os glicerol dialquil – glicerol tetraéteres (GDGTs – "*Glycerol Dialkyl-Glycerol Tetraethers*"), os *n*-alcanóis, os esteróis e os diols de cadeia longa.

Os AHs podem estar presentes nas ceras epicuticulares de plantas superiores, além de serem biossintetizados pelo fitoplâncton, bactérias e macrófitas aquáticas (Eglinton & Eglinton, 2008; Volkman et al., 1987; Zhou et al., 2010). Dentre os AHs, os compostos mais utilizados para avaliar as fontes de matéria orgânica no ambiente marinho são os *n*-alcanos, hidrocarbonetos de cadeia aberta e não ramificada. De modo geral, os *n*-alcanos biossintetizados apresentam predominantemente número ímpar de carbonos na sua cadeia. Compostos de cadeias curtas (15 a 19 átomos de carbono) são geralmente associados ao fitoplâncton (Volkman et al., 1992b). Já *n*-alcanos contendo 21, 23 e 25 átomos de carbono são geralmente associados a plantas submersas e flutuantes (macrófitas). Compostos contendo de 27 a 35 átomos de carbono são geralmente produzidos por plantas superiores (Eglinton & Eglinton, 2008; Holland et al., 2013; Zhou et al., 2010). Cadeias mais curtas, contendo entre 15 e 17 átomos de carbono também podem ser associadas à presença de microalgas e cianobactérias

Na paleoceanografia, o termo "alquenonas" se refere a uma série de cetonas de cadeia longa (C_{35} – C_{40}) di- ($C_{n:2}$), tri- ($C_{n:3}$) e tetra-insaturadas ($C_{n:4}$) (Ho et al., 2013). Atualmente, elas são sintetizadas por um número restrito de algas haptófitas, as quais incluem principalmente os cocolitoforídeos da família *Gephyrocapsaceae* (como a *Emiliania huxleyi* e a *Gephyrocapsa oceanica*), que vivem nas camadas superficiais dos oceanos em temperaturas que variam entre 2 e 29 °C (Ho et al., 2013; Volkman et al., 1980). Assim, a concentração das alquenonas pode ser utilizadas como indicadoras de paleoprodutividade de algas haptófitas. Temperaturas mais quentes favorecem a produção de alquenonas di-insaturadas ($C_{37:2}$) se comparado às tri-insaturadas ($C_{37:3}$) (Prahl & Wakeham, 1987). Com o intuito de correlacionar o grau de insaturação com a temperatura da superfície do mar (SST), foram desenvolvidos experimentos de cultivo de *E. huxleyi* sob diferentes temperaturas. Os resultados mostraram uma relação linear entre o índice $U^{K'}_{37}$ (índice de insaturação das alquenonas) e temperaturas na faixa entre 8 e 25 °C

(Conte et al., 2006; Prahl & Wakeham, 1987). No entanto, o uso dessa razão pode apresentar desvios ocasionais em função da redistribuição lateral de sedimentos, da exportação da produção advinda da região abaixo da zona eufótica e de estresses fisiológicos (como baixa disponibilidade de luz e de nutrientes) (Ho et al., 2013; Mollenhauer et al., 2015). Ainda assim, as alquenonas vêm sendo muito utilizadas em estudos de paleoceanografia (Chen et al., 2014; Jaccard et al., 2016; Kaiser et al., 2014), inclusive no Atlântico Sul (Lourenço et al., 2016; Pahnke and Sachs, 2006; Schneider et al., 1996), sendo considerado um dos *proxies* de SST mais robustos devido ao baixo erro associado às suas calibrações (Ho et al., 2013).

Os GDGTs estão presentes nas membranas lipídicas biossintetizadas por arqueias e bactérias (Schouten et al., 2002). Eles ocorrem no ambiente sob duas formas principais: isoprenoide (isoGDGTs – "*isoprenoid GDGTs*") e ramificada (brGDGTs – "*branched GDGTs*"), dependendo do organismo-fonte. Os isoGDGTs são produzidos principalmente por arqueias, podendo apresentar até oito anéis pentacíclicos e um anel hexacíclico. Os isoGDGTs mais comuns nos ambientes marinho e lacustre são o isoGDGT-0 e o crenarqueol (Schouten et al., 2002; Sinninghe Damsté et al., 2002). O aumento no número de anéis pentacíclicos nos isoGDGTs presentes na composição das membranas de arqueias é uma adaptação para suportar aumentos na temperatura (Sinninghe Damsté et al., 2002). Com base nesse aumento, foi sugerido o uso do índice TEX_{86} ("*TetraEther Index*"), baseado em GDGTs contendo 86 átomos de carbono. Ele reflete, principalmente, variações das médias anuais da SST entre 5 e 30 °C (Schouten et al., 2002). Baseado nesse índice, diversas calibrações para determinar a SST já foram desenvolvidas, sendo as mais recentes de Kim et al. (2010) e Tierney e Tingley (2014).

Os brGDGTs, por sua vez, possuem uma cadeia linear com número variável de ramificações (dois a seis radicais metil) e de anéis pentacíclicos (zero a dois). Eles podem ser produzidos tanto por bactérias quanto por arqueias. Suas biossínteses ocorrem principalmente em solos e turfas (Schouten et al., 2013), mas também podem ser produzidos por arqueias em sedimentos marinhos e lagunares (Pearson et al., 2011). Uma vez que os isoGDGTs são encontrados principalmente em ambientes aquáticos, e os brGDGTs são associados principalmente a bactérias encontradas em solos e turfas, Hopmans et al. (2004) sugeriram o uso do índice BIT ("*Branched and Isoprenoid Tetraether Index*") para avaliar a influência de aportes terrígenos no ambiente aquático.

Os *n*-alcanóis são compostos de cadeia aberta e não ramificada que contêm um grupo funcional hidroxila na extremidade da cadeia carbônica. Ao contrário do que acontece com os *n*-alcanos, os *n*-alcanóis biossintetizados tendem a apresentar uma forte predominância de cadeias carbônicas contendo número par de átomos de carbono (Eglinton & Eglinton, 2008). Entretanto, assim como os *n*-alcanos, os *n*-alcanóis podem ser utilizados para distinguir as fontes da matéria orgânica dependendo do tamanho da cadeia carbônica (Volkman, 2006). Compostos de cadeia carbônica curta, com menos de 22 átomos de carbono, geralmente são associados a fontes marinhas, enquanto compostos contendo entre 22 e 32 átomos de carbono podem ser associados a ceras epicuticulares de plantas superiores, líquens e musgos (Hu et al., 2009; Volkman, 2006; Wisnieski et al., 2014). O fitol encontrado em ambientes marinhos é derivado principalmente da degradação da clorofila-*a* (Shi et al., 2001; Volkman et al., 2008), mas também pode ser produzido pela degradação bacteriana da matéria orgânica (Bechtel and Schubert, 2009). Apesar da sua natureza mais lábil se comparado aos *n*-alcanóis, altas concentrações de fitol geralmente indicam importantes contribuições de matéria orgânica marinha (Costa et al., 2010).

Assim como no caso das alquenonas, em paleoceanografia o termo “diols” se refere a uma série de *n*-alcanóis de cadeia longa (C_{24} – C_{36}), contendo dois grupos hidroxila, sendo um deles na posição 1 e o outro no meio da cadeia carbônica (Rampen et al., 2012). São sintetizadas principalmente por algas eustigmatofíceas, podendo também ser sintetizadas por alguns grupos de diatomáceas (Volkman et al., 1998, 1992a). Apesar de raramente serem encontrados em algas marinhas, Rampen et al. (2012) observaram que existe uma relação entre a SST e a razão entre alguns diols, sugerindo assim o uso do índice LDI (“*Long chain Diol Index*”) para reconstruções de paleotemperatura em ambientes marinhos.

Os esteróis estão entre os marcadores mais fonte-específicos e com maior diversidade estrutural dentre os diversos marcadores orgânicos, e podem ser utilizados para identificar aportes de algas marinhas, zooplâncton, animais homeotérmicos e plantas superiores (Burns & Brinkman, 2011; Faux et al., 2011; Volkman, 1986). Em se tratando da sua estrutura química, são compostos derivados do ciclopentanoperidrofenantreno que apresentam um esqueleto carbônico básico constituído de 17 a 30 átomos de carbono e um grupo hidroxila no carbono da posição 3, podendo apresentar radicais metil, em especial nos carbonos 10 e 13

(Volkman, 2003). Dentre os principais esteróis em ambientes marinhos, encontram-se os esteróis colesterol ($27\Delta^{5}$), dehidrocolesterol ($27\Delta^{5,22E}$), brassicasterol ($28\Delta^{5,22E}$), campesterol ($27\Delta^{5}$), estigmasterol ($29\Delta^{5,22E}$), sitosterol ($29\Delta^{5}$) e dinosterol ($30\Delta^{22}$). O colesterol está presente em algumas espécies de microalgas, cianobactérias, no zooplâncton e nas suas pelotas fecais, sendo esta a principal fonte de colesterol para os sedimentos marinhos (Volkman, 1986). O dehidrocolesterol e o brassicasterol estão geralmente associados a florações fitoplanctônicas, especialmente de diatomáceas (Mudge et al., 1999; Volkman, 1986). O sitosterol e o estigmasterol podem estar relacionados ao fitoplâncton, às macroalgas e às plantas vasculares (Volkman, 1986), assim como o campesterol, que ainda pode indicar a presença de fungos (Volkman, 2003). O dinosterol é um esterol específico, sendo predominantemente relacionado à presença de dinoflagelados (Volkman, 1986).

CAPÍTULO 2

Reconstrução das temperaturas de superfície e de subsuperfície do mar no Oceano Atlântico Sudoeste ao longo dos últimos 75 mil anos baseada em marcadores moleculares

"*Multi-proxy reconstruction of sea surface and subsurface temperatures in the western South Atlantic over the last ~ 75 kyr*"

Manuscrito formatado segundo as normas da revista:

Quaternary Science Reviews; ISSN (0277-3791); Fator de Impacto: 4,334

© Thomson Reuters Journal Citation Reports 2017

Qualis CAPES (Biodiversidade): Estrato A2

Status do artigo: Aceito (dia 23/abril/2019).

* Ana Lúcia L. Dauner [1,2], * Gesine Mollenhauer [3,4], * Márcia Caruso Bícego [5], Mihael Machado de Souza [6], Renata Hanae Nagai [1], Rubens César Lopes Figueira [5], Michel Michaelovitch de Mahiques [5,7], Silvia Helena de Mello e Sousa [5], * César C. Martins [1]

[1] Center for Marine Studies, Federal University of Paraná, 83255-976 Pontal do Paraná, PR, Brazil

[2] Graduate Program in Coastal and Oceanic Systems (PGSISCO) of the Federal University of Paraná, 83255-976 Pontal do Paraná, PR, Brazil

[3] Alfred Wegener Institute, Helmholtz Center for Polar and Marine Research, D-27515 Bremerhaven, Germany

[4] MARUM Center for Marine Environmental Sciences, University of Bremen, D-28334 Bremen, Germany

[5] Oceanographic Institute, University of São Paulo, 05508-120 São Paulo, Brazil

[6] Institute of Oceanography, Hamburg University, D-20146 Hamburg, Germany

[7] Institute of Energy and Environment, University of São Paulo, 05508-120 São Paulo, Brazil

Corresponding authors:

* anadauner@gmail.com (A.L.L. Dauner)

* gesine.mollenhauer@awi.de (G. Mollenhauer)

* marciabicego@usp.br (M.C. Bícego)

* ccmart@ufpr.br (C.C. Martins)

Research Highlights

> Distinct proxies represented different water depths based on the local biota.

> A more mixed water column (0-30 m) was observed during cooling periods.

> The SST presented a millennial-scale oscillation with an 8 kyr periodicity.

> NADW formation may have caused SST millennial-oscillations in the SW Atlantic.

Abstract

Millennial-scale oscillations are known to be important in the climatic evolution of the Atlantic basin, but which internal processes originates these oscillations are still uncertain. In this study, we investigated how the Greenland and Antarctic climates affect the SW Atlantic through basin-wide oceanographic features (such as the NADW formation and the Agulhas leakage). We reconstructed sea surface and subsurface temperatures (SST and subT) using three lipid-based biomarker proxies ($U^{K'}_{37}$, TEX_{86} and LDI indexes) from a sediment core (NAP 63-1) retrieved from the SW Atlantic slope (24.8°S, 44.3°W). This location permitted to evaluate the temperature oscillations of the Brazil Current without any terrigenous or upwelling-derived biases. Both TEX_{86}-based and LDI-based estimates represent the mean annual SST, while the $U^{K'}_{37}$-based estimates represent the subT (around 30 m water depth). The periods with the most well-mixed water column were observed during intervals of cooling orbital trends due to the time required to transfer the surface cooling to the subsurface. The temperature reconstructions showed a general colder MIS 3 when compared to the MIS 4. They also showed evidence of a late response to the deglaciation, with its onset in the SW Atlantic occurring in the middle of the Last Glacial Maximum. Based on these reconstructions, the NAP 63-1 SST orbital-scale trend seems to be linked to the Antarctic climate, influenced by local insolation changes. These temperature records also presented a clear millennial periodicity around 8 kyr. On this timescale, the millennial oscillations in the SW Atlantic's SST are likely linked to the NADW formation.

Keywords: $U^{K'}_{37}$; TEX_{86}; LDI; Holocene; Pleistocene; Paleoceanography; Organic geochemistry.

Resumo

Oscilações na escala milenar são reconhecidamente importantes na evolução climática do Oceano Atlântico, mas os processos internos que originam essas oscilações ainda não são bem conhecidos. Neste estudo, nós investigamos como os climas da Antártica e da Groelândia afetam o sudoeste do Oceano Atlântico através de fenômenos oceanográficos que abrangem toda a bacia Atlântica (como a formação da Água Profunda do Atlântico Norte e o vazamento da Corrente das Agulhas). Nós reconstruímos das temperaturas de superfície e de subsuperfície do mar (SST e subT), utilizando três classes de marcadores orgânicos geoquímicos (índices $U^{K'}_{37}$, TEX_{86} e LDI), a partir de um testemunho sedimentar (NAP 63-1) coletado no talude continental do sudoeste do Atlântico Sul (24,8°S; 44,3°W). A localização do testemunho nos permitiu avaliar as oscilações de temperatura da Corrente do Brasil sem interferências geradas pelo aporte continental ou pela ressurgência costeira. Tanto as estimativas de temperatura baseadas no índice TEX_{86} quanto as baseadas no índice LDI representaram a média anual da SST, enquanto as estimativas baseadas no índice $U^{K'}_{37}$ representaram a temperatura da subsuperfície (por volta dos 30 m de profundidade). Uma coluna d'água mais homogênea foi observada durante os períodos com tendência orbital de resfriamento da superfície. O tempo necessário para o resfriamento superficial ser transferido para camadas mais fundas da coluna d'água causou essa homogeneização das temperaturas. As reconstruções das temperaturas apresentaram um Estágio Marinho Isotópico (MIS) 3 mais frio se comparado ao MIS 4. Além disso, foi observada uma resposta tardia à última deglaciação, sendo que o seu início, para a região estudada, ocorreu durante o meio do Último Máximo Glacial. Baseado nas três reconstruções, a tendência de temperaturas na escala orbital parece estar ligada às mudanças no clima da Antártica, que por sua vez é influenciado por mudanças locais de insolação. As reconstruções de temperatura também apresentaram uma periodicidade na escala milenar por volta dos 8 mil anos. Nessa escala temporal, as oscilações milenares foram relacionadas com a formação da Água Profunda do Atlântico Norte.

Palavras-chave: $U^{K'}_{37}$, TEX_{86}, LDI, Holoceno, Pleistoceno, Paleoceanografia, Geoquímica Orgânica.

1. Introduction

Earth's climate oscillates at multiple timescales and is forced by different environmental triggers (Crowley and Hyde, 2008; Zachos et al., 2001). Millennial-scale oscillations are known to be important in the climatic evolution of the Atlantic basin and the Southern Ocean, especially during the Last Glacial Period (Clark et al., 2007). Nevertheless, there is an uncertainty as to which internal processes these cycles originate from (Barrows et al., 2007; Capron et al., 2010; Jaeschke et al., 2007; Sanchez Goñi and Harrison, 2010). The European Project for Ice Coring in Antarctica (EPICA) Community Members (2006) suggested that the Atlantic Meridional Overturning Circulation (AMOC) causes a strong interhemispheric coupling of bipolar millennial-scale oscillations, such as the Dansgaard-Oeschger (D-O) events (Delworth et al., 2008) and the warm Antarctic Isotope Maxima (AIM) events (EPICA Community Members 2006). However, there is an ongoing debate regarding how these oscillations are transferred from the poles to the oceans. In the South Atlantic, the propagation of thermal anomalies between Antarctica and the ocean is slowed by the presence of the Antarctic Circumpolar Current (ACC), which represents a dynamical and thermal boundary between high and mid-latitudes (Barker et al., 2009). Thus, the ACC may limit Antarctica's influence on the Southern Hemisphere's climate. Moreover, a response of the Southern Hemisphere climate to changes in Greenland, or the drivers behind them, has also been observed (Costa et al., 2016; Lourenço et al., 2016; Rommerskirchen et al., 2011).

The South Atlantic acts as a unifying link, exchanging water and heat between the world's major ocean basins. It is the only basin in the Southern Hemisphere in which heat is transported equatorward (Clauzet et al., 2007). Stocker and Johnsen (2003) suggested that the South Atlantic should be considered as a heat reservoir which dampens and integrates in time the abrupt climate signals that originate in the North Atlantic. In this context, the gradual Antarctic response may be the consequence of heat accumulation within the South Atlantic during the AMOC slowdown periods combined with a possible increase in the Agulhas leakage (Barker et al., 2009; Clark et al., 2007; Dyez et al., 2014). On the other hand, Garzoli and Matano (2011) concluded that the South Atlantic is not just a passive conduit for the passage of water masses formed in other regions of the world ocean but instead actively participates in their transformation. They observed that a shutdown of the Agulhas Current influences the deep-water formation in the North Atlantic with conspicuous consequences for the AMOC. This same relation between the Agulhas leakage and the AMOC was reported by Caley et al. (2014) during the last 640 kyr. Studying the Drake Passage, Roberts et al. (2017a)

found that variations in the relative density of southern water masses, when compared to the North Atlantic Deep Water (NADW) could affect the AMOC re-invigorations.

The identification of the climate evolution in the oceans to a large extent relied on the use of biogeochemical proxies, among which are the geochemical organic markers based on lipid biomarkers. The most common lipid classes used in oceanic paleotemperature reconstructions are the alkenones (Conte et al., 2006), the glycerol dialkyl glycerol tetraethers (GDGTs; Schouten et al. 2002) and, more recently, the long-chain diols (Rampen et al., 2012). The alkenones are used for metabolic storage of haptophyte algae (Epstein et al., 2001), while GDGTs and long-chain diols are present in lipid membranes of bacteria and archaea (Schouten et al., 2002) and eustigmatophyte algae (Volkman et al., 1992), respectively.

Our goal is to analyze the evolution of the sea surface and subsurface paleotemperatures during the Late Quaternary (especially the Last Glacial Period and the Holocene) in the Southwest Atlantic Ocean using these biomarker-based temperature proxies. The analyzed sediment core was collected on the continental slope in order to avoid biases from terrigenous influences and from permanent upwellings, which could mix the signals from the surface and intermediate water masses. We aim to analyze the periodicity and forcings that have triggered temperature variations. This is achieved by reconstructing the paleotemperatures based on the $U^{K'}_{37}$ (degree of alkenone unsaturation; Prahl and Wakeham 1987), the TEX_{86} (GDGTs TetraEther Index; Schouten et al. 2002) and the LDI (Long chain Diol Index; Rampen et al. 2012) indices. The paleotemperature reconstructions can then be compared to basin-wide oceanographic features (such as the NADW formation and the Agulhas leakage) to test if the SW Atlantic is more influenced by the Greenland or by Antarctic climate.

2. Oceanographic Setting

The South Brazil Bight (SBB) extends between 22° S and 34° S, from Cabo Frio to the Santa Marta Cape (Mahiques et al., 2010) (Fig. 2.1). The main water masses present in the slope region are the Tropical Water (TW; T > 20 °C and S > 36.4), the South Atlantic Central Water (SACW; T = 6-20 °C and S = 34.5-36.4), the Antarctic Intermediate Water (AAIW; T = 3-7 °C and S = 24.6-34.4), the Upper Circumpolar Deep Water (UCDW; T = 1-2 °C and S ~ 34.6) and the North Atlantic Deep Water (NADW; T ~ 3 °C and S ~ 34.8) (Campos et al.,

2000, 1995; Piola et al., 2000; Piola and Matano, 2001; Schmid et al., 2000; Silveira et al., 2000).

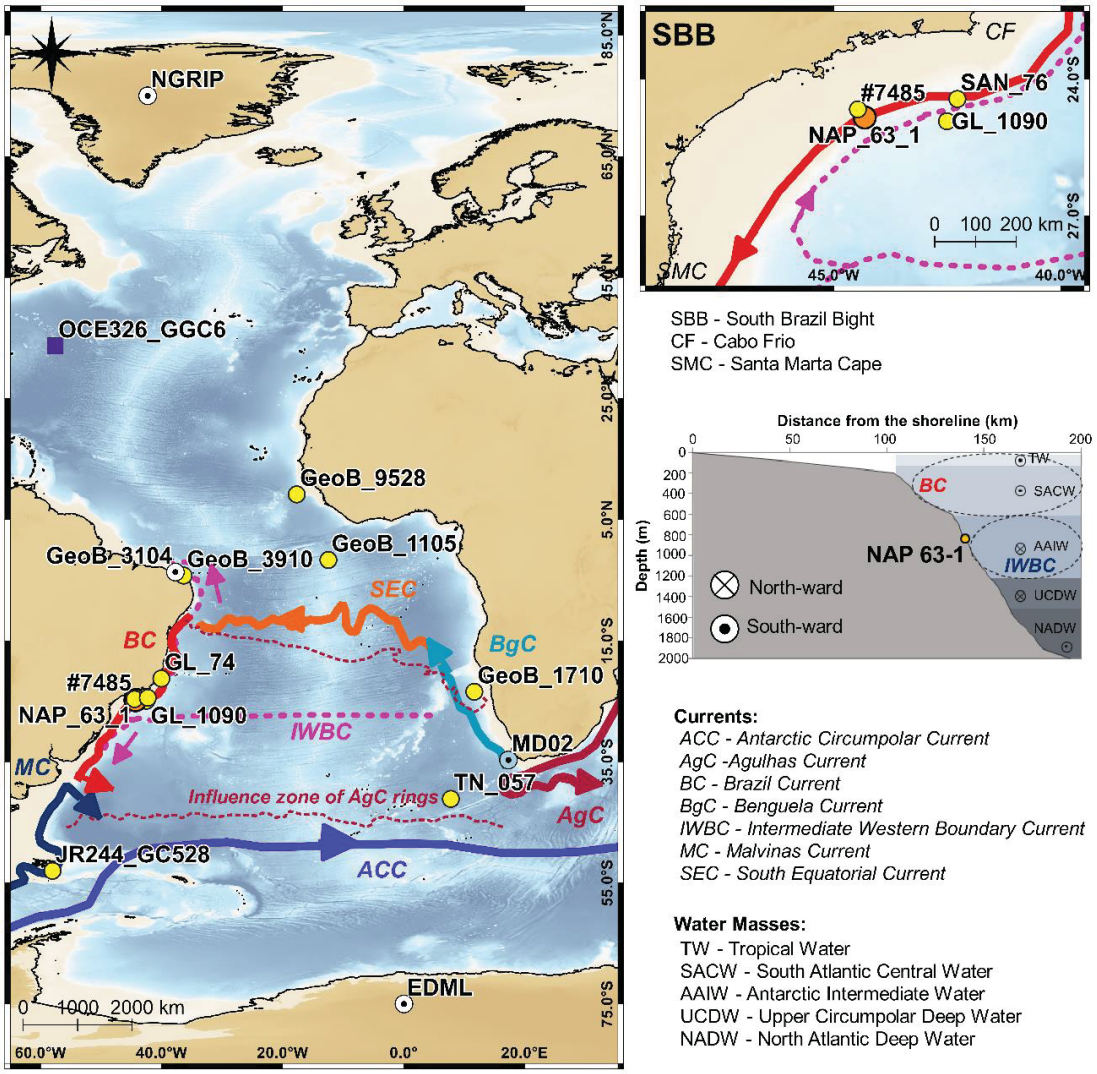

Fig. 2.1. Map of the study area with the location of the NAP 63-1 sediment core as well as the main currents and water masses in the region (based on Biastoch et al., 2008; Campos et al., 1995; Castellanos et al., 2017; Peterson and Stramma, 1991; Piola and Matano, 2001; Schmid, 2014; Schmid et al., 2000 and Silveira et al., 2000). The indicated cores are used in discussion of the climate evaluation of the SW Atlantic.

The SBB area is bordered by the western contour of the South Atlantic Subtropical Gyre. This system exhibits a complex baroclinic structure with reversal flows at different latitudes in different levels of the water column and transports distinct water masses either equator- or poleward (Pereira et al., 2014). The surface circulation offshore is dominated by the Brazil Current (BC), which carries TW and SACW, flowing southward at the surface and meandering around the 200 m isobath (Campos et al., 2000; Peterson and Stramma, 1991). The TW is influenced by both the wind field and the geostrophic component (Peterson and

Stramma, 1991). Below the TW, but still within the Brazil Current, the SACW presents itself as a sharp thermocline and halocline layer (Piola and Matano, 2001). It is formed mainly in the Brazil-Malvinas Confluence Zone by the mixture of TW and Subantarctic Water (Souza and Robinson, 2004). Another important contribution to the SACW is the Indian Central Water, that is brought into the Atlantic Ocean by Agulhas Current intrusions (Poole and Tomczak, 1999; Stramma and England, 1999). The SACW enters as part of the Subtropical Gyre, circulates with the South Atlantic and Benguela Currents, and reaches the coast of South America being transported by the South Equatorial Current. When it reaches the Brazilian coast (around 22° S), it bifurcates, one part flowing south and the other flowing north off the Brazilian coast (Pereira et al., 2014; Silveira et al., 2000). At intermediate levels, below the BC and between 600 and 1200 m water depth, the AAIW also recirculates within the Subtropical Gyre, reaching the Brazilian coast and bifurcating at 28° S (Pereira et al., 2014; Schmid et al., 2000). The northward branch AAIW is transported by the Intermediate Western Boundary Current (IWBC) (Boebel et al., 1999). Similarly, the UCDW is formed in the Antarctic Polar Front (around 50 °C), recirculates within the Subtropical Gyre and bifurcates at around 30 – 32° S (Campos et al., 1995; Speer et al., 2000). Below these levels, near 2000 m water depth, a relatively intense and well organized flow carries the NADW southward as a Deep Western Boundary Current (DWBC) (Pereira et al., 2014).

The annual mean sea surface temperature (SST) in SSB ranged from 16 °C to 27 °C across the basin, and the temperature at 75 m depth is about 20 °C, due to the influence of the SACW (Locarnini et al., 2013; Pereira et al., 2013). The BC presents a relatively strong eddy activity in the SBB. The change in the coastline orientation at Cabo Frio induces a meandering pattern, which frequently becomes unstable forming strong cyclonic and anticyclonic frontal eddies. These eddies are resposible for shallowing the SACW (Campos et al., 2000, 1995).

3. Material and Methods

3.1. Sampling

Sediment core NAP 63-1 was collected from the continental slope of the southwestern Atlantic, in a subtropical region (24° 50.304’ S; 44° 19.124’ W; 840 m depth; 2.24 m long). The sampling took place on February 26th, 2013, during a cruise onboard R.V. Alpha Crucis, from the Oceanographic Institute of the University of São Paulo (IO-USP, Brazil), using a

piston corer (Fig. 2.1). The core was sectioned every 2 cm, totaling 112 samples. The samples were stored frozen in pre-combusted aluminum trays for further analysis.

3.2. Age Model

The core chronology and calculation of sedimentation rates is based in two complementary approaches, using a combination of radiometric dating (AMS ^{14}C) and benthic foraminifera stable oxygen isotopes ($\delta^{18}O$) tie points aligned to two reference curves (Lisiecki and Raymo, 2005; Lisiecki and Stern, 2016). For the first ca. 40,000 years, six samples were analyzed for ^{14}C at Beta Analytic Inc. (Miami, USA) and at Poznan Radiocarbon Laboratory (Poznań, Poland), using 10 mg (ca. 600-700 specimens) of well-preserved planktonic foraminifera (*Globigerinoides ruber* + *Globigerinoides sacculifer*) in the fraction > 150 μm.

The chronology of sediments older than 40,000 years was determined by correlation of benthic $\delta^{18}O$. Oxygen isotopic composition ($\delta^{18}O$) of benthic foraminifera Uvigerina sp. (3-5 tests, in the fraction > 250 μm) was obtained using an Elemental Isoprime 100 analyzer. The δ18O tie points were obtained by correlating the isotopic curve of NAP 63-1 with the LR04 (Lisiecki and Raymo, 2005) and the ISA (Lisiecki and Stern, 2016) $\delta^{18}O$ curves, using the software Analyseries 2.0 (Paillard et al., 1996). The error estimations of the $\delta^{18}O$ tie points were calculated based on Govin et al. (2015).

The age-depth curve was modelled using BACON software version 2.3.5 (Blaauw and Christen, 2011). The ^{14}C ages were calibrated with the Marine13 Calibration Dataset (Reimer et al., 2013), with a reservoir age correction (ΔR) of 28 ± 52 years (Alves et al., 2015), and are reported in thousand years before present (kyr BP).

3.3. Lipid extraction and purification

The laboratorial procedure was conducted at the Alfred-Wegener Institute in Bremerhaven (Germany). About 5 g of freeze-dried and homogenized samples were extracted three times using an ultrasonic bath with 25 mL of methanol:dichloromethane (MeOH:DCM) (1:9; v:v). Known amounts of C_{19} ketone, androstanol, C_{46} GDGT were added as internal standards before extraction. The combined extracts were evaporated by rotary evaporation under vacuum at 40 °C. The total lipid extracts (TLE) was saponified for 2 h at 80 °C with 1 mL of 0.1 mol L^{-1} KOH in MeOH:H_2O (9:1; v:v). After that. the neutral extracts were purified by passing them over a silica gel column (1% deactivated with water). They were

239 eluted with 4 mL of *n*-hexane, 4 mL of *n*-hexane:DCM (1:2; v:v; recovery of ketones) and 4
240 mL of DCM:MeOH (1:1; v:v; recovery of diols and GDGTs) and dried using a Silli-Therm at
241 50 °C under a stream of nitrogen.
242 The alkenone fraction was re-dissolved in 100 µL of *n*-hexane before the capillary gas
243 chromatography. The dry polar fractions were weighed to ensure that their concentrations
244 before the injection were lower than 2 mg mL^{-1}. They were resuspended with isopropanol:*n*-
245 hexane (1:99; v:v) and then filtered (PTFE® filter - 4 mm diameter and 0.45 µm porosity) for
246 the retention of any remaining particles. These extracts were injected into a high-performance
247 liquid chromatograph coupled to a mass spectrometer (HPLC-MS). The remaining extracts
248 were then dried and derivatized by adding 30 µL of acetonitrile and 30 µL of N,O-bis
249 (trimethylsilyltrifluoroacetamide):trimethylchlorosilane (BSTFA:TMCS; 99:1) and leaving
250 for 60 min at approximately 60 °C. The reagents were dried, and the fraction was re-dissolved
251 in 50 µL of *n*-hexane before the capillary gas chromatography.
252
253 *3.4. Analytical methods*
254 The instrumental analysis procedures were conducted at the Alfred-Wegener Institute
255 (Germany) and at the Center for Marine Studies (UFPR, Brazil). Alkenones were analyzed by
256 injecting 2 µL sample aliquots in the splitless mode in an Agilent 7890-A series gas
257 chromatograph (GC) equipped with a flame ionization detector, an Agilent HP-5 capillary
258 fused silica column coated with 5% phenyl/methylpolysiloxane (50 m length, 0.32 mm ID,
259 and 0.17 µm film thickness). Hydrogen was used as the carrier gas with a constant flow rate
260 of 1.2 mL min^{-1}. Initial oven temperature was 40 °C, increased to 60 °C at a rate of 20 °C min^{-1},
261 then raised to 320 °C at a rate of 5 °C min^{-1} and held for 15 min with a total run-time of 68
262 min. The injector and detector temperatures were adjusted to 300 °C and 325 °C, respectively.
263 GDGT analyses were performed using an Agilent 1200 Series high-performance liquid
264 chromatography (HPLC) system coupled with an Agilent 6120 mass spectrometer. The 20 µL
265 aliquots were injected into an Alltech Prevail® Cyano column (2.1 x 150 mm^2, 3 µm; Grace)
266 maintained at 30 °C. GDGTs were eluted using the following gradient with solvent A (*n*-
267 hexane: isopropanol: chloroform; 98:1:1) and solvent B (*n*-hexane:isopropanol:chloroform;
268 89:10:1): 100% A for 5 min, linear gradient to 10% B in 20 min, linear gradient to 100% B in
269 10 min, and then held for 7 min. The flow rate was 0.2 mL min^{-1}. After each analysis, the
270 column was cleaned by back-flushing with 100% B at 0.6 mL min^{-1} for 5 min and then held
271 for 10 min in the initial conditions (100% A at 0.2 mL min^{-1}).

Diols were analyzed by injecting 2 µL sample aliquots in splitless mode in an Agilent 6850-A series GC equipped with an Agilent 5975C VL MSD mass spectrometer and a Restek Rxi-1ms capillary fused silica column coated with 1% diphenyl/ dimethylsiloxane (30 m length, 0.25 mm ID, and 0.25 µm film thickness) and a 5 m pre-column. Helium was used as the carrier gas with a constant flow rate of 1.2 mL min^{-1}. Initial oven temperature was 100 °C, held for 8 min, and subsequently increased to 300 °C at a rate of 4 °C min^{-1} with a total run-time of 58 min. The injector temperature was adjusted to 280 °C. The splitless injection mode was adopted, and detector and ion source temperatures were adjusted to 280 °C and 230 °C, respectively.

Alkenones were individually identified by matching retention times against a standard containing C_{19} ketone, $C_{37:2}$ and $C_{37:3}$ alkenones. GDGTs were analyzed using SIM (Selected Ion Monitoring) mode, and diols were analyzed using SCAN mode, and they were identified by the ions or fragments characteristic of each compound (Tables A-1 and A-2). Procedural blanks were analyzed for each set of 15 samples, and they showed no significant level peaks in the analyses of target compounds. Finally, four replicates of the same sediment sample were extracted and used as a laboratory internal reference. Their internal variability was lower than the calibration error.

3.5. Data analysis

Temperature estimates were obtained using the $U^{K'}_{37}$ (degree of alkenone unsaturation; formula 1; Prahl and Wakeham 1987), TEX_{86} (TetraEther Index; formula 2; Schouten et al. 2002) and LDI (Long chain Diol Index; formula 3; Rampen et al. 2012) indices.

(1) $$U_{37}^{K\prime} = \frac{[C_{37:2}]}{[C_{37:2}] + [C_{37:3}]}$$

(2) $$TEX_{86} = \frac{([isoGDGT-2]+[isoGDGT-3]+[cren'])}{([isoGDGT-1]+[isoGDGT-2]+[isoGDGT-3]+[cren'])}$$

(3) $$LDI = \frac{C_{30}\ 1{,}15-diol}{C_{28}\ 1{,}13-diol + C_{30}\ 1{,}13-diol + C_{30}\ 1{,}15-diol}$$

The statistical analyses were performed using Python (van Rossum, 1995) and the libraries NumPy (Oliphant, 2006), MatplotLib (Hunter, 2007) and SciPy (Jones et al., 2015). PyCWT (available at https://github.com/regeirk/pycwt) was used to perform the wavelet

303 analysis and follows the procedure described by Torrence and Compo (1998) for the
304 evaluation of cycles in the temperature data. For the correlation and wavelet analysis, all data
305 were converted to equally-spaced time-series . In order to examine the divers of the
306 millennial-scale variability of SST in the SW Atlantic, a Pearson correlation was performed
307 relative to selected records of annual mean SST from cores from the North, Equatorial and
308 South Atlantic . To this analysis, the following paleotemperatures records were used (Fig.
309 2.1): GeoB 9528 ($U^{K'}_{37}$-based SST; Lopes dos Santos et al. 2010), GeoB 1105 ($U^{K'}_{37}$-based
310 SST; Schneider et al., 1996), GeoB 3104 ($\delta^{18}O$; Arz et al., 1999), GeoB 3910 ($U^{K'}_{37}$-based
311 SST; Jaeschke et al. 2007), GL-74 (foraminifera-based SST; Portilho-Ramos et al., 2015),
312 GeoB 1710-3 ($U^{K'}_{37}$-based SST; Kirst and Müller 2001), SAN-76 (SIMMAX-based summer
313 SST; Toledo et al., 2007), #7485 ($U^{K'}_{37}$-based SST; Lourenço et al., 2016), GL-1090 (Mg/Ca-
314 based SST; Santos et al., 2017), TN 057-21 ($U^{K'}_{37}$-based SST; Pahnke and Sachs 2006), and
315 JR 244-GC528 ($U^{K'}_{37}$-based SST; Roberts et al. 2017). We also used the following records in
316 the discussion: the ice cores EDML ($\delta^{18}O_{ice}$; EPICA Community Members 2010) and NGRIP
317 $\delta^{18}O_{ice}$; Andersen et al. 2004), the NW Atlantic sediment cores OCE326-GGC6 and ODP
318 1063 (Nd excess; Böhm et al., 2015; Roberts et al., 2010), and the SE Atlantic sediment core
319 MD 02-2594 (local $\delta^{18}O_{sw}$ anomaly; Dyez et al., 2014).
320 For the wavelet analysis, all periodicities above 10 kyr were removed through the use
321 of a moving average filter, with a window of 11 kyr in order to eliminate all unresolved
322 frequencies and the general trend. Cross-wavelet and wavelet coherence were performed to
323 compare the NAP 63-1 signals with other time series. Since our time series is not long enough
324 to resolve Milankovitch cycles appropriately, we have analyzed only periodicities below 11
325 kyr (half cycle of the precessional forcing; Covey 1984). Finally, cycles can only be
326 (robustly) identified having at least 4 "samples" per cycle, according to the Nyquist
327 frequency. The mean temporal lag between the samples in NAP 63-1 record is 0.7 yr (i.e.,
328 each sample represents 0.7 kyr). Therefore, only cycles larger than 2.8 kyr (4 * 0.7) can be
329 robustly interpreted.
330
331 **4. Results**

332 The core material covered approximately the past 78 kyr (Table 2.1; Fig. 2.2) with no
333 observed age inversion in the radiocarbon ages . The record has been subdivided into Marine
334 Isotope Stage (MIS) 4 (71 – 57 kyr), MIS 3 (57 – 29 kyr), MIS 2 (29 – 14 kyr) and MIS 1 (14
335 kyr to present), as defined by Xiao et al. (2016b).

336

Table 2.1. Age control points for the core NAP 63-1.

Sample N°	Age Model Method	Lab N°	Conventional Age (yr BP)	Calibrated probability median (yr BP)	2σ range (yr)
2 – 4 cm	calibrated ^{14}C age	Beta 405803	2,750 ± 30	2,465	2,340 – 2,635
14 – 16 cm	calibrated ^{14}C age	Poz 95945	7,710 ± 40	8,180	8,050 – 8,290
46 – 48 cm	calibrated ^{14}C age	Poz 95946	19,430 ± 110	22,900	22,560 – 23,270
52 – 54 cm	calibrated ^{14}C age	Beta 405804	24,710 ± 100	28,350	28,040 – 28,650
74 – 76 cm	calibrated ^{14}C age	Poz 95947	33,500 ± 400	37,290	36,280 – 38,322
100 – 102 cm	calibrated ^{14}C age	Beta 405805	40,130 ± 440	43,410	42,720 – 44,240
128 – 130 cm	δ^{18}O stratigraphy	X	X	47,000	X
140 – 142 cm	δ^{18}O stratigraphy	X	X	51,500	X
152 – 154 cm	δ^{18}O stratigraphy	X	X	58,500	X
186 – 188 cm	δ^{18}O stratigraphy	X	X	64,500	X
212 – 214 cm	δ^{18}O stratigraphy	X	X	75,000	X

337

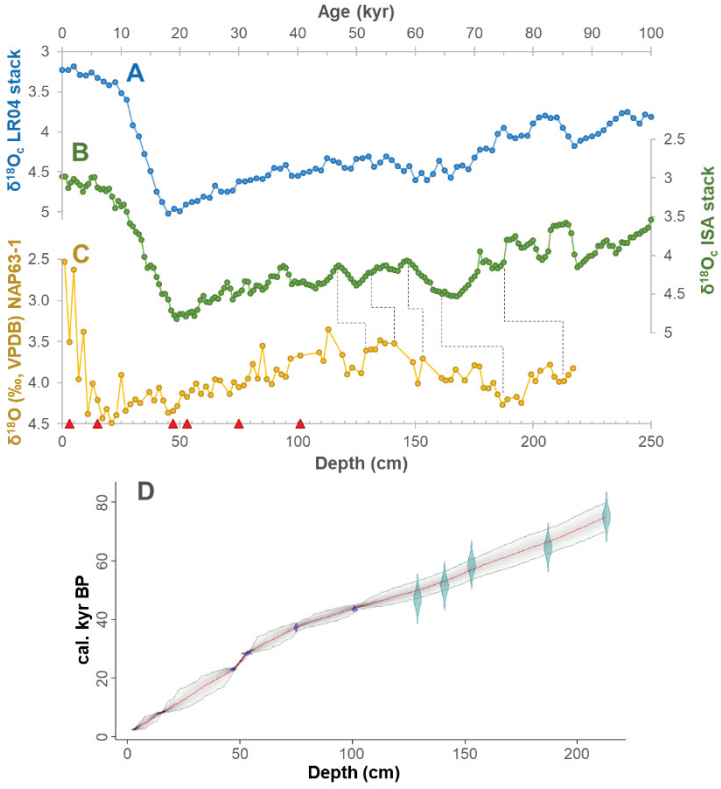

Fig. 2.2. Reference curves and age–depth model of NAP 63-1sediment core. A: benthic foraminifera δ^{18}O of LR04 stack (Lisiecki and Raymo, 2005). B: benthic foraminifera δ^{18}O of Intermediate South Atlantic (ISA) stack (Lisiecki and Stern, 2016). C: benthic foraminifera δ^{18}O of NAP 63-1 core, with the indication of the calibrated ^{14}C ages (red triangles). D: Age-depth model based on Bacon v. 2.3.5 (Blaauw and Christen, 2011). Symbols in panel D represent the positions of calibrated ^{14}C ages and benthic δ^{18}O tie-points.

338

339 The three proxy records yield different trends (Fig. 2.3). The $U^{K'}_{37}$ values remained
340 between 0.64 and 0.85. Between 75 and 70 kyr BP, the index remained above 0.74 followed

by a sharp decrease. An increasing trend is observed between 65 and 54 kyr BP, with the exception of two negative incursions: at 60.4 and 58.1 kyr BP, when indexes lower than 0.70 were observed. This increasing trend was followed by a similar decreasing trend until 39 kyr BP. The values, then, increased sharply between 38 and 35 kyr BP, returning to around 0.75. In the last part of the record, it was possible to observe two opposing patterns. First, $U^{K'}_{37}$ values presented a decreasing trend until 18 kyr BP. During this period, the lowest value (0.64) was observed around 22.9 kyr BP. It was followed by a marked increase, reaching 0.84 at the top of the core.

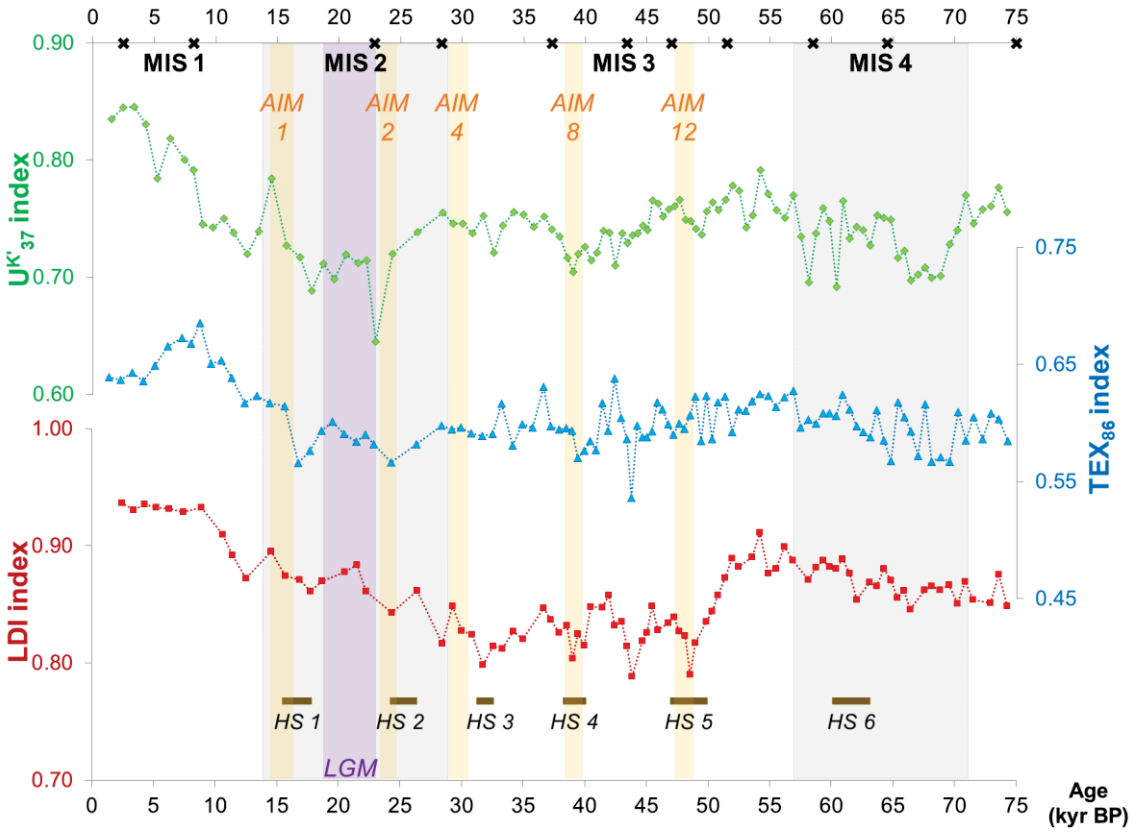

Fig. 2.3. Evolution of $U^{K'}_{37}$ (a), TEX_{86} (b) and LDI (c) indexes in the core NAP 63-1. Grey bars indicate MIS 2 and MIS 4 duration, the orange bars indicate the AIM events and the purple bar indicates the Last Glacial Maximum (LGM). Horizontal brown lines and indicate Heinrich Stadials (HS). Black symbols at the top of the panel depict age model tie points.

The TEX_{86} values oscillated between 0.54 and 0.69 (Fig. 2.3), with several conspicuous oscillations during the record. The TEX_{86} values remained around 0.60 until 42 kyr BP, with the exception of one negative incursion at 43.8 kyr BP representing the lowest value of the record. Between 42 and 17 kyr BP, the TEX_{86} values decreased. Despite this trend, two local maxima were registered at 37 and 33 kyr BP. Between 17 and 4.3 kyr BP, it was possible to observe two marked and opposing patterns. First, TEX_{86} values presented

increased markedly until 9 kyr BP, when they reached 0.69. This was followed by a sharp decrease that occurred at a similar rate. The record ends with a stabilization phase, with values around 0.64.

The LDI values ranged between 0.79 and 0.94, with few abrupt variations (Fig. 2.3). From 75 kyr BP interval, a gradual increase is observed until 54 kyr BP, when the LDI values exceeded 0.90. Subsequently, the LDI decreased sharply, reaching 0.79 at 48.5 kyr BP. This LDI values drop was followed by an oscillation period until 31 kyr BP. A new warming trend occurred between 31 and 9 kyr BP, reaching 0.93, followed by a stabilization phase.

5. Discussion

5.1. Temperature calibrations

Several authors studied the sea surface palaeothermometry using multiple organic proxies (Lopes dos Santos et al., 2010; Mollenhauer et al., 2015; Rodrigo-Gámiz et al., 2014; Smith et al., 2013). However, each proxy may present a bias, depending on the season or water column depth that the source organism better reflects. This relation between the surrounding environment and the source organisms varies with the studied location.

The alkenones are among the oldest and most well-established paleotemperature molecular proxies for the sea surface temperature. Although the relationship between $U^{K'}_{37}$ and SST is well established (Conte et al., 2006), some deviations can be caused by different seasonal production of source organisms and/or depth habitats (Chen et al., 2014). Lopes dos Santos et al. (2013) associated the $U^{K'}_{37}$ proxy with the annual mean SST offshore South Australia, while Rodrigo-Gámiz et al. (2014) related this proxy to the summer season in the western Mediterranean Sea. On the other hand, Smith et al. (2013) and Mollenhauer et al. (2015) associated it with the winter season in the southern and eastern Australian coast, and off Mauritania (NW Africa), respectively. Algae from the Haptophyceae (or Prymnesiophyceae) class are usually associated with the ocean's surface layer (~ 10 m), but some exceptions to this general pattern were found in shelf regions (Nanninga and Tyrrell 1996 and references therein).

Another exception was observed by Rodrigues et al. (2014) and Ribeiro et al. (2016) in the SW Atlantic shelf-break and slope. They observed maximum abundance of photosynthetic nano-eukaryote (including Haptophytes) right above the thermocline, in the upper layer of the SACW (between 50 and 100 m). This phenomenon is called a Deep Chlorophyll Maximum and would suggest that the alkenone-based index could reflect

390 subsurface waters in the SBB. Rodrigues et al. (2014) argued that the presence of
391 nanoflagellate species in the shelf break and slope region are related to circulation patterns
392 that produce internal waves in the BC resulting in nutrient inputs from the SACW. Regarding
393 the seasonality, Ceccopieri et al. (2018) found that the SST-$U^{K'}_{37}$ shows a better agreement
394 with the austral winter (July-September), which may be related to a maximum abundance of
395 haptophytes during this period (Rodrigues et al., 2014). This higher haptophyte abundance in
396 winter is probably related to the change of the wind direction in the SBB region (Palma and
397 Matano, 2009). During the winter, the mixed layer deepens, and, consequently, mass is
398 transferred from deeper layers into the mixed layer, mixing the SACW with TW (Donners et
399 al., 2005; Pereira et al., 2013). Müller et al. (1998) proposed several $U^{K'}_{37}$ calibrations,
400 including seasonal surface calibrations and seven different water depth calibrations (0 m, 10
401 m, 20 m, 30 m, 50 m, 75 m and 100 m). Therefore, to test the seasonality and subsurface
402 signal, we have redone the analysis presented by Ceccopieri et al. (2018), excluding the
403 stations located on the continental shelf and in an upwelling region. We also included the
404 different water depth calibrations from Müller et al. (1998). Based on the evaluation of the
405 discrepancies between the $U^{K'}_{37}$-based estimates and the World Ocean Atlas 2013
406 temperatures (Locarnini et al., 2013) (Table A-3), the $U^{K'}_{37}$ 30 m calibration presented the
407 best fit with modern data (formula 4), considering an annual mean.
408
409 (4) $Temp_{UK'}\ (°C) = \frac{\left(U^{K'}_{37} - 0.069\right)}{0.033}$; standard error (SE) = ± 1.5 °C
410
411 The TEX_{86} index has been reported to reflect the mean temperature in the subsurface
412 layer of the water column (between 50 and 400 m, depending on the region), below the mixed
413 layer but above the permanent thermocline (Hernández-Sánchez et al., 2014; Kim et al., 2010;
414 Lopes dos Santos et al., 2010; Rommerskirchen et al., 2011; Smith et al., 2013). However, it
415 is not yet well established whether the GDGTs represent the annual or seasonal temperature
416 average since the archaea cannot compete well with phytoplankton for the available resources,
417 especially during blooming periods (Chen et al., 2014), and seasonal abundance of
418 Thaumarchaeota may be different in different regions. Offshore southern Australia, Lopes dos
419 Santos et al. (2013) associated the TEX_{86} proxy with the winter SST, while Mollenhauer et al.
420 (2015) associated it with the summer SST offshore Mauritania (NW Africa). In the SBB,
421 Zubkov et al. (2000) observed that the heterotrophic prokaryotes (bacteria and archaea) are
422 more abundant in the surface, rather than in the subsurface. One possible explanation is that

423 they are more competitive in the SBB oligotrophic surface waters when compared to the
424 upper thermocline zone, where the SACW fertilizes the environment. The trophic status of the
425 surface TW may explain why archaea can be associated with subsurface waters in eutrophic
426 regions (such as in SE Atlantic under the influence of the Benguela Current; Hernández-
427 Sánchez et al. 2014) and with surface waters in oligotrophic regions (such as SW Atlantic
428 under the influence of Brazil Current). Ceccopieri et al. (2018) tested the applicability of
429 several pre-existing TEX_{86} calibrations in the SW Atlantic, and they found that the global
430 SST calibration of Kim et al. (2010) for high temperatures was more suitable to this
431 geographic location (formula 5). Therefore, we assume that the TEX_{86} signal in NAP 63-1
432 record represents the mean annual temperature of the surface layer of the SBB.
433
434 (5) $Temp_{TEX}\ (°C) = 38.6 + (68.4 * TEX_{86}^{H})$,

435 where $TEX_{86}^{H} = \log_{10} TEX_{86}$; SE = ± 2.5 °C

436
437 One of the most significant uncertainties about the use of long-chain diols for
438 paleoreconstruction is the origin of the compounds since the Eustigmatophyceae are common
439 in estuarine environments but rarely reported in marine environments (Rampen et al., 2012).
440 However, there is no large riverine input into the SBB region. Therefore, the use of LDI in
441 paleoreconstructions is limited by the uncertainty surrounding the source organism(s) and the
442 unknown mechanism underlying the link between long chain diol synthesis and SST (Smith et
443 al., 2013). When compared with the TEX_{86}-based temperature estimates, the LDI-based
444 values are in the same range, suggesting a mean annual surface signal (formula 6). However,
445 several SST reconstructions based on the LDI proxy (Lopes dos Santos et al., 2013; Rodrigo-
446 Gámiz et al., 2014; Smith et al., 2013) observed a warm bias, which could be caused by a
447 summer production of the long-chain diols. Thus, considering the calibration error, a possible
448 seasonality bias should not be completely refuted.
449
450 (6) $Temp_{LDI}\ (°C) = \frac{(LDI - 0.095)}{0.033}$; SE = ± 2.0 °C

451

452 *5.2. Comparison of SST proxy records*

453 Based on the previous discussion, the indices were converted to temperature estimates
454 based on the calibrations from Müller et al. (1998; $U^{K'}_{37}$ index; 30 m water depth), Kim et al.
455 (2010; TEX_{86} index for subtropical oceans) and Rampen et al. (2012; LDI index) (Fig. 2.4).
456 The use of three indices provides information about different water column depths, as was
457 also observed by Lattaud et al. (2018). However, in contrast to their findings, the TEX_{86}-
458 based and the LDI-based SST presented a significant correlation ($r^2 = 0.67$, p-value < 0.05),
459 reinforcing that both proxies are reflecting the same water depth or depths that show co-
460 varying temperatures. When the TEX_{86}-based and the LDI-based SST values were compared
461 with the $U^{K'}_{37}$-based winter subT (subsurface temperature), the correlations dropped ($r^2 =$
462 0.54 between $U^{K'}_{37}$-based subT and TEX_{86}-based SST, $r^2 = 0.49$ between $U^{K'}_{37}$-based subT
463 and LDI-based SST, p-value < 0.05). The lack of similarity between the LDI-based and $U^{K'}_{37}$-
464 based temperatures was also observed in the eastern and southern coast of Australia (Smith et
465 al., 2013), in the northern Arabian Sea (Rodrigo-Gámiz et al., 2016) and in the northwestern
466 Pacific Ocean (Lattaud et al., 2018). Long-chain diols are usually associated with marine
467 eustigmatophyte algae of the genus *Nannochloropsis* (Volkman et al., 1992). Despite being a
468 phytoplankton group, the eustigmatophyte algae may not require large quantities of nutrients,
469 and upwelling appears to affect very little on their flux (Li et al., 2015; Rampen et al., 2007).
470 This difference in nutrient requirements between haptophyte and eustigmatophyte algae may
471 explain the different temperature profiles.
472

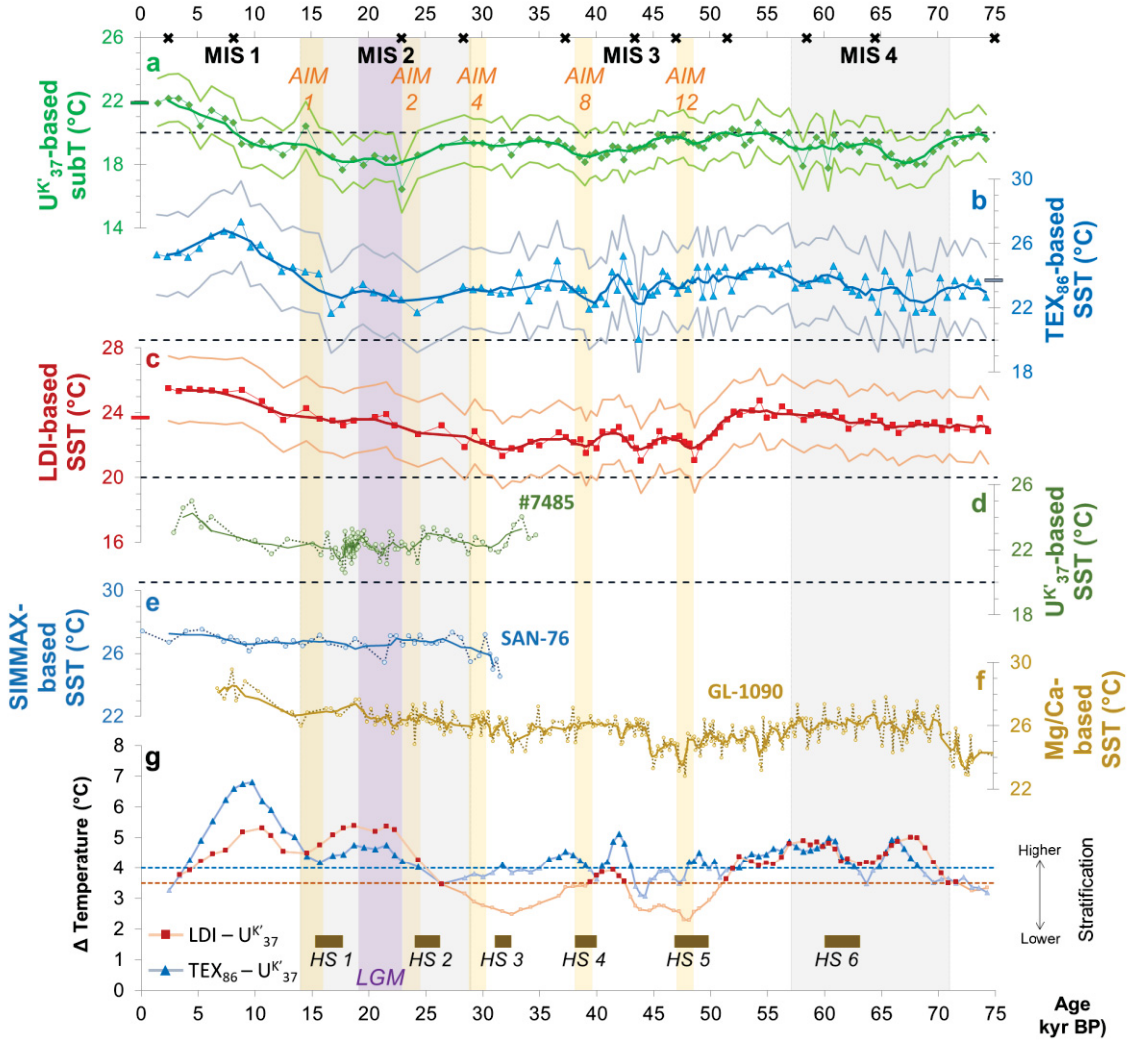

Fig. 2.4. Temperature reconstructions for the SW Atlantic.
Black symbols at the top of the panel depict age model tie points.
(a) $U^{K'}_{37}$-based temperature of 30m water depth, (b) TEX_{86}-based SST and (c) LDI-based SST; all for the NAP 63-1 sediment core. They include the standard errors and the present observed temperatures. (d) $U^{K'}_{37}$-based SST for the #7485 sediment core (Lourenço et al., 2016). (e) SIMMAX-based summer SST for the SAN-76 sediment core (Toledo et al., 2007). (f) Mg/Ca-based SST for the Gl-1090 sediment core (Santos et al., 2017). (g) Vertical temperature difference between LDI-based SST and $U^{K'}_{37}$-based subT (red squares) and between TEX_{86}^{H}-based SST and $U^{K'}_{37}$-based subT (blue triangles), calculated for the NAP 63-1 sediment core. The dashed lines indicate the accumulated error of the indexes (red = LDI + $U^{K'}_{37}$ errors; blue = TEX_{86}^{H} + $U^{K'}_{37}$ errors).
All the temperature records are presented using a 4-pt running average (continuous bold line).
The black dashed line (20°C) represents the South Atlantic Central Water (SACW) delimitation.
Grey bars indicate MIS 2 and MIS 4 duration, the orange bars indicate the AIM events and the purple bar indicates the Last Glacial Maximum (LGM). Horizontal brown lines indicate Heinrich Stadials (HS).

The NAP 63-1 SST estimates are in the same range as observed in other palaeothermometry from the SBB, with some common features among them (#7485 - Lourenço et al., 2016; GL-1090 - Santos et al., 2017; SAN-76 - Toledo et al., 2007). As observed by Santos et al. (2017) and Pahnke and Sachs (2006), our results indicated a warmer MIS 4 when compared to MIS 3. They argued that this mid-MIS 3 minimum may have been

caused by a conjunction of orbital forcings, especially a high obliquity that resulted in decreased mean annual insolation in subtropical regions. Regarding MIS 2, between AIM 1, 2 and 4 events, it is possible to observe some millennial-scale oscillations in the NAP 63-1 TEX_{86}-based SST and in the #7485 SST, with warmer temperatures at the end of the AIM events. Both records also show a late response to the deglaciation, with its onset occurring in the late MIS 2.

Considering a periodicity above 10 kyr (orbital scale), $U^{K'}_{37}$-based subT and TEX_{86}-based SST presented a similar pattern with both NGRIP and EDML records (Fig. 2.5). A slight warming (0.1 °C/kyr) can be seen until around 50 kyr BP, followed by a similar cooling until the Last Glacial Maximum (LGM). In the last part of the records, the warming of the Last Deglaciation started at the beginning of the LGM in the ice records and in the middle of the LGM in the SW Atlantic. This late deglaciation onset is probably related to a weakening of the AMOC. The deglacial warming of the Northern Hemisphere around 19 kyr BP leads to the retreat of the ice sheets, increasing the input of freshwater into the North Atlantic. This caused a weakening of the AMOC around 16 kyr BP that warmed the Southern Hemisphere through the bipolar seesaw (McManus et al., 2004; Shakun et al., 2012). Chiessi et al. (2015) also observed that a sluggish AMOC may have triggered a strengthening in the BC, warming the subtropical SW Atlantic surface.

497

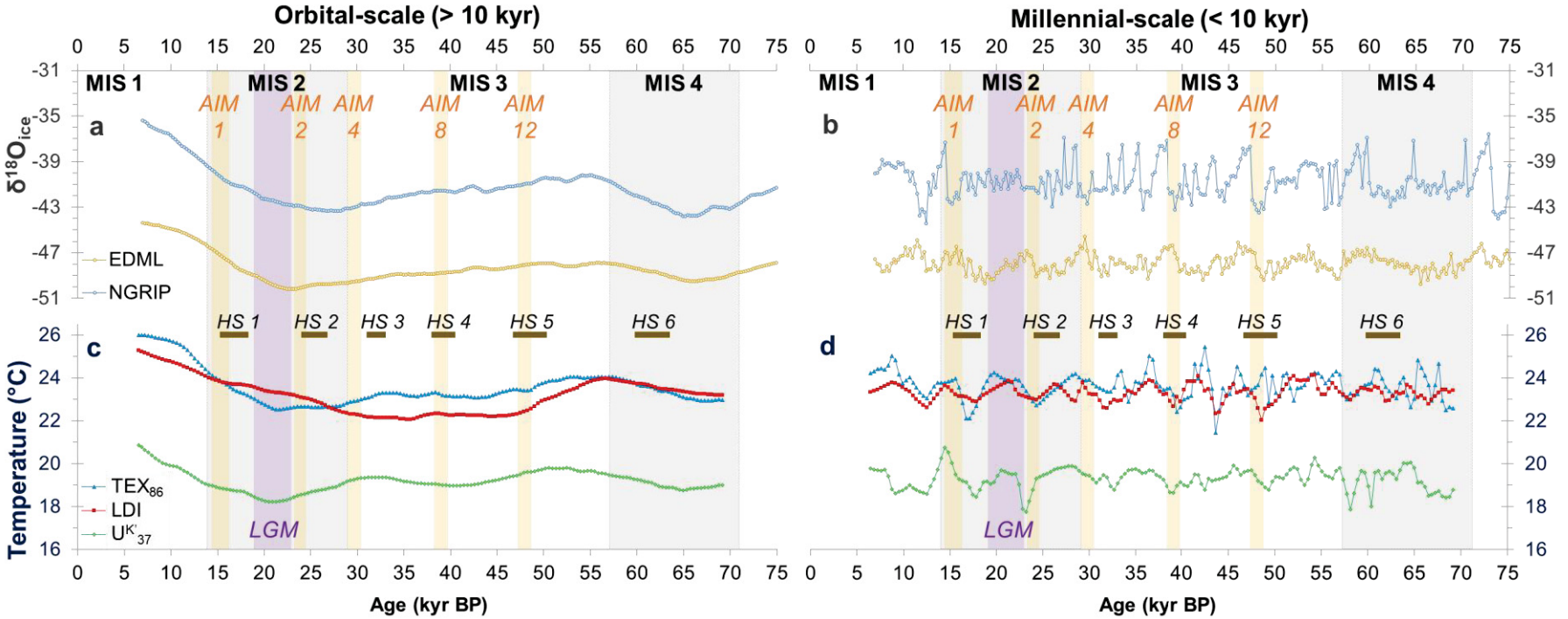

Fig. 2.5. Orbital-scale (> 10 kyr) and millennial-scale (< 10 kyr) records based on the ice cores EDML ($\delta^{18}O_{ice}$; EPICA Community Members 2010) and NGRIP $\delta^{18}O_{ice}$; Andersen et al. 2004), and on the sediment core NAP 63 -1 (TEX_{86}-based SST; LDI-based SST and $U^{K'}_{37}$-based subT; this study). Grey bars indicate MIS 2 and MIS 4 duration, the orange bars indicate the AIM events and the purple bar indicates the Last Glacial Maximum (LGM). Horizontal brown lines indicate Heinrich Stadials (HS).

On the other hand, when the high-frequency variations are considered (periods less than 10 kyr, millennial-scale), the TEX_{86}-based SST and the LDI-based SST are more similar to each other when compared to $U^{K'}_{37}$-based subT (Fig. 2.5, Table A-5). The difference between the SST and the subT records may suggest that the subsurface layer is less affected by millennial-scale climate changes than the surface. The SST records show some oscillations that resemble the AIM periods (EPICA Community Members et al., 2006), especially the AIM 1, 4 and 12 compared to the LDI-based SST. These oscillations also coincide with some Heinrich stadials (HS; Sanchez Goñi and Harrison 2010), especially HS 6, 4 and 1, when relatively higher temperatures were recorded. This behavior is consistent with the observations of Rampen et al. (2012) who reported warming of the surface and intermediate waters in the South Atlantic during Heinrich events, due to a weakening of the AMOC (Jaeschke et al., 2007).

In addition to the orbital tendencies and millennial oscillations, the late part of the records was also marked by different trends among the three NAP 63-1 reconstructions (Fig. 2.4). While the observed $U^{K'}_{37}$-based subT warmed continuously, the LDI-based SST presented a stabilization trend, and a cooling trend is present in the TEX_{86}-based SST. The stabilization trend in SST during the late Holocene was also observed in the SW Atlantic by Chiessi et al. (2014; 32.5° S, 50.2° W), based on *G. ruber* (white) Mg/Ca ratios. In the Northern Hemisphere, this mid-to-late Holocene cooling is related to the decreasing orbital precession since 9 kyr BP, which is represented by insolation changes at 65° N (Ayache et al., 2018). However, the annual mean insolation in the Southern Hemisphere does not explain this cooling trend. Xiao et al. (2016a), after a thorough analysis of the climate variability during the Holocene in the Atlantic sector of the Southern Ocean, attributed this cooling to the decrease of summer duration rather than to maximum summer insolation. Shorter summer seasons boosted the cold surface water generation under the Antarctic shelf ice. This cold water is then transported by the Weddell Gyre to the open Atlantic Ocean, cooling it. Huguet et al. (2006) also observed an apparent discrepancy between two organic-based ($U^{K'}_{37}$-based and TEX_{86}-based) SST records in the Arabian Sea during the Holocene. They argued that a seasonality bias could cause it. Ceccopieri et al. (2018) concluded that TEX_{86}-based temperatures in the SBB indeed represent the mean annual SST. Since the source organism of the long chain diols in marine environments are not yet well known and other multi-proxy palaeothermometry observed a warm bias in the LDI signal (Lopes dos Santos et al., 2013; Rodrigo-Gámiz et al., 2014; Smith et al., 2013), it may be recording a seasonal SST.

Finally, when the SST records are compared to the subT record, it is possible to infer about the vertical stratification of the water column (Fig. 2.3). However, some caution should be taken considering the standard errors of the calibration methods. Based on the calibrations used in this study, the calibrations errors are: $U^{K'}_{37}$-based temperatures = ± 1.5 °C (Müller et al., 1998), TEX_{86}-based temperatures = ± 2.5 °C (Kim et al., 2010) and LDI-based temperatures = ± 2.0 °C (Rampen et al., 2012). For the comparison between LDI-based and $U^{K'}_{37}$-based temperatures, we considered a stratified water column only during the periods when the temperature difference was higher than 3.5 °C (1.5 °C from the $U^{K'}_{37}$ calibration and 2.0 °C from the LDI calibration; red dashed line). In the same sense, when we analyzed the difference between the TEX_{86}-based and the $U^{K'}_{37}$-based temperatures, we considered only periods with a temperature difference higher than 4.0 °C (1.5 °C from the $U^{K'}_{37}$ calibration and 2.5 °C from the TEX_{86} calibration; blue dashed line). Besides, only the tie intervals when more than one excursion occurred were considered on this discussion. The subT remained below 20 °C during almost the whole Last Glacial Period, suggesting a shallow SACW in the region, reaching water depths around 30 m. The temperature differences between 0 and 30 m water depth for both SST proxies (Fig. 2.3), presented a similar pattern. A more mixed water column between 0 and 30 m water depth was observed between 50 and 30 kyr BP. Considering the orbital trend and the millennial oscillations, this interval corresponds to a cooling orbital trend. The subsurface layer was beginning to cool, while the surface was already colder. This temporal lag in the cooling of the subsurface, when compared to the surface, seems to have caused a greater homogenization of the water column between 0 and 30 m. On the other hand, the early MIS 4, the LGM and the period between 6 and 13 kyr presented a more stratified water column. These periods coincide with lower subT, when compared to the surroundings. The stratified water column combined with the low subT may suggest a shallow thermocline during these periods. These results are in agreement with the relatively higher values of the *Globigerina bulloides* / *Globigerinoides ruber* (white) (Gb/Gr) ratio observed by Toledo et al. (2008) in the vicinities. High Gb/Gr ratios suggest periods influenced by colder and nutrient-rich waters, whereas low values suggest a predominance of warm and oligotrophic surface waters (Toledo et al., 2008).

5.3. Orbital- and Millennial-scale influences

The EPICA Community Members (2006) observed coupling between Antarctic and Greenland warm events during the Last Glacial Cycle, named as the bipolar seesaw. This

mechanism could be caused by a reduction in the AMOC. More recently, West Antarctic Ice Sheet (WAIS) Divide Project Members (2015) demonstrated a north-to-south directionality of the abrupt climatic signal, which is propagated to the Southern Hemisphere high latitudes by oceanic processes. However, these processes are related to the formation of deep water masses and are not necessarily reflected in the SST in the same way (Lynch-Stieglitz, 2017).

The Pearson correlation analysis (Table 2.2) indicates that both the TEX_{86}-based and the LDI-based SST evolution are more similar to the Antarctic air temperature evolution when compared to Greenland's time series. Also, the NAP 63-1 SST evolution presented high correlation with the records from the subtropical South Atlantic (TN 057-21, GeoB 1710-3) and from the Western Equatorial Atlantic (GeoB 3910 and GeoB 3104, the latter being $\delta^{18}O$ data), evidencing the importance of the South Atlantic Subtropical Gyre in the heat transfer.

Table 2.2. Pearson correlation (R) between the TEX_{86}-based and the LDI-based SST from NAP 63-1 and other Atlantic SST reconstructions. Underlined *R* values: *p*-value < 0.05.

		TEX_{86}		LDI	
Core	Location	*p*-value	R	*p*-value	R
NGRIP	Greenland	0.0000	0.75	0.0000	0.67
GeoB 9528	E Equator	0.0000	0.43	0.0000	0.36
GeoB 3104	W Equator	0.0000	-0.69	0.0000	-0.60
GeoB 1105	E Equator	0.0000	0.62	0.0002	0.28
GeoB 3910	W Equator	0.0000	0.77	0.0000	0.62
GL-74	W S Atlantic	0.0000	0.34	0.0000	0.55
GL-1090	W S Atlantic	0.0000	0.34	0.0000	0.49
NAP 63-1 – LDI-SST	W S Atlantic	0.0000	0.71	X	X
NAP 63-1 – TEX_{86}-SST	W S Atlantic	X	X	0.0000	0.71
NAP 63-1 – $U^{K'}_{37}$-subT	W S Atlantic	0.0000	0.62	0.0000	0.52
GeoB 1710-3	E S Atlantic	0.0000	0.75	0.0000	0.73
TN057	SE S Atlantic	0.0000	0.63	0.0000	0.74
JR 244-GC528	SW S Atlantic	0.0000	0.60	0.0000	0.63
EDML	Antarctica	0.0000	0.77	0.0000	0.67

When the orbital-scale trend is considered apart from the millennial-scale oscillations (Fig. 2.4), both TEX_{86}-based and LDI-based SST records are more similar to the Antarctic climate than to the Greenland climate (Table A-4). Jouzel et al. (2007) related these orbital temperature variations in Antarctica to local insolation changes. However, regarding the millennial frequencies, half of the correlations were not significant (*p*-value > 0.05), indicating that they may not reliable (Table A-5). It suggests that the atmospheric temperature variations observed in both poles (EDML and NGRIP ice records) were not directly responsible for the millennial-scale variations in the SW Atlantic SST.

586 To identify the relevant millennial-scale SST variability over the whole 70 kyr signal,
587 we calculated the continuous wavelet transform of the LDI-based SST and TEX_{86}-based SST
588 (Fig. 2.6). The LDI-based SST power spectrum shows a significant energy signal in the 4-8
589 kyr timescale between 30 and 60 kyr BP. This same signal is also apparent in the TEX_{86}-
590 based SST power spectrum, although less pronounced. Clark et al. (2007) observed a ~7-kyr
591 oscillation occurring during MIS 3 and linked it to changes in the AMOC and, consequently,
592 in the cross-equatorial ocean heat transport. In the Northern Hemisphere, the D-O events
593 present a similar periodicity (around 5 kyr; Stocker and Johnsen, 2003). The Southern
594 Hemisphere counterparts to D-O events are the AIM (Blunier and Brook, 2001; EPICA
595 Community Members, 2006; Jaccard et al., 2016), especially during the Last Glacial Period.
596 Jouzel et al. (2007) concluded that the millennial oscillations in Antarctic, that compose the
597 AIM, are induced by changes in NADW formation through the thermal bipolar seesaw. In
598 turn, these changes on the NADW formation are one of the controlling factors of the short-
599 term variability of the AMOC, along with the Agulhas leakage (Biastoch et al., 2008).
600 Ultimately, this AMOC variability is responsible for the variability of the BC on a centennial
601 timescale, as demonstrated by Chiessi et al. (2014) during the late Holocene.
602

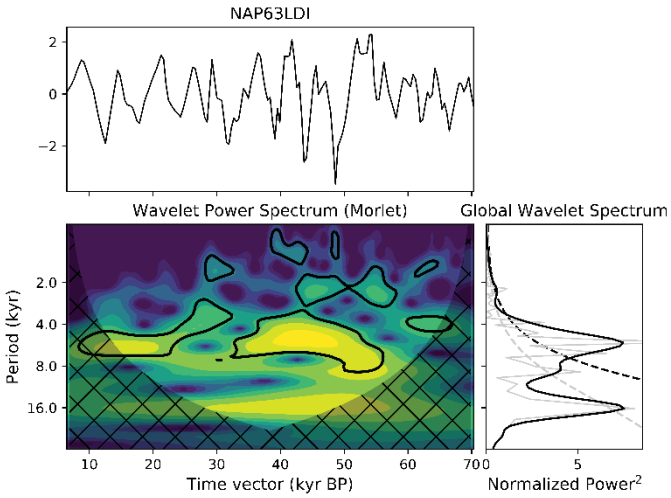

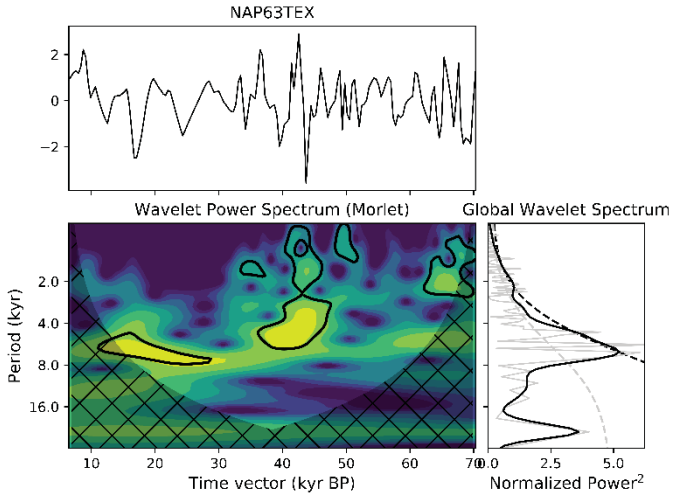

Fig. 2.6. At the top of each panel, normalized time series of sea surface temperatures at the NAP 63-1 core. At the bottom, the wavelet power spectrum (left) and global wavelet (black line) and Fourier spectrum (gray line) of the normalized signal on the time-frequency domain. Marked regions on the wavelet spectrum indicate significant power to a 95% confidence interval. The areas under the gray cone of influence show where edge effects are important. The sequence of the panels: (top) LDI-based SST and (bottom) TEX_{86}-based SST.

To asses whether the changes in the NADW formation and/or in the Agulhas leakage are indeed forcings for the SST millennial variations in the SW Atlantic, we computed the cross-wavelet and wavelet coherence between the LDI-based SST and two relevant proxies of these forcings. The LDI-based SST was chosen due to its higher correlation twith the Antarctic record, considering the millennial timescale. As for the NADW formation proxy, we used the Nd excess from the NW Atlantic (εNd for the NADW formation; based on OCE326-GGC6 and ODP 1063 sediment cores – Böhm et al., 2015; Roberts et al., 2010). High values of εNd indicate more NADW formation, and low (more negative) values εNd indicate less NADW formation (Bereiter et al., 2012; Piotrowski et al., 2005). As for the Agulhas leakage proxy, we used the local $\delta^{18}O_{sw}$ anomaly from the SE Atlantic (based on MD 02-2594 sediment core – Dyez et al., 2014). High values of $\delta^{18}O_{sw}$ anomaly indicate a stronger Agulhas leakage and low $\delta^{18}O_{sw}$ anomaly values indicate less input of Agulhas water in the South Atlantic (Dyez et al., 2014). The cross wavelet analysis exposes regions with high common power between the two time series and reveals information about the phase relationship. If the two time series are physically related, a consistent or slowly varying phase lag would be expected. But, even if the cross wavelet analysis does not reveal high common power, the wavelet coherence can find locally phase locked behavior through a correlation analysis (Grinsted et al., 2004).

First, the cross-wavelet between the εNd and the LDI-based annual SST (Fig. 2.7) shows a common high energy on the scale of 8 kyr throughout the analyzed period, with the

increase in NADW formation in antiphase with the warming on the SW Atlantic. This result agrees with the bipolar seesaw model, in which the slowdown of the thermohaline circulation results in the warming of the water masses in the South Atlantic basin (Stocker and Johnsen, 2003). Second, the cross-wavelet and the wavelet coherence between the SE Atlantic local $\delta^{18}O_{sw}$ anomaly and the TEX_{86}-based annual SST also presented a common high energy on the 8 kyr scale, but with the signals presenting a varying phase (Fig. 2.8). Poole and Tomczak (1999) observed that a large portion of the Agulhas leakage waters is transported northward by the North Brazil Current, contributing little to the southward flow of the Brazil Current. The variation in the phase indicates that the phenomena do not present a relation of cause and effect between them. Even so, the high energy in the same timescale suggests that the two processes respond to the same forcing, but in different ways. In general, these results suggest that changes in the NADW formation rather than in the Agulhas leakage may be the main driving mechanism of the millennial-scale oscillations observed during MIS 3 in the SW Atlantic.

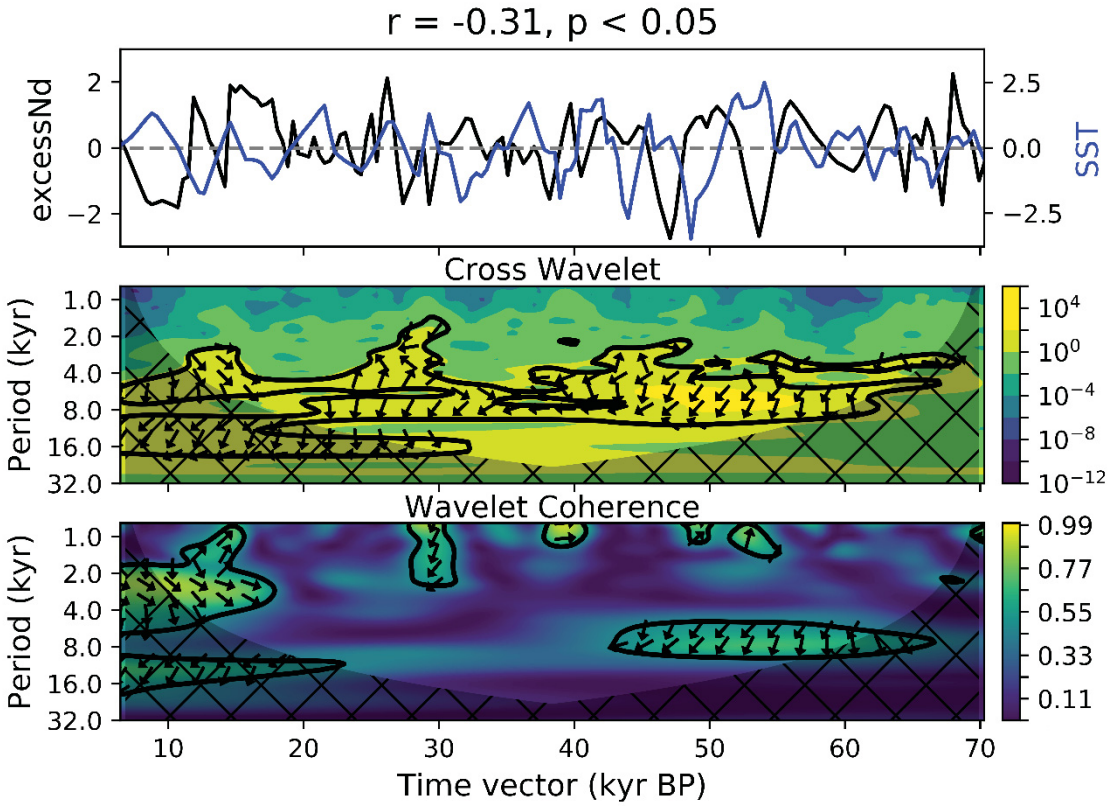

Fig. 2.7. Cross-wavelet and wavelet coherence between the Nd excess from NW Atlantic (εNd; OCE326-GGC6 and ODP 1063 cores; Böhm et al., 2015; Roberts et al., 2010) and TEX_{86}-based annual SST. At the top, the normalized time series. The phase arrows in the cross-wavelet power spectrum rotate clockwise with 'north' origin. The vectors indicate the phase relationship, where in phase signals point upwards (N), anti-phase signals point downwards (S). If X (εNd) leads Y, arrows point to the right (E) and if X lags Y, arrow points to the left (W). Marked regions on the wavelet spectrum indicate significant power to a 95% confidence interval, and areas under the gray cone of influence show where edge effects are important and the analysis unreliable.

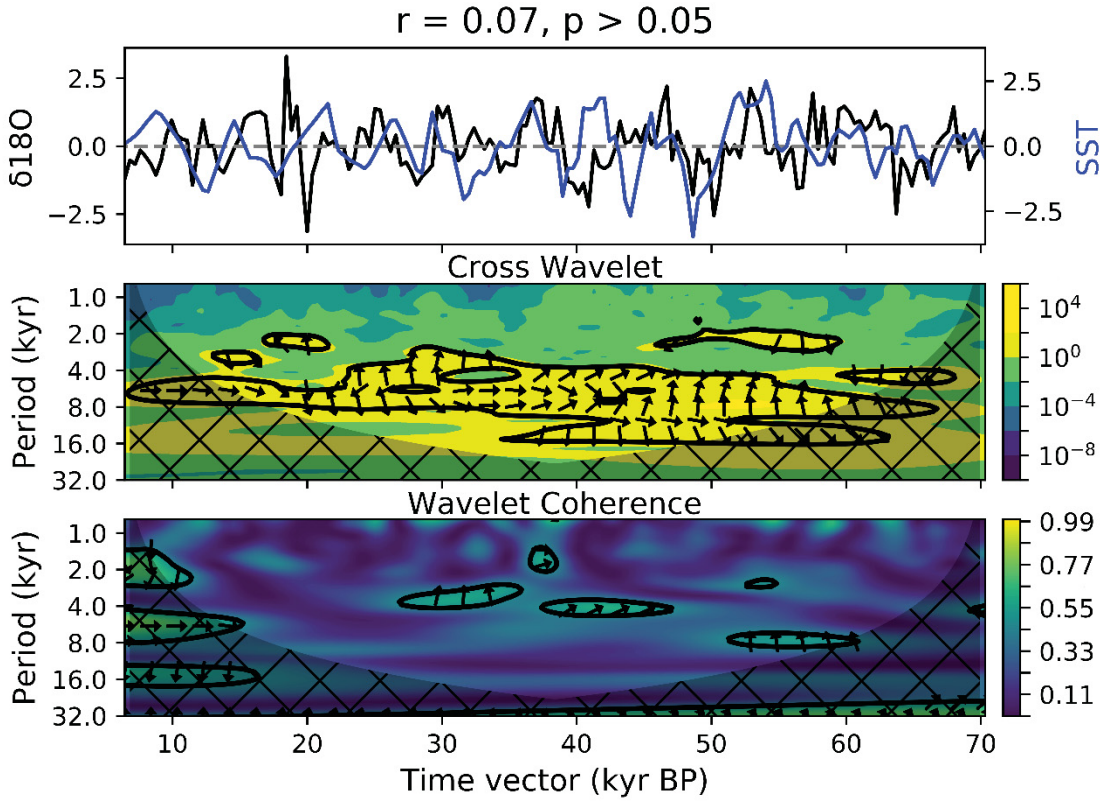

Fig. 2.8. Cross-wavelet and wavelet coherence between the local $\delta^{18}O_{sw}$ anomaly from the SE Atlantic (MD 02-2594 core; Dyez et al. 2014) and TEX_{86}-based annual SST. At the top, the normalized time series. The phase arrows in the cross-wavelet power spectrum rotate clockwise with 'north' origin. The vectors indicate the phase relationship, where in phase signals point upwards (N), anti-phase signals point downwards (S). If X ($\delta^{18}O_{sw}$ anomaly) leads Y, arrows point to the right (E) and if X lags Y, arrow points to the left (W). Marked regions on the wavelet spectrum indicate significant power to a 95% confidence interval, and areas under the gray cone of influence show where edge effects are important and the analysis unreliable.

6. Conclusions

In this study, we presented three paleotemperature reconstructions from the SW Atlantic based on molecular proxies. Although $U^{K'}_{37}$-based temperatures are usually associated with the sea surface, we inferred that they reflect the subsurface layer (around 30 m water depth). This was assumed since the maximum abundance of Haptophytes occurs right above the thermocline in the region, being under the influence of the SACW. On the other hand, the heterotrophic prokaryotes are more competitive in the surface, probably due to its oligotrophic condition. Thus, the TEX_{86}-signal was associated with the sea surface layer. The last index used was the LDI, which was also associated with the surface layer, since both TEX_{86}- and LDI-based temperatures presented the same range. However, as also observed by other studies, the LDI-signal presented a warm bias.

Regarding the temporal evolution of the SST, the SW Atlantic presented a colder MIS 3 than MIS 4, and a late deglaciation onset. The colder MIS 3 was observed by other authors

652 in the subtropical Atlantic and related to a conjunction of orbital forcings. The late response to
653 the deglaciation onset is probably related to a weakening of the AMOC. When the subT
654 record was compared with the SST records, a more mixed water column was observed during
655 intervals of cooling trends, which could be due to the time required to transfer the surface
656 cooling to the subsurface layer.
657 Finally, when the orbital trend and the millennial oscillations were considered apart,
658 they presented distinct triggers. In the orbital-scale, both the LDI-based and TEX_{86}-based SST
659 records were mainly influenced by the Antarctic climate, probably because of local insolation
660 variations. In the millennial-scale, both SST records presented a clear periodicity around 8
661 kyr, which is probably related to the AIM events. The millennial oscillations in Antarctic are
662 thought to be induced by AMOC oscillations, which in turn is controlled by the NADW
663 formation and the Agulhas leakage. We observed that, on this timescale, the millennial-scale
664 oscillations in the SW Atlantic SST are likely linked to the NADW formation.
665
666 **Acknowledgments**
667 A.L.L. Dauner would like to thank CAPES (Coordenação de Aperfeiçoamento de
668 Pessoal de Ensino Superior) for the Ph.D. Scholarship, to Dr. Jens Hefter for all assistance
669 and teachings in the laboratory analysis. M.M. Souza would like to thank the Deutscher
670 Akademischer Austauschdienst (DAAD) for the doctoral scholarship (reference number:
671 91621623). M.C. Bícego and M.M. Mahiques would like to thank FAPESP (São Paulo
672 Science Foundation) for the financial support (FAPESP: 2010/06147-5 and 2015/21834-2).
673 C.C. Martins would like to thank CNPq (Brazilian National Council for Scientific and
674 Technological Development) for a research grant (305763/2011-3). The authors would like to
675 thank Dr. Peter DeMenocal from the Lamont-Doherty Earth Observatory (LDEO), Columbia
676 University (New York, USA) for the oxygen isotopic composition analysis. The authors also
677 thank two anonymous reviewers for their useful comments on this manuscript.
678
679 **Supplementary Data**
680 The supplementary data related to this article can be found in Appendix A.
681
682 **Data Availability**
683 The temperature estimates are available in Appendix B and in
684 https://doi.pangaea.de/10.1594/PANGAEA.901238.
685

686 **References**

687 Alves, E.Q., Macario, K.D., Souza, R., Pimenta, A., Douka, K., Oliveira, F., Chanca,
688 I., Angulo, R.J., 2015. Quaternary Geochronology Radiocarbon reservoir corrections on the
689 Brazilian coast from pre-bomb marine shells. Quat. Geochronol. 29, 30–35.
690 https://doi.org/10.1016/j.quageo.2015.05.006
691 Arz, H.W., Pätzold, J., Wefer, G., 1999. The deglacial history of the western tropical
692 Atlantic as inferred from high resolution stable isotope records off northeastern Brazil. Earth
693 Planet. Sci. Lett. 167, 105–117. https://doi.org/10.1016/S0012-821X(99)00025-4
694 Ayache, M., Swingedouw, D., Mary, Y., Eynaud, F., Colin, C., 2018. Multi-centennial
695 variability of the AMOC over the Holocene: A new reconstruction based on multiple proxy-
696 derived SST records. Glob. Planet. Change 170, 172–189.
697 https://doi.org/10.1016/J.GLOPLACHA.2018.08.016
698 Barker, S., Diz, P., Vautravers, M.J., Pike, J., Knorr, G., Hall, I.R., Broecker, W.S.,
699 2009. Interhemispheric Atlantic seesaw response during the last deglaciation. Nature 457,
700 1097–1102. https://doi.org/10.1038/nature07770
701 Barrows, T.T., Juggins, S., De Deckker, P., Calvo, E., Pelejero, C., 2007. Long-term
702 sea surface temperature and climate change in the Australian-New Zealand region.
703 Paleoceanography 22, 1–17. https://doi.org/10.1029/2006PA001328
704 Bereiter, B., Luthi, D., Siegrist, M., Schupbach, S., Stocker, T.F., Fischer, H., 2012.
705 Mode change of millennial CO_2 variability during the last glacial cycle associated with a
706 bipolar marine carbon seesaw. Proc. Natl. Acad. Sci. 109, 9755–9760.
707 https://doi.org/10.1073/pnas.1204069109
708 Biastoch, A., Böning, C.W., Lutjeharms, J.R.E., 2008. Agulhas leakage dynamics
709 affects decadal variability in Atlantic overturning circulation. Nature 456, 489–492.
710 https://doi.org/10.1038/nature07426
711 Blaauw, M., Christen, J.A., 2011. Flexible paleoclimate age-depth models using an
712 autoregressive gamma process. Bayesian Anal. 6, 457–474. https://doi.org/10.1214/11-BA618
713 Blunier, T., Brook, E.J., 2001. Timing of millenial-scale climate change in Antarctica
714 and Greenland. Science (80-.). 291, 109–112.
715 Boebel, O., Davis, R.E., Ollitrault, M., Peterson, R.G., Richardson, P.L., Schmid, C.,
716 Zenk, W., 1999. The intermediate depth circulation of the western South Atlantic. Geophys.
717 Res. Lett. 26, 3329–3332. https://doi.org/10.1029/1999GL002355

718 Böhm, E., Lippold, J., Gutjahr, M., Frank, M., Blaser, P., Antz, B., Fohlmeister, J.,
719 Frank, N., Andersen, M.B., Deininger, M., 2015. Strong and deep Atlantic meridional
720 overturning circulation during the last glacial cycle. Nature 517, 73–76.
721 https://doi.org/10.1038/nature14059
722 Caley, T., Peeters, F.J.C., Biastoch, A., Rossignol, L., van Sebille, E., Durgadoo, J.,
723 Malaizé, B., Giraudeau, J., Arthur, K., Zahn, R., 2014. Quantitative estimate of the paleo-
724 Agulhas leakage. Geophys. Res. Lett. 41, 1238–1246. https://doi.org/10.1002/2014GL059278
725 Campos, E.J.D., Miller, J.L., Moiler, T.J., Peterson, R.G., 1995. Physical
726 Oceanography of the southwest Atlantic Ocean. Oceanography 8, 87–91.
727 Campos, E.J.D., Velhote, D., Silveira, I.C.A., 2000. Shelf break upwelling driven by
728 Brazil current cyclonic meanders. Geophys. Res. Lett. 27, 751–754.
729 https://doi.org/10.1029/1999GL010502
730 Capron, E., Landais, A., Chappellaz, J., Schilt, A., Buiron, D., Dahl-Jensen, D.,
731 Johnsen, S.J., Jouzel, J., Lemieux-Dudon, B., Loulergue, L., Leuenberger, M., Masson-
732 Delmotte, V., Mayer, H., Oerter, H., Stenni, B., 2010. Millennial and sub-millennial scale
733 climatic variations recorded in polar ice cores over the last glacial period. Clim. Past Discuss.
734 6, 135–183. https://doi.org/10.5194/cpd-6-135-2010
735 Castellanos, P., Campos, E.J.D., Piera, J., Sato, O.T., Silva Dias, M.A.F., 2017.
736 Impacts of Agulhas leakage on the tropical Atlantic western boundary systems. J. Clim. 30,
737 6645–6659. https://doi.org/10.1175/JCLI-D-15-0878.1
738 Ceccopieri, M., Carreira, R.S., Wagener, A.L.R., Hefter, J., Mollenhauer, G., 2018. On
739 the application of alkenone- and GDGT-based temperature proxies in the southeastern
740 Brazilian continental margin. Org. Geochem. 126, 43–56.
741 https://doi.org/https://doi.org/10.1016/j.orggeochem.2018.10.009
742 Chen, W., Mohtadi, M., Schefuß, E., Mollenhauer, G., 2014. Organic-geochemical
743 proxies of sea surface temperature in surface sediments of the tropical eastern Indian Ocean.
744 Deep. Res. Part I Oceanogr. Res. Pap. 88, 17–29. https://doi.org/10.1016/j.dsr.2014.03.005
745 Chiessi, C.M., Mulitza, S., Groeneveld, J., Silva, J.B., Campos, M.C., Gurgel, M.H.C.,
746 2014. Variability of the Brazil Current during the late Holocene. Palaeogeogr. Palaeoclimatol.
747 Palaeoecol. 415, 28–36. https://doi.org/10.1016/j.palaeo.2013.12.005
748 Chiessi, C.M., Mulitza, S., Mollenhauer, G., Silva, J.B., Groeneveld, J., Prange, M.,
749 2015. Thermal evolution of the western South Atlantic and the adjacent continent during
750 Termination 1. Clim. Past 11, 915–929. https://doi.org/10.5194/cp-11-915-2015

751 Clark, P.U., Hostetler, S.W., Pisias, N.G., Schmittner, A., Meissner, K.J., 2007.
752 Mechanisms for an ~7-kyr climate and sea-level oscillation during Marine Isotope Stage 3, in:
753 Schmittner, A., Chiang, J.C.H., Hemming, S.R. (Eds.), Geophysical Monograph Series 173.
754 American Geophysical Union, Washington DC, pp. 209–246. https://doi.org/10.1029/GM173
755 Clauzet, G., Wainer, I.E.K.C., Lazar, A., Brady, E., Otto-Bliesner, B.L., 2007. A
756 numerical study of the South Atlantic circulation at the Last Glacial Maximum. Palaeogeogr.
757 Palaeoclimatol. Palaeoecol. 253, 509–528. https://doi.org/10.1016/j.palaeo.2007.06.018
758 Conte, M.H., Sicre, M.-A., Rühlemann, C., Weber, J.C., Schulte, S., Schulz-Bull, D.,
759 Blanz, T., 2006. Global temperature calibration of the alkenone unsaturation index ($U^{K'}_{37}$) in
760 surface waters and comparison with surface sediments. Geochemistry, Geophys. Geosystems
761 7, 1–22. https://doi.org/10.1029/2005GC001054
762 Costa, K.B., Cabarcos, E., Santarosa, A.C.A., Battaglin, B.B.F., Toledo, F.A.L., 2016.
763 A multiproxy approach to the climate and marine productivity variations along MIS 5 in SE
764 Brazil: A comparison between major components of calcareous nannofossil assemblages and
765 geochemical records. Palaeogeogr. Palaeoclimatol. Palaeoecol. 449, 275–288.
766 https://doi.org/10.1016/j.palaeo.2016.02.032
767 Covey, C., 1984. The Earth's Orbit and the Ice Ages. Sci. Am. 250, 58–66.
768 Crowley, T.J., Hyde, W.T., 2008. Transient nature of late Pleistocene climate
769 variability. Nature 456, 226–230. https://doi.org/10.1038/nature07365
770 Delworth, T.L., Clark, P.U., Holland, M., Johns, W.E., Kuhlbrodt, T., Lynch-Stieglitz,
771 J., Morrill, C., Seager, R., Weaver, A.J., Zhang, R., 2008. The potential for abrupt change in
772 the Atlantic Meridional Overturning Circulation. Abrupt Clim. Chang. Final Rep. 258–359.
773 Donners, J., Drijfhout, S.S., Hazeleger, W., 2005. Water mass transformation and
774 subduction in the South Atlantic. J. Phys. Oceanogr. 35, 1841–1860.
775 https://doi.org/10.1175/JPO2782.1
776 Dyez, K.A., Zahn, R., Hall, I.R., 2014. Multicentennial Agulhas leakage variability
777 and links to North Atlantic climate during the past 80,000 years. Paleoceanography 1238–
778 1248. https://doi.org/10.1002/2014PA002698.
779 [dataset] EPICA Community Members, 2010. Stable oxygen isotopes of ice core
780 EDML. https://doi.org/https://doi.org/10.1594/PANGAEA.754444
781 EPICA Community Members, 2006. One-to-one coupling of glacial climate variability
782 in Greenland and Antarctica. Nature 444, 195–198. https://doi.org/10.1038/nature05301

Epstein, B.L., D'Hondt, S., Hargraves, P.E., 2001. The possible metabolic role of C_{37} alkenones in *Emiliania huxleyi*. Org. Geochem. 32, 867–875. https://doi.org/10.1016/S0146-6380(01)00026-2

Garzoli, S.L., Matano, R.P., 2011. The South Atlantic and the Atlantic Meridional Overturning Circulation. Deep. Res. Part II Top. Stud. Oceanogr. 58, 1837–1847. https://doi.org/10.1016/j.dsr2.2010.10.063

Govin, A., Capron, E., Tzedakis, P.C., Verheyden, S., Ghaleb, B., Hillaire-Marcel, C., St-Onge, G., Stoner, J.S., Bassinot, F., Bazin, L., Blunier, T., Combourieu-Nebout, N., El Ouahabi, A., Genty, D., Gersonde, R., Jimenez-Amat, P., Landais, A., Martrat, B., Masson-Delmotte, V., Parrenin, F., Seidenkrantz, M.-S., Veres, D., Waelbroeck, C., Zahn, R., 2015. Sequence of events from the onset to the demise of the Last Interglacial: Evaluating strengths and limitations of chronologies used in climatic archives. Quat. Sci. Rev. 129, 1–36. https://doi.org/10.1016/j.quascirev.2015.09.018

Grinsted, A., Moore, J.C., Jevrejeva, S., 2004. Application of the cross wavelet transform and wavelet coherence to geophysical time series. Nonlinear Process. Geophys. 11, 561–566. https://doi.org/10.5194/npg-11-561-2004

Hernández-Sánchez, M.T., Woodward, E.M.S., Taylor, K.W.R., Henderson, G.M., Pancost, R.D., 2014. Variations in GDGT distributions through the water column in the South East Atlantic Ocean. Geochim. Cosmochim. Acta 132, 337–348. https://doi.org/10.1016/j.gca.2014.02.009

Huguet, C., Kim, J.H., Sinninghe Damsté, J.S., Schouten, S., 2006. Reconstruction of sea surface temperature variations in the Arabian Sea over the last 23 kyr using organic proxies (TEX_{86} and $U^{K'}_{37}$). Paleoceanography 21, 1–13. https://doi.org/10.1029/2005PA001215

Hunter, J.D., 2007. Matplotlib: A 2D Graphics Environment. Comput. Sci. Eng. 9, 90–95. https://doi.org/10.1109/MCSE.2007.55

Jaccard, S.L., Galbraith, E.D., Martínez-García, A., Anderson, R.F., 2016. Covariation of deep Southern Ocean oxygenation and atmospheric CO_2 through the last ice age. Nature 530, 207–10. https://doi.org/10.1038/nature16514

Jaeschke, A., Rühlemann, C., Arz, H.W., Heil, G., Lohmann, G., 2007. Coupling of millennial-scale changes in sea surface temperature and precipitation off northeastern Brazil with high-latitude climate shifts during the last glacial period. Paleoceanography 22, 1–10. https://doi.org/10.1029/2006PA001391

Jones, E., Oliphant, T., Peterson, P., 2015. SciPy: Open source scientific tools for Python, 2001. URL http//www. scipy. org.

Jouzel, J., Masson-Delmotte, V., Cattani, O., Dreyfus, G., Falourd, S., Hoffmann, G., Minster, B., Nouet, J., Barnola, J.M., Chappellaz, J., Fischer, H., Gallet, J.C., Johnsen, S.J., Leuenberger, M., Loulergue, L., Luethi, D., Oerter, H., Parrenin, F., Raisbeck, G., Raynaud, D., Schilt, A., Schwander, J., Selmo, E., Souchez, R., Spahni, R., Stauffer, B., Steffensen, J.P., Stenni, B., Stocker, T.F., Tison, J.L., Werner, M., Wolff, E.W., 2007. Orbital and Millennial Antarctic Climate Variability over the Past 800,000 Years. Science (80-.). 317, 793–796. https://doi.org/10.1126/science.1141038

Kim, J.H., van der Meer, J., Schouten, S., Helmke, P., Willmott, V., Sangiorgi, F., Koç, N., Hopmans, E.C., Sinninghe Damsté, J.S., 2010. New indices and calibrations derived from the distribution of crenarchaeal isoprenoid tetraether lipids: Implications for past sea surface temperature reconstructions. Geochim. Cosmochim. Acta 74, 4639–4654. https://doi.org/10.1016/j.gca.2010.05.027

[dataset] Kirst, G., Müller, P.J., 2001. Total organic carbon, alkenones and sea surface temperature of sediment core GeoB1710-3 (PANGAEA database). https://doi.org/https://doi.org/10.1594/PANGAEA.58041

Lattaud, J., Lo, L., Huang, J.J., Chou, Y.M., Gorbarenko, S.A., Sinninghe Damsté, J.S., Schouten, S., 2018. A comparison of Late Quaternary organic proxy-based paleotemperature records of the Central Sea of Okhotsk. Paleoceanogr. Paleoclimatology 33, 732–744. https://doi.org/10.1029/2018PA003388

Li, L., Li, Q., He, J., Wang, H., Ruan, Y., Li, J., 2015. Biomarker-derived phytoplankton community for summer monsoon reconstruction in the western South China Sea over the past 450ka. Deep. Res. Part II Top. Stud. Oceanogr. 122, 118–130. https://doi.org/10.1016/j.dsr2.2015.11.006

Lisiecki, L.E., Raymo, M.E., 2005. A Pliocene-Pleistocene stack of 57 globally distributed benthic $\delta^{18}O$ records. Paleoceanography 20, 1–17. https://doi.org/10.1029/2004PA001071

Lisiecki, L.E., Stern, J. V., 2016. Regional and global benthic $\delta^{18}O$ stacks for the last glacial cycle. Palaeogeography 31, 1368–1394. https://doi.org/10.1002/2016PA003002

[dataset] Locarnini, R.A., Mishonov, A. V., Antonov, J.I., Boyer, T.P., Garcia, H.E., Baranova, O.K., Zweng, M.M., Paver, C.R., Reagan, J.R., Johnson, D.R., Hamilton, M., Seidov, D., 2013. World Ocean Atlas 2013, Volume 1: Temperature, in: Levitus, S.E. (Ed.), NOAA Atlas NESDIS 73. A. Mishonov Technical, p. 40.

Lopes dos Santos, R.A., Prange, M., Castañeda, I.S., Schefuß, E., Mulitza, S., Schulz, M., Niedermeyer, E.M., Sinninghe Damsté, J.S., Schouten, S., 2010. Glacial-interglacial variability in Atlantic meridional overturning circulation and thermocline adjustments in the tropical North Atlantic. Earth Planet. Sci. Lett. 300, 407–414. https://doi.org/10.1016/j.epsl.2010.10.030

Lopes dos Santos, R.A., Spooner, M.I., Barrows, T.T., De Deckker, P., Sinninghe Damsté, J.S., Schouten, S., 2013. Comparison of organic ($U^{K'}_{37}$, TEX^{H}_{86}, LDI) and faunal proxies (foraminiferal assemblages) for reconstruction of late Quaternary sea surface temperature variability from offshore southeastern Australia. Paleoceanography 28, 377–387. https://doi.org/10.1002/palo.20035

Lourenço, R.A., Mahiques, M.M., Wainer, I.E.K.C., Rosell-Melé, A., Bícego, M.C., 2016. Organic biomarker records spanning the last 34,800 years from the southeastern Brazilian upper slope: links between sea surface temperature, displacement of the Brazil Current, and marine productivity. Geo-Marine Lett. 36, 361–369. https://doi.org/10.1007/s00367-016-0453-7

Lynch-Stieglitz, J., 2017. The Atlantic Meridional Overturning Circulation and abrupt climate change. Ann. Rev. Mar. Sci. 9, 83–104. https://doi.org/10.1146/annurev-marine-010816-060415

Mahiques, M.M., Sousa, S.H.M., Furtado, V.V., Tessler, M.G., Toledo, F.A.L., Burone, L., Figueira, R.C.L., Klein, D.A., Martins, C.C., Alves, D.P.V., 2010. The Southern Brazilian shelf: General characteristics, quaternary evolution and sediment distribution. Brazilian J. Oceanogr. 58, 25–34. https://doi.org/10.1590/S1679-87592010000600004

McManus, J.F., Francois, R., Gherardl, J.M., Kelgwin, L., Drown-Leger, S., 2004. Collapse and rapid resumption of Atlantic meridional circulation linked to deglacial climate changes. Nature 428, 834–837. https://doi.org/10.1038/nature02494

Mollenhauer, G., Basse, A., Kim, J.H., Sinninghe Damsté, J.S., Fischer, G., 2015. A four-year record of $U^{K'}_{37}$- and TEX_{86}-derived sea surface temperature estimates from sinking particles in the filamentous upwelling region off Cape Blanc, Mauritania. Deep. Res. Part I Oceanogr. Res. Pap. 97, 67–79. https://doi.org/10.1016/j.dsr.2014.11.015

Müller, P.J., Kirst, G., Ruhland, G., von Storch, I., Rosell-Melé, A., 1998. Calibration of the alkenone paleotemperature index $U^{K'}_{37}$ based on core-tops from the eastern South Atlantic and the global ocean (60°N - 60°S). Geochim. Cosmochim. Acta 62, 1757–1772. https://doi.org/10.1016/S0016-7037(98)00097-0

Nanninga, H.J., Tyrrell, T., 1996. Importance of light for the formation of algal blooms by *Emiliania huxleyi*. Mar. Ecol. Prog. Ser. 136, 195–203. https://doi.org/10.3354/meps136195

NGRIP Members, 2004. High-resolution record of Northern Hemisphere climate extending into the last interglacial period. Nature 431, 147–151. https://doi.org/10.1038/nature02805

Oliphant, T.E., 2006. A guide to NumPy.

Pahnke, K., Sachs, J.P., 2006. Sea surface temperatures of southern midlatitudes 0 – 160 kyr B . P . Paleoceanography 21, 1–17. https://doi.org/10.1029/2005PA001191

Paillard, D., Labeyrie, L.D., Yiou, P., 1996. AnalySeries 1.0: a Macintosh software for the analysis of geophysical time-series.

Palma, E.D., Matano, R.P., 2009. Disentangling the upwelling mechanisms of the South Brazil Bight. Cont. Shelf Res. 29, 1525–1534. https://doi.org/10.1016/j.csr.2009.04.002

Pereira, J., Cirano, M., Marta-Almeida, M., Amorim, F.N., 2013. A regional study of the Brazilian shelf/slope circulation (13°-31°S) using climatological open boundaries. Rev. Bras. Geofísica 31, 289–305.

Pereira, J., Gabioux, M., Marta-Almeida, M., Cirano, M., Paiva, A.M., Aguiar, A.L., 2014. The bifurcation of the western boundary current system of the South Atlantic Ocean. Rev. Bras. Geofísica 32, 241–257.

Peterson, R.G., Stramma, L., 1991. Upper-level circulation in the South-Atlantic Ocean. Prog. Oceanogr. 26, 1–73. https://doi.org/10.1016/0079-6611(91)90006-8

Piola, A.R., Campos, E.J.D., Möller Jr., O.O., Charo, M., Martinez, C., 2000. Subtropical Shelf Front off eastern South America. J. Geophys. Res. Ocean. 105, 6565–6578. https://doi.org/10.1029/1999JC000300

Piola, A.R., Matano, R.P., 2001. Brazil and Falklands (Malvinas) Currents, in: Steele, J.H., Thorpe, S.A., Turekian, K.K. (Eds.), Ocean Currents: A Derivative of the Encyclopedia of Ocean Sciences. Elsevier Inc., pp. 35–43. https://doi.org/10.1016/B978-0-12-409548-9.10541-X

Piotrowski, A.M., Goldstein, S.L., Hemming, S.R., Fairbanks, R.G., 2005. Temporal relationship of carbon cycling and ocean circulation at glacial boundaries. Science (80-.). 307, 1933–1938. https://doi.org/10.1126/science.1104883

Poole, R., Tomczak, M., 1999. Optimim multiparameter analysis of the water mass structure in the Atlantic Ocean thermocline. Deep. Res. Part I Oceanogr. Res. Pap. 46, 1895–1921.

Portilho-Ramos, R.C., Ferreira, F., Calado, L., Frontalini, F., Toledo, M.B., 2015. Variability of the upwelling system in the southeastern Brazilian margin for the last 110,000 years. Glob. Planet. Change 135, 179–189. https://doi.org/10.1016/j.gloplacha.2015.11.003

Prahl, F.G., Wakeham, S.G., 1987. Calibration of unsaturation patterns in long-chain ketone compositions for palaeotemperature assessment. Nature 330, 367–369. https://doi.org/10.1038/330367a0

Rampen, S.W., Schouten, S., Wakeham, S.G., Sinninghe Damsté, J.S., 2007. Seasonal and spatial variation in the sources and fluxes of long chain diols and mid-chain hydroxy methyl alkanoates in the Arabian Sea. Org. Geochem. 38, 165–179. https://doi.org/10.1016/j.orggeochem.2006.10.008

Rampen, S.W., Willmott, V., Kim, J.H., Uliana, E., Mollenhauer, G., Schefuß, E., Sinninghe Damsté, J.S., Schouten, S., 2012. Long chain 1,13- and 1,15-diols as a potential proxy for palaeotemperature reconstruction. Geochim. Cosmochim. Acta 84, 204–216. https://doi.org/10.1016/j.gca.2012.01.024

Reimer, P.J., Bard, E., Bayliss, A., Beck, J.W., Blackewll, P.G., Ramsey, C.B., Buck, C.E., Cheng, H., Edwards, R.L., Friedrich, M., Grootes, P.M., Guilderson, T.P., Haflidason, H., Hajdas, I., Hatté, C., Heaton, T.J., Hoffmann, D.L., Hogg, A.G., Hughen, K.A., Kaiser, K.F., Kromer, B., Manning, S.W., Niu, M., Reimer, R.W., Richards, D.A., Scott, E.M., Southon, J.R., Staff, R.A., Turney, C.S.M., Pflicht, J. van der, 2013. IntCal13 and Marine13 radiocarbon age calibration curves 0–50,000 years cal BP. Radiocarbon 55, 1869–1887. https://doi.org/10.2458/azu_js_rc.55.16947

Ribeiro, C.G., Lopes dos Santos, A., Marie, D., Pellizari, V.H., Brandini, F.P., Vaulot, D., 2016. Pico and nanoplankton abundance and carbon stocks along the Brazilian Bight. PeerJ 4, e2587. https://doi.org/10.7717/peerj.2587

Roberts, J., McCave, I.N., McClymont, E.L., Kender, S., Hillenbrand, C.-D., Matano, R.P., Hodell, D.A., Peck, V.L., 2017a. Deglacial changes in flow and frontal structure through the Drake Passage. Earth Planet. Sci. Lett. 474, 397–408. https://doi.org/10.1016/j.epsl.2017.07.004

[dataset] Roberts, J., McCave, I.N., McClymont, E.L., Kender, S., Hillenbrand, C.-D., Matano, R.P., Hodell, D.A., Peck, V.L., 2017b. Alkenones and calculated sea surface temperature of sediment core JR244-GC528 (PANGAEA database). https://doi.org/10.1594/PANGAEA.878265

949 Roberts, N.L., Piotrowski, A.M., McManus, J.F., Keigwin, L.D., 2010. Synchronous
950 deglacial overturning and water mass source changes. Science. 327, 75–78.
951 https://doi.org/10.1126/science.1178068
952 Rodrigo-Gámiz, M., Martínez-Ruiz, F., Rampen, S.W., Schouten, S., Sinninghe
953 Damsté, J.S., 2014. Sea surface temperature variations in the western Mediterranean Sea over
954 the last 20 kyr: A dual-organic proxy ($U^{K'}_{37}$ and LDI) approach. Paleoceanography 29, 87–98.
955 https://doi.org/10.1002/2013PA002466.Received
956 Rodrigo-Gámiz, M., Rampen, S.W., Schouten, S., Sinninghe Damsté, J.S., 2016. The
957 impact of oxic degradation on long chain alkyl diol distributions in Arabian Sea surface
958 sediments. Org. Geochem. 100, 1–9. https://doi.org/10.1016/j.orggeochem.2016.07.003
959 Rodrigues, S. V., Marinho, M.M., Cubas Jonck, C.C., Gonçalves, E.S., Brant, V.F.,
960 Paranhos, R., Curbelo, M.P., Falcão, A.P., 2014. Phytoplankton community structures in shelf
961 and oceanic waters off southeast Brazil (20°-25°S), as determined by pigment signatures.
962 Deep. Res. Part I Oceanogr. Res. Pap. 88, 47–62. https://doi.org/10.1016/j.dsr.2014.03.006
963 Rommerskirchen, F., Condon, T., Mollenhauer, G., Dupont, L., Schefuß, E., 2011.
964 Miocene to Pliocene development of surface and subsurface temperatures in the Benguela
965 Current system. Paleoceanography 26, 1–15. https://doi.org/10.1029/2010PA002074
966 Sanchez Goñi, M.F., Harrison, S.P., 2010. Millennial-scale climate variability and
967 vegetation changes during the Last Glacial: Concepts and terminology. Quat. Sci. Rev. 29,
968 2823–2827. https://doi.org/10.1016/j.quascirev.2009.11.014
969 Santos, T.P., Lessa, D.V.O., Venancio, I.M., Chiessi, C.M., Mulitza, S., Kuhnert, H.,
970 Govin, A., Machado, T., Costa, K.B., Toledo, F.A.L., Dias, B.B., Albuquerque, A.L.S., 2017.
971 Prolonged warming of the Brazil Current precedes deglaciations. Earth Planet. Sci. Lett. 463,
972 1–12. https://doi.org/10.1016/j.epsl.2017.01.014
973 Schmid, C., 2014. Mean vertical and horizontal structure of the subtropical circulation
974 in the South Atlantic from three-dimensional observed velocity fields. Deep. Res. Part I
975 Oceanogr. Res. Pap. 91, 50–71. https://doi.org/10.1016/j.dsr.2014.04.015
976 Schmid, C., Siedler, G., Zenk, W., 2000. Dynamics of Intermediate Water Circulation
977 in the Subtropical South Atlantic. J. Phys. Oceanogr. 30, 3191–3211.
978 https://doi.org/10.1175/1520-0485(2000)030<3191:DOIWCI>2.0.CO;2
979 [dataset] Schneider, R.R., Müller, P.J., Ruhland, G., Meinecke, G., Schmidt, H.,
980 Wefer, G., 1996. Alkenones, sea surface temperature and $\delta^{18}O$ of *Globigerinoides ruber* of
981 sediment core GeoB1105-4 (PANGAEA database).
982 https://doi.org/doi.org/10.1594/PANGAEA.54864

983 Schouten, S., Hopmans, E.C., Schefuß, E., Sinninghe Damsté, J.S., 2002.
984 Distributional variations in marine crenarchaeol membrane lipids: a new tool for
985 reconstructing ancient sea water temperatures? Earth Planet. Sci. Lett. 204, 265–274.
986 Shakun, J.D., Clark, P.U., He, F., Marcott, S.A., Mix, A.C., Liu, Z., Otto-Bliesner,
987 B.L., Schmittner, A., Bard, E., 2012. Global warming preceded by increasing carbon dioxide
988 concentrations during the last deglaciation. Nature 484, 49–54.
989 https://doi.org/10.1038/nature10915
990 Silveira, I.C.A., Schmidt, A.C.K., Campos, E.J.D., Godoi, S.S., Ikeda, Y., 2000. A
991 corrente do Brasil ao largo da costa leste brasileira. Rev. Bras. Oceanogr. 48, 171–183.
992 https://doi.org/10.1590/S1413-77392000000200008
993 Smith, M., De Deckker, P., Rogers, J., Brocks, J., Hope, J., Schmidt, S., Lopes dos
994 Santos, R.A., Schouten, S., 2013. Comparison of $U^{K'}_{37}$, TEX_{86}^{H} and LDI temperature proxies
995 for reconstruction of southeast Australian ocean temperatures. Org. Geochem. 64, 94–104.
996 https://doi.org/10.1016/j.orggeochem.2013.08.015
997 Souza, R.B. de, Robinson, I.S., 2004. Lagrangian and satellite observations of the
998 Brazilian Coastal Current. Cont. Shelf Res. 24, 241–262.
999 https://doi.org/10.1016/j.csr.2003.10.001
1000 Speer, K., Rintoul, S.R., Sloyan, B., 2000. The Diabatic Deacon Cell. J. Phys.
1001 Oceanogr. 30, 3212–3222.
1002 Stocker, T.F., Johnsen, S.J., 2003. A minimum thermodynamic model for the bipolar
1003 seesaw. Paleoceanography 18, 1–9. https://doi.org/10.1029/2003PA000920
1004 Stramma, L., England, M., 1999. On the water masses and mean circulation of the
1005 South Atlantic Circulation. J. Geophys. Res. Ocean. 104, 20863–20883.
1006 https://doi.org/10.1029/1999JC900139
1007 Toledo, F.A.L., Costa, K.B., Pivel, M.A.G., 2007. Salinity changes in the western
1008 tropical South Atlantic during the last 30 kyr. Glob. Planet. Change 57, 383–395.
1009 https://doi.org/10.1016/j.gloplacha.2007.01.001
1010 Toledo, F.A.L., Costa, K.B., Pivel, M.A.G., Campos, E.J.D., 2008. Tracing past
1011 circulation changes in the western South Atlantic based on planktonic foraminifera. Rev.
1012 Bras. Paleontol. 11, 169–178. https://doi.org/10.4072/rbp.2008.3.03
1013 Torrence, C., Compo, G.P., 1998. A Practical Guide to Wavelet Analysis. Bull. Am.
1014 Meteorol. Soc. 79, 61–78.
1015 van Rossum, G., 1995. Python tutorial - Technical Report CS-R9526.

Volkman, J.K., Barrett, S.M., Dunstan, G.A., Jeffrey, S.W., 1992. C_{30} - C_{32} alkyl diols and unsaturated alcohols in microalgae of the class Eustigmatophyceae. Org. Geochem. 18, 131–138. https://doi.org/10.1016/0146-6380(92)90150-V

WAIS Divide Project Members, 2015. Precise interpolar phasing of abrupt climate change during the last ice age. Nature 520, 661–665. https://doi.org/10.1038/nature14401

Xiao, W., Esper, O., Gersonde, R., 2016a. Last Glacial - Holocene climate variability in the Atlantic sector of the Southern Ocean. Quat. Sci. Rev. 135, 115–137. https://doi.org/10.1016/j.quascirev.2016.01.023

Xiao, W., Frederichs, T., Gersonde, R., Kuhn, G., Esper, O., Zhang, X., 2016b. Constraining the dating of late Quaternary marine sediment records from the Scotia Sea (Southern Ocean). Quat. Geochronol. 31, 97–118. https://doi.org/10.1016/j.quageo.2015.11.003

Zachos, J., Pagani, M., Sloan, L., Thomas, E., Billups, K., 2001. Trends, rhythms, and aberrations in global climate 65 Ma to present. Science (80-.). 292, 686–693. https://doi.org/10.1126/science.1059412

Zubkov, M. V., Sleigh, M.A., Burkill, P.H., Leakey, R.J.G., 2000. Picoplankton community structure on the Atlantic Meridional Transect: A comparison between seasons. Prog. Oceanogr. 45, 369–386. https://doi.org/10.1016/S0079-6611(00)00008-2

CAPÍTULO 3

Aporte de material orgânico terrígeno e marinho e mudanças oceanográficas durante o Pleistoceno Tardio e Holoceno no oeste do Atlântico Sul

"*Input of terrestrial and marine organic matter and oceanographic changes during late Pleistocene and Holocene in the western South Atlantic*"

Manuscrito formatado para submissão segundo as normas da revista:

Earth and Planetary Science Letters; ISSN (0012-821X); Fator de Impacto 2017: 4,581

© Thomson Reuters Journal Citation Reports 2017

Qualis CAPES (Biodiversidade): Estrato B1

* Ana Lúcia L. Dauner [1,2], Gesine Mollenhauer [3,4], Márcia Caruso Bícego [5], Michel Michaelovitch de Mahiques [5], * César C. Martins [1]

[1] Center for Marine Studies, Federal University of Paraná, 83255-976 Pontal do Paraná, PR, Brazil

[2] Graduate Program in Coastal and Oceanic Systems (PGSISCO) of the Federal University of Paraná, 83255-976 Pontal do Paraná, PR, Brazil

[3] Alfred Wegener Institute, Helmholtz Center for Polar and Marine Research, D-27515 Bremerhaven, Germany

[4] MARUM Center for Marine Environmental Sciences, University of Bremen, D-28334 Bremen, Germany

[5] Oceanographic Institute, University of São Paulo, 05508-120 São Paulo, Brazil

* Corresponding authors:

anadauner@gmail.com (A.L.L. Dauner)

ccmart@ufpr.br (C.C. Martins)

Research Highlights

> Marine organisms were the main source of organic matter (OM) to the slope.

> Distinct mechanisms governed marine OM production and terrestrial OM export.

> Terrestrial OM was controlled by changes in sea level and continental moisture.

> Marine OM was controlled by changes in surface circulation and continental moisture.

Abstract

In this study, we investigated the sources of the terrestrial and marine organic matter (OM) to the central portion of the South Brazil Bight slope, and the main mechanisms that controlled the marine OM productivity and terrestrial OM export. We analyzed OM geochemical (bulk and molecular) proxies in sediment samples from a sediment core (NAP 63-1) retrieved from the SW Atlantic slope (24.8°S, 44.3°W, 840 m water depth). The organic proxies were classified into "terrestrial-source" and "marine-source" groups based on a cluster analysis. The two sources presented different stratigraphical zones, indicating distinct mechanisms governing the marine OM production and the terrestrial OM export. Bulk proxies indicate the predominance of marine OM source, although the terrestrial input also affected the total OM evolution. Terrestrial OM may have had two sources. It may have been exported by the Rio de la Plata and reworked and transported northward by the Intermediate Western Boundary Current. However, it could also have been originated in the drainage basins near the study site, especially the Paraíba do Sul River basin, and was carried southward by the Brazil Current. The highest terrestrial export occurred between 20 and 30 kyr BP (thousand years before present), with its temporal evolution controlled mainly by sea level fluctuations and the continental moisture evolution. The highest marine productivity was observed between 40 and 50 kyr BP and was driven by the South Atlantic Central Water upwelling promoted by the Brazil Current cyclonic eddies. Fluvial nutrient inputs from the adjacent coast controlled the marine productivity during Marine Isotopic Stages 4 and 2. After the last deglaciation, a stronger presence of the oligotrophic Tropical Water in the region was suggested by a decrease of the phytoplanktonic productivity and an increase of the archaeal productivity. In short, the OM input to the central portion of the South Brazil Bight was mainly controlled by the surface circulation, sea level fluctuations and the continental moisture evolution during the last 80 kyr.

Keywords: continental slope; South Brazil Bight; stratigraphical zones; mass accumulation rates; organic proxies.

Resumo

Neste estudo, nós investigamos as fontes da matéria orgânica (MO) terrestre para a porção central do talude do Embaiamento Sul do Brasil, assim como os principais mecanismos que governam a produção de MO marinha e a exportação de MO terrestre. Para isso, nós analisamos diversos marcadores geoquímicos (inorgânicos e moleculares) da MO em amostras de um testemunho sedimentar (NAP 63-1) coletado no Atlântico Sudoeste (24,8°S, 44,3°W, 840 m de profundidade). Os marcadores orgânicos foram classificados em dois grupos, baseado em uma análise de agrupamento: os de "fonte terrestre" e os de "fonte marinha". Os grupos apresentaram zonas bioestratigráficas distintas, indicando que mecanismos diferentes governam a produção de MO marinha e a exportação de MO terrestre. Os marcadores inorgânicos indicaram a predominância de MO marinha. Apesar disso, a MO terrestre também afetou o aporte de MO total. A MO terrestre pode ter sido exportada pelo rio da Prata, e retrabalhada e transportada para norte pela Corrente de Contorno Intermediária. No entanto, ela também pode ser oriunda das bacias de drenagem próximos ao local coletado, especialmente a bacia do rio Paraíba do Sul. Ao chegar no ambiente marinho, esse material pôde então ter sido transportado para sul pela Corrente do Brasil. As maiores taxas de aporte continental ocorreram entre 20 e 30 kyr BP (mil anos antes do presente), sendo que a sua evolução foi controlada principalmente pelas flutuações no nível do mar e pela umidade continental. As maiores taxas de produção de MO marinha foram observadas entre 40 e 50 kyr BP, as quais foram estimuladas pela ressurgência da Água Central do Atlântico Sul, sendo essa promovida pelos vórtices ciclônicos da Corrente do Brasil. Durante os estágios marinhos isotópicos 2 e 4, aportes de nutrientes fluviais controlaram a produtividade marinha. Por fim, depois da última deglaciação, a diminuição da produtividade fitoplanctônica e um aumento da produtividade de arqueias sugerem uma presença mais forte da Água Tropical, uma massa d'água tipicamente oligotrófica. Assim, o aporte de MO na porção central do talude do Embaiamento Sul do Brasil durante os últimos 80 mil anos foi governado principalmente pela circulação oceânica superficial, pelas flutuações no nível do mar e pela evolução da umidade continental.

Palavras-chave: talude continental, Embaiamento Sul do Brasil, zonas estratigráficas, taxas de acumulação de massa, *proxies* orgânicos.

1. Introduction

Temporal changes in carbon source delivery have been frequently recorded in ocean sediments and can provide an understanding of the linkages among climate, organic matter biogeochemical cycling and sequestration over different time scales (Faux et al., 2011). The South Atlantic Ocean plays an important role in the global climate system through the formation of nutrient-rich dense water masses and heat transport into the Southern Ocean (Garzoli and Matano, 2011). It also receives large amounts of terrestrial organic matter (OM) originated from South America (e.g. Rio de la Plata – RdlP – Basin) and Africa (e.g. Congo Basin) (Braga et al., 2008; Muelbert et al., 2008; Weijers et al., 2007).

Hessler et al. (2010) used the seasonal variations of the Intertropical Convergence Zone (ITCZ) to explain how the humidity variations in the tropical Atlantic over the Last Glacial Period affects differently the margins of the Atlantic basin. During cold phases (such as the Heinrich events and the Last Glacial Maximum), the ITCZ migrated southward, enhancing the humidity over the tropical and subtropical South America. The increased humidity promoted the development of forests (Freeman and Pancost, 2013) and the exportation of terrestrial OM to the ocean through riverine flows (Almeida et al., 2015; Hessler et al., 2010). The cold phases may also have induced the strengthening of the Southern Hemisphere mid-latitude westerlies (WAIS Divide Project Members, 2015), which promoted the deposition of atmospheric dust in the temperate portion of the west South Atlantic (Chapori et al., 2014). However, during the warm phases (such as the Dansgaard-Oeschger events), the ITCZ migrated northward, promoting a humid climate in the tropical and subtropical Africa (Hessler et al., 2010; Kallweit et al., 2012). This humid climate increased the fluvial OM and nutrient inputs from the Congo river, which consequently promoted the marine productivity in the eastern South Atlantic (Benthien et al., 2005; Kallweit et al., 2012). The northern most ITCZ may also have promoted a cyclonic circulation in the east South Atlantic, piling up warm waters near the African continent (Rodrigues et al., 2007), which could have hindered the Benguela upwelling in its southern portion (Kirst et al., 1999).

Regarding the subtropical SW Atlantic, a number of studies have reported temporal variations in OM input to the continental margin (Costa et al., 2016; Gu et al., 2018, 2017; Lourenço et al., 2016) and have observed contrasting mechanisms governing the marine paleoproductivity and the terrestrial input. Portilho-Ramos et al.

(2015) and Pereira et al. (2018) related the highest abundance of planktonic foraminifera, and, hence, paleoproductivity in the SW Atlantic, to the upwelling of the South Atlantic Central Water (SACW). During cold stages, the thermal gradient between the Northern and the Southern Hemisphere caused a strengthening of the NE trade winds (Chang et al., 2000). This, in turn, resulted in a northward migration of the South Equatorial Current (SEC) bifurcation on the Brazilian coast, which strengthened the Brazil Current (BC) (Rodrigues et al., 2007). A stronger BC enhanced the formation of eddies, intensifying the cold and nutrient-rich SACW upwelling (Portilho-Ramos et al., 2015). Moreover, the strong NE trade winds also caused a southward migration of the ITCZ (Hessler et al., 2010; Rodrigues et al., 2007), promoting humid conditions in SE Brazil (Costa et al., 2016; Ledru et al., 1998b). The intensified fluvial discharge coupled to a low relative sea level (RSL) increased the nutrient input to the outer continental shelf. This terrestrial nutrient supply could also be responsible for the increased marine productivity as found by previous authors for the South Brazil Bight (SBB) upper slope (Lourenço et al., 2016; Mahiques et al., 2007; Nagai et al., 2010), the southern SBB mid-slope (Gu et al., 2017) and the mid-slope of the Campos basin (Costa et al., 2016) . On the other hand, warm periods with relatively high RSL resulted in an onshore displacement of the BC, lower terrestrial OM input and, consequently, lower marine productivity rates. Notwithstanding, even the source of the terrestrial sediments has changed over the Holocene. In the southern portion of the SBB shelf, Mathias et al. (2014) observed that during the Mid-Holocene its main sediment source was the Pampean loess. This material reached the Argentinean and Uruguayan continental shelves by eolian transport and was then carried northward by the Patagonian Coastal Current and by the Brazilian Coastal Current (BCC). Later on, due to the increase in precipitation over SE South America (Cruz-Jr. et al., 2005), the RdlP drainage basin became the main source of sediments to the southern portion of the SBB during the late Holocene (Mathias et al., 2014).

Based on these previous findings, there are some gaps in knowledge regarding both the marine and terrestrial OM evolution in the central portion of the SBB. During the Last Glacial Period, Portilho-Ramos et al. (2015) and Pereira et al. (2018) associated the marine productivity in the SW Atlantic with the SACW upwelling promoted by the BC eddies. However, Gu et al. (2017) related it to stronger terrestrial inputs from the RdlP in the southern portion of the SBB. In this scenario, it is still unclear what was the main mechanism controlling the marine productivity in the SBB central portion, since

this region is currently out of the influence of the RdlP. Regarding the terrestrial input to the SBB central portion, previous studies in the region (Lourenço et al., 2016; Mahiques et al., 2007; Nagai et al., 2010) and in the Campos basin (Portilho-Ramos et al., 2015) did not addressed its source. Nowadays, the RdlP influences only the southern portion of the SBB (Mahiques et al., 1999; Nagai et al., 2014; Razik et al., 2015), while the northern portion receives sediments carried by the southward BC (Nagai et al., 2014). A recent study (Mahiques et al., 2017) of the continental shelf and slope in the SBB central portion suggested that the terrestrial input to the mid-slope is influenced by the northward Intermediate Western Boundary Current (IWBC) rather than by the southward BC. Hence, the main source of the terrestrial OM to the central region is unclear during the Last Glacial Period.

In this study, we applied several organic biomarkers (*n*-alkanes, long-chain alkenones, glycerol dialkyl-glycerol tetraethers – GDGTs, *n*-alkanols, sterols and long-chain diols) to track the sources of organic material in the SBB mid-slope. Molecular organic biomarkers can serve as proxies to provide insights into how aquatic systems process, metabolize and sequester carbon in both the water column and sediments over decadal to geological time scales. Therefore, they are extremely useful in resolving the complexity of systems with multiple organic carbon sources (Andersson and Meyers, 2012; Holland et al., 2013; Laureillard et al., 1997; Yunker et al., 2005). Based on their temporal evolution, we associated the OM flux with the evolution of oceanographic and climatological processes during the late Pleistocene and Holocene. We compared the evolution of these organic biomarkers with other paleoreconstructions from the vicinities to identify the possible source of terrestrial OM and the mechanism that mainly governed the marine productivity during the Last Glacial Period. Assuming the terrestrial and marine OM in the SBB slope are strongly interlinked and are subject to similar driving factors, we expect to observe low concentrations of organic proxies during warmer stages and higher concentrations of both terrestrial and marine proxies during cold stages.

2. Study Area

Nowadays, the region of the SBB (latitudes 22 – 34° S) is governed mainly by mesoscale processes at the continental margin, that carry significant amounts of heat, salt and nutrients, thus controlling biological production and physical dynamics (Campos et al., 2001; Mahiques et al., 2010). The circulation is characterized by the

western boundary currents, the Brazil Current (BC) and the Intermediate Western Boundary Current (IWBC) (Fig. 3.1). The BC flows southward and meanders around the 200 m isobath (Campos et al., 2000; Peterson and Stramma, 1991). It transports the warm and oligotrophic Tropical Water (TW; T > 20 °C and S > 36.4) in the first 100 m of the water column, and the cold and nutrient-rich South Atlantic Central Water (SACW; T = 6-20 °C and S = 34.5-36.4) below 100 m and down to around 600 m depth (Silveira et al., 2015, 2000). Below the BC, the IWBC flows northward in the SBB, carrying the Antarctic Intermediate Water (AAIW; T = 3-7 °C and S = 24.6-34.4) down to around 1,100 m depth (Schmid et al., 2000; Silveira et al., 2015).

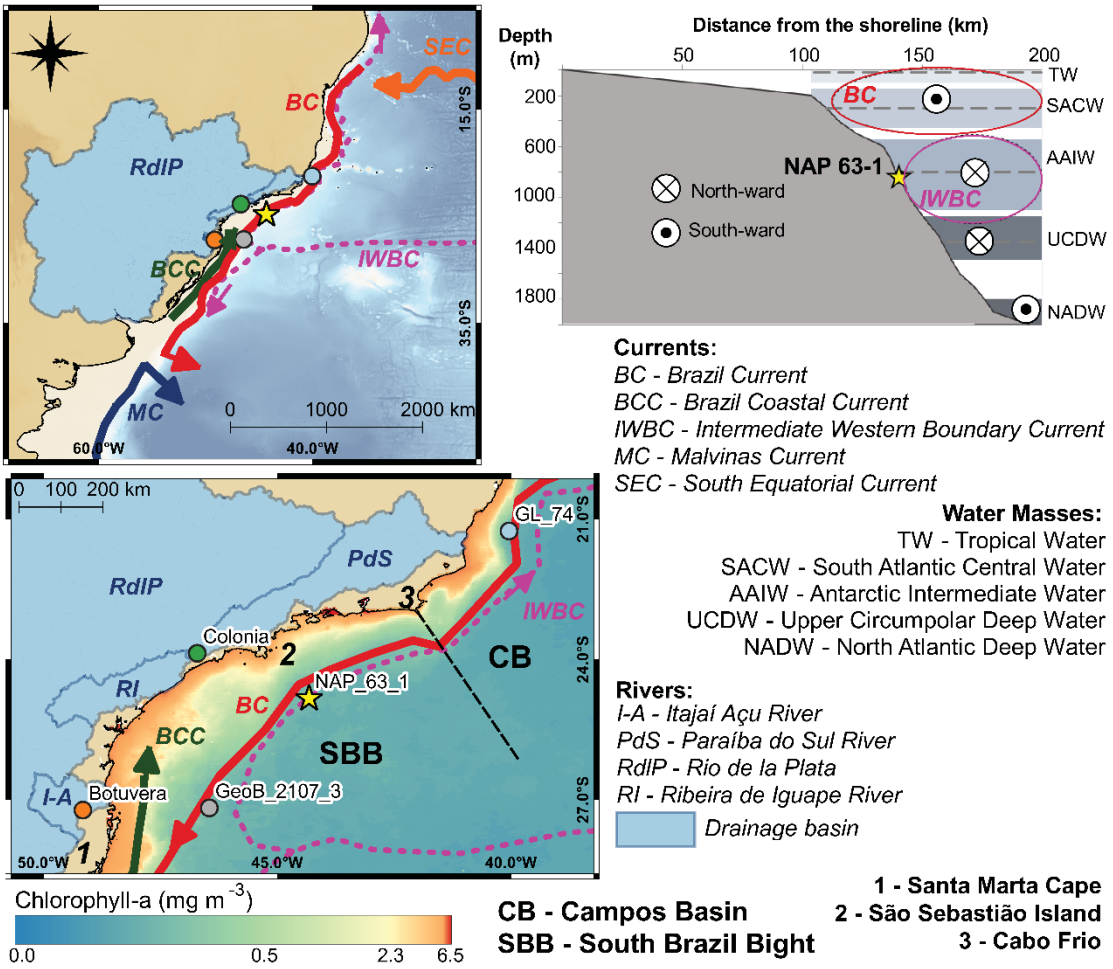

Fig. 3.1. Map of the study area with the location of sediment core NAP 63-1 (yellow star) as well as the main currents and water masses in the region (based on Campos et al., 2001, 1995; Piola et al., 2008; Schmid, 2014; Schmid et al., 2000; Silveira et al., 2015, 2000). The core sites indicated by colored dots are used in the discussion of the terrestrial and marine OM evaluation.

Eddy activity in the SBB along the flow path of the BC is relatively strong. The change in the coastline orientation at Cabo Frio induces a meandering pattern, which frequently becomes unstable forming strong cyclonic and anticyclonic frontal eddies

(Campos et al., 2000, 1995). These eddies represent an efficient mechanism for the generation of vertical speeds, acting decisively in the upwelling of the SACW. This type of meander-induced upwelling brings SACW to shallower depths and fertilizes the otherwise typically oligotrophic waters (Campos et al., 2000; Ribeiro et al., 2016).

The SBB can also be considered as a convergence zone with regards to sediment transport, receiving material from the south through the advancement of the RdlP plume, and from the North through the upwelling region of the SACW (Mahiques et al., 2004). The area off São Sebastião island (24° S; 45°30' W) marks a regional boundary between the two sedimentary provinces. The RdlP drains the second largest drainage basin in South America and brings to the SW Atlantic around 9.2 x 10^7 ton $year^{-1}$ of silt and clay (Razik et al., 2015). This material is redistributed northward up to 27° S by the BCC (Nagai et al., 2014; Piola et al., 2008). Besides the RdlP, the SSB region receives only small contributions of terrestrial material from the adjacent coast, especially from SE Brazil. The most important contributors are the Paraíba do Sul river, which delivers around 4.2 x 10^6 ton $year^{-1}$ of sediments and up to 3,000 m^3 s^{-1} of water (Bernardes et al., 2012); the Ribeira de Iguape river, which deliver around 280 m^3 s^{-1} of water (Santana, 2008); and the Itajaí-Açu river, which delivers around 230 m^3 s^{-1} of water (Schettini, 2002). A recent study of the SBB shelf (Mantovanelli et al., 2018) observed a signature of Paraíba do Sul River sediments near Cabo Frio. However, the sediments on the continental shelf off the Ribeira de Iguape river mouth showed the signature of the RdlP drainage basin. Therefore, they concluded that the influence of the RdlP drainage basin is higher than the influence of the local river discharges in the southern portion of the SBB. Also, Mahiques et al. (2017) observed that there is a differentiation between the terrigenous input in the SBB upper and mid-slope. The upper slope presented sediments enriched in Ca and Sr, while the mid-slope presented sediments enriched in Fe, Mg and V. Since the upper slope is bathed by the southward BC and the mid-slope is bathed by the northward IWBC, the authors attributed the different geochemical signatures to the different overlying currents.

The adjacent continent is characterized by a narrow (> 80 km) coastal lowland (< 100 m altitude), limited by the "Serra do Mar" coastal mountain ranges, which extends approximately parallel to the coast (Almeida and Carneiro, 1998; Bigarella, 2001). The Atlantic rainforest is the typical vegetation of the lowland and the slopes of the "Serra do Mar" mountain range. It has one of the highest biodiversity in Brazil, but its current expansion is strongly reduced to 36 % and 7 % of its original extent,

254 considering the “Serra do Mar” and interior regions, respectively (Ribeiro et al., 2009).
255 In the SE and S of Brazil, the Atlantic rainforest is formed by dense ombrophilous
256 forests along the coast, by mixed ombrophilous forests (Araucaria biogeographical sub-
257 region) in the S Brazil interior, and by deciduous and semi-deciduous seasonal forests in
258 the SE Brazil interior (Interior Forest biogeographical sub-region) (Garcia and Pirani,
259 2005; Silva and Casteleti, 2003). The mean annual rainfall in the SE and S of Brazil,
260 where the Atlantic rainforest is currently most extensive, varies between 1,200 and
261 2,500 mm (Sant’Anna Netto, 2005; Wrege et al., 2012). The seasonal rainfall
262 distribution depends on the latitude and on the altitude, varying from a humid climate in
263 the coastal areas (with rainfall distributed evenly throughout the year) to a warm and
264 humid climate with only a short dry period in the central region (more than a 100 km
265 away from the coast; Keller Filho et al., 2005; Sant’Anna Netto, 2005). The rainfall
266 distribution during the austral summer is mainly controlled by the presence of the South
267 Atlantic Convergence Zone (SACZ) in the northern portion of the SBB (Carvalho et al.,
268 2004) and by the development of large mesoscale convective systems in the southern
269 portion of the SBB (Cavalcanti, 2012). During the austral winter, the passage of
270 transient frontal systems attenuates the short dry season in both regions (Cavalcanti,
271 2012; Nieto-Ferreira and Rickenbach, 2011).
272
273 **3. Material and Methods**
274 *3.1. Sampling and Age Model*
275 Sediment core NAP 63-1 was retrieved from the continental slope of the
276 southwestern Atlantic, in a subtropical region (24°50.304’ S; 44°19.124’ W; 840 m
277 depth; 2.24 m long). The distance of the coring site to the coast is nowadays of about
278 140 km. The sampling took place on February 26th, 2013, during a R.V. Alpha Crucis
279 cruise, from the Oceanographic Institute of the University of São Paulo (IO-USP,
280 Brazil), using a piston corer (Fig. 3.1). The core was sectioned every 2 cm, totaling 112
281 samples. The samples were stored frozen in pre-combusted aluminum trays for further
282 analysis.
283 The age model was described by Dauner et al. (2019). Briefly, it was based on
284 radiometric dating of planktonic foraminifera (AMS ^{14}C) and benthic foraminifera
285 stable oxygen isotopes ($\delta^{18}O$) tie points aligned to two reference curves (Lisiecki and
286 Raymo, 2005; Lisiecki and Stern, 2016). The downcore ages were modeled using
287 BACON software version 2.3.5 (Blaauw and Christen, 2011). The ^{14}C ages were

calibrated with the Marine13 Calibration Dataset (Reimer et al., 2013), with a reservoir age correction (ΔR) of 28 ± 52 years (Alves et al., 2015), and are reported in thousand years before present (kyr BP). The $\delta^{18}O$ tie points were obtained using the software Analyseries 2.0 (Paillard et al., 1996) and the error estimations of the $\delta^{18}O$ tie points were calculated based on Govin et al. (2015). The core material covered approximately the past 78 kyr with no observed age inversion in the radiocarbon ages.

3.2. Bulk Parameters

The analyses of total organic carbon (TOC) content and carbon isotope composition ($\delta^{13}C$) were performed on decarbonated dry sediment samples (acid treatment with 1 mol L^{-1} HCl solution), while the determinations of total nitrogen (TN) content and the nitrogen isotope composition ($\delta^{15}N$) were performed on dry sediment. The samples were analyzed by an EA-Costech elemental analyzer coupled to a Thermo Scientific Delta V Advantage Isotope ratio MS (EA-IRMS) isotope ratio mass spectrometry detector. The analytical accuracy was verified using the USGS-40 (L-glutamic acid, United States Geological Survey) and IAEA-600 (caffeine, International Atomic Energy Agency) standards before and after each group of 40 samples. The standard deviation for calibration standards and isotopic ratios was within the expected range, being 0.01 ‰ for both ratios for the USGS-40 standard, and 0.03 ‰ for $\delta^{13}C$ and 0.09 ‰ for $\delta^{15}N$ for the standard IAEA-600. The standard used as reference for carbon and nitrogen contents was Soil LECO (LECO Corporation, USA), whose estimated levels are 13.55% and 0.81% dry weight, respectively.

3.3. Lipid extraction and purification

The samples were analyzed following the method adapted from Chen et al. (2014). About 5 g of freeze-dried and homogenized samples were extracted three times using an ultrasonic bath with 25 mL of methanol:dichloromethane (MeOH:DCM) (1:9; v:v). Known amounts of squalene, C_{19} ketone, 5α-androstanol, and C_{46} GDGT were added as internal standards before extraction. The combined extracts were evaporated by rotary evaporation under vacuum at 40 °C. The total lipid extracts (TLE) were saponified for 2 h at 80 °C with 1 mL of 0.1 mol L^{-1} KOH in MeOH/H_2O (9:1; v:v). After saponification, neutral lipids were liquid-liquid extracted into *n*-hexane and further purified by passing them over a silica gel column (1% deactivated with water). They were eluted with 4 mL of *n*-hexane (recovery of *n*-alkanes), 4 mL of *n*-

hexane:DCM (1:2; v:v; recovery of ketones) and 4 mL of DCM:MeOH (1:1; v:v; recovery of *n*-alkanols, sterols, diols and GDGTs) and dried using a Silli-Therm at 50°C under a stream of nitrogen.

The *n*-alkane and alkenone fractions were re-dissolved in 100 µL of *n*-hexane before the capillary gas chromatography analyses. The dry polar fractions were weighed and adjusted to concentrations of approximately 2 mg mL^{-1} by dissolution with isopropanol: *n*-hexane (1:99; v:v). Prior to analysis, the polar fractions were filtered (Thermo Scientific PTFE filter - 4 mm in diameter and 0.45 µm porosity) for the retention of any remaining particles. These extracts were injected into a high-performance liquid chromatograph coupled to a mass spectrometer (HPLC-MS). The remaining extracts were then dried and derivatized by adding 30 µL of acetonitrile and 30 µL of N,O-bis (trimethylsilyltrifluoroacetamide):trimethylchlorosilane (BSTFA:TMCS; 99:1) and heated for 60 min at approximately 60 °C. After derivatization, the reagents were dried, and the fraction was re-dissolved in 50 µL of *n*-hexane before capillary gas chromatography.

3.4. Analytical Methods

n-Alkanes were analyzed by injecting 2 µL sample aliquots in split mode in an Agilent 7890A series gas chromatograph (GC) equipped with a flame ionization detector and an Agilent DB-5ms capillary fused silica column coated with 5% phenyl/dimethylarylene siloxane (60 m length, 0.25 mm ID, and 0.25 µm film thickness). Helium was used as the carrier gas with a constant flow rate of 1.5 mL min^{-1}. Initial oven temperature was 60 °C, held for 1 min, increased to 150 °C at a rate of 20 °C min^{-1}, then raised to 320 °C at a rate of 6 °C min^{-1} and held for 35 min with a total run-time of 69 min. The injector and detector temperatures were adjusted to 250 °C and 330 °C, respectively.

Alkenones were analyzed by injecting 2 µL sample aliquots in splitless mode in an Agilent 7890A series GC equipped with a flame ionization detector and an Agilent HP-5 capillary fused silica column coated with 5% phenyl/methylpolysiloxane (50 m length, 0.32 mm ID, and 0.17 µm film thickness). Hydrogen was used as the carrier gas with a constant flow rate of 1.2 mL min^{-1}. Initial oven temperature was 40 °C, increased to 60 °C at a rate of 20 °C min^{-1}, then raised to 320 °C at a rate of 5 °C min^{-1} and held for 15 min with a total run-time of 68 min. The injector and detector temperatures were adjusted to 300 °C and 325 °C, respectively.

GDGT analyses were performed using an Agilent 1200 Series high-performance liquid chromatography (HPLC) system coupled with an Agilent 6120 mass spectrometer. The 20 µL aliquots were injected into an Alltech Prevail® Cyano column (2.1 x 150 mm^2, 3 µm; Grace) maintained at 30 °C. GDGTs were eluted using the following gradient with solvent A (*n*-hexane: isopropanol: chloroform; 98:1:1) and solvent B (*n*-hexane: isopropanol: chloroform; 89:10:1): 100% A for 5 min, linear gradient to 10% B in 20 min, linear gradient to 100% B in 10 min, and then held for 7 min. The flow rate was 0.2 mL min^{-1}. After each analysis, the column was cleaned by back-flushing with 100% B at 0.6 mL min^{-1} for 5 min and then held for 10 min in the initial conditions (100% A at 0.2 mL min^{-1}).

n-Alkanols, sterols and diols were analyzed by injecting 2 µL sample aliquots in splitless mode in an Agilent 6850A series GC equipped with an Agilent 5975C VL MSD mass spectrometer, a Restek Rxi-1ms capillary fused silica column coated with 1% diphenyl/ dimethylsiloxane (30 m length, 0.25 mm ID, and 0.25 µm film thickness) and a 5 m pre-column. Helium was used as the carrier gas with a constant flow rate of 1.2 mL min^{-1}. Initial oven temperature was 100 °C, held for 8 min, and subsequently increased to 300 °C at a rate of 4 °C min^{-1} with a total run-time of 58 min. The injector temperature was adjusted to 280 °C and operated in splitless injection mode. The detector and ion source temperatures were adjusted to 280 °C and 230 °C, respectively.

n-Alkanes were individually identified by matching retention times against a standard containing the homologous series from *n*-C_{14} to *n*-C_{40}. Long-chain alkenones were individually identified by matching retention times against a standard containing C_{19} ketone, $C_{37:2}$ and $C_{37:3}$ alkenones. *n*-Alkanols, sterols and diols data were acquired using SIM (Selected Ion Monitoring) mode and they were identified by the ion fragments characteristic of each compound (Tables SM 1 – 3; Fig. SM 1 – 4). GDGT data were also acquired using SIM mode, but they were identified by the molecular ions (Tables SM 4).

The following compounds were quantified and used in the following discussion: i) *n*-alkanes: odd-numbered *n*-C_{15} to *n*-C_{39}; ii) long-chain alkenones: $C_{37:3}$, $C_{37:2}$, $C_{38:3}$, $C_{38:2}$, $C_{39:3}$, $C_{39:2}$; iii) *n*-alkanols: even-numbered *n*-C_{12}-OH to *n*-C_{34}-OH; iv) phytol; v) steroids: $27\Delta^{5,22E}$, $27\Delta^{22E}$, $27\Delta^{5}$, $27\Delta^{0}$, $28\Delta^{5,22E}$, $28\Delta^{22E}$, $28\Delta^{5}$, $28\Delta^{0}$, $29\Delta^{5,22E}$, $29\Delta^{22E}$, $29\Delta^{5}$, $29\Delta^{0}$, and $30\Delta^{22E}$; vi) long-chain diols: C_{28}1,14 and C_{30}1,14; and vii) GDGTs: crenarchaeol, branched GDGT-IIIa, branched GDGT-IIa, and branched GDGT-Ia.

Procedural blanks were analyzed for each set of 15 samples, and they showed no significant level peaks in the analyses of target compounds. Finally, four replicates of the same sediment sample were extracted and used as a laboratory internal reference. The coefficient of variation of each compound among the four replicates was lower than 25% (Denoux et al., 1998), for all the compounds.

3.5. Data Processing

Although some organic geochemical markers have a wide variety of sources, others are more-source specific (Volkman, 2006, 1986). A cluster analysis may be helpful to group compounds with a similar source. Therefore, the cluster analysis using SAX representation (Lin et al., 2007) in the dissimilarity measure calculation was used to group the different proxies according to their evolutions through the time. The description of the method used for the SAX clustering is described in Appendix SM 1. Two groups were formed: the "terrestrial-source" group and the "marine-source" group. For all samples, the concentrations of the organic biomarkers (in ng g^{-1} dry weight) were converted to mass accumulation rates (MAR) using the sedimentation rates (from Dauner et al., 2019) and the mean dry bulk density values obtained by Müller (2004) for another sediment core in the SBB (core GeoB 2107-3).

After the organic markers were separated into these two groups, we performed a constrained cluster analysis in order to define stratigraphical zones. In order to assess whether the marine and the terrestrial organic matter responds to similar forcings, such as observed by Gu et al. (2017), we performed constrained cluster analyses considering them separately. Also, for each cluster, we have selected an organic proxy that best illustrates the OM variability, based on previous knowledge about the sources (e.g. Volkman, 2006; Volkman et al., 1992) and on the highest percentages of explanation obtained from a Principal Component Analysis (Fig. SM 5). For this analysis, we used the normalized data of the accumulation rates of the following organic compounds: short-chain odd-numbered *n*-alkanes (*n*-C_{15} – *n*-C_{17}), mid-chain odd-numbered *n*-alkanes (*n*-C_{19} – *n*-C_{23}), long-chain odd-numbered *n*-alkanes (*n*-C_{25} – *n*-C_{39}), long-chain alkenones (LCA), crenarchaeol, branched GDGTs, short-chain even-numbered *n*-alkanols (*n*-C_{12}-OH – *n*-C_{18}-OH), long-chain even-numbered *n*-alkanols (*n*-C_{20}-OH – *n*-C_{34}-OH), phytol, C_{28} and C_{30} 1,14-diols, and the sterols dehydrocholesterol ($27\Delta^{5,22E}$), cholesterol ($27\Delta^{5}$), brassicasterol ($28\Delta^{5,22E}$), campesterol ($28\Delta^{5}$), stigmasterol ($29\Delta^{5,22E}$), sitosterol ($29\Delta^{5}$), and dinosterol ($30\Delta^{22E}$).

In order to define the periodicity of the OM input (marine and terrigenous), wavelet analyses were performed using Python (van Rossum, 1995) and the libraries NumPy (Oliphant, 2006), MatplotLib (Hunter, 2007) and SciPy (Jones et al., 2015). PyCWT (available at https://github.com/regeirk/pycwt) was used to perform the wavelet analysis and follows the procedure described by Torrence and Compo (1998) for the evaluation of cycles in the OM data. For the correlation and wavelet analysis, the data of the accumulation rates of the two organic compounds selected previously were converted to equally-spaced time-series. For the wavelet analysis, cycles can only be (robustly) identified where at least 4 "samples" per cycle are available, according to the Nyquist frequency. The mean temporal lag between the samples in the NAP 63-1 record is 0.7 yr (i.e., each sample represents 0.7 kyr). Therefore, only cycles larger than 2.8 kyr (4 * 0.7) can be robustly interpreted. We also removed all periodicities above 10 kyr using a moving average filter, with a window of 11 kyr in order to eliminate all unresolved frequencies and the general trend. Cross-wavelet and a wavelet coherence analyses were performed to compare the NAP 63-1 OM signal with the water temperature time series, obtained from Dauner et al. (2019). In the discussion about the source of the OM, the following records were used (Fig. 3.1): GeoB 2107-3 (% arboreal pollen – AP; Gu et al., 2017), GL-74 (% *Globigerina bulloides*; Portilho-Ramos et al., 2015), Colônia (% arboreal pollen – AP; Ledru et al., 2009) and Botuverá (Mg/Ca and Sr/Ca ratios; Cruz-Jr. et al., 2007).

The Branched and Isoprenoid Tetraether Index (BIT; formula 1) was calculated in order to determine the OM source in addition to the isotopic composition. Since isoprenoid GDGTs (isoGDGTSs; especially crenarchaeol) are found primarily in aquatic environments and branched GDGTs (brGDGTs) are mainly associated with bacteria found in soils and peat, BIT index is used to evaluate the influence of terrigenous inputs in the aquatic environment. BIT values close to 1.0 indicates terrestrial input, while values close to 0.0 are considered indicative for marine input (Hopmans et al., 2004). The P_{aq} index (formula 2) was originally proposed to reflect the aquatic macrophyte input to lake sediments relative to that from the terrestrial plants (Ficken et al., 2000). Since the *n*-alkane distributions of submerged and floating macrophytes differ from those of subaerial vascular plants, Zhou et al. (2010) used the changes in the relative proportions of these biomarker compounds to reconstruct the history of moisture availability. In order to identify the organic degradation degree (Martins et al., 2012; Nakakuni et al., 2017; Routh et al., 2014; Sawada et al., 2013), the

5α(H)-stanol/Δ^5-stenol ratios for six pairs of structurally related compounds were calculated (formulas 3a-f). Their results were presented as a mean and standard deviations. Stanol/stenol values greater than 1.0 usually indicate bacterial and hydrogenation diagenetic processes, since saturated sterols are not commonly found in large amounts in organisms (Canuel and Martens, 1993). Further, in order to compare the marine productivity from different producers, the content of dinosterol ($30\Delta^{22E}$), LCA and crenarchaeol were compared to the brassicasterol ($28\Delta^{5,22E}$) content (formulas 4a-c). For the values to be in the same order of magnitude, the concentrations (of each compound per sample) were transformed into percentages in relation to the highest concentration obtained for each class of compound.

$$(1)\ BIT = \frac{([brGDGT-Ia] + [brGDGT-IIa] + [brGDGT-IIIa])}{([brGDGT-Ia] + [brGDGT-IIa] + [brGDGT-IIIa] + [crenarqueol])}$$

$$(2)\ P_{aq} = \frac{[n-C_{23}] + [n-C_{25}]}{[n-C_{23}] + [n-C_{25}] + [n-C_{29}] + [n-C_{31}]}$$

(3) (a) $\frac{[27\Delta^{22E}]}{[27\Delta^{5,22E}]}$; (b) $\frac{[27\Delta^{0}]}{[27\Delta^{5}]}$; (c) $\frac{[28\Delta^{22E}]}{[28\Delta^{5,22E}]}$;

(d) $\frac{[28\Delta^{0}]}{[28\Delta^{5}]}$; (e) $\frac{[29\Delta^{22E}]}{[29\Delta^{5,22E}]}$; and (f) $\frac{[29\Delta^{0}]}{[29\Delta^{5}]}$.

(4) (a) $\frac{\%\ 30\Delta^{22E}}{(\%\ 28\Delta^{5,22E} + \%\ 30\Delta^{22E})}$; (b) $\frac{\%\ LCA}{(\%\ 28\Delta^{5,22E} + \%\ LCA)}$; and (c) $\frac{\%\ crenarchaeol}{(\%\ 28\Delta^{5,22E} + \%\ crenarchaeol)}$.

4. Results and Discussion

The profiles of the proxies' mass accumulation rates are presented in Fig. 3.2. The use of organic geochemical proxies to distinguish the OM sources is common in paleoenvironmental studies (Holland et al., 2013; Meyers, 2003, 1997). However, although some compounds occur only in certain group of species, others are widely distributed, which hampers their interpretation. For example, sitosterol ($29\Delta^5$) is usually attributed to terrestrial plants, but in most marine sediments a contribution from microalgae may also be important (Volkman, 2006). Therefore, the cluster analysis using SAX representation (Lin et al., 2007) was used to group the different compounds into a "terrestrial-source" group and a "marine-source" group according to their temporal evolution. Based on these two groups, a constrained cluster analysis was performed to identify if they were controlled by the same overlying processes, and to evaluate the evolution of the mass accumulation rates through the time. Finally, temporal records of other proxies were compared to NAP 63-1 profiles to identify the possible sources of the organic matter.

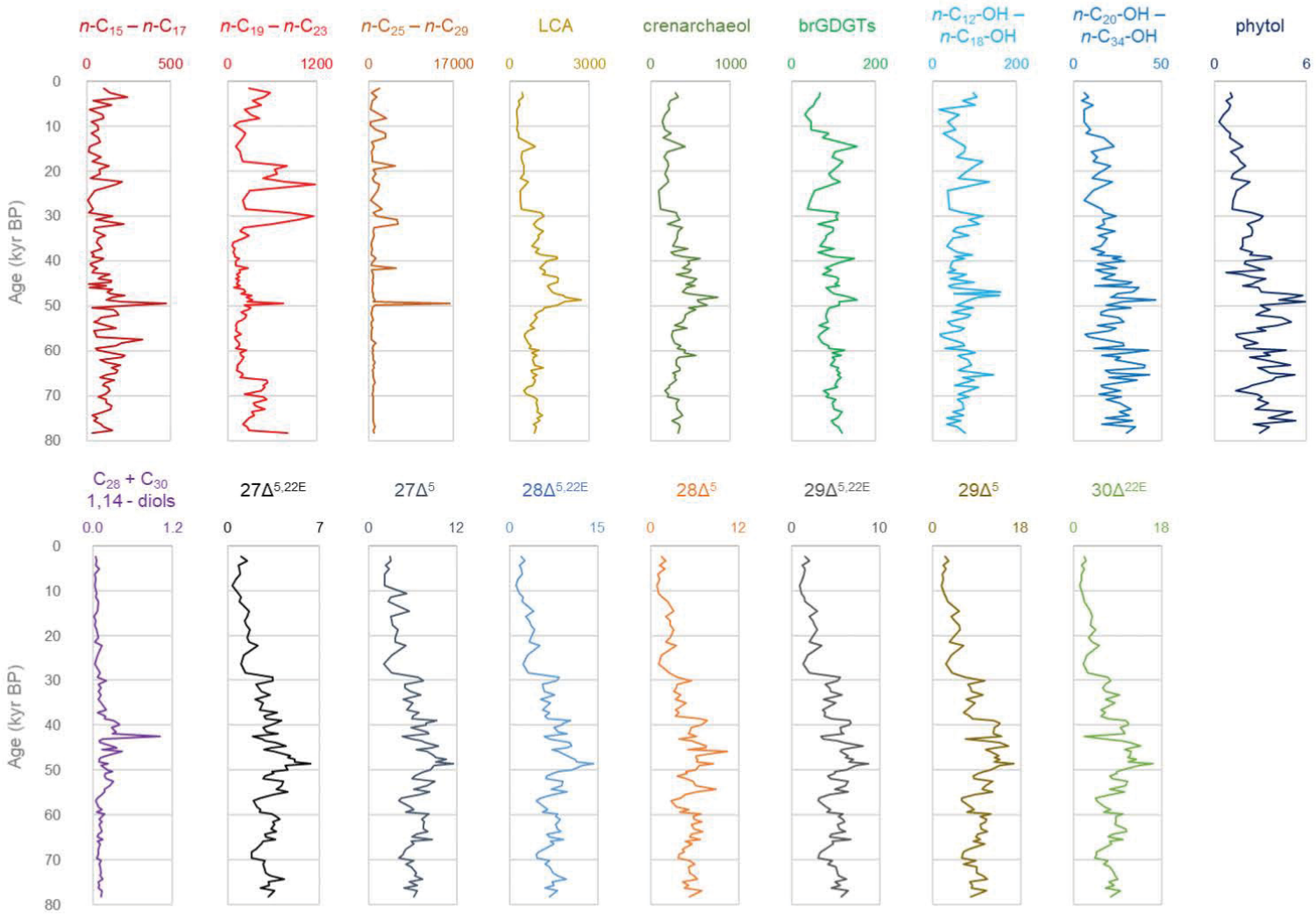

Fig. 3.2. Mass accumulation rates (in ng cm^{-2} yr^{-1}) profiles of the organic molecular markers analysed in NAP 63-1 sediment core.

488 *4.1. Grouping the proxies according to their temporal evolutions*

489 The cluster analysis using SAX representation (Fig. 3.3) presented a "terrestrial-
490 source" group composed by all odd-chain *n*-alkanes (short-chain *n*-C_{15} – *n*-C_{17}, mid-
491 chain *n*-C_{19} – *n*-C_{23}, and long-chain *n*-C_{25} – *n*-C_{29}), the short-chain even-numbered *n*-
492 alkanols (*n*-C_{12}-OH – *n*-C_{18}-OH), and the branched GDGTs. However, caution should
493 be taken regarding the short-chain *n*-alkanes since they usually are associated with
494 aquatic and/or microbial organisms (Venkatesan and Kaplan, 1987; Volkman, 2006).
495 They are more susceptible to biodegradation when compared to long-chain *n*-alkanes
496 (Colombo et al., 1989; Volkman et al., 1992), which is evidenced by the discrepancy in
497 their concentration ranges (short-chain *n*-alkanes = 454 – 20,129 ng g TOC^{-1}; long-
498 chain *n*-alkanes = 30,355 – 628,577 ng g TOC^{-1}). Because of this probable degradation
499 of the short-chain *n*-alkanes, they may have been grouped with other "terrestrial-source"
500 compounds, despite their known marine/microbial origin. On the other hand, short-
501 chain *n*-alkanols were predominant in the *n*-alkanols, especially the *n*-C_{16}-OH which
502 alone accounted for around 50% of the total *n*-alkanols. Usually, aquatic algae and
503 bacteria have *n*-alkanol distributions dominated by C_{16} to C_{22} components (Meyers,
504 2003). Hu et al. (2009) observed that a high correlation of short-chain *n*-alkanols with
505 bacterial fatty acids indicated a bacterial source, instead of aquatic algae for the former
506 compounds. In our samples, a high correlation between the short-chain *n*-alkanols and
507 the branched GDGTs (R = 0.58) suggests a microbial origin for the short-chain *n*-
508 alkanols.
509

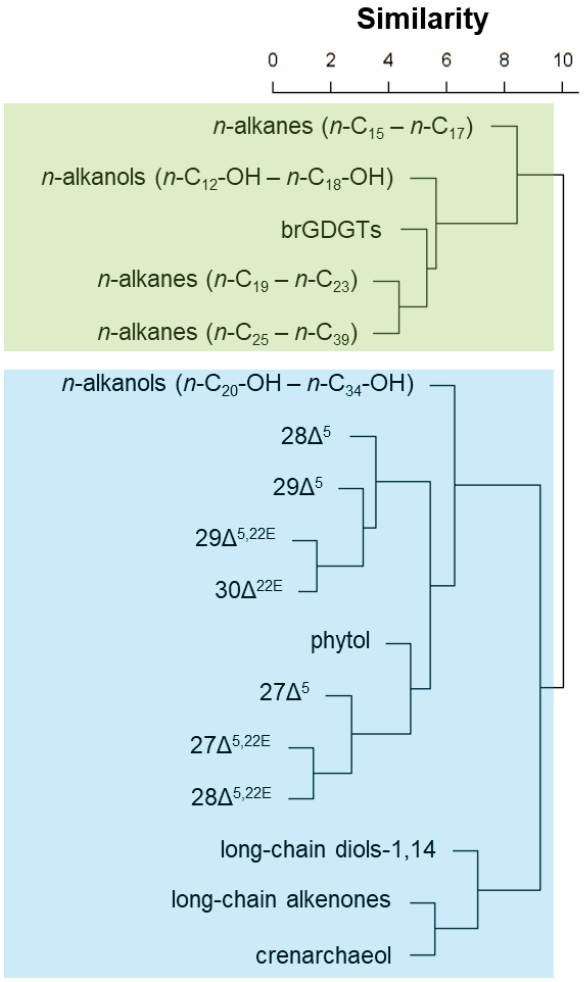

Fig. 3.3. Cluster analysis based on the temporal evolution of each organic compound group, using the SAX representation as the dissimilarity measure. The green rectangle indicates the "terrestrial-source" group and the blue rectangle indicates the "marine-source" group.

The "marine-source" group was composed of long-chain even-numbered *n*-alkanols (*n*-C_{20}-OH – *n*-C_{34}-OH), phytol, crenarchaeol, long-chain alkenones (LCA), C_{28} and C_{30} 1,14-diols, and the sterols cholesterol ($27\Delta^{5}$), dehydrocholesterol ($27\Delta^{5,22E}$), brassicasterol ($28\Delta^{5,22E}$), campesterol ($28\Delta^{5}$), stigmasterol ($29\Delta^{5,22E}$), sitosterol ($29\Delta^{5}$), and dinosterol ($30\Delta^{22E}$). As observed before, sterols containing 29 carbon atoms, such as stigmasterol and sitosterol, are usually associated with higher plants but can also be produced by marine algae (Derrien et al., 2017; Patterson, 1971; Volkman, 1986). In our samples, the high correlation between stigmasterol, sitosterol and brassicasterol (stigmasterol and brassicasterol: R = 0.92; sitosterol and brassicasterol: R = 0.82) corroborates their marine source. The long-chain even-numbered *n*-alkanols are also usually attributed to an input from higher plant waxes, but some aquatic sources of them has also been suggested (Volkman, 2006). Volkman et al. (1998) observed a strong predominance of the *n*-C_{22} alkanol in cultures of the freshwater eustigmatophyte

524 *Vischeria punctata*. However, if the freshwater eustigmatophyte were the source of the
525 long-chain even-numbered *n*-alkanols, they should not be grouped with the marine OM
526 proxies. A possible marine source of the long-chain even-numbered *n*-alkanols was
527 proposed by Sinninghe Damsté et al. (2001). They found high abundances of
528 glycolipids in the sediments of Ace Lake, an Antarctic saltwater lake, which were
529 attributed to a cyanobacterial origin. These glycolipids are composed of methylated
530 sugar moieties linked to C_{22} and C_{24} *n*-alcohols with relatively labile glycosidic bonds.
531 The stable carbon isotopic composition of the C_{22} and C_{24} *n*-alkyl of these glycolipids
532 was identical to that of C_{22} and C_{24} *n*-alcohols present as free alcohols in the surface
533 sediments. Thus, they argued that the most probable marine source of these long-chain
534 *n*-alkanols is the hydrolysis of cyanobacterial glycolipids, releasing the *n*-alkanols.
535 As it is possible to see in the "terrestrial-source" and "marine-source"
536 constrained dendrograms (Fig. 3.4), the two organic matter sources present distinct
537 stratigraphical zones, which indicates distinct forcings. The terrestrial organic proxies
538 were grouped in four zones: from 78 to 66 kyr BP (TZ-I; TZ = terrestrial zone), from 66
539 to 42 kyr BP (TZ-II), from 42 to 32 kyr BP (TZ-III) and from 32 kyr BP to the present
540 (TZ-IV). Regarding the marine organic proxies, only three zones were formed: from 78
541 to 50 kyr BP (MZ-I; MZ = marine zone), from 50 to 29 kyr BP (MZ-II) and from 29 kyr
542 BP to present (MZ-III). They also presented distinct periodicities. While the input of
543 mid-chain and long-chain odd-numbered *n*-alkanes ("terrestrial-source" representatives)
544 did not present any significant periodicity through the whole analyzed period, the input
545 brassicasterol ($28\Delta^{5,22E}$; "marine-source" representative) showed a significant energy at
546 a periodicity of around 8 kyr over the analyzed period.
547

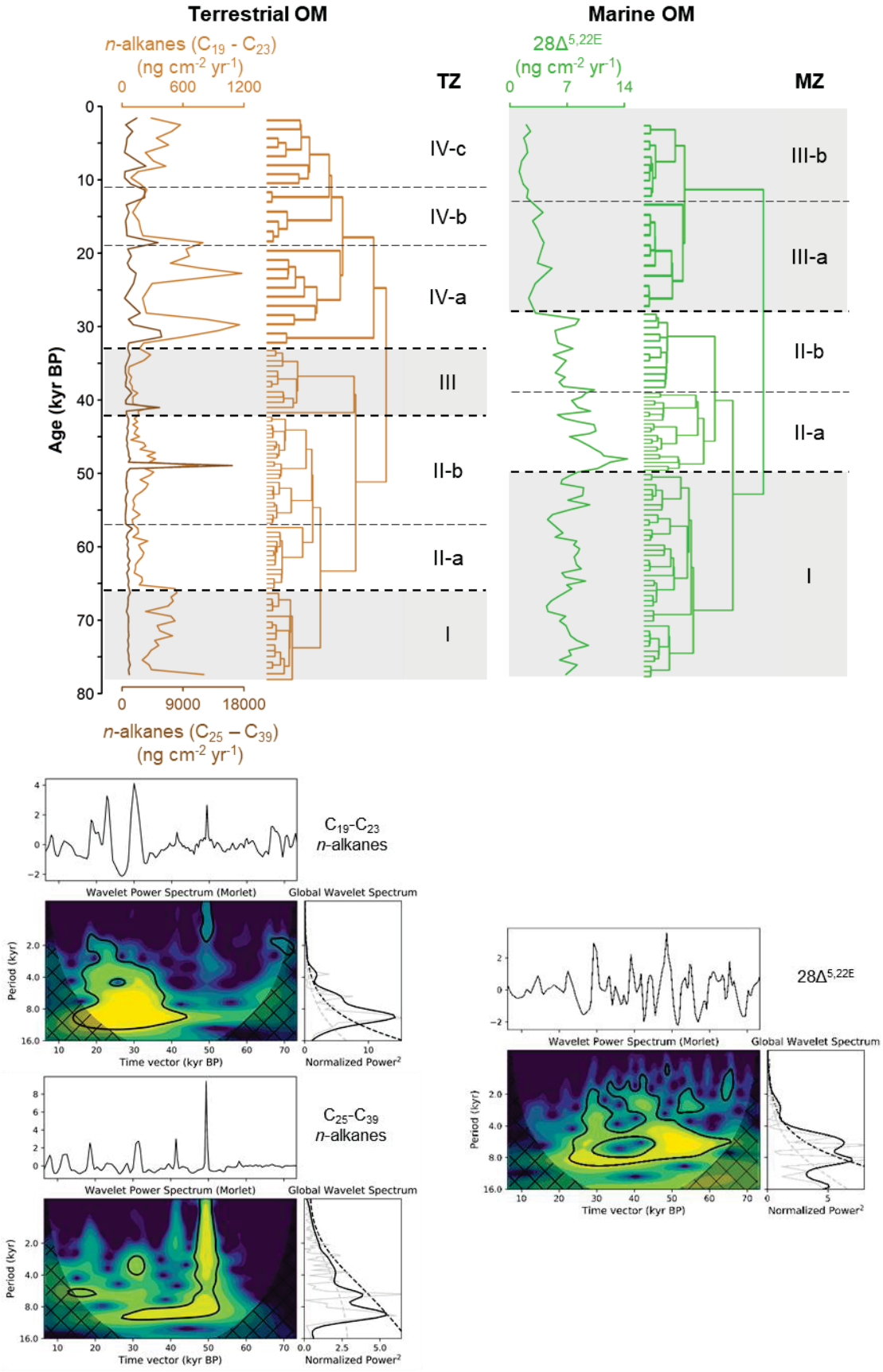

Fig. 3.4. Terrestrial (left) and marine (right) organic matter (OM) dendrograms (top) and wavelets (bottom) for core NAP 63-1. The terrestrial OM evolution is represented by the C_{19}-C_{23} and C_{25}-C_{39} *n*-alkanes, and marine OM evolution is represented by brassicasterol ($28\Delta^{5,22E}$) accumulation rates (ng cm^{-2} yr^{-1}).

548

549 *4.2. Predominance of sources*

550 The elemental and isotopic compositions of the organic matter have been
551 extensively used to identify the OM source, since they can indicate the predominance of
552 one organic source over the other (Bechtel et al., 2007; Mahiques et al., 2007; Meyers,
553 1994; Nagai et al., 2010; Xu et al., 2017). The % TOC varied between 0.17 and 0.81 %
554 (mean = 0.48 ± 0.09 %), the % TN ranged from 0.04 to 0.10 % (mean = 0.08 ± 0.01 %)
555 (Fig. 3.5) and the TOC/TN ratio varied between 3.67 and 10.98 (mean = 6.34 ± 1.15).
556 The relatively low TOC content (close to 0.3 %; Meyers, 1997) coupled to a low
557 Pearson correlation between % TOC and % TN (R = 0.48) indicates a limited
558 applicability of the TOC/TN ratio as a proxy for OM source (Bianchi and Canuel, 2011;
559 Meyers, 1997; Quirós-Collazos et al., 2017).

560

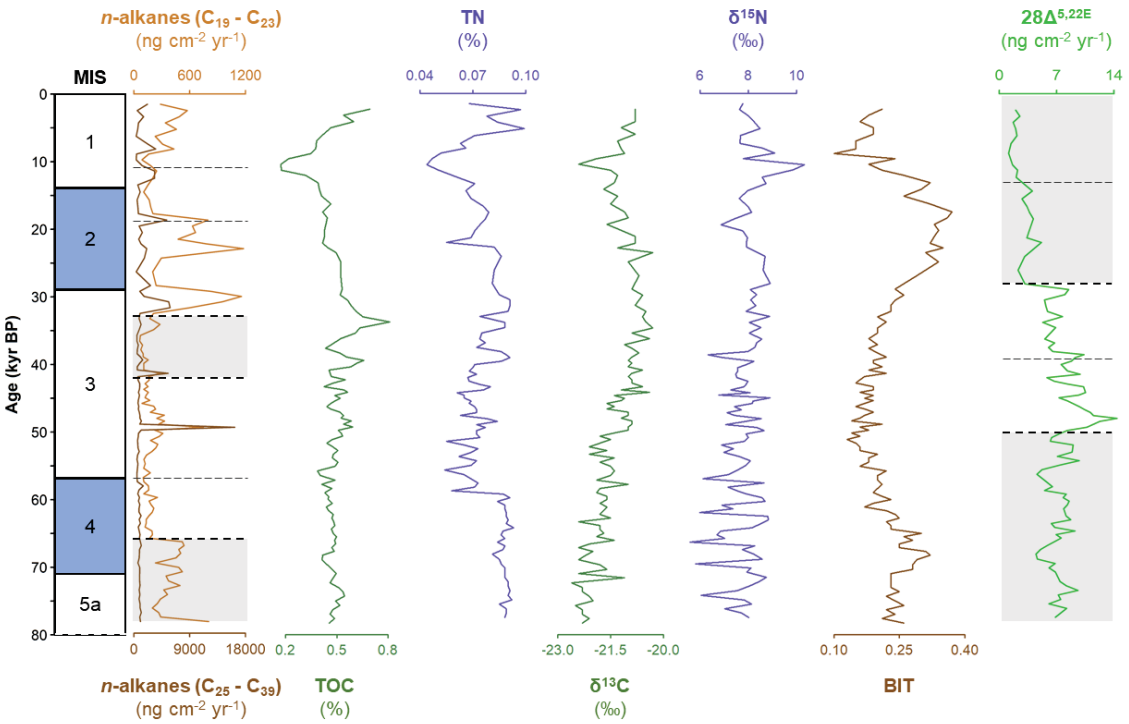

Fig. 3.5. Records of the terrestrial and marine OM proxies (mass accumulation rates of C_{19}-C_{23} and C_{25}-C_{39} *n*-alkanes and $28\Delta^{5,22E}$, respectively), elemental and isotopic composition, and BIT values for core NAP 63-1.

561

562 Regarding the isotopic composition, the $\delta^{13}C$ varied between -22.6 and -20.3 ‰
563 (mean = -21.4 ‰ ± 0.6) and the $\delta^{15}N$ ranged from 5.57 to 10.33 ‰ (mean = 7.87 ‰ ±
564 0.76). Values of $\delta^{13}C$ also indicate the predominance of marine OM ($\delta^{13}C$ = -22 to -20
565 ‰; Meyers, 1994; Quirós-Collazos et al., 2017) and were in the same range as observed
566 in the SBB surface sediments ($\delta^{13}C$ = -21.0 to -20.5 ‰; Mahiques et al., 2004). $\delta^{15}N$

values varied slightly through the core, but remained around 7.5 ‰, reinforcing the marine and/or microbial nature of the OM (Meyers, 1997; Middelburg and Herman, 2007) (Fig. SM 6 and Fig. 3.5). The overall low BIT values (mean = 0.22 ± 0.06) corroborates the mainly marine OM source (BIT < 0.3; Hopmans et al., 2004; Weijers et al., 2006).

Although the $\delta^{13}C$ values were always indicative of the predominance of primary marine production, the long-term increasing trend from 80 kyr BP to 40 kyr BP coincides with a decreasing trend of the terrestrial OM input. A reduced input of soil ($\delta^{13}C$ = -27 to -23 ‰; Bianchi and Canuel, 2011) and vascular plants ($\delta^{13}C$ = -30 to -26 ‰; Bianchi and Canuel, 2011) may have caused the increase of the $\delta^{13}C$ values. Similarly, as for the $\delta^{13}C$ evolution, the BIT values were indicative of marine OM (BIT < 0.3) but were mainly affected by the terrestrial OM input. The increase in the terrestrial OM input during MIS 2, due to the narrowing of the continental shelf, even caused the BIT values to exceed the limit of 0.3 (Hopmans et al., 2004; Weijers et al., 2006).

During the Holocene (from 11 kyr BP to the present), the TOC content increased despite the low accumulation rate of brassicasterol. The increasing trend of BIT values and C_{19}-C_{23} *n*-alkanes accumulation rate suggests that this TOC increment is related to terrestrial OM sources rather than with marine OM sources. This could be caused by a higher terrestrial OM input, in response to higher precipitation in Southeast America and the expansion of the Atlantic rainforest (Ledru et al., 2009, 1998b). However, it should have caused a decrease in the $\delta^{13}C$ values. The increase in the abundance of C_4 (such as Asteraceae) and CAM (such as Ericaceae, Isoetes and ferns) plants in the southern and southeastern Brazil (Gu et al., 2018; Ledru et al., 2009) may have caused these relatively high $\delta^{13}C$ values.

4.3. Terrestrial OM

The terrestrial OM input in the continental margin depends on the amount of OM produced in the continent and exported to the ocean, and on sea level fluctuations, which affect the continental shelf width. A possible source of terrestrial organic matter to the SBB is the Rio de la Plata. It has the second largest drainage basin in the South America and discharges around 710 km^3 yr^{-1} of freshwater at the Rio de La Plata estuary at ~35° S (Razik et al., 2015). In the southern part of the SBB (around 27º S), Gu et al. (2017) observed that the input of the Rio de La Plata was probably responsible

for the pollen distribution over the last 70 kyr. The proportions of the different ecological groups of pollen from the GeoB 2107-3 sediment core were used to define the pollen zones (Fig. 3.6), as presented by them (Gu et al., 2017). The pollen zones related to the Rio de la Plata input also do not coincide with the TZs from the NAP 63-1 record. When the proportion of the arboreal pollen is considered, relatively high proportions were observed until 40 kyr BP, which coincides with moments of low terrestrial input at our study site. The stratigraphical units observed off South Brazil do not coincide directly with the TZs from the SSB slope, suggesting that the Rio de la Plata is the not the primary source of the terrestrial organic matter that reaches the SBB. However, Mahiques et al. (2017), studying the SBB continental shelf and slope, verified that the main sediment source is remote and delivered by the IWBC to this region. The material delivered by the Rio de La Plata reaches the continental shelf and the continental slope. After its deposition in the slope off Southern Brazil, this material may be reworked by the IWBC and, after some time, transported northward to our sampling location.

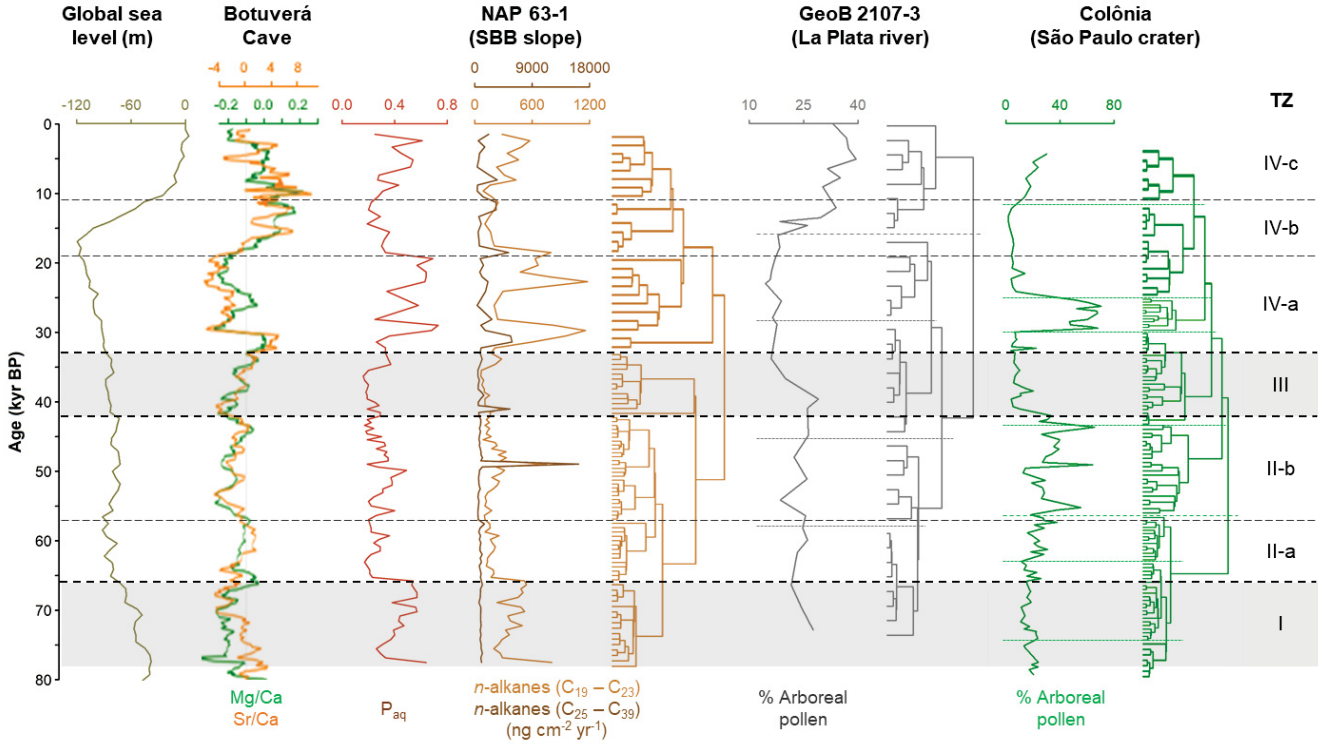

Fig. 3.6. Dendrograms and terrestrial proxies for cores NAP 63-1, GeoB 2107-3 and Colônia cores, with the global sea level evolution, the anomalies (in 10^3) of Mg/Ca and Sr/Ca in the Botuverá Cave and the *n*-alkane P_{aq} index calculated for the NAP 63-1 sediment core.

Another possible source of terrestrial OM to our site are the rivers that drain near our coring site (Pivel, 2009). Among them, the largest one is the Paraíba do Sul river, that discharge around 28 km^3 yr^{-1} of freshwater at ~ 21º S (Bernardes et al., 2012). As mentioned before, the coastal region of the SBB is formed by lowlands and the high relief Atlantic Serra do Mar mountain range, which is covered mainly by the Atlantic rainforest and the semideciduous forest (Garcia and Pirani, 2005; Silva and Casteleti, 2003). The Colônia crater (SE Brazil) is in the Serra do Mar mountain range, only a few kilometers from the shoreline. The pollen composition from the Colônia crater (Ledru et al., 2009) presents zones (Fig. 3.6) similar with the TZs from the SBB slope, especially from TZ-IIb. The similar stratigraphical zones found in the both records suggest that they have been caused by the same underlying process, i.e., likely the local humidity. Periods of more terrestrial OM production should coincide with periods of more terrestrial OM export to the adjacent ocean. But the arboreal pollen profile itself does not explain the entire terrestrial record from NAP 63-1 core. The changes in the relative sea level may help to explain these oscillations.

From 78 to 66 kyr BP (TZ-I), the sea-level dropped (Miller et al., 2011) and, consequently, the continental shelf shortened. Also during TZ-I, the rainfall increased in the Southern Brazil (decreasing Sr/Ca ratios in Botuverá Cave; Cruz-Jr. et al., 2007), although it did not represent an increase in the arboreal vegetation. The increasing P_{aq} index corroborates the increase in the humidity in the study area (Zhou et al., 2010). During this time interval, the rainforest was degraded and replaced mainly by shrubs (Ledru et al., 2009). The short continental shelf coupled to a wet climate in the region of the SBB may explain the relatively high terrestrial OM input in SBB slope. From 66 to 42 kyr BP (TZ-II), low terrestrial OM accumulation rates were observed, with a slight increase during the middle of TZ-IIb. This zone (TZ-II) corresponds to a widening of the continental shelf and a dryer climate in the SE South America (higher Sr/Ca and Mg/Ca ratios in Botuverá Cave; Cruz-Jr. et al., 2007). Therefore, although the Atlantic rainforest expanded, the soil moisture decreased (Ledru et al., 2009) and the wide continental shelf coupled to low precipitation rates hampered the terrestrial input to the slope. During TZ-III (from 42 to 32 kyr BP), the low terrestrial accumulation rates in the slope are probably caused by the dry climate. This climate created conditions that supported a low delivery of terrestrial material to the coast and caused a decrease in the extent and biodiversity of the Atlantic rainforest (Ledru et al., 2009). During the TZ-IV, the terrestrial input in the SBB slope was controlled by both the climate over the SE

South America and the sea-level variations. When the sea-level dropped and, consequently, the continental shelf shortened (from 32 to 19 kyr BP, TZ-IVa), the terrestrial input to site NAP 63-1 increased, as indicated by the highest *n*-alkanes accumulation rates. At the end of the TZ-IVa, the continental shelf reached its minimum width, and the river mouths were closer to the continental shelf break. The expansion of the Atlantic rainforest, as indicated by the high proportion of arboreal pollen in SE Brazil, and the presence of a wet climate (high P_{aq} values) with no dry season (Cruz-Jr. et al., 2007; Ledru et al., 2009, 1998a) promoted a high input of terrestrial OM to the SBB slope. During the last deglaciation (TZ-IVb; from 18 to 11 kyr BP), the sharp sea level rise caused the widening of the continental shelf, what reduced the terrestrial input to the slope. The dry climate (low P_{aq} values) observed in the SE South America (Cruz-Jr. et al., 2007) contributed to the low terrestrial OM export. Lastly, the Holocene (TZ-IVc; from 11 kyr BP) was marked by a slight increase in the terrestrial OM accumulation rates, despite the stabilization of the sea level and the continental shelf width. It may be associated with the expansion of the Atlantic rainforest caused by the increasing humidity (Cruz-Jr. et al., 2007; Ledru et al., 2009, 1998b). The increasing humidity was corroborated by the increasing P_{aq} values (Zhou et al., 2010). Thus, the terrestrial input to the SBB slope was controlled by the changes in the local continental shelf width and in the Atlantic rainforest expansion/contraction, which in turn were primarily controlled by the sea level fluctuations and by the continental moisture evolution (as observed by Ledru et al., 2009), respectively.

4.4. Marine OM

As observed before, the accumulation of marine OM presented a different temporal evolution from that observed for terrestrial OM, suggesting distinct forcings. The highest brassicasterol accumulation rates were observed during the MZ-II, which coincides with MIS 3. Nevertheless, a slight increase was observed during the glacial stages (MIS 4 and MIS 2; Fig. 3.7). Almeida et al. (2015) also observed that, although the flux of OM was greater during the cold stages than in the warm stages in SBB, the benthic foraminiferal accumulation rate was greater in MIS 3 during the Last Glacial Period. They attributed the high benthic foraminiferal production to an increased surface productivity fostered by nutrient supply. They proposed three mechanisms to explain the enhanced nutrient flux into the surface ocean in the region: increased delivery of

685 nutrients by extension of the influence of the Rio de la Plata plume, supply of aeolian
686 dust to the SBB, and upwelling driven by BC cyclonic meanders.
687

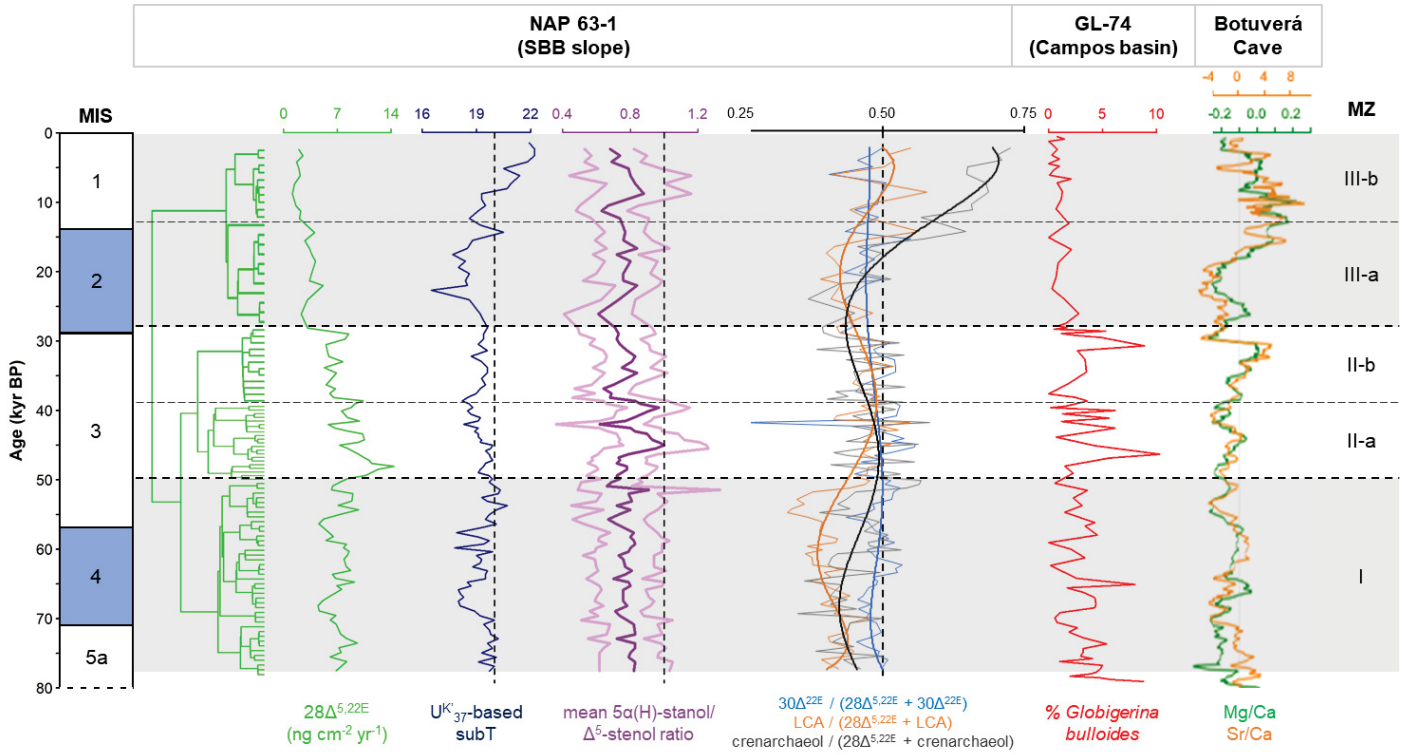

Fig. 3.7. Temporal evolution regarding the marine organic matter in the sediment core NAP 63-1: dendrogram; brassicasterol ($28\Delta^{5,22E}$) accumulation rates; $U^{K'}_{37}$-based sea subsurface temperature (subT); mean and standard deviations of the 5α(H)-stanol/Δ^5-stenol ratio; and the contents of dinosterol ($30\Delta^{22E}$), long-chain alkenones (LCA) and crenarchaeol normalised by the brassicasterol ($28\Delta^{5,22E}$) content. The % *Globigerina bulloides*, a planktonic foraminiferal species typically associated with upwelling waters, from the sediment core GL-74 and the anomalies (in 10^3) of Mg/Ca and Sr/Ca in the Botuverá Cave are also shown.
688

689 During periods of wet climate in the SE South America (especially MIS 4 and
690 MIS 2; Cruz-Jr. et al., 2007), the increased precipitation in the Rio de la Plata drainage
691 basin probably have increased the influence of the Rio de la Plata plume in the SBB. Gu
692 et al. (2017) observed that the marine productivity in the southern portion of the SBB
693 was highly influenced by the Rio de la Plata discharge of nutrient rich waters. The
694 strong relationship between continental and marine environmental changes was clearly
695 showed by the similar dendrograms of pollen/spore and dinocyst assemblages. Thus, if
696 the Rio de la Plata plume was the main fertilization mechanism of the surface waters in
697 the central portion of the SBB, the observed zones of the NAP 63-1 terrestrial and
698 marine OM should have similar a pacing to the pollen zones and dinocyst zones
699 observed by Gu et al. (2017). Since they do not present the same pacing, the plume of
700 the Rio de la Plata probably did not reach as far north as our coring site during the Last
701 Glacial Period. However, nutrients from the SE South America watershed could have

reached the SBB through the rivers that flow directly in the SSB and in the Campos basin. The small increases in the marine productivity observed in the beginning and at the end of the MZ-I, and in the MZ-III coincide with a wet climate in the SE South Atlantic. The increased precipitation in the continent could have enriched in nutrients the surface waters of the SBB.

During glacial intervals, dust supply could have increased, as the westerlies shifted northward, from the present 50° S to around 41° S (Moreno et al., 1999; Toggweiler et al., 2006). However, this northward advance does not explain a possible nutrient increase at 24° S. Chapori et al. (2014) observed that, during glacial times, the main source of the terrestrial material in the Argentine continental shelf and slope (around 38° S) was the atmospheric dust, produced in Patagonia and Argentinean Pampas. Once the dust reached the Argentine shelf break, it could have been transported to northern latitudes by the northward Malvinas Current (MC). However, when the MC encounters the BC (Brazil-Malvinas Confluence; BMC) near 38° S, both currents are deflected westward to form the South Atlantic Current (SAC) (Piola and Matano, 2001). Voigt et al. (2015) observed a latitudinal deviation of the BMC position during the Holocene. The maximum shift they observed was 1° northward of its present position. Therefore, it is unlikely that over the last 80 kyr, the BMC has migrated almost 14° northward, so that the dust and nutrient enriched MC could have reached the SBB.

The last possible explanation for the increased marine productivity during glacial stages proposed by Almeida et al. (2015) was the SACW upwelling driven by BC cyclonic meanders. A fertilization associated with increased SACW upwelling during MIS 3 was observed at the slope of Campos basin (GL-74 sediment core, 1279 m water column) (Portilho-Ramos et al., 2015) and at the slope of the SBB southern portion (GeoB 2107-3 sediment core, 1048 m water column) (Pereira et al., 2018). To assess whether SACW upwelling was indeed the forcing for the marine productivity variations during MIS 3, we computed the cross-wavelet and wavelet coherence between the shallow subsurface temperature based on the $U^{K'}_{37}$ ratio (Dauner et al., 2019) and the brassicasterol accumulation rates. This anaysis reveals a common high energy on the scale of 4 to 10 kyr through the whole analyzed period, with both signals in antiphase, i.e., the subsurface cooling coincides with increase brassicasterol accumulation rates (Fig. 3.8). This same antiphase relationship was observed between the subsurface temperature and the other marine productivity proxies, such as dinosterol, long-chain alkenones and crenarchaeol (not shown). This result supports the

736 hypothesis that SACW upwelling caused by the BC meandering along the shelf-break
737 may have fertilized the SBB, especially in the MZ-II.

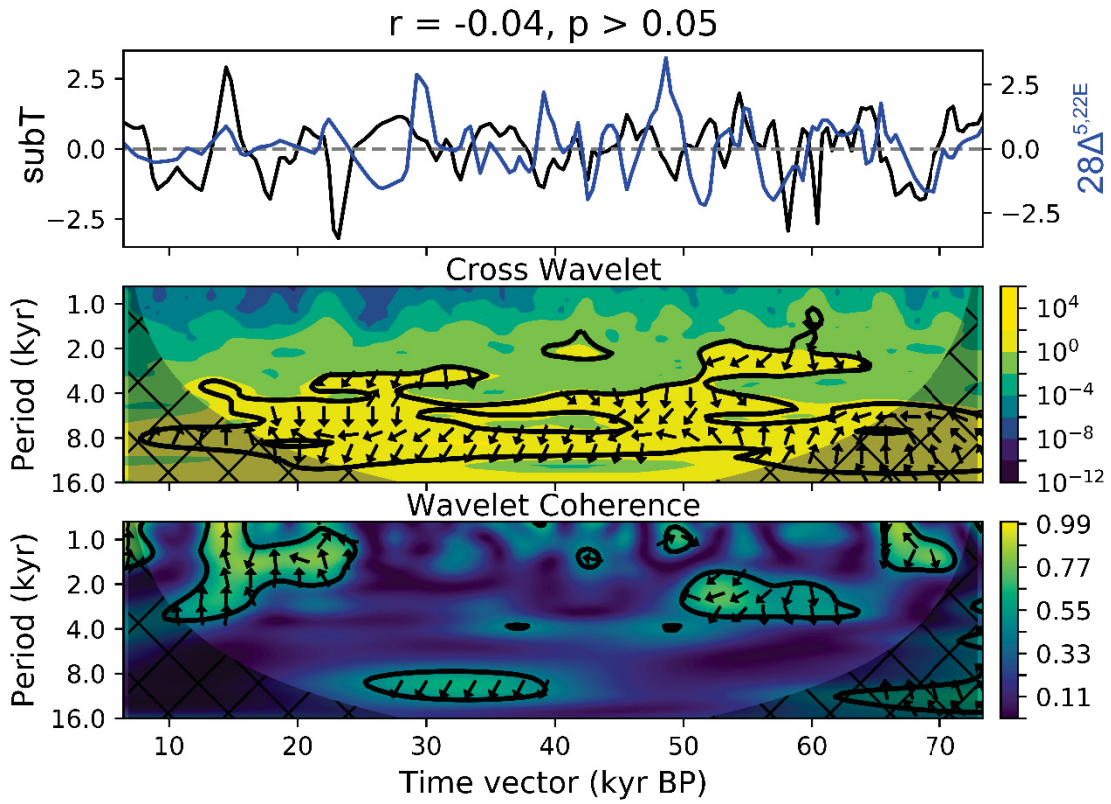

Fig. 3.8. Cross-wavelet and wavelet coherence between the subsurface temperature ($U^{K'}_{37}$-based subT) (Dauner et al., 2019), and brassicasterol ($28\Delta^{5,22E}$) accumulation rates (ng cm^{-2} yr^{-1}).
At the top, the normalized time series. The phase arrows in the cross-wavelet power spectrum rotate clockwise with 'north' origin. The vectors indicate the phase relationship, where in phase signals point upwards (N), anti-phase signals point downwards (S). If X (subT) leads Y (brassicasterol), arrows point to the right (E) and if X lags Y, arrow points to the left (W). Marked regions on the wavelet spectrum indicate significant power to a 95% confidence interval, and areas under the gray cone of influence show where edge effects are important and the analysis unreliable.

738

739 Finally, the decrease in marine productivity observed in the MZ-III (28 kyr BP
740 to present) coincides with the onset of the last deglaciation and with the greatest
741 increase in SST (Dauner et al., 2019). It suggests a stronger presence of the oligotrophic
742 TW in the region.

743 The variations in the marine OM productivity were also reflected in the variation
744 of the 5α(H)-stanol/Δ^5-stenol ratios (Fig. 3.7). Almost all values were lower than 1.0
745 (Table SM 5), indicating bottom oxic conditions (Jeng and Han, 1994), but higher than
746 0.5, indicating alteration of the sedimentary OM due to diagenetic processes (Wakeham
747 and Canuel, 2006). Nakakuni et al. (2017) observed that these ratios, especially
748 $28\Delta^{22E}/28\Delta^{5,22E}$, could be used as anoxic tracers in the southern California coast during
749 the Holocene. However, in our study area, it is unlikely that the sterol reductions have

been caused by suboxic or dysoxic bottom water conditions. The NAP 63-1 coring site is bathed by the core of the IWBC (Pereira et al., 2014; Silveira et al., 2004), which carries the low-salinity and oxygen-rich AAIW (Wienders et al., 2000). As the sea-level variations were not so drastic as to change the water mass overlying the NAP 63-1 coring site, this region probably was not subjected to dysoxic conditions. In our study, the degradation degree was probably related to changes in the marine productivity. During periods of higher productivity (such as around 48 kyr BP), the organic markers were better preserved. But during the Holocene, the high 5α(H)-stanol/Δ^5-stenol ratios suggest a stronger diagenetic reduction of the sterols.

The MZ also were characterized by distinct main primary producers (Fig. 3.7). Although differential degradation among different compounds during diagenesis makes it difficult to match the abundance of living compounds with the biomarker data, their standardized abundance may reflect the contribution changes of each specific group of organisms (Li et al., 2015). During MZ-I, there was a predominance of diatoms and dinoflagellates, indicated by the concentrations above the long-term mean of brassicasterol and dinosterol, respectively (Mudge et al., 1999; Volkman, 1986). A similarity between brassicasterol and dinosterol contents was also observed by Li et al. (2015), indicating that diatoms and dinoflagellates present a similar response to the hydrological variability. During the MZ-II, an increase in the LCA contents, proxies for coccolithophores (Epstein et al., 2001; Volkman et al., 1980), was observed. Finally, during MZ-IIIa, a decrease occurred in the contents of the three microalgae proxies. This decrease of the microalgae proxies coincided with an increase in the crenarchaeol accumulation rates, a proxy for Thaumarchaeota (Sinninghe Damsté et al., 2002).

The diatoms are common in eutrophic waters, like coastal regions (Fawcett and Ward, 2011; Libes, 2009), while the coccolithophores are usually associated with oligotrophic environments, such as the subtropical gyres (Furukawa et al., 2018; Perrin et al., 2016). The change in the phytoplankton group dominance suggests a shift from a more eutrophic environment during MZ-I to a less nutrient rich environment during MZ-IIa. During the MZ-I, the surface waters enriched in terrestrial-derived nutrients favored the diatom and dinoflagellate productivity. The hydrodynamic condition changed entering the MZ-II, and the transient SACW upwelling driven by BC cyclonic meanders (Almeida et al., 2015) was probably responsible for the comparative success of the coccolithophores. During this period, the BC cyclonic meanders may have occurred more frequently, or the SACW may have reached shallower depths than today.

After the last deglaciation, the decrease in the phytoplankton proxies and the increase of the Thaumarchaeota proxies suggests a further decrease in nutrient availability towards the present oligotrophic conditions of the BC (Lourenço et al., 2016; Portilho-Ramos et al., 2015). Thaumarchaeota are a group of chemolithotrophic ammonia oxidizing archaea, which compete poorly with phytoplankton for nutrients but endure in particularly oligotrophic conditions (Francis et al., 2005; Könneke et al., 2005; Santoro et al., 2019). They can also use organic compounds, such as urea and cyanate, as both an energy and nitrogen source (Kitzinger et al., 2019). These abilities allowed the Thaumarchaeota to thrive in the Holocene, becoming an important link in the microbial loop and trophic web of the present BC in the SBB (Moser et al., 2016; Zubkov et al., 2000).

5. Summary and Conclusions

In this study, we presented the paleoreconstruction of marine and terrestrial organic matter in the central portion of the South Brazil Bight. According to their temporal evolution, the organic geochemical proxies were classified into “terrestrial-source” and “marine-source” groups. The two organic matter sources presented distinct stratigraphical zones, indicating mechanisms governing the marine OM production and the terrestrial OM production and export.

The stratigraphical zones of the terrestrial OM were used to assess its source during the Last Glacial Period and has been connected to the drainage basins near the study site. The terrestrial material may have had two sources. It may have been exported by the Rio de la Plata and, after reaching the continental slope, reworked and transported northward by the Intermediate Western Boundary Current. However, it could also have been exported by the Paraíba do Sul river and then transported southward by the Brazil Current. In general, the terrestrial input to the central South Brazil Bight slope was probably controlled by changes in the local continental shelf width and in the Atlantic rainforest expansion/contraction, which in turn were primarily controlled by sea level fluctuations and the continental moisture evolution, respectively.

Marine organisms were the main source of OM for the slope in the last 80 kyr. The South Atlantic Central Water upwelling promoted by the Brazil Current cyclonic eddies was found to be the main mechanism controlling the marine productivity during MIS 3, while the nutrient input from the adjacent coast seems to have controlled the marine productivity during MIS 4 and MIS 2. After the last deglaciation, a stronger

presence of the oligotrophic Tropical Water in the region was suggested by a decrease of the phytoplanktonic productivity and an increase of the archaeal productivity. Due to the ability of using organic compounds and ammonia as energy and nitrogen source, the Thaumarchaeota became an important link in the microbial loop and trophic web of the present Brazil Current in the South Brazil Bight.

Acknowledgements

A.L.L. Dauner would like to thank CAPES (Coordenação de Aperfeiçoamento de Pessoal de Ensino Superior) for the Ph.D. Scholarship and to Dr. Jens Hefter for all assistance and teachings in the laboratory analysis M.C. Bícego and M.M. Mahiques would like to thank FAPESP (São Paulo Science Foundation) for the financial support (FAPESP: 2010/06147-5 and 2015/21834-2). C.C. Martins would like to thank CNPq (Brazilian National Council for Scientific and Technological Development) for a research grant (305763/2011-3).

References

Almeida, F.F.M., Carneiro, C. dal R., 1998. Origem e evolução da Serra do Mar. Rev. Bras. Geociências 28, 135–150. https://doi.org/10.5327/rbg.v28i2.617

Almeida, F.K., de Mello, R.M., Costa, K.B., Toledo, F.A.L., 2015. The response of deep-water benthic foraminiferal assemblages to changes in paleoproductivity during the Pleistocene (last 769.2 kyr), western South Atlantic Ocean. Palaeogeogr. Palaeoclimatol. Palaeoecol. 440, 201–212. https://doi.org/10.1016/j.palaeo.2015.09.005

Alves, E.Q., Macario, K.D., Souza, R., Pimenta, A., Douka, K., Oliveira, F., Chanca, I., Angulo, R.J., 2015. Quaternary Geochronology Radiocarbon reservoir corrections on the Brazilian coast from pre-bomb marine shells. Quat. Geochronol. 29, 30–35. https://doi.org/10.1016/j.quageo.2015.05.006

Andersson, R.A., Meyers, P.A., 2012. Effect of climate change on delivery and degradation of lipid biomarkers in a Holocene peat sequence in the Eastern European Russian Arctic. Org. Geochem. 53, 63–72. https://doi.org/10.1016/j.orggeochem.2012.05.002

Bechtel, A., Woszczyk, M., Reischenbacher, D., Sachsenhofer, R.F., Gratzer, R., Püttmann, W., Spychalski, W., 2007. Biomarkers and geochemical indicators of Holocene environmental changes in coastal Lake Sarbsko (Poland). Org. Geochem. 38, 1112–1131. https://doi.org/10.1016/j.orggeochem.2007.02.009

852 Belicka, L.L., Macdonald, R.W., Yunker, M.B., Harvey, H.R., 2004. The role of
853 depositional regime on carbon transport and preservation in Arctic Ocean sediments.
854 Mar. Chem. 86, 65–88. https://doi.org/10.1016/j.marchem.2003.12.006
855 Benthien, A., Andersen, N., Schulte, S., Müller, P.J., Schneider, R.R., Wefer, G.,
856 2005. The carbon isotopic record of the $C_{37:2}$ alkenone in the South Atlantic: Last
857 Glacial Maximum (LGM) vs. Holocene. Palaeogeogr. Palaeoclimatol. Palaeoecol. 221,
858 123–140. https://doi.org/10.1016/j.palaeo.2005.02.008
859 Bernardes, M.C., Knoppers, B.A., Rezende, C.E., Souza, W.F.L., Ovalle,
860 A.R.C., 2012. Land-sea interface features of four estuaries on the South America
861 Atlantic coast. Brazilian J. Biol. 72, 761–774.
862 Bianchi, T.S., Canuel, E.A., 2011. Chemical Biomarkers in Aquatic Ecosystems.
863 Princeton University Press, Woodstock, Oxfordshire.
864 Bigarella, J.J., 2001. Contribuição ao Estudo da Planície Litorânea do Estado do
865 Paraná. Brazilian Arch. Biol. Technol. Jubilee Vo, 65–110.
866 https://doi.org/10.1590/S1516-89132001000500005
867 Blaauw, M., Christen, J.A., 2011. Flexible paleoclimate age-depth models using
868 an autoregressive gamma process. Bayesian Anal. 6, 457–474.
869 https://doi.org/10.1214/11-BA618
870 Braga, E.S., Chiozzini, V.C., Berbel, G.B.B., Maluf, J.C.C., Aguiar, V.M.C.,
871 Charo, M., Molina, D., Romero, S.I., Eichler, B.B., 2008. Nutrient distributions over the
872 Southwestern South Atlantic continental shelf from Mar del Plata (Argentina) to Itajaí
873 (Brazil): Winter–summer aspects. Cont. Shelf Res. 28, 1649–1661.
874 https://doi.org/10.1016/j.csr.2007.06.018
875 Campos, E.J.D., Busalacchi, A., Garzoli, S.L., Lutjeharms, J.R.E., Matano, R.P.,
876 Nobre, P., Olson, D., Piola, A.R., Tanajura, C., Wainer, I.E.K.C., 2001. The South
877 Atlantic and the climate. Obs. Ocean. 21st Century A Strateg. Glob. Ocean Obs. 20.
878 Campos, E.J.D., Miller, J.L., Moiler, T.J., Peterson, R.G., 1995. Physical
879 Oceanography of the southwest Atlantic Ocean. Oceanography 8, 87–91.
880 Campos, E.J.D., Velhote, D., Silveira, I.C.A., 2000. Shelf break upwelling
881 driven by Brazil current cyclonic meanders. Geophys. Res. Lett. 27, 751–754.
882 https://doi.org/10.1029/1999GL010502
883 Canuel, E.A., Martens, C.S., 1993. Seasonal variations in the sources and
884 alteration of organic matter associated with recently-deposited sediments. Org.
885 Geochem. 20, 563–577. https://doi.org/10.1016/0146-6380(93)90024-6

886 Carvalho, L.M. V., Jones, C., Liebmann, B., 2004. The South Atlantic
887 convergence zone: Intensity, form, persistence, and relationships with intraseasonal to
888 interannual activity and extreme rainfall. J. Clim. 17, 88–108.
889 https://doi.org/10.1175/1520-0442(2004)017<0088:TSACZI>2.0.CO;2
890 Cavalcanti, I.F.A., 2012. Large scale and synoptic features associated with
891 extreme precipitation over South America: A review and case studies for the first
892 decade of the 21st century. Atmos. Res. 118, 27–40.
893 https://doi.org/10.1016/j.atmosres.2012.06.012
894 Chang, P., Saravanan, R., Ji, L., Hegerl, G.C., 2000. The effect of local sea
895 surface temperatures on atmospheric circulation over the tropical Atlantic sector. J.
896 Clim. 13, 2195–2216. https://doi.org/10.1175/1520-
897 0442(2000)013<2195:TEOLSS>2.0.CO;2
898 Chapori, N.G., Laprida, C., Watanabe, S., Totah, V., Violante, R.A., 2014. Mid-
899 Late Pleistocene benthic foraminifera from Southwestern South Atlantic: driven by
900 primary productivity or water mass properties? Micropaleontology 60, 195–210.
901 Chen, W., Mohtadi, M., Schefuß, E., Mollenhauer, G., 2014. Organic-
902 geochemical proxies of sea surface temperature in surface sediments of the tropical
903 eastern Indian Ocean. Deep. Res. Part I Oceanogr. Res. Pap. 88, 17–29.
904 https://doi.org/10.1016/j.dsr.2014.03.005
905 Colombo, J.C., Pelletier, E., Brochu, C., Khalll, M., 1989. Determination of
906 hydrocarbon sources using *n*-alkane and polyaromatic hydrocarbon distribution indexes.
907 Case study: Rio de La Plata estuary, Argentina. Environ. Sci. Technol. 23, 888–894.
908 Costa, K.B., Cabarcos, E., Santarosa, A.C.A., Battaglin, B.B.F., Toledo, F.A.L.,
909 2016. A multiproxy approach to the climate and marine productivity variations along
910 MIS 5 in SE Brazil: A comparison between major components of calcareous
911 nannofossil assemblages and geochemical records. Palaeogeogr. Palaeoclimatol.
912 Palaeoecol. 449, 275–288. https://doi.org/10.1016/j.palaeo.2016.02.032
913 Cruz-Jr., F.W., Burns, S.J., Jercinovic, M., Karmann, I., Sharp, W.D., Vuille,
914 M., 2007. Evidence of rainfall variations in Southern Brazil from trace element ratios
915 (Mg/Ca and Sr/Ca) in a Late Pleistocene stalagmite. Geochim. Cosmochim. Acta 71,
916 2250–2263. https://doi.org/10.1016/j.gca.2007.02.005
917 Cruz-Jr., F.W., Burns, S.J., Karmann, I., Sharp, W.D., Vuille, M., Cardoso,
918 A.O., Ferrari, J.A., Dias, P.L.S., Viana-Jr., O., 2005. Insolation-driven changes in

919 atmospheric circulation over the past 116,000 years in subtropical Brazil. Lett. to Nat.
920 434, 63–66. https://doi.org/10.1029/2003JB002684
921 Dauner, A.L.L., Mollenhauer, G., Bícego, M.C., Souza, M.M., Nagai, R.H.,
922 Figueira, R.C.L., Mahiques, M.M., Sousa, S.H.M., Martins, C.C., 2019. Multi-proxy
923 reconstruction of sea surface and subsurface temperatures in the western South Atlantic
924 over the last ~ 75 kyr. Quat. Sci. Rev. 215, 1–9.
925 https://doi.org/10.1016/j.quascirev.2019.04.020
926 Denoux, G.J., Gardinali, P.R., Wade, T.L., 1998. Quantitative determination of
927 polynuclear aromatic hydrocarbons by gas chromatography/mass spectrometry
928 (GC/MS)-selected ion monitoring (SIM) mode, in: Lauenstein, G.G., Cantillo, A.Y.
929 (Eds.), Sampling and Analytical Methods of the National Status and Trends Program
930 Mussel Watch Project: 1993-1996 Update. Silver Spring, USA, pp. 144–147.
931 https://doi.org/10.1016/S0740-624X(98)90030-2
932 Derrien, M., Yang, L., Hur, J., 2017. Lipid biomarkers and spectroscopic indices
933 for identifying organic matter sources in aquatic environments: A review. Water Res.
934 112, 58–71. https://doi.org/10.1016/j.watres.2017.01.023
935 Epstein, B.L., D'Hondt, S., Hargraves, P.E., 2001. The possible metabolic role
936 of C_{37} alkenones in *Emiliania huxleyi*. Org. Geochem. 32, 867–875.
937 https://doi.org/10.1016/S0146-6380(01)00026-2
938 Faux, J.F., Belicka, L.L., Rodger Harvey, H., 2011. Organic sources and carbon
939 sequestration in Holocene shelf sediments from the western Arctic Ocean. Cont. Shelf
940 Res. 31, 1169–1179. https://doi.org/10.1016/j.csr.2011.04.001
941 Fawcett, S.E., Ward, B.B., 2011. Phytoplankton succession and nitrogen
942 utilization during the development of an upwelling bloom. Mar. Ecol. Prog. Ser. 428,
943 13–31. https://doi.org/10.3354/meps09070
944 Ficken, K.J., Li, B., Swain, D.L., Eglinton, G., 2000. An *n*-alkane proxy for the
945 sedimentary input of submerged/floating freshwater aquatic macrophytes. Org.
946 Geochem. 31, 745–749.
947 Francis, C.A., Roberts, K.J., Beman, J.M., Santoro, A.E., Oakley, B.B., 2005.
948 Ubiquity and diversity of ammonia-oxidizing archaea in water columns and sediments
949 of the ocean. Proc. Natl. Acad. Sci. 102, 14683–14688.
950 https://doi.org/10.1073/pnas.0506625102

951 Freeman, K.H., Pancost, R.D., 2013. Biomarkers for Terrestrial Plants and
952 Climate, in: Turekian, K., Holland, H. (Eds.), Treatise on Geochemistry: Second
953 Edition. Elsevier, pp. 395–416. https://doi.org/10.1016/B978-0-08-095975-7.01028-7
954 Furukawa, M., Sato, T., Suzuki, Y., Casareto, B.E., Hirabayashi, S., 2018.
955 Numerical modelling of physiological and ecological impacts of ocean acidification on
956 coccolithophores. J. Mar. Syst. 182, 12–30.
957 https://doi.org/10.1016/j.jmarsys.2018.02.008
958 Garcia, R.J.F., Pirani, J.R., 2005. Análise florística, ecológica e fitogeográfica do
959 Núcleo Curucutu, Parque Estadual da Serra do Mar (São Paulo, SP), com ênfase nos
960 campos junto à crista da Serra do Mar. Hoehnea 32, 1–48.
961 Garzoli, S.L., Matano, R.P., 2011. The South Atlantic and the Atlantic
962 Meridional Overturning Circulation. Deep. Res. Part II Top. Stud. Oceanogr. 58, 1837–
963 1847. https://doi.org/10.1016/j.dsr2.2010.10.063
964 Govin, A., Capron, E., Tzedakis, P.C., Verheyden, S., Ghaleb, B., Hillaire-
965 Marcel, C., St-Onge, G., Stoner, J.S., Bassinot, F., Bazin, L., Blunier, T., Combourieu-
966 Nebout, N., El Ouahabi, A., Genty, D., Gersonde, R., Jimenez-Amat, P., Landais, A.,
967 Martrat, B., Masson-Delmotte, V., Parrenin, F., Seidenkrantz, M.-S., Veres, D.,
968 Waelbroeck, C., Zahn, R., 2015. Sequence of events from the onset to the demise of the
969 Last Interglacial: Evaluating strengths and limitations of chronologies used in climatic
970 archives. Quat. Sci. Rev. 129, 1–36. https://doi.org/10.1016/j.quascirev.2015.09.018
971 Gu, F., Chiessi, C.M., Zonneveld, K.A.F., Behling, H., 2018. Late Quaternary
972 environmental dynamics inferred from marine sediment core GeoB6211-2 off southern
973 Brazil. Palaeogeogr. Palaeoclimatol. Palaeoecol. 496, 48–61.
974 https://doi.org/10.1016/j.palaeo.2018.01.015
975 Gu, F., Zonneveld, K.A.F., Chiessi, C.M., Arz, H.W., Jürgen, P., Behling, H.,
976 2017. Long-term vegetation, climate and ocean dynamics inferred from a 73,500 years
977 old marine sediment core (GeoB2107-3) off southern Brazil. Quat. Sci. Rev. 172, 55–
978 71. https://doi.org/10.1016/j.quascirev.2017.06.028
979 Hessler, I., Dupont, L., Bonnefille, R., Behling, H., González, C., Helmens,
980 K.F., Hooghiemstra, H., Lebamba, J., Ledru, M.P., Lézine, A.M., Maley, J., Marret, F.,
981 Vincens, A., 2010. Millennial-scale changes in vegetation records from tropical Africa
982 and South America during the last glacial. Quat. Sci. Rev. 29, 2882–2899.
983 https://doi.org/10.1016/j.quascirev.2009.11.029

Holland, A.R., Petsch, S.T., Castañeda, I.S., Wilkie, K.M., Burns, S.J., Brigham-Grette, J., 2013. A biomarker record of Lake El'gygytgyn, Far East Russian Arctic: investigating sources of organic matter and carbon cycling during marine isotope stages 1-3. Clim. Past 9, 243–260. https://doi.org/10.5194/cp-9-243-2013

Hopmans, E.C., Weijers, J.W.H., Schefuß, E., Herfort, L., Sinninghe Damsté, J.S., Schouten, S., 2004. A novel proxy for terrestrial organic matter in sediments based on branched and isoprenoid tetraether lipids. Earth Planet. Sci. Lett. 224, 107–116. https://doi.org/10.1016/j.epsl.2004.05.012

Hu, J., Peng, P., Chivas, A.R., 2009. Molecular biomarker evidence of origins and transport of organic matter in sediments of the Pearl River estuary and adjacent South China Sea. Appl. Geochemistry 24, 1666–1676. https://doi.org/10.1016/j.apgeochem.2009.04.035

Hunter, J.D., 2007. Matplotlib: A 2D Graphics Environment. Comput. Sci. Eng. 9, 90–95. https://doi.org/10.1109/MCSE.2007.55

Jeng, W.-L., Han, B., 1994. Sedimentary coprostanol in Kaohsiung Harbour and the Tan-Shui Estuary, Taiwan. Mar. Pollut. Bull. 28, 494–499.

Jones, E., Oliphant, T., Peterson, P., 2015. SciPy: Open source scientific tools for Python, 2001. URL http//www. scipy. org.

Kallweit, W., Mollenhauer, G., Zabel, M., 2012. Multi-proxy reconstruction of terrigenous input and sea-surface temperatures in the eastern Gulf of Guinea over the last ~35ka. Mar. Geol. 319–322, 35–46. https://doi.org/10.1016/j.margeo.2012.06.007

Keller Filho, T., Assad, E.D., De Rezende Lima, P.R.S., 2005. Regiões pluviometricamente homogêneas no Brasil. Pesqui. Agropecu. Bras. 40, 311–322.

Kirst, G., Schneider, R.R., Müller, P.J., von Storch, I., Wefer, G., 1999. Late Quaternary temperature variability in the Benguela Current system derived from alkenones. Quat. Res. 52, 92–103. https://doi.org/10.1006/qres.1999.2040

Kitzinger, K., Padilla, C.C., Marchant, H.K., Hach, P.F., Herbold, C.W., Kidane, A.T., Könneke, M., Littmann, S., Mooshammer, M., Niggemann, J., Petrov, S., Richter, A., Stewart, F.J., Wagner, M., Kuypers, M.M.M., Bristow, L.A., 2019. Cyanate and urea are substrates for nitrification by Thaumarchaeota in the marine environment. Nat. Microbiol. 4, 234–243. https://doi.org/10.1038/s41564-018-0316-2

Könneke, M., Bernhard, A.E., de la Torre, J.R., Walker, C.B., Waterbury, J.B., Stahl, D.A., 2005. Isolation of an autotrophic ammonia-oxidizing marine archaeon. Nature 437, 543–546. https://doi.org/10.1038/nature03911

Laureillard, J., Pinturier-Geiss, L., Fillaux, J., Saliot, A., 1997. Organic geochemistry of marine sediments of the Subantarctic Indian Ocean sector: Lipid classes — sources and fate. Deep. Res. Part II Top. Stud. Oceanogr. 44, 1085–1108. https://doi.org/10.1016/S0967-0645(96)00111-7

Ledru, M.P., Bertaux, J., Sifeddine, A., 1998a. Absence of Last Glacial Maximum records in lowland tropical forests. Quat. Res. 84, 487–492.

Ledru, M.P., Mourguiart, P., Riccomini, C., 2009. Related changes in biodiversity, insolation and climate in the Atlantic rainforest since the last interglacial. Palaeogeogr. Palaeoclimatol. Palaeoecol. 271, 140–152. https://doi.org/10.1016/j.palaeo.2008.10.008

Ledru, M.P., Salgado-Labouriau, M.L., Lorscheitter, M.L., 1998b. Vegetation dynamics in southern and central Brazil during the last 10,000 yr B.P. Rev. Palaeobot. Palynol. 99, 131–142. https://doi.org/10.1016/S0034-6667(97)00049-3

Li, L., Li, Q., He, J., Wang, H., Ruan, Y., Li, J., 2015. Biomarker-derived phytoplankton community for summer monsoon reconstruction in the western South China Sea over the past 450ka. Deep. Res. Part II Top. Stud. Oceanogr. 122, 118–130. https://doi.org/10.1016/j.dsr2.2015.11.006

Libes, S.M., 2009. Introduction to marine biogeochemistry, 2nd ed, Marine Chemistry. Elsevier, London.

Lin, J., Keogh, E., Wei, L., Lonardi, S., 2007. Experiencing SAX: A novel symbolic representation of time series. Data Min. Knowl. Discov. 15, 107–144. https://doi.org/10.1007/s10618-007-0064-z

Lisiecki, L.E., Raymo, M.E., 2005. A Pliocene-Pleistocene stack of 57 globally distributed benthic $\delta^{18}O$ records. Paleoceanography 20, 1–17. https://doi.org/10.1029/2004PA001071

Lisiecki, L.E., Stern, J. V., 2016. Regional and global benthic $\delta^{18}O$ stacks for the last glacial cycle. Palaeogeography 31, 1368–1394. https://doi.org/10.1002/2016PA003002

Lourenço, R.A., Mahiques, M.M., Wainer, I.E.K.C., Rosell-Melé, A., Bícego, M.C., 2016. Organic biomarker records spanning the last 34,800 years from the southeastern Brazilian upper slope: links between sea surface temperature, displacement of the Brazil Current, and marine productivity. Geo-Marine Lett. 36, 361–369. https://doi.org/10.1007/s00367-016-0453-7

Mahiques, M.M., Fukumoto, M.M., Silveira, I.C.A., Figueira, R.C.L., Bícego, M.C., Lourenço, R.A., Sousa, S.H.M., 2007. Sedimentary changes on the Southeastern Brazilian upper slope during the last 35,000 years. An. Acad. Bras. Cienc. 79, 171–181. https://doi.org/10.1590/S0001-37652007000100018

Mahiques, M.M., Hanebuth, T.J.J., Nagai, R.H., Bícego, M.C., Figueira, R.C.L., Sousa, S.H.M., Burone, L., Franco-Fraguas, P., Taniguchi, S., Salaroli, A.B., Dias, G.P., Prates, D.M., Freitas, M.E.F., 2017. Inorganic and organic geochemical fingerprinting of sediment sources and ocean circulation on a complex continental margin (São Paulo Bight, Brazil). Ocean Sci. 13, 209–222. https://doi.org/10.5194/os-13-209-2017

Mahiques, M.M., Mishima, Y., Rodrigues, M., 1999. Characteristics of the sedimentary organic matter on the inner and middle continental shelf between Guanabara Bay and São Francisco do Sul, southeastern Brazilian margin. Cont. Shelf Res. 19, 775–798. https://doi.org/10.1016/S0278-4343(98)00105-8

Mahiques, M.M., Sousa, S.H.M., Furtado, V.V., Tessler, M.G., Toledo, F.A.L., Burone, L., Figueira, R.C.L., Klein, D.A., Martins, C.C., Alves, D.P.V., 2010. The Southern Brazilian shelf: General characteristics, quaternary evolution and sediment distribution. Brazilian J. Oceanogr. 58, 25–34. https://doi.org/10.1590/S1679-87592010000600004

Mahiques, M.M., Tessler, M.G., Maria Ciotti, A., Silveira, I.C.A., Sousa, S.H.M., Figueira, R.C.L., Tassinari, C.C.G., Furtado, V.V., Passos, R.F., 2004. Hydrodynamically driven patterns of recent sedimentation in the shelf and upper slope off Southeast Brazil. Cont. Shelf Res. 24, 1685–1697. https://doi.org/10.1016/j.csr.2004.05.013

Mantovanelli, S.S., Tassinari, C.C.G., Mahiques, M.M., Jovane, L., Bongiolo, E., 2018. Characterization of Nd radiogenic isotope signatures in sediments from the Southwestern Atlantic margin. Front. Earth Sci. 6, 1–13. https://doi.org/10.3389/feart.2018.00074

Martins, C.C., Bícego, M.C., Figueira, R.C.L., Angelli, J.L.F., Combi, T., Gallice, W.C., Mansur, A.V., Nardes, E., Rocha, M.L., Wisnieski, E., Ceschim, L.M.M., Ribeiro, A.P., 2012. Multi-molecular markers and metals as tracers of organic matter inputs and contamination status from an Environmental Protection Area in the SW Atlantic (Laranjeiras Bay, Brazil). Sci. Total Environ. 417–418, 158–68. https://doi.org/10.1016/j.scitotenv.2011.11.086

Mathias, G.L., Nagai, R.H., Trindade, R.I.F., Mahiques, M.M., 2014. Magnetic fingerprint of the late Holocene inception of the Río de la Plata plume onto the southeast Brazilian shelf. Palaeogeogr. Palaeoclimatol. Palaeoecol. 415, 183–196. https://doi.org/10.1016/j.palaeo.2014.03.034

Meyers, P.A., 2003. Application of organic geochemistry to paleolimnological reconstruction: a summary of examples from the Laurention Great Lakes. Org. Geochem. 34, 261–289. https://doi.org/10.1016/S0146-6380(02)00168-7

Meyers, P.A., 1997. Organic geochemical proxies of paleoceanographic, paleolimnologic, and paleoclimatic processes. Org. Geochem. 27, 213–250.

Meyers, P.A., 1994. Preservation of elemental and isotopic source identification of sedimentary organic matter. Chem. Geol. 114, 289–302. https://doi.org/10.1016/0009-2541(94)90059-0

Middelburg, J.J., Herman, P.M.J., 2007. Organic matter processing in tidal estuaries. Mar. Chem. 106, 127–147. https://doi.org/10.1016/j.marchem.2006.02.007

Miller, K.G., Mountain, G.S., Wright, J.D., Browning, J. V., 2011. A 180-million-year record of sea level and ice volume variations from continental margin and deep-sea isotopic records. Oceanography 24, 40–53. https://doi.org/10.5670/oceanog.2011.26

Moreno, P.I., Lowell, T. V., Jacobson Jr, G.L., Denton, G.H., 1999. Abrupt vegetation and climate changes during the Last Glacial Maximum and Last Termination in the Chilean Lake District: a case study from Canal de La Puntilla (41°S). Geogr. Ann. Ser. A, Phys. Geogr. 81, 285–311. https://doi.org/10.1111/1468-0459.00059

Moser, G.A.O., Castro, N.O., Takanohashi, R.A., Fernandes, A.M., Pollery, R.C.G., Tenenbaum, D.R., Varela-Guerra, J., Barrera-Alba, J.J., Ciotti, A.M., 2016. The influence of surface low-salinity waters and cold subsurface water masses on picoplankton and ultraplankton distribution in the continental shelf off Rio de Janeiro, SE Brazil. Cont. Shelf Res. 120, 82–95. https://doi.org/10.1016/j.csr.2016.02.017

Mudge, S.M., Bebianno, M.J.A.F., East, J.A., Barreira, L.A., 1999. Sterols in the Ria Formosa lagoon, Portugal. Water Res. 33, 1038–1048. https://doi.org/10.1016/S0043-1354(98)00283-8

Muelbert, J.H., Acha, M., Mianzan, H., Guerrero, R., Reta, R., Braga, E.S., Garcia, V.M.T., Berasategui, A., Gomez-Erache, M., Ramírez, F., 2008. Biological, physical and chemical properties at the Subtropical Shelf Front Zone in the SW Atlantic

Continental Shelf. Cont. Shelf Res. 28, 1662–1673. https://doi.org/10.1016/j.csr.2007.08.011

Müller, P.J., 2004. Density and water content of sediment core GeoB2107-3. https://doi.org/10.1594/PANGAEA.143110

Nagai, R.H., Ferreira, P.A.L., Mulkherjee, S., Martins, M.V.A., Figueira, R.C.L., Sousa, S.H.M., Mahiques, M.M., 2014. Hydrodynamic controls on the distribution of surface sediments from the southeast South American continental shelf between 23° S and 38° S. Cont. Shelf Res. 89, 51–60. https://doi.org/10.1016/j.csr.2013.09.016

Nagai, R.H., Sousa, S.H.M., Lourenço, R.A., Bícego, M.C., Mahiques, M.M., 2010. Paleoproductivity changes during the late Quaternary in the southeastern Brazilian upper continental margin of the southwestern Atlantic. Brazilian J. Oceanogr. 58, 31–41. https://doi.org/10.1590/S1679-87592010000500004

Nakakuni, M., Dairiki, C., Kaur, G., Yamamoto, S., 2017. Stanol to sterol ratios in late Quaternary sediments from southern California: An indicator for continuous variability of the oxygen minimum zone. Org. Geochem. 111, 126–135. https://doi.org/10.1016/j.orggeochem.2017.06.009

Nieto-Ferreira, R., Rickenbach, T.M., 2011. Regionality of monsoon onset in South America: A three-stage conceptual model. Int. J. Climatol. 31, 1309–1321. https://doi.org/10.1002/joc.2161

Oliphant, T.E., 2006. A guide to NumPy.

Paillard, D., Labeyrie, L.D., Yiou, P., 1996. AnalySeries 1.0: a Macintosh software for the analysis of geophysical time-series.

Patterson, G.W., 1971. The distribution of sterols in algae. Lipids 6, 120–127.

Pereira, J., Gabioux, M., Marta-Almeida, M., Cirano, M., Paiva, A.M., Aguiar, A.L., 2014. The bifurcation of the western boundary current system of the South Atlantic Ocean. Rev. Bras. Geofísica 32, 241–257.

Pereira, L.S., Arz, H.W., Pätzold, J., Portilho-Ramos, R.C., 2018. Productivity evolution in the South Brazilian Bight during the last 40,000 years. Paleoceanogr. Paleoclimatology 33, 1339–1356. https://doi.org/10.1029/2018PA003406

Perrin, L., Probert, I., Langer, G., Aloisi, G., 2016. Growth of the coccolithophore Emiliania huxleyi in light- and nutrient-limited batch reactors: Relevance for the BIOSOPE deep ecological niche of coccolithophores. Biogeosciences 13, 5983–6001. https://doi.org/10.5194/bg-13-5983-2016

Peterson, R.G., Stramma, L., 1991. Upper-level circulation in the South-Atlantic Ocean. Prog. Oceanogr. 26, 1–73. https://doi.org/10.1016/0079-6611(91)90006-8

Piola, A.R., Matano, R.P., 2001. Brazil and Falklands (Malvinas) Currents, in: Steele, J.H., Thorpe, S.A., Turekian, K.K. (Eds.), Ocean Currents: A Derivative of the Encyclopedia of Ocean Sciences. Elsevier Inc., pp. 35–43. https://doi.org/10.1016/B978-0-12-409548-9.10541-X

Piola, A.R., Romero, S.I., Zajaczkovski, U., 2008. Space-time variability of the Plata plume inferred from ocean color. Cont. Shelf Res. 28, 1556–1567. https://doi.org/10.1016/j.csr.2007.02.013

Pivel, M.A.G., 2009. Reconstrução da hidrografia superficial do Atlântico Sul Ocidental desde o Último Máximo Glacial a partir do estudo de foraminíferos planctônicos. Universidade de São Paulo (USP).

Portilho-Ramos, R.C., Ferreira, F., Calado, L., Frontalini, F., Toledo, M.B., 2015. Variability of the upwelling system in the southeastern Brazilian margin for the last 110,000 years. Glob. Planet. Change 135, 179–189. https://doi.org/10.1016/j.gloplacha.2015.11.003

Quirós-Collazos, L., Pedrosa-Pàmies, R., Sanchez-Vidal, A., Guillén, J., Duran, R., Cabello, P., 2017. Distribution and sources of organic matter in size-fractionated nearshore sediments off the Barcelona city (NW Mediterranean). Estuar. Coast. Shelf Sci. 189, 267–280. https://doi.org/10.1016/j.ecss.2017.03.004

Razik, S., Govin, A., Chiessi, C.M., von Dobeneck, T., 2015. Depositional provinces, dispersal, and origin of terrigenous sediments along the SE South American continental margin. Mar. Geol. 363, 261–272. https://doi.org/10.1016/j.margeo.2015.03.001

Reimer, P.J., Bard, E., Bayliss, A., Beck, J.W., Blackwell, P.G., Ramsey, C.B., Buck, C.E., Cheng, H., Edwards, R.L., Friedrich, M., Grootes, P.M., Guilderson, T.P., Haflidason, H., Hajdas, I., Hatté, C., Heaton, T.J., Hoffmann, D.L., Hogg, A.G., Hughen, K.A., Kaiser, K.F., Kromer, B., Manning, S.W., Niu, M., Reimer, R.W., Richards, D.A., Scott, E.M., Southon, J.R., Staff, R.A., Turney, C.S.M., Pflicht, J. van der, 2013. IntCal13 and Marine13 radiocarbon age calibration curves 0–50,000 years cal BP. Radiocarbon 55, 1869–1887. https://doi.org/10.2458/azu_js_rc.55.16947

Ribeiro, C.G., Lopes dos Santos, A., Marie, D., Pellizari, V.H., Brandini, F.P., Vaulot, D., 2016. Pico and nanoplankton abundance and carbon stocks along the Brazilian Bight. PeerJ 4, e2587. https://doi.org/10.7717/peerj.2587

Ribeiro, M.C., Metzger, J.P., Martensen, A.C., Ponzoni, F.J., Hirota, M.M., 2009. The Brazilian Atlantic Forest: How much is left, and how is the remaining forest distributed? Implications for conservation. Biol. Conserv. 142, 1141–1153. https://doi.org/10.1016/j.biocon.2009.02.021

Rodrigues, R.R., Rothstein, L.M., Wimbush, M., 2007. Seasonal variability of the South Equatorial Current bifurcation in the Atlantic Ocean: a numerical study. J. Phys. Oceanogr. 37, 16–30. https://doi.org/10.1175/JPO2983.1

Routh, J., Hugelius, G., Kuhry, P., Filley, T., Tillman, P.K., Becher, M., Crill, P., 2014. Multi-proxy study of soil organic matter dynamics in permafrost peat deposits reveal vulnerability to climate change in the European Russian Arctic. Chem. Geol. 368, 104–117. https://doi.org/10.1016/j.chemgeo.2013.12.022

Sant'Anna Netto, J.L., 2005. Decálogo da climatologia do Sudeste brasileiro. Rev. Bras. Climatol. 1, 43–6.

Santana, C.L., 2008. Geomorfologia da planície fluvial do rio Ribeira de Iguape entre Sete Barras e Eldorado (SP): Subsídios ao planejamento fício-territorial de áreas inundáveis. Universidade de São Paulo (USP).

Santoro, A.E., Richter, R.A., Dupont, C.L., 2019. Planktonic Marine Archaea. Ann. Rev. Mar. Sci. 11, 131–158. https://doi.org/10.1146/annurev-marine-121916-063141

Sawada, K., Nakamura, H., Arai, T., Tsukagoshi, M., 2013. Evaluation of paleoenvironment using terpenoid biomarkers in lignites and plant fossil from the Miocene Tokiguchi Porcelain Clay Formation at the Onada mine, Tajimi, central Japan. Int. J. Coal Geol. 107, 78–89. https://doi.org/10.1016/j.coal.2012.10.013

Schettini, C.A.F., 2002. Near bed sediment transport in the Itajaí-Açu river estuary, southern Brazil. Proc. Mar. Sci. 5, 499–512. https://doi.org/10.1016/S1568-2692(02)80036-5

Schmid, C., 2014. Mean vertical and horizontal structure of the subtropical circulation in the South Atlantic from three-dimensional observed velocity fields. Deep. Res. Part I Oceanogr. Res. Pap. 91, 50–71. https://doi.org/10.1016/j.dsr.2014.04.015

Schmid, C., Siedler, G., Zenk, W., 2000. Dynamics of Intermediate Water Circulation in the Subtropical South Atlantic. J. Phys. Oceanogr. 30, 3191–3211. https://doi.org/10.1175/1520-0485(2000)030<3191:DOIWCI>2.0.CO;2

1216 Silva, J.M.C., Casteleti, C.H.M., 2003. Status of the biodiversity of the Atlantic
1217 Forest of Brazil, in: The Atlantic Forest of South America: Biodiversity Status, Threats,
1218 and Outlook. CABS and Island Press, Washigton, D.C., pp. 43–59.
1219 Silveira, I.C.A., Calado, L., Castro, B.M., Cirano, M., Lima, J.A.M.,
1220 Mascarenhas, A. d. S., 2004. On the baroclinic structure of the Brazil Current –
1221 Intermediate Western Boundary Current system at 22 ° – 23 ° S. Geophys. Res. Lett. 31,
1222 1–5. https://doi.org/10.1029/2004GL020036
1223 Silveira, I.C.A., Foloni Neto, H., Costa, T.P., Schmidt, A.C.K., Pereira, A.F.,
1224 Castro Filho, B.M., Soutelino, R.G., Grossmann-Matheson, G.S., 2015. Caracterização
1225 da oceanografia física do talude continental e região oceânica da Bacia de Campos, in:
1226 Martins, R.P., Grossmann-Matheson, G.S. (Eds.), Meteorologia e Oceanografia.
1227 Elsevier, Rio de Janeiro, RJ, pp. 133–188.
1228 Silveira, I.C.A., Schmidt, A.C.K., Campos, E.J.D., Godoi, S.S., Ikeda, Y., 2000.
1229 A corrente do Brasil ao largo da costa leste brasileira. Rev. Bras. Oceanogr. 48, 171–
1230 183. https://doi.org/10.1590/S1413-77392000000200008
1231 Sinninghe Damsté, J.S., Schouten, S., Hopmans, E.C., van Duin, A.C.T.,
1232 Geenevasen, J.A.J., 2002. Crenarchaeol: the characteristic core glycerol dibiphytanyl
1233 glycerol tetraether membrane lipid of cosmopolitan pelagic crenarchaeota. J. Lipid Res.
1234 43, 1641–1651. https://doi.org/10.1194/jlr.M200148-JLR200
1235 Sinninghe Damsté, J.S., Van Dongen, B.E., Rijpstra, W.I.C., Schouten, S.,
1236 Volkman, J.K., Geenevasen, J.A.J., 2001. Novel intact glycolipids in sediments from an
1237 Antarctic lake (Ace Lake). Org. Geochem. 32, 321–332. https://doi.org/10.1016/S0146-
1238 6380(00)00165-0
1239 Toggweiler, J.R., Russell, J.L., Carson, S.R., 2006. Midlatitude westerlies,
1240 atmospheric CO_2, and climate change during the ice ages. Paleoceanography 21, 1–15.
1241 https://doi.org/10.1029/2005PA001154
1242 Torrence, C., Compo, G.P., 1998. A Practical Guide to Wavelet Analysis. Bull.
1243 Am. Meteorol. Soc. 79, 61–78.
1244 van Rossum, G., 1995. Python tutorial - Technical Report CS-R9526.
1245 Venkatesan, M.I., Kaplan, I.R., 1987. The lipid geochemistry of Antarctic
1246 marine sediments: Bransfield Strait. Mar. Chem. 21, 347–375.
1247 Voigt, I., Chiessi, C.M., Prange, M., Mulitza, S., Groeneveld, J., Varma, V.,
1248 Henrich, R., 2015. Holocene shifts of the southern westerlies across the South Atlantic.
1249 Paleoceanography 39–51. https://doi.org/10.1002/2014PA002677

1250 Volkman, J.K., 2006. Lipid markers for marine organic matter. Handb. Environ.
1251 Chem. 2, 27–70. https://doi.org/10.1007/698
1252 Volkman, J.K., 1986. A review of sterol markers for marine and terrigenous
1253 organic matter. Org. Geochem. 9, 83–99. https://doi.org/10.1016/0146-6380(86)90089-
1254 6
1255 Volkman, J.K., Barrett, S.M., Blackburn, S.I., Mansour, M.P., Sikes, E.L., Gelin,
1256 F., 1998. Microalgal biomarkers: A review of recent research developments. Org.
1257 Geochem. 29, 1163–1179. https://doi.org/10.1016/S0146-6380(98)00062-X
1258 Volkman, J.K., Eglinton, G., Corner, E.D.S., Forsberg, T.E. V., 1980. Long-
1259 chain alkenes and alkenones in the marine coccolithophorid *Emiliania huxleyi*.
1260 Phytochemistry 19, 2619–2622. https://doi.org/10.1016/S0031-9422(00)83930-8
1261 Volkman, J.K., Holdsworth, D.G., Neill, G.P., Bavor-Jr, H.J., 1992.
1262 Identification of natural, anthropogenic and petroleum hydrocarbons in aquatic
1263 sediments. Sci. Total Environ. 112, 203–19.
1264 WAIS Divide Project Members, 2015. Precise interpolar phasing of abrupt
1265 climate change during the last ice age. Nature 520, 661–665.
1266 https://doi.org/10.1038/nature14401
1267 Wakeham, S.G., Canuel, E.A., 2006. Degradation and preservation of organic
1268 matter in marine sediments. Handb. Environ. Chem. 2, 295–321.
1269 https://doi.org/10.1007/698
1270 Weijers, J.W.H., Schefuß, E., Schouten, S., Sinninghe Damsté, J.S., 2007.
1271 Coupled thermal and hydrological evolution of Tropical Africa over the last
1272 deglaciation. Science 315, 1701–1704. https://doi.org/10.1126/science.1138131
1273 Weijers, J.W.H., Schouten, S., Spaargaren, O.C., Sinninghe Damsté, J.S., 2006.
1274 Occurrence and distribution of tetraether membrane lipids in soils: Implications for the
1275 use of the TEX_{86} proxy and the BIT index. Org. Geochem. 37, 1680–1693.
1276 https://doi.org/10.1016/j.orggeochem.2006.07.018
1277 Wienders, N., Arhan, M., Mercier, H., 2000. Circulation at the western boundary
1278 of the South and Equatorial Atlantic: Exchanges with the ocean interior. J. Mar. Res. 58,
1279 1007–1039.
1280 Wrege, M.S., Steinmetz, S., Reisser Júnior, C., Almeida, I.R. de, 2012. Atlas
1281 climático da Região Sul do Brasil: Estados do Paraná, Santa Catarina e Rio Grande do
1282 Sul, 2nd ed. Embrapa, Brasília, DF.

Xu, F.-L., Yang, C., He, W., He, Q.-S., Li, Y.-L., Kang, L., Liu, W.-X., Xiong, Y.-Q., Xing, B., 2017. Bias and association of sediment organic matter source apportionment indicators: A case study in a eutrophic Lake Chaohu, China. Sci. Total Environ. 581–582, 874–884. https://doi.org/10.1016/j.scitotenv.2017.01.037

Yunker, M.B., Belicka, L.L., Harvey, H.R., Macdonald, R.W., 2005. Tracing the inputs and fate of marine and terrigenous organic matter in Arctic Ocean sediments: A multivariate analysis of lipid biomarkers. Deep. Res. Part II Top. Stud. Oceanogr. 52, 3478–3508. https://doi.org/10.1016/j.dsr2.2005.09.008

Zhou, W., Zheng, Y., Meyers, P.A., Jull, A.J.T., Xie, S., 2010. Postglacial climate-change record in biomarker lipid compositions of the Hani peat sequence, Northeastern China. Earth Planet. Sci. Lett. 294, 37–46. https://doi.org/10.1016/j.epsl.2010.02.035

Zubkov, M. V., Sleigh, M.A., Burkill, P.H., Leakey, R.J.G., 2000. Picoplankton community structure on the Atlantic Meridional Transect: A comparison between seasons. Prog. Oceanogr. 45, 369–386. https://doi.org/10.1016/S0079-6611(00)00008-2

CAPÍTULO 4 – CONSIDERAÇÕES FINAIS

O Oceano Atlântico Sul apresenta um papel fundamental no transporte de calor entre as diversas bacias oceânicas, assim como na formação de massas d'água. Por esta razão, entender as oscilações climáticas naturais ocorridas nele permite compreender melhor as mudanças climáticas recentes. Além disso, compreender como elas afetaram a produção da matéria orgânica provê uma base para prever como a teia trófica marinha poderá reagir às mudanças recentes.

Com base em um testemunho sedimentar coletado na região do talude (24,8°S; 44,3°W; aproximadamente 840 m de profundidade), foi possível estudar a região central do Embaiamento Sul do Brasil, um ambiente atualmente governado pela presença das correntes do Brasil e de Contorno Intermediária. A partir de diversos marcadores geoquímicos, foi possível estimar as variações das temperaturas da superfície e da subsuperfície do mar, assim como entender a evolução da produção de matéria orgânica autóctone e do aporte de matéria orgânica alóctone nesta região.

Através da reconstrução das temperaturas do mar, foi possível diferenciar entre as forçantes responsáveis pelas oscilações climáticas de maior e menor escala temporal (orbital e milenar, respectivamente) no Embaiamento Sul do Brasil. Na escala orbital, as oscilações de temperatura foram dependentes das mudanças climáticas na Antártica, em especial a radiação solar incidente. No entanto, as variações da temperatura na escala milenar estiveram relacionadas à formação da Água Profunda do Atlântico Norte. Assim, em períodos de maior formação de águas profundas no Hemisfério Norte, o calor do Atlântico Sul é transportado através das correntes superficiais para o Hemisfério Norte, causando um relativo resfriamento no oeste do Atlântico Sul. Localmente, o Estágio Marinho Isotópico (MIS) 3 apresentou temperaturas de superfície do mar mais frias do que o MIS 4, assim como uma coluna d'água mais homogênea. Além disso, apresentou um sinal tardio da última deglaciação, podendo ser relacionado à Circulação Meridional do Atlântico. O tempo necessário para o aquecimento atmosférico nos polos causar uma redução na formação da Água Profunda do Atlântico Norte e, por

sua vez, causar um acúmulo de calor da superfície do mar no oeste do Atlântico Sul, provavelmente causou esse atraso no sinal da deglaciação.

Em relação à produção e ao aporte de matéria orgânica, a principal contribuição encontrada foi de origem autóctone, controlada por fatores hidrodinâmicos. As maiores taxas de produtividade marinha foram observadas durante o MIS 3, quando a intensificação da ressurgência da Água Central do Atlântico Sul no talude indica uma maior formação de vórtices provindos da Corrente do Brasil. Já durante o MIS 4 e o MIS 2, a produção primária marinha possivelmente esteve associada ao aporte fluvial de nutrientes. No entanto, após a última deglaciação, quando a temperatura da água do mar dos primeiros 30 m de profundidade aumentou aproximadamente 3 °C, as condições se tornaram mais oligotróficas. Isso causou um declínio na produção fitoplanctônica e estimulou a produção das arqueias, o que provavelmente gerou mudanças na teia trófica da região. Assim, a produção primária na região central do Embaiamento Sul do Brasil não foi controlada pelo aporte fluvial do Rio da Prata, como observado para a porção sul do Embaiamento. Na porção central, o aporte de material terrígeno foi controlado por duas forçantes distintas: a variação do nível do mar e a pluviosidade no continente adjacente. Níveis mais baixos do mar fizeram com que a plataforma continental ficasse mais curta, o que por sua vez aproximou a desembocadura dos rios, especialmente o rio Paraíba do Sul, do talude continental. Já a pluviosidade no continente estimulou tanto uma maior produção primária quanto uma maior exportação desse material através dos rios.

Pensando no atual cenário de aquecimento global, as previsões climáticas sugerem um aquecimento da superfície do mar do Atlântico Sul de até 0,5 °C até o final deste século (Rhein et al., 2013) ou seja, um sexto do valor observado para o intervalo de 10 mil anos durante a última deglaciação. Assim, o derretimento das calotas polares da Groelândia provavelmente acarretará a diminuição da densidade da água superficial e na consequente diminuição da formação da Água Profunda do Atlântico Norte. Se a relação observada nos últimos 80 mil anos entre essa formação e as temperaturas do mar do oeste do Atlântico Sul se mantiver, é esperado que ocorra um aquecimento das águas superficiais e subsuperficiais. Esse aquecimento pode levar ao declínio mais pronunciado dos principais grupos fitoplanctônicos da

região, o que pode acarretar uma mudança da teia trófica local. Apesar disso, o possível fortalecimento da Corrente do Brasil pode intensificar a formação de vórtices, o que por sua vez, pode promover a fertilização da região pela Água Central do Atlântico Sul. Ainda, o avanço do desmatamento nas regiões sul e sudeste do Brasil (Ribeiro et al., 2009) aliado a um provável aumento no nível relativo do mar sugerem uma menor contribuição terrígena para o talude continental. Assumindo que o oeste do Atlântico Sul passe por mudanças ambientais similares às observadas durante a última deglaciação, estudos que foquem teias tróficas baseados no plâncton procarionte e no meandramento de uma futura Corrente do Brasil fortalecida possivelmente indicarão como o Embaiamento Sul do Brasil irá se comportar até o final do século.

REFERÊNCIAS

Alley, R.B., 2000. The Younger Dryas cold interval as viewed from central Greenland. Quat. Sci. Rev. 19, 213–226.

Arz, H.W., Pätzold, J., Wefer, G., 1999. The deglacial history of the western tropical Atlantic as inferred from high resolution stable isotope records off northeastern Brazil. Earth Planet. Sci. Lett. 167, 105–117. https://doi.org/10.1016/S0012-821X(99)00025-4

Barrows, T.T., Juggins, S., De Deckker, P., Calvo, E., Pelejero, C., 2007. Long-term sea surface temperature and climate change in the Australian-New Zealand region. Paleoceanography 22, 1–17. https://doi.org/10.1029/2006PA001328

Bechtel, A., Schubert, C.J., 2009. Biogeochemistry of particulate organic matter from lakes of different trophic levels in Switzerland. Org. Geochem. 40, 441–454. https://doi.org/10.1016/j.orggeochem.2009.01.011

Bechtel, A., Woszczyk, M., Reischenbacher, D., Sachsenhofer, R.F., Gratzer, R., Püttmann, W., Spychalski, W., 2007. Biomarkers and geochemical indicators of Holocene environmental changes in coastal Lake Sarbsko (Poland). Org. Geochem. 38, 1112–1131. https://doi.org/10.1016/j.orggeochem.2007.02.009

Bereiter, B., Luthi, D., Siegrist, M., Schupbach, S., Stocker, T.F., Fischer, H., 2012. Mode change of millennial CO_2 variability during the last glacial cycle associated with a bipolar marine carbon seesaw. Proc. Natl. Acad. Sci. 109, 9755–9760. https://doi.org/10.1073/pnas.1204069109

Berger, A., Loutre, M.F., 1991. Insolation values for the climate of the last 10 million years. Quat. Sci. Rev. 10, 297–317. https://doi.org/10.1016/0277-3791(91)90033-Q

Biastoch, A., Böning, C.W., Lutjeharms, J.R.E., 2008. Agulhas leakage dynamics affects decadal variability in Atlantic overturning circulation. Nature 456, 489–492. https://doi.org/10.1038/nature07426

Böhm, E., Lippold, J., Gutjahr, M., Frank, M., Blaser, P., Antz, B., Fohlmeister, J., Frank, N., Andersen, M.B., Deininger, M., 2015. Strong and deep Atlantic meridional overturning circulation during the last glacial cycle. Nature 517, 73–76. https://doi.org/10.1038/nature14059

Bond, G., Broecker, W.S., Johnsen, S.J., McManus, J.F., Labeyrie, L.D., Jouzel, J., Bonani, G., 1993. Correlations between climate records from North Atlantic sediments and Greenland ice. Nature 365, 143–147. https://doi.org/10.1038/365143a0

Broccoli, A.J., Dahl, K.A., Stouffer, R.J., 2006. Response of the ITCZ to Northern Hemisphere cooling. Geophys. Res. Lett. 33, 1–4. https://doi.org/10.1029/2005GL024546

Buizert, C., Schmittner, A., 2015. Southern Ocean control of glacial AMOC stability and Dansgaard-Oeschger interstadial duration. Paleoceanography 30, 1595–1612. https://doi.org/10.1002/2015PA002795

Burns, K.A., Brinkman, D., 2011. Organic biomarkers to describe the major carbon inputs and cycling of organic matter in the central Great Barrier Reef region. Estuar. Coast. Shelf Sci. 93, 132–141. https://doi.org/10.1016/j.ecss.2011.04.001

Campos, E.J.D., Miller, J.L., Moiler, T.J., Peterson, R.G., 1995. Physical Oceanography of the southwest Atlantic Ocean. Oceanography 8, 87–91.

Carvalho, L.M. V., Jones, C., Liebmann, B., 2004. The South Atlantic convergence zone: Intensity, form, persistence, and relationships with intraseasonal to interannual activity and extreme rainfall. J. Clim. 17, 88–108. https://doi.org/10.1175/1520-0442(2004)017<0088:TSACZI>2.0.CO;2

Castellanos, P., Campos, E.J.D., Piera, J., Sato, O.T., Silva Dias, M.A.F., 2017. Impacts of Agulhas leakage on the tropical Atlantic western boundary systems. J. Clim. 30, 6645–6659. https://doi.org/10.1175/JCLI-D-15-0878.1

Chavez, F.P., Ryan, J., Lluch-Cota, S.E., Ñiquen, M., 2003. From anchovies to sardines and back: Multidecadal change in the Pacific Ocean. Science 299, 217–221. https://doi.org/10.1126/science.1075880

Chen, W., Mohtadi, M., Schefuß, E., Mollenhauer, G., 2014. Organic-geochemical proxies of sea surface temperature in surface sediments of the tropical eastern Indian Ocean. Deep. Res. Part I Oceanogr. Res. Pap. 88, 17–29. https://doi.org/10.1016/j.dsr.2014.03.005

Chiessi, C.M., Mulitza, S., Groeneveld, J., Silva, J.B., Campos, M.C., Gurgel, M.H.C., 2014. Variability of the Brazil Current during the late Holocene. Palaeogeogr. Palaeoclimatol. Palaeoecol. 415, 28–36. https://doi.org/10.1016/j.palaeo.2013.12.005

Clark, P.U., Dyke, A.S., Shakun, J.D., Carlson, A.E., Clark, J., Wohlfarth, B., Mitrovica, J.X., Hostetler, S.W., McCabe, A.M., 2009. The Last Glacial Maximum. Science 325, 710–714. https://doi.org/10.1126/science.1172873

Clark, P.U., Hostetler, S.W., Pisias, N.G., Schmittner, A., Meissner, K.J., 2007. Mechanisms for an ~7-kyr climate and sea-level oscillation during Marine Isotope Stage 3, in: Schmittner, A., Chiang, J.C.H., Hemming, S.R. (Eds.), Geophysical Monograph Series 173. American Geophysical Union, Washington DC, pp. 209–246. https://doi.org/10.1029/GM173

Clauzet, G., Wainer, I.E.K.C., Lazar, A., Brady, E., Otto-Bliesner, B.L., 2007. A numerical study of the South Atlantic circulation at the Last Glacial Maximum. Palaeogeogr. Palaeoclimatol. Palaeoecol. 253, 509–528. https://doi.org/10.1016/j.palaeo.2007.06.018

Conte, M.H., Sicre, M.-A., Rühlemann, C., Weber, J.C., Schulte, S., Schulz-Bull, D., Blanz, T., 2006. Global temperature calibration of the alkenone unsaturation index ($U^{K'}_{37}$) in surface waters and comparison with surface sediments. Geochemistry, Geophys. Geosystems 7, 1–22. https://doi.org/10.1029/2005GC001054

Costa, T.L.F., Araújo, M.P., Knoppers, B.A., Carreira, R.S., 2010. Sources and distribution of particulate organic matter of a tropical Estuarine-Lagoon System from NE Brazil as indicated by lipid biomarkers. Aquat. Geochemistry 17, 1–19. https://doi.org/10.1007/s10498-010-9104-1

Covey, C., 1984. The Earth's Orbit and the Ice Ages. Sci. Am. 250, 58–66.

Crowley, T.J., Hyde, W.T., 2008. Transient nature of late Pleistocene climate variability. Nature 456, 226–230. https://doi.org/10.1038/nature07365

De Deckker, P., Moros, M., Perner, K., Jansen, E., 2012. Influence of the tropics and southern westerlies on glacial interhemispheric asymmetry. Nat. Geosci. 5, 266–269. https://doi.org/10.1038/ngeo1431

Delworth, T.L., Clark, P.U., Holland, M., Johns, W.E., Kuhlbrodt, T., Lynch-Stieglitz, J., Morrill, C., Seager, R., Weaver, A.J., Zhang, R., 2008. The potential for abrupt change in the Atlantic Meridional Overturning Circulation, in: McGeehin, J.P., Watson, J.M., Hendrick, K.E. (Eds.), Abrupt Climate Change: Final Report, Synthesis and Assessment Product 3.4. DIANE Publishing, pp. 258–359.

Derrien, M., Yang, L., Hur, J., 2017. Lipid biomarkers and spectroscopic indices

for identifying organic matter sources in aquatic environments: A review. Water Res. 112, 58–71. https://doi.org/10.1016/j.watres.2017.01.023

Dong, S., Garzoli, S., Baringer, M., 2011. The role of interocean exchanges on decadal variations of the meridional heat transport in the South Atlantic. J. Phys. Oceanogr. 41, 1498–1511. https://doi.org/10.1175/2011jpo4549.1

Eglinton, T.I., Eglinton, G., 2008. Molecular proxies for paleoclimatology. Earth Planet. Sci. Lett. 275, 1–16. https://doi.org/10.1016/j.epsl.2008.07.012

Emiliani, C., 1955. Pleistocene Temperatures. J. Geol. 63, 538–578.

EPICA Community Members, 2006. One-to-one coupling of glacial climate variability in Greenland and Antarctica. Nature 444, 195–198. https://doi.org/10.1038/nature05301

Faux, J.F., Belicka, L.L., Rodger Harvey, H., 2011. Organic sources and carbon sequestration in Holocene shelf sediments from the western Arctic Ocean. Cont. Shelf Res. 31, 1169–1179. https://doi.org/10.1016/j.csr.2011.04.001

Garzoli, S.L., Matano, R.P., 2011. The South Atlantic and the Atlantic Meridional Overturning Circulation. Deep. Res. Part II Top. Stud. Oceanogr. 58, 1837–1847. https://doi.org/10.1016/j.dsr2.2010.10.063

Graham, A.G.C., Kuhn, G., Meisel, O., Hillenbrand, C.-D., Hodgson, D.A., Ehrmann, W., Wacker, L., Wintersteller, P., Ferreira, C. dos S., Römer, M., White, D., Bohrmann, G., 2017. Major advance of South Georgia glaciers during the Antarctic Cold Reversal following extensive sub-Antarctic glaciation. Nat. Commun. 8, 14798. https://doi.org/10.1038/ncomms14798

Hemming, S.R., 2004. Heinrich events: Massive late Pleistocene ditritus layers of the North Atlanitc and their global climate imprint. Rev. Geophys. 42, 1–43. https://doi.org/10.1029/2003RG000128

Hessler, I., Dupont, L., Bonnefille, R., Behling, H., González, C., Helmens, K.F., Hooghiemstra, H., Lebamba, J., Ledru, M.P., Lézine, A.M., Maley, J., Marret, F., Vincens, A., 2010. Millennial-scale changes in vegetation records from tropical Africa and South America during the last glacial. Quat. Sci. Rev. 29, 2882–2899. https://doi.org/10.1016/j.quascirev.2009.11.029

Ho, S.L., Naafs, B.D.A., Lamy, F., 2013. Alkenone paleothermometry based on the haptophyte algae. Encycl. Quat. Sci. 2, 755–764. https://doi.org/10.1016/B978-0-444-53643-3.00278-8

Holland, A.R., Petsch, S.T., Castañeda, I.S., Wilkie, K.M., Burns, S.J., Brigham-

Grette, J., 2013. A biomarker record of Lake El'gygytgyn, Far East Russian Arctic: investigating sources of organic matter and carbon cycling during marine isotope stages 1-3. Clim. Past 9, 243–260. https://doi.org/10.5194/cp-9-243-2013

Hopmans, E.C., Weijers, J.W.H., Schefuß, E., Herfort, L., Sinninghe Damsté, J.S., Schouten, S., 2004. A novel proxy for terrestrial organic matter in sediments based on branched and isoprenoid tetraether lipids. Earth Planet. Sci. Lett. 224, 107–116. https://doi.org/10.1016/j.epsl.2004.05.012

Hu, J., Peng, P., Chivas, A.R., 2009. Molecular biomarker evidence of origins and transport of organic matter in sediments of the Pearl River estuary and adjacent South China Sea. Appl. Geochemistry 24, 1666–1676. https://doi.org/10.1016/j.apgeochem.2009.04.035

IPCC, 2014. Climate Change 2014: Synthesis Report, in: IPCC Core Writing Team, Pachauri, R.K., Meyer, L. (Eds.), Contribution of Working Groups I, II and III to the Fifth Assessment Report of the Intergovernmental Panel on Climate Change. IPCC, Geneva, Switzerland, p. 151.

Jaccard, S.L., Galbraith, E.D., Martínez-García, A., Anderson, R.F., 2016. Covariation of deep Southern Ocean oxygenation and atmospheric CO_2 through the last ice age. Nature 530, 207–10. https://doi.org/10.1038/nature16514

Kaiser, J., Ruggieri, N., Hefter, J., Siegel, H., Mollenhauer, G., Arz, H.W., Lamy, F., 2014. Lipid biomarkers in surface sediments from the Gulf of Genoa, Ligurian sea (NW Mediterranean sea) and their potential for the reconstruction of palaeo-environments. Deep. Res. Part I Oceanogr. Res. Pap. 89, 68–83. https://doi.org/10.1016/j.dsr.2014.04.009

Kim, J.H., Schneider, R.R., 2003. Low-latitude control of interhemispheric sea-surface temperature contrast in the tropical Atlantic over the past 21 kyears: The possible role of SE trade winds. Clim. Dyn. 21, 337–347. https://doi.org/10.1007/s00382-003-0341-5

Kim, J.H., van der Meer, J., Schouten, S., Helmke, P., Willmott, V., Sangiorgi, F., Koç, N., Hopmans, E.C., Sinninghe Damsté, J.S., 2010. New indices and calibrations derived from the distribution of crenarchaeal isoprenoid tetraether lipids: Implications for past sea surface temperature reconstructions. Geochim. Cosmochim. Acta 74, 4639–4654.

https://doi.org/10.1016/j.gca.2010.05.027

Kuhlbrodt, T., Griesel, A., Montoya, M., Levermann, A., Hofmann, M., Rahmstorf, S., 2007. On the driving processes of the Atlantic Meridional Overturning Circulation. Rev. Geophys. 45. https://doi.org/10.1029/2004RG000166

Laureillard, J., Pinturier-Geiss, L., Fillaux, J., Saliot, A., 1997. Organic geochemistry of marine sediments of the Subantarctic Indian Ocean sector: Lipid classes — sources and fate. Deep. Res. Part II Top. Stud. Oceanogr. 44, 1085–1108. https://doi.org/10.1016/S0967-0645(96)00111-7

Lisiecki, L.E., Raymo, M.E., 2005. A Pliocene-Pleistocene stack of 57 globally distributed benthic $\delta^{18}O$ records. Paleoceanography 20, 1–17. https://doi.org/10.1029/2004PA001071

Lisiecki, L.E., Raymo, M.E., Curry, W.B., 2008. Atlantic overturning responses to Late Pleistocene climate forcings. Nature 456, 85–88. https://doi.org/10.1038/nature07425

Lourenço, R.A., Mahiques, M.M., Wainer, I.E.K.C., Rosell-Melé, A., Bícego, M.C., 2016. Organic biomarker records spanning the last 34,800 years from the southeastern Brazilian upper slope: links between sea surface temperature, displacement of the Brazil Current, and marine productivity. Geo-Marine Lett. 36, 361–369. https://doi.org/10.1007/s00367-016-0453-7

Lynam, C.P., Hay, S.J., Brierley, A.S., 2004. Interannual variability in abundance of North Sea jellyfish and links to the North Atlantic Oscillation. Limnol. Oceanogr. 49, 637–643.

Lynch-Stieglitz, J., 2017. The Atlantic Meridional Overturning Circulation and abrupt climate change. Ann. Rev. Mar. Sci. 9, 83–104. https://doi.org/10.1146/annurev-marine-010816-060415

Marchitto, T.M., Broecker, W.S., 2006. Deep water mass geometry in the glacial Atlantic Ocean: A review of constraints from the paleonutrient proxy Cd/Ca. Geochemistry, Geophys. Geosystems 7. https://doi.org/10.1029/2006GC001323

Marengo, J.A., Chou, S.C., Kay, G., Alves, L.M., Pesquero, J.F., Soares, W.R., Santos, D.C., Lyra, A.A., Sueiro, G., Betts, R., Chagas, D.J., Gomes, J.L., Bustamante, J.F., Tavares, P., 2012. Development of regional future climate change scenarios in South America using the Eta CPTEC/HadCM3

climate change projections: climatology and regional analyses for the Amazon, São Francisco and the Paraná River basins. Clim. Dyn. 38, 1829–1848. https://doi.org/10.1007/s00382-011-1155-5

McManus, J.F., Francois, R., Gherardl, J.M., Kelgwin, L., Drown-Leger, S., 2004. Collapse and rapid resumption of Atlantic meridional circulation linked to deglacial climate changes. Nature 428, 834–837. https://doi.org/10.1038/nature02494

Mix, A.C., Bard, E., Schneider, R.R., 2001. Environmental processes of the ice age: Land, oceans, glaciers (EPILOG). Quat. Sci. Rev. 20, 627–657. https://doi.org/10.1016/S0277-3791(00)00145-1

Mollenhauer, G., Basse, A., Kim, J.H., Sinninghe Damsté, J.S., Fischer, G., 2015. A four-year record of $U^{K'}_{37}$- and TEX_{86}-derived sea surface temperature estimates from sinking particles in the filamentous upwelling region off Cape Blanc, Mauritania. Deep. Res. Part I Oceanogr. Res. Pap. 97, 67–79. https://doi.org/10.1016/j.dsr.2014.11.015

Mudge, S.M., Bebianno, M.J.A.F., East, J.A., Barreira, L.A., 1999. Sterols in the Ria Formosa lagoon, Portugal. Water Res. 33, 1038–1048. https://doi.org/10.1016/S0043-1354(98)00283-8

Muir, L.C., Fedorov, A. V., 2015. How the AMOC affects ocean temperatures on decadal to centennial timescales: the North Atlantic versus an interhemispheric seesaw. Clim. Dyn. 45, 151–160. https://doi.org/10.1007/s00382-014-2443-7

Pahnke, K., Sachs, J.P., 2006. Sea surface temperatures of southern midlatitudes 0 – 160 kyr B.P. Paleoceanography 21, 1–17. https://doi.org/10.1029/2005PA001191

PBMC, 2014. Contribuição do grupo de trabalho 1 do Painel Brasileiro de Mudanças Climáticas ao primeiro relatório da avaliação nacional sobre mudanças climáticas, in: Ambrizzi, T., Araujo, M. (Eds.), Base Científica Das Mudanças Climáticas. Painel Brasileiro de Mudanças Climáticas (PBMC), Rio de Janeiro, RJ, p. 348.

Pearson, E.J., Juggins, S., Talbot, H.M., Weckström, J., Rosén, P., Ryves, D.B., Roberts, S.J., Schmidt, R., 2011. A lacustrine GDGT-temperature calibration from the Scandinavian Arctic to Antarctic: Renewed potential for the application of GDGT-paleothermometry in lakes. Geochim.

Cosmochim. Acta 75, 6225–6238. https://doi.org/10.1016/j.gca.2011.07.042

Pereira, L.S., Arz, H.W., Pätzold, J., Portilho-Ramos, R.C., 2018. Productivity evolution in the South Brazilian Bight during the last 40,000 years. Paleoceanogr. Paleoclimatology 33, 1339–1356. https://doi.org/10.1029/2018PA003406

Peterson, R.G., Stramma, L., 1991. Upper-level circulation in the South-Atlantic Ocean. Prog. Oceanogr. 26, 1–73. https://doi.org/10.1016/0079-6611(91)90006-8

Piola, A.R., Matano, R.P., 2001. Brazil and Falklands (Malvinas) Currents, in: Steele, J.H., Thorpe, S.A., Turekian, K.K. (Eds.), Ocean Currents: A Derivative of the Encyclopedia of Ocean Sciences. Elsevier Inc., pp. 35–43. https://doi.org/10.1016/B978-0-12-409548-9.10541-X

Prahl, F.G., Wakeham, S.G., 1987. Calibration of unsaturation patterns in long-chain ketone compositions for palaeotemperature assessment. Nature 330, 367–369. https://doi.org/10.1038/330367a0

Rahmstorf, S., Box, J.E., Feulner, G., Mann, M.E., Robinson, A., Rutherford, S., Schaffernicht, E.J., 2015. Exceptional twentieth-century slowdown in Atlantic Ocean overturning circulation. Nat. Clim. Chang. 5, 475–480. https://doi.org/10.1038/nclimate2554

Railsback, L.B., Gibbard, P.L., Head, M.J., Voarintsoa, N.R.G., Toucanne, S., 2015. An optimized scheme of lettered marine isotope substages for the last 1.0 million years, and the climatostratigraphic nature of isotope stages and substages. Quat. Sci. Rev. 111, 94–106. https://doi.org/10.1016/j.quascirev.2015.01.012

Rampen, S.W., Willmott, V., Kim, J.H., Uliana, E., Mollenhauer, G., Schefuß, E., Sinninghe Damsté, J.S., Schouten, S., 2012. Long chain 1,13- and 1,15-diols as a potential proxy for palaeotemperature reconstruction. Geochim. Cosmochim. Acta 84, 204–216. https://doi.org/10.1016/j.gca.2012.01.024

Rhein, M., Rintoul, S.R., Aoki, S., Campos, E.J.D., Chambers, D., Feely, R.A., Gulev, S., Johnson, G.C., Josey, S.A., Kostianoy, A., Mauritzen, C., Roemmich, D., Talley, L.D., Wang, F., 2013. Observations: Ocean, in: Stocker, T.F., Qin, D., Plattner, G.-K., Tignor, M., Allen, S.K., Boschung, J., Nauels, A., Xia, Y., Bex, V., Midgley, P.M. (Eds.), Climate Change 2013:

The Physical Science Basis. Contribution of Working Group I to the Fifth Assessment Report of the Intergovernmental Panel on Climate Change. Cambridge University Press, Cambridge, United Kingdom and New York, NY, USA, pp. 255–315.

Ribeiro, M.C., Metzger, J.P., Martensen, A.C., Ponzoni, F.J., Hirota, M.M., 2009. The Brazilian Atlantic Forest: How much is left, and how is the remaining forest distributed? Implications for conservation. Biol. Conserv. 142, 1141–1153. https://doi.org/10.1016/j.biocon.2009.02.021

Rodrigues, R.R., Rothstein, L.M., Wimbush, M., 2007. Seasonal variability of the South Equatorial Current bifurcation in the Atlantic Ocean: a numerical study. J. Phys. Oceanogr. 37, 16–30. https://doi.org/10.1175/JPO2983.1

Santos, T.P., Lessa, D.V.O., Venancio, I.M., Chiessi, C.M., Mulitza, S., Kuhnert, H., Govin, A., Machado, T., Costa, K.B., Toledo, F.A.L., Dias, B.B., Albuquerque, A.L.S., 2017. Prolonged warming of the Brazil Current precedes deglaciations. Earth Planet. Sci. Lett. 463, 1–12. https://doi.org/10.1016/j.epsl.2017.01.014

Schmid, C., 2014. Mean vertical and horizontal structure of the subtropical circulation in the South Atlantic from three-dimensional observed velocity fields. Deep. Res. Part I Oceanogr. Res. Pap. 91, 50–71. https://doi.org/10.1016/j.dsr.2014.04.015

Schmid, C., Siedler, G., Zenk, W., 2000. Dynamics of Intermediate Water Circulation in the Subtropical South Atlantic. J. Phys. Oceanogr. 30, 3191–3211. https://doi.org/10.1175/1520-0485(2000)030<3191:DOIWCI>2.0.CO;2

Schmidt, M.W., Vautravers, M.J., Spero, H.J., 2006. Western Caribbean sea surface temperatures during the late Quaternary. Geochemistry, Geophys. Geosystems 7, 1–17. https://doi.org/10.1029/2005GC000957

Schneider, R.R., Müller, P.J., Ruhland, G., Meinecke, G., Schmidt, H., Wefer, G., 1996. Alkenones, sea surface temperature and $\delta^{18}O$ of *Globigerinoides ruber* of sediment core GeoB1105-4 (PANGAEA database). https://doi.org/doi.org/10.1594/PANGAEA.54864

Schouten, S., Hopmans, E.C., Schefuß, E., Sinninghe Damsté, J.S., 2002. Distributional variations in marine crenarchaeol membrane lipids: a new tool for reconstructing ancient sea water temperatures? Earth Planet. Sci.

Lett. 204, 265–274.

Schouten, S., Hopmans, E.C., Sinninghe Damsté, J.S., 2013. The organic geochemistry of glycerol dialkyl glycerol tetraether lipids: A review. Org. Geochem. 54, 19–61. https://doi.org/10.1016/j.orggeochem.2012.09.006

Shi, W., Sun, M.-Y., Molina, M., Hodson, R.E., 2001. Variability in the distribution of lipid biomarkers and their molecular isotopic composition in Altamaha estuarine sediments: implications for the relative contribution of organic matter from various sources. Org. Geochem. 32, 453–467. https://doi.org/10.1016/S0146-6380(00)00189-3

Silveira, I.C.A., Schmidt, A.C.K., Campos, E.J.D., Godoi, S.S., Ikeda, Y., 2000. A corrente do Brasil ao largo da costa leste brasileira. Rev. Bras. Oceanogr. 48, 171–183. https://doi.org/10.1590/S1413-77392000000200008

Sinninghe Damsté, J.S., Schouten, S., Hopmans, E.C., van Duin, A.C.T., Geenevasen, J.A.J., 2002. Crenarchaeol: the characteristic core glycerol dibiphytanyl glycerol tetraether membrane lipid of cosmopolitan pelagic crenarchaeota. J. Lipid Res. 43, 1641–1651. https://doi.org/10.1194/jlr.M200148-JLR200

Srokosz, M., Baringer, M., Bryden, H., Cunningham, S., Delworth, T., Lozier, S., Marotzke, J., Sutton, R., 2012. Past, present, and future changes in the Atlantic Meridional Overturning Circulation. Bull. Am. Meteorol. Soc. 93, 1663–1676. https://doi.org/10.1175/BAMS-D-11-00151.1

Stocker, T.F., Johnsen, S.J., 2003. A minimum thermodynamic model for the bipolar seesaw. Paleoceanography 18, 1–9. https://doi.org/10.1029/2003PA000920

Stramma, L., England, M., 1999. On the water masses and mean circulation of the South Atlantic Circulation. J. Geophys. Res. Ocean. 104, 20863–20883. https://doi.org/10.1029/1999JC900139

Thiagarajan, N., Subhas, A. V., Southon, J.R., Eiler, J.M., Adkins, J.F., 2014. Abrupt pre-Bølling–Allerød warming and circulation changes in the deep ocean. Nature 511, 75–78. https://doi.org/10.1038/nature13472

Tierney, J.E., Tingley, M.P., 2014. A Bayesian, spatially-varying calibration model for the TEX86 proxy. Geochim. Cosmochim. Acta 127, 83–106. https://doi.org/10.1016/j.gca.2013.11.026

Toledo, F.A.L., Costa, K.B., Pivel, M.A.G., Campos, E.J.D., 2008. Tracing past circulation changes in the western South Atlantic based on planktonic foraminifera. Rev. Bras. Paleontol. 11, 169–178. https://doi.org/10.4072/rbp.2008.3.03

Venancio, I.M., Mulitza, S., Govin, A., Santos, T.P., Lessa, D.V.O., Albuquerque, A.L.S., Chiessi, C.M., Tiedemann, R., Vahlenkamp, M., Bickert, T., Schulz, M., 2018. Millennial- to orbital-scale responses of western equatorial Atlantic thermocline depth to changes in the trade wind system since the Last Interglacial. Paleoceanogr. Paleoclimatology 33, 1490–1507. https://doi.org/10.1029/2018PA003437

Venkatesan, M.I., Kaplan, I.R., 1987. The lipid geochemistry of Antarctic marine sediments: Bransfield Strait. Mar. Chem. 21, 347–375.

Voelker, A.H.L., 2013. The stratigraphy and nomenclature of millennial-scale climate change. Ciencias da Terra 18 18, 111–116.

Volkman, J.K., 2006. Lipid markers for marine organic matter. Handb. Environ. Chem. 2, 27–70. https://doi.org/10.1007/698

Volkman, J.K., 2003. Sterols in microorganisms. Appl. Microbiol. Biotechnol. 60, 495–506. https://doi.org/10.1007/s00253-002-1172-8

Volkman, J.K., 1986. A review of sterol markers for marine and terrigenous organic matter. Org. Geochem. 9, 83–99. https://doi.org/10.1016/0146-6380(86)90089-6

Volkman, J.K., Barrett, S.M., Blackburn, S.I., Mansour, M.P., Sikes, E.L., Gelin, F., 1998. Microalgal biomarkers: A review of recent research developments. Org. Geochem. 29, 1163–1179. https://doi.org/10.1016/S0146-6380(98)00062-X

Volkman, J.K., Barrett, S.M., Dunstan, G.A., Jeffrey, S.W., 1992a. C_{30} - C_{32} alkyl diols and unsaturated alcohols in microalgae of the class Eustigmatophyceae. Org. Geochem. 18, 131–138. https://doi.org/10.1016/0146-6380(92)90150-V

Volkman, J.K., Eglinton, G., Corner, E.D.S., Forsberg, T.E. V., 1980. Long-chain alkenes and alkenones in the marine coccolithophorid *Emiliania huxleyi*. Phytochemistry 19, 2619–2622. https://doi.org/10.1016/S0031-9422(00)83930-8

Volkman, J.K., Farrington, J.W., Gagosian, R.B., 1987. Marine and terrigenous

lipids in coastal sediments from the Peru upwelling region at 15°S: Sterols and triterpene alcohols. Org. Geochem. 11, 463–477. https://doi.org/10.1016/0146-6380(87)90003-9

Volkman, J.K., Holdsworth, D.G., Neill, G.P., Bavor-Jr, H.J., 1992b. Identification of natural, anthropogenic and petroleum hydrocarbons in aquatic sediments. Sci. Total Environ. 112, 203–19.

Volkman, J.K., Revill, A.T., Holdsworth, D.G., Fredericks, D., 2008. Organic matter sources in an enclosed coastal inlet assessed using lipid biomarkers and stable isotopes. Org. Geochem. 39, 689–710. https://doi.org/10.1016/j.orggeochem.2008.02.014

WAIS Divide Project Members, 2015. Precise interpolar phasing of abrupt climate change during the last ice age. Nature 520, 661–665. https://doi.org/10.1038/nature14401

Wisnieski, E., Bícego, M.C., Montone, R.C., Figueira, R.C.L., Ceschim, L.M.M., Mahiques, M.M., Martins, C.C., 2014. Characterization of sources and temporal variation in the organic matter input indicated by n-alkanols and sterols in sediment cores from Admiralty Bay, King George Island, Antarctica. Polar Biol. 37, 483–496. https://doi.org/10.1007/s00300-014-1445-6

Zachos, J., Pagani, M., Sloan, L., Thomas, E., Billups, K., 2001. Trends, rhythms, and aberrations in global climate 65 Ma to present. Science 292, 686–693. https://doi.org/10.1126/science.1059412

Zhou, W., Zheng, Y., Meyers, P.A., Jull, A.J.T., Xie, S., 2010. Postglacial climate-change record in biomarker lipid compositions of the Hani peat sequence, Northeastern China. Earth Planet. Sci. Lett. 294, 37–46. https://doi.org/10.1016/j.epsl.2010.02.035

APÊNDICE 1 – MATERIAL SUPLEMENTAR "A" DO CAPÍTULO 2

Reconstrução das temperaturas de superfície e de subsuperfície do mar no Oceano Atlântico Sudoeste ao longo dos últimos 75 mil anos baseada em marcadores moleculares

"*Multi-proxy reconstruction of sea surface and subsurface temperatures in the western South Atlantic over the last ~ 75 kyr*"

* Ana Lúcia L. Dauner, * Gesine Mollenhauer, * Márcia Caruso Bícego, Mihael Machado de Souza, Renata Hanae Nagai, Rubens César Lopes Figueira, Michel Michaelovitch de Mahiques, Silvia Helena de Mello e Sousa, * César C. Martins

* Corresponding authors:
anadauner@gmail.com (A.L.L. Dauner)
gesine.mollenhauer@awi.de (G. Mollenhauer)
marciabicego@usp.br (M.C. Bícego)
ccmart@ufpr.br (C.C. Martins)

Table A-1. Ions used to identify GDGTs.

Compound	Group	m/z
C_{46}-GDGT		744
GDGT-0	isoprenoid	1302
GDGT-1	isoprenoid	1300
GDGT-2	isoprenoid	1298
GDGT-3	isoprenoid	1296
crenarchaeol	isoprenoid	1292
iso-crenarchaeol (cren')	isoprenoid	1292
GDGT-Ia	branched	1022
GDGT-Ib	branched	1020
GDGT-Ic	branched	1018
GDGT-IIa	branched	1036
GDGT-IIb	branched	1034
GDGT-IIc	branched	1032
GDGT-IIIa	branched	1050
GDGT-IIIb	branched	1048
GDGT-IIIc	branched	1046

Table A-2. Ion fragments used to identify diols.

Compound	m/z 1	m/z 2
androstanol	75	333
C_{28}-1,12	327	345
C_{28}-1,13	313	359
C_{28}-1,14	299	373
C_{30}-1,13	341	359
C_{30}-1,14	327	373
C_{30}-1,15	313	387
C_{32}-1,15	341	387
C_{32}-1,16	327	401
C_{32}-1,17	313	415

Table A-3. $U^{K'}_{37}$-based temperature (°C) estimates minus instrumental temperatures (°C) from the WOA13, based on Ceccopieri et al. (2018).

Station	Latitude	Longitude	Alkenone-based estimates minus annual mean SST-WOA13			
			Global [1]	SE Atlantic [2]	SE Atlantic [3]	SE Atlantic [4]
			annual mean	annual mean	annual mean	winter
			surface	surface	30 m	surface
A05	-23.6047	-41.3587	1.09	0.34	-0.40	-0.58
A06	-23.6327	-41.3284	1.70	0.94	0.17	0.01
A07	-23.6561	-41.3089	0.79	0.03	-0.68	-0.88
A08	-23.6867	-41.2693	1.70	0.94	0.17	0.01
A09	-23.7527	-41.1972	1.81	1.05	-1.27	0.17
A10	-23.8675	-41.0784	1.67	0.91	-1.27	0.13
G05	-22.1033	-40.0521	1.98	1.22	0.82	-0.01
G07	-22.1258	-39.9018	1.16	0.40	0.06	-0.69
G08	-22.1227	-39.8733	0.86	0.10	-0.22	-0.98
G09	-22.1231	-39.8164	1.16	0.40	0.06	-0.69
G10	-22.1232	-39.7408	1.30	0.54	-0.56	-0.47
H5	-21.7109	-40.1504	0.70	-0.06	-1.10	-1.28
H6	-21.7398	-40.0888	1.00	0.24	-0.82	-0.98
H7	-21.7402	-40.0398	1.00	0.24	-0.82	-0.98
H10	-21.6233	-39.5956	0.91	0.15	-0.31	-0.87
I05	-21.3848	-40.2534	1.79	1.03	2.06	-0.31
I06	-21.2278	-40.2499	1.95	1.19	1.08	-0.08
I07	-21.1872	-40.2149	1.71	0.95	-0.27	-0.21
I08	-21.1850	-40.1533	1.10	0.34	-0.84	-0.80
I09	-21.1858	-40.0522	1.10	0.34	-0.84	-0.80
I10	-21.1850	-39.6611	1.08	0.32	-1.45	-0.70
		Mean	1.31	0.55	-0.31	-0.52

Calibration equations based on Müller et al. (1998):

[1] Temp (°C) = ($U^{K'}_{37}$ – 0.044) / 0.033

[2] Temp (°C) = ($U^{K'}_{37}$ – 0.069) / 0.033

[3] Temp (°C) = ($U^{K'}_{37}$ – 0.068) / 0.035

[4] Temp (°C) = ($U^{K'}_{37}$ – 0.129) / 0.034

Table A-4. Pearson correlation (R) between the TEX_{86}-based and the LDI-based SST from NAP 63-1 and other Atlantic SST reconstructions, considering only the orbital trend (periodicity > 10 kyr). Underlined R values: *p*-value > 0.05.

		TEX_{86}		LDI	
Core	Location	*p*-value	R	*p*-value	R
NGRIP	Greenland	0.0000	0.94	0.0000	0.67
GeoB 9528	E Equator	0.0000	0.83	0.0000	0.60
GeoB 3104	W Equator	0.0000	-0.88	0.0000	-0.63
GeoB 1105	E Equator	0.0000	0.84	0.0000	0.36
GeoB 3910	W Equator	0.0000	0.90	0.0000	0.62
GL-74	W S Atlantic	0.0000	0.35	0.0000	0.67
GL-1090	W S Atlantic	0.0000	0.54	0.0000	0.69
NAP 63-1 – LDI-SST	W S Atlantic	0.0000	0.77	X	X
NAP 63-1 – TEX_{86}-SST	W S Atlantic	X	X	0.0000	0.77
NAP 63-1 – $U^{K'}_{37}$-subT	W S Atlantic	0.0000	0.79	0.0000	0.36
GeoB 1710-3	E S Atlantic	0.0000	0.91	0.0000	0.81
TN057	SE S Atlantic	0.0000	0.72	0.0000	0.85
JR 244-GC528	SW S Atlantic	0.0000	0.89	0.0000	0.94
EDML	Antarctica	0.0000	0.97	0.0000	0.73

Table A-5. Pearson correlation (R) between the TEX_{86}-based and the LDI-based SST from NAP 63-1 and other Atlantic SST reconstructions, considering only the millennial oscillations (periodicity < 10 kyr). Underlined R values: *p*-value > 0.05.

		TEX_{86}		LDI	
Core	Location	*p*-value	R	*p*-value	R
NGRIP	Greenland	0.3247	0.08	0.0037	0.22
GeoB 9528	E Equator	0.1063	0.13	0.4926	-0.05
GeoB 3104	W Equator	0.0060	-0.21	0.7154	-0.03
GeoB 1105	E Equator	0.000	0.32	0.0006	0.27
GeoB 3910	W Equator	0.0011	0.27	0.6177	0.04
GL-74	W S Atlantic	0.1060	-0.13	0.0031	-0.23
GL-1090	W S Atlantic	0.1858	-0.10	0.5493	0.05
NAP 63-1 – LDI-SST	W S Atlantic	0.0000	0.34	X	X
NAP 63-1 – TEX_{86}-SST	W S Atlantic	X	X	0.0000	0.34
NAP 63-1 – $U^{K'}_{37}$-subT	W S Atlantic	0.0017	0.24	0.0000	0.35
GeoB 1710-3	E S Atlantic	0.0048	0.22	0.0913	0.13
TN057	SE S Atlantic	0.0126	0.19	0.0038	0.22
JR 244-GC528	SW S Atlantic	0.0001	0.52	0.0082	0.37
EDML	Antarctica	0.5114	0.05	0.1529	0.11

APÊNDICE 2 – MATERIAL SUPLEMENTAR "B" DO CAPÍTULO 2

Reconstrução das temperaturas de superfície e de subsuperfície do mar no Oceano Atlântico Sudoeste ao longo dos últimos 75 mil anos baseada em marcadores moleculares

"*Multi-proxy reconstruction of sea surface and subsurface temperatures in the western South Atlantic over the last ~ 75 kyr*"

* Ana Lúcia L. Dauner, * Gesine Mollenhauer, * Márcia Caruso Bícego, Mihael Machado de Souza, Renata Hanae Nagai, Rubens César Lopes Figueira, Michel Michaelovitch de Mahiques, Silvia Helena de Mello e Sousa, * César C. Martins

* Corresponding authors:
anadauner@gmail.com (A.L.L. Dauner)
gesine.mollenhauer@awi.de (G. Mollenhauer)
marciabicego@usp.br (M.C. Bícego)
ccmart@ufpr.br (C.C. Martins)

Table B-1. $U^{K'}_{37}$, TEX_{86} and LDI indices, and temperature estimates for NAP 63-1 sediment core.

Age (kyr BP)	$U^{K'}_{37}$	$U^{K'}_{37}$-based temperatures (°C) [1]	TEX_{86}	TEX_{86}-based temperatures (°C) [2]	LDI	LDI-based temperatures (°C) [3]
1.518	0.84	21.9	0.64	25.3	n.a.	n.a.
2.448	0.84	22.2	0.64	25.2	0.94	25.5
3.369	0.85	22.2	0.64	25.5	0.93	25.3
4.283	0.83	21.8	0.64	25.2	0.94	25.5
5.240	0.78	20.5	0.65	25.8	0.93	25.4
6.269	0.82	21.4	0.67	26.5	0.93	25.3
7.441	0.80	20.9	0.67	26.8	0.93	25.3
8.160	0.79	20.7	0.67	26.6	n.a.	n.a.
8.901	0.75	19.3	0.69	27.4	0.93	25.4
9.764	0.74	19.3	0.65	25.8	n.a.	n.a.
10.630	0.75	19.5	0.65	26.0	0.91	24.7
11.426	0.74	19.1	0.64	25.3	0.89	24.2
12.506	0.72	18.6	0.62	24.3	0.87	23.6
13.490	0.74	19.2	0.62	24.6	n.a.	n.a.
14.538	0.78	20.5	0.62	24.2	0.90	24.3
15.715	0.73	18.8	0.61	24.1	0.87	23.6
16.832	0.72	18.5	0.57	21.7	0.87	23.5

17.751	0.69	17.7	0.58	22.2	0.86	23.2
18.702	0.71	18.4	0.59	23.1	0.87	23.5
19.595	0.70	18.0	0.60	23.5	n.a.	n.a.
20.549	0.72	18.6	0.59	23.0	0.88	23.7
21.534	0.71	18.4	0.58	22.6	0.88	23.9
22.241	0.71	18.5	0.59	22.9	0.86	23.2
22.951	0.64	16.5	0.58	22.5	n.a.	n.a.
24.346	0.72	18.6	0.57	21.7	0.84	22.7
26.389	0.74	19.2	0.58	22.5	0.86	23.2
28.422	0.75	19.6	0.60	23.3	0.82	21.9
29.266	0.75	19.4	0.59	23.1	0.85	22.8
30.025	0.75	19.4	0.60	23.2	0.83	22.2
30.823	0.74	19.1	0.59	23.0	0.82	22.1
31.715	0.75	19.6	0.59	22.9	0.80	21.3
32.552	0.72	18.7	0.59	23.0	0.81	21.8
33.321	0.74	19.3	0.62	24.2	0.81	21.7
34.184	0.76	19.6	0.58	22.5	0.83	22.2
34.963	0.75	19.6	0.60	23.4	0.82	22.0
35.816	0.74	19.3	0.60	23.2	n.a.	n.a.
36.677	0.75	19.5	0.63	24.9	0.85	22.8
37.259	0.74	19.2	0.60	23.3	0.84	22.5
37.935	0.73	19.0	0.59	23.1	0.83	22.2
38.547	0.72	18.5	0.60	23.2	0.83	22.3
39.014	0.70	18.2	0.59	23.1	0.80	21.5
39.454	0.72	18.6	0.57	21.9	0.82	22.1
39.975	0.73	18.8	0.58	22.2	0.81	21.8
40.479	0.71	18.5	0.58	22.7	0.85	22.8
40.948	0.72	18.7	0.58	22.3	n.a.	n.a.
41.452	0.74	19.2	0.62	24.3	0.85	22.8
41.944	0.74	19.1	0.59	23.1	0.86	23.1
42.446	0.71	18.3	0.64	25.2	0.83	22.3
42.982	0.74	19.1	0.60	23.7	0.84	22.4
43.421	0.73	18.9	0.59	22.7	0.81	21.8
43.819	0.74	19.1	0.54	20.1	0.79	21.0
44.257	0.74	19.1	0.60	23.3	n.a.	n.a.
44.674	0.74	19.3	0.59	22.8	0.82	21.9
45.054	0.74	19.2	0.59	22.8	0.83	22.2
45.462	0.77	19.9	0.59	23.1	0.85	22.8
45.909	0.76	19.8	0.62	24.3	0.83	22.2
46.318	0.75	19.5	0.61	24.0	n.a.	n.a.
46.774	0.76	19.7	0.60	23.4	0.83	22.4
47.221	0.76	19.8	0.59	22.9	0.84	22.5
47.653	0.77	19.9	0.60	23.4	0.83	22.2
48.114	0.75	19.5	0.59	23.2	0.82	22.1
48.539	0.75	19.4	0.61	23.8	0.79	21.1
48.989	0.74	19.2	0.62	24.5	0.82	21.9

49.449	0.74	19.1	0.58	22.7	n.a.	n.a.
49.866	0.76	19.7	0.62	24.6	0.84	22.4
50.348	0.76	19.9	0.59	22.7	0.84	22.7
50.815	0.76	19.7	0.62	24.3	0.86	23.1
51.395	0.77	20.0	0.62	24.5	0.87	23.6
51.962	0.78	20.3	0.59	23.1	0.89	24.1
52.505	0.77	20.2	0.61	24.0	0.88	23.9
53.042	0.74	19.3	0.61	23.9	n.a.	n.a.
53.574	0.75	19.6	0.62	24.4	0.89	24.1
54.228	0.79	20.7	0.62	24.6	0.91	24.7
54.868	0.77	20.1	0.62	24.6	0.88	23.7
55.517	0.76	19.7	0.61	24.1	0.88	23.8
56.217	0.75	19.5	0.62	24.5	0.90	24.4
56.902	0.77	20.1	0.63	24.8	0.89	24.0
57.527	0.73	19.1	0.60	23.2	n.a.	n.a.
58.147	0.70	17.9	0.60	23.6	0.87	23.5
58.752	0.74	19.1	0.60	23.4	0.88	23.8
59.327	0.76	19.7	0.61	23.8	0.89	24.0
59.853	0.75	19.4	0.61	23.8	0.88	23.9
60.396	0.69	17.8	0.61	23.7	0.88	23.8
60.918	0.77	19.9	0.62	24.6	0.89	24.0
61.474	0.73	19.0	0.61	24.0	0.88	23.7
62.051	0.74	19.3	0.60	23.3	0.85	23.0
62.574	0.74	19.2	0.59	23.0	n.a.	n.a.
63.129	0.73	18.8	0.59	22.8	0.87	23.5
63.697	0.75	19.6	0.61	24.0	0.87	23.3
64.252	0.75	19.5	0.59	22.7	0.88	23.8
64.830	0.75	19.5	0.57	21.8	0.87	23.5
65.374	0.72	18.5	0.62	24.3	0.86	23.1
65.906	0.72	18.7	0.60	23.7	0.86	23.2
66.430	0.70	18.0	0.59	23.1	0.85	22.7
67.007	0.70	18.1	0.57	22.0	n.a.	n.a.
67.580	0.71	18.3	0.62	24.2	0.86	23.2
68.139	0.70	18.0	0.57	21.7	0.87	23.4
68.833	0.70	18.1	0.57	22.0	0.86	23.2
69.568	0.73	18.9	0.57	21.8	0.87	23.4
70.238	0.74	19.2	0.61	23.9	0.85	22.9
70.882	0.77	20.0	0.59	22.7	0.87	23.5
71.521	0.75	19.4	0.61	23.7	0.85	23.0
72.234	0.76	19.7	0.59	22.7	n.a.	n.a.
72.934	0.76	19.8	0.61	23.8	0.85	22.9
73.575	0.78	20.2	0.60	23.6	0.88	23.6
74.259	0.76	19.6	0.58	22.6	0.85	22.8
74.936	0.77	19.9	0.59	22.9	0.86	23.3
75.603	0.74	19.3	0.59	22.7	0.85	22.8
76.269	0.77	20.1	0.54	20.4	0.87	23.5

76.936	0.74	19.1	0.59	22.8	0.85	23.0
77.603	0.77	20.0	0.57	22.1	n.a.	n.a.
78.269	0.76	19.7	0.60	23.3	0.86	23.1

Calibration equations:

[1] based on Müller et al. (1998): Temp (°C) = ($U^{K'}_{37}$ – 0.068) / 0.035

[2] based on Kim et al. (2010): Temp (°C) = (68.4 * TEX^{H}_{86}) + 38.6, where $TEX^{H}_{86} = \log_{10}TEX_{86}$

[3] based on Rampen et al. (2012): Temp (°C) = (LDI – 0.095) / 0.033

APÊNDICE 3 – MATERIAL SUPLEMENTAR DO CAPÍTULO 3

Impactos do aporte de material terrígeno e das mudanças oceanográficas durante o Pleistoceno Tardio e Holoceno na matéria orgânica sedimentar do oeste do Atlântico Sul

"*Impact of terrestrial material delivery and oceanographic changes during late Pleistocene and Holocene on the sedimentary organic matter from western South Atlantic*"

* Ana Lúcia L. Dauner, Gesine Mollenhauer, Márcia Caruso Bícego, Michel Michaelovitch de Mahiques, * César C. Martins

* Corresponding authors:
anadauner@gmail.com (A.L.L. Dauner)
ccmart@ufpr.br (C.C. Martins)

Appendix SM 1:

A crucial question in cluster analysis is establishing a suitable similarity/dissimilarity measure between two objects. In the specific context of time series data, the concept of dissimilarity is particularly complex due to the dynamic character of the series. Dissimilarities usually considered in conventional clustering could not work adequately with time dependent data because they ignore the interdependence relationship between values (Montero and Vilar, 2014). According to these authors, the first issue is to decide whether clustering must be governed by a "shape-based" or "structure-based" dissimilarity concept. Shape-based dissimilarities, such as the Euclidean distance, aim to compare the geometric profiles of the series and are mainly dominated by local comparisons. Thus, they work well with short time series, which does not present a high amount of noise. On the other hand, structure-based dissimilarity is aimed to compare underlying dependence structures, being more suitable for long time series. Among several "structure-based" dissimilarity indices available, the symbolization involves transformation of time series into sequences of discretized symbols that can be efficiently processed to extract information about the underlying processes. The symbolic representation SAX (symbolic aggregate approximation) allows a dimensionality/numerosity reduction and keep the distance

measures defined on the original time series (Lin et al., 2007). Therefore, the cluster analysis using SAX representation in the dissimilarity measure calculation was used to group the different proxies according to their evolutions through the time.

Firstly, each time-series was normalized to have a mean of zero and a standard deviation of one before converting it to the discrete representation (PAA - Piecewise Aggregate Approximation). During the discretization, it was used a technique that produced symbols (letters, in our example) with equiprobability. This was easily achieved since normalized time-series have a Gaussian distribution. Given that the normalized time-series have highly Gaussian distribution, it is possible to determine the "breakpoints" (*w* and *alpha*) that will produce equal-sized areas under Gaussian curve (Lin et al., 2007). During the conversion to the discrete representation, we have chosen not to use moving averages (95 samples; $w = 95$) and to use nine windows of equal-sized areas under the Gaussian curve ($alpha = 9$). After the discretization, each sample of the time-series received a letter (in our case, from "a" to "i"), and each value was converted to a value based on the lookup table from Lin et al. (2003). Once each time-series (A, B, C, …) was converted to a string of values ($a_{1\text{-}n}$, $b_{1\text{-}n}$, $c_{1\text{-}n}$, …), the distance matrix was calculated based on the formula:

$$Distance\,(A,B) = \sqrt{\sum_{i=1}^{n}(a_i - b_i)^2}$$

alpha	2	3	4	5	6	7	8	9
a	-0.43	-0.67	-0.84	-0.97	-1.07	-1.15	-1.22	-1.28
b	0.43	0	-0.25	-0.43	-0.57	-0.67	-0.76	-0.84
c		0.67	0.25	0	-0.18	-0.32	-0.43	-0.52
d			-0.84	0.43	0.18	0	-0.14	-0.25
e				0.97	0.57	0.32	0.14	0
f					1.07	0.67	0.43	0.25
g						1.15	0.76	0.52
h							1.22	0.84
i								1.28

Lookup table containing the breakpoints that divide a Gaussian distribution in an arbitrary number (from 2 to 9) of equiprobable regions (adapted from Lin et al., 2003).

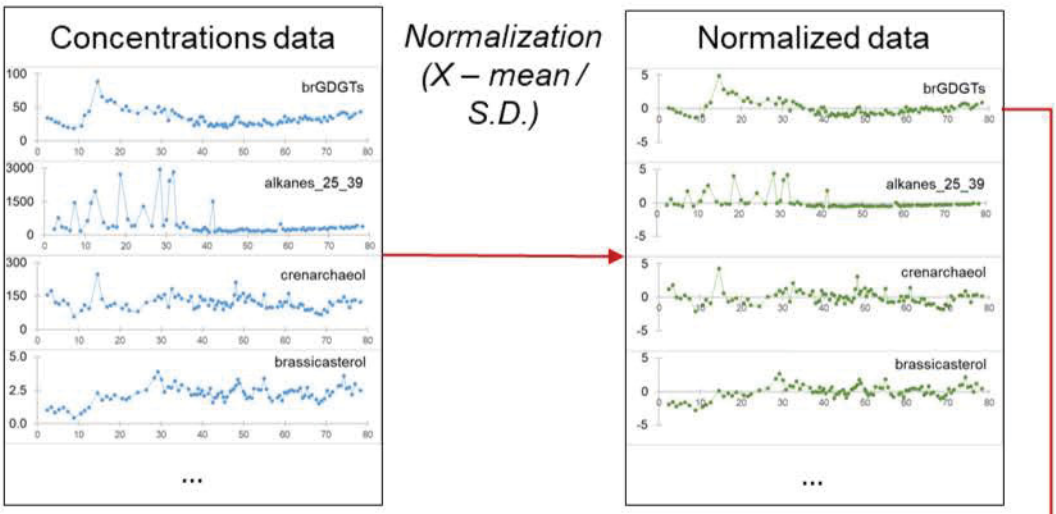

Discretization

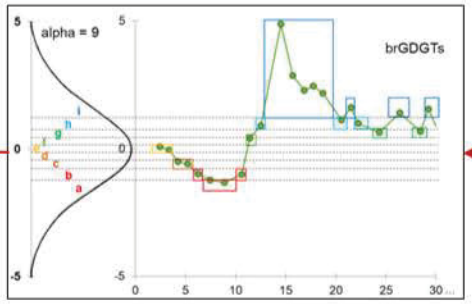

brGDGTs: e / e / c / c / b / a / a / b / f / h / i / i / i / i / i / h / i / h / g / i / g / i / ...

One discretized series by parameter

brGDGTs	e	e	c	c	b	a	a	b	...
alkanes_25_39	d	g	d	d	g	i	g	f	...
...									

Values obtained from the "Lookup" table

brGDGTs	0	0	-0.52	-0.52	-0.84	-1.28	-1.28	-0.84	...
alkanes_25_39	-0.25	0.52	-0.25	-0.25	0.52	1.28	0.52	0.25	...
...									

Distance matrix

	brGDGTs	alkanes_25_39	crenarchaeol	brassicasterol	...
brGDGTs					
alkanes_25_39					
crenarchaeol					
brassicasterol					
...					

Example of the discretization process based on the SAX representation (based on Lin et al., 2007).

References:

Lin, J., Keogh, E., Wei, L., Lonardi, S., 2007. Experiencing SAX: A novel symbolic representation of time series. Data Min. Knowl. Discov. 15, 107–144. https://doi.org/10.1007/s10618-007-0064-z

Lin, J., Keogh, E., Lonardi, S., Chiu, B., 2003. A symbolic representation of time series, with implications for streaming algorithms. In: Proceedings of the 8th ACM SIGMOD workshop on Research issues in data mining and knowledge discovery (pp. 2-11). ACM.

Montero, P., Vilar, J.A., 2014. TSclust: an R Package for time series clustering. J. Stat. Softw. 62, 1–43.

Tables:

Table SM 1. Ion fragments used to identify *n*-alkanols.

Compound	*m/z* 1 (Target Ion)	*m/z* 2	*m/z* 3
5α-androstanol	75	333	
n-C_{12}-OH	75	103	243
n-C_{14}-OH	75	103	271
n-C_{16}-OH	75	103	299
n-C_{18}-OH	75	103	327
phytol	75	103	143
n-C_{20}-OH	75	103	355
n-C_{22}-OH	75	103	383
n-C_{24}-OH	75	103	411
n-C_{26}-OH	75	103	439
n-C_{28}-OH	75	103	467
n-C_{30}-OH	75	103	495
n-C_{32}-OH	75	103	523
n-C_{34}-OH	75	103	551

Table SM 2. Ion fragments used to identify sterols.

Compound	Abbreviation	*m/z* 1 (Target Ion)	*m/z* 2	*m/z* 3
5α-androstanol		75	333	
dehydrocholesterol	$27\Delta^{5,22E}$	129	255	456
dehydrocholestanol	$27\Delta^{22E}$	215	257	458
cholesterol	$27\Delta^{5}$	129	329	458
cholestanol	$27\Delta^{0}$	215	355	460
brassicasterol	$28\Delta^{5,22E}$	129	255	470
brassicastanol	$28\Delta^{22E}$	215	257	472
campesterol	$28\Delta^{5}$	129	343	472
campestanol	$28\Delta^{0}$	215	369	474
stigmasterol	$29\Delta^{5,22E}$	129	255	484
stigmastanol	$29\Delta^{22E}$	215	257	486
sitosterol	$29\Delta^{5}$	129	357	486
sitostanol	$29\Delta^{0}$	215	383	488
dinosterol	$30\Delta^{22E}$	69	271	500

Table SM 3. Ion fragments used to identify diols.

Compound	*m/z* 1	*m/z* 2
5α-androstanol	75	333
C_{28}-1,14	299	373
C_{30}-1,14	327	373

Table SM 4. Molecular ions used to identify GDGTs.

Compound	Group	*m/z*
C_{46}-GDGT		744
crenarchaeol	isoprenoid	1292
GDGT-Ia	branched	1022
GDGT-IIa	branched	1036
GDGT-IIIa	branched	1050

Table SM 5. 5α(H)-stanol/Δ^5-stenol ratios calculated for core NAP 63-1.

Age [kyr BP]	[27Δ^{22E}] / [27$\Delta^{5,22E}$]	[27Δ^0] / [27Δ^5]	[28Δ^{22E}] / [28$\Delta^{5,22E}$]	[28Δ^0] / [28Δ^5]	[29Δ^{22E}] / [29$\Delta^{5,22E}$]	[29Δ^0] / [29Δ^5]
2.448	0.67	0.68	0.67	0.63	0.46	0.95
3.369	0.67	0.87	0.75	0.63	0.50	1.01
4.283	0.65	0.72	0.63	0.69	0.46	1.01
5.240	0.94	0.81	0.79	0.56	0.58	1.09
6.269	0.56	0.72	0.50	1.42	0.44	1.14
7.441	0.89	0.82	0.85	0.75	0.54	1.12
8.901	1.28	0.66	0.88	0.63	0.58	1.23
10.630	0.55	0.38	0.69	0.68	0.84	0.91
11.426	0.51	0.68	0.52	0.65	0.48	0.92
12.506	0.77	0.77	0.68	0.48	0.69	1.06
14.538	0.90	0.74	0.70	0.61	0.71	0.94
15.715	0.65	0.79	0.62	0.78	0.61	1.11
16.832	0.76	0.95	0.72	0.62	0.85	1.18
17.751	0.79	0.84	0.59	0.62	0.56	0.90
18.702	0.66	0.88	0.72	0.65	0.80	1.10
20.549	0.72	0.82	0.56	0.65	0.73	1.07
21.534	0.63	0.77	0.51	0.85	0.57	1.21
22.241	0.76	0.89	0.73	0.69	0.89	1.09
24.346	0.61	0.76	0.57	0.75	0.82	0.84
26.389	0.28	0.75	0.49	0.76	0.51	0.87
28.422	0.60	0.95	0.58	0.48	0.58	1.06
29.266	0.52	0.73	0.37	0.91	0.79	1.03
30.025	0.70	0.87	0.60	0.52	0.76	0.91
30.823	0.74	0.90	0.58	0.57	0.60	1.03
31.715	0.68	0.98	0.66	0.66	0.70	0.98
32.552	0.75	1.02	0.67	0.88	0.60	1.08
33.321	0.70	0.96	0.68	0.75	0.69	1.09
34.184	0.74	0.86	0.61	0.56	0.65	1.07
34.963	0.78	0.97	0.65	0.81	0.64	1.16
36.677	0.66	0.83	0.54	0.62	0.64	0.92

37.259	0.52	0.67	0.45	0.67	0.54	0.98
37.935	0.57	0.80	0.60	0.62	0.73	0.83
38.547	0.58	0.94	0.55	0.38	0.65	1.00
39.014	0.75	0.97	0.65	0.56	0.95	1.10
39.454	0.74	1.09	0.83	0.62	0.72	1.19
39.975	0.80	1.17	0.96	0.75	0.86	1.25
40.479	0.86	1.25	0.82	0.69	0.77	1.06
41.452	0.79	0.93	0.68	0.72	0.80	1.02
41.944	0.74	0.93	0.59	0.68	0.67	1.01
42.446	0.64	1.12	0.75	0.40	0.39	0.41
42.982	0.68	0.91	0.62	0.63	0.84	1.13
43.421	0.86	1.01	0.68	0.75	0.63	1.06
43.819	0.89	1.18	0.82	0.65	0.79	1.06
44.674	0.83	1.18	0.89	0.74	0.75	1.20
45.054	1.03	1.23	0.85	0.65	0.76	1.30
45.462	0.82	1.29	0.95	0.75	0.82	1.40
45.909	0.69	1.26	0.89	0.52	0.91	1.43
46.774	0.61	1.01	0.68	0.66	0.71	1.05
47.221	0.57	0.90	0.59	0.70	0.63	0.99
47.653	0.64	0.87	0.61	0.64	0.64	1.04
48.114	0.58	0.90	0.57	0.61	0.65	1.00
48.539	0.66	0.94	0.62	0.64	0.73	1.10
48.989	0.76	1.03	0.61	0.65	0.65	0.99
49.866	0.60	0.96	0.58	0.58	0.61	0.98
50.348	0.64	0.85	0.61	0.66	0.77	0.91
50.815	0.53	0.88	0.60	0.56	0.57	0.99
51.395	0.45	0.81	0.57	0.63	0.57	0.91
51.962	1.75	0.94	0.60	0.52	0.62	1.04
52.505	0.66	0.92	0.70	0.67	0.70	1.11
53.574	0.69	1.00	0.70	0.59	0.70	1.18
54.228	0.60	1.09	0.67	0.29	0.66	1.02
54.868	0.70	1.02	0.70	0.63	0.70	1.03
55.517	0.47	0.89	0.62	0.64	0.71	1.03
56.217	0.57	0.92	0.55	0.40	0.60	0.98
56.902	0.50	0.95	0.59	0.65	0.62	0.98
58.147	0.64	0.93	0.69	0.75	0.92	1.00
58.752	0.77	0.97	0.65	0.59	0.71	1.10
59.327	0.61	1.03	0.68	0.70	0.70	1.17
59.853	0.73	0.97	0.73	0.64	0.77	1.12
60.396	0.58	0.94	0.70	0.65	0.74	1.16
60.918	0.59	1.08	0.62	0.70	0.70	1.05
61.474	0.53	0.99	0.59	0.56	0.66	1.04
62.051	0.59	0.95	0.61	0.65	0.72	1.05
63.129	0.68	0.94	0.64	0.59	0.70	1.06
63.697	0.71	1.05	0.66	0.59	0.76	1.11
64.252	0.63	0.95	0.66	0.55	0.73	1.08

64.830	0.58	0.94	0.54	0.57	0.68	0.91
65.374	0.78	0.89	0.61	0.60	0.65	1.19
65.906	0.89	0.97	0.57	0.63	0.68	1.07
66.430	0.79	0.95	0.61	0.59	0.74	0.89
67.580	0.77	0.91	0.60	0.61	0.66	1.00
68.139	0.96	0.87	0.59	0.57	0.61	0.97
68.833	0.70	0.90	0.69	0.62	0.72	1.03
69.568	0.65	0.90	0.59	0.57	0.61	0.94
70.238	0.73	0.92	0.62	0.60	0.67	0.92
70.882	0.72	1.05	0.65	0.40	0.67	1.21
71.521	0.76	1.01	0.68	0.65	0.81	1.01
72.934	0.80	0.99	0.66	0.67	0.73	1.10
73.575	0.63	0.99	0.57	0.56	0.66	0.89
74.259	0.71	1.06	0.64	0.73	0.89	0.96
74.936	0.75	1.05	0.65	0.67	0.71	1.12
75.603	0.70	0.91	0.68	0.67	0.67	1.14
76.269	0.73	1.04	0.65	0.62	0.70	1.01
76.936	0.68	1.15	0.75	0.56	0.79	1.08
78.269	0.76	1.01	0.70	0.62	0.66	1.18

Figures:

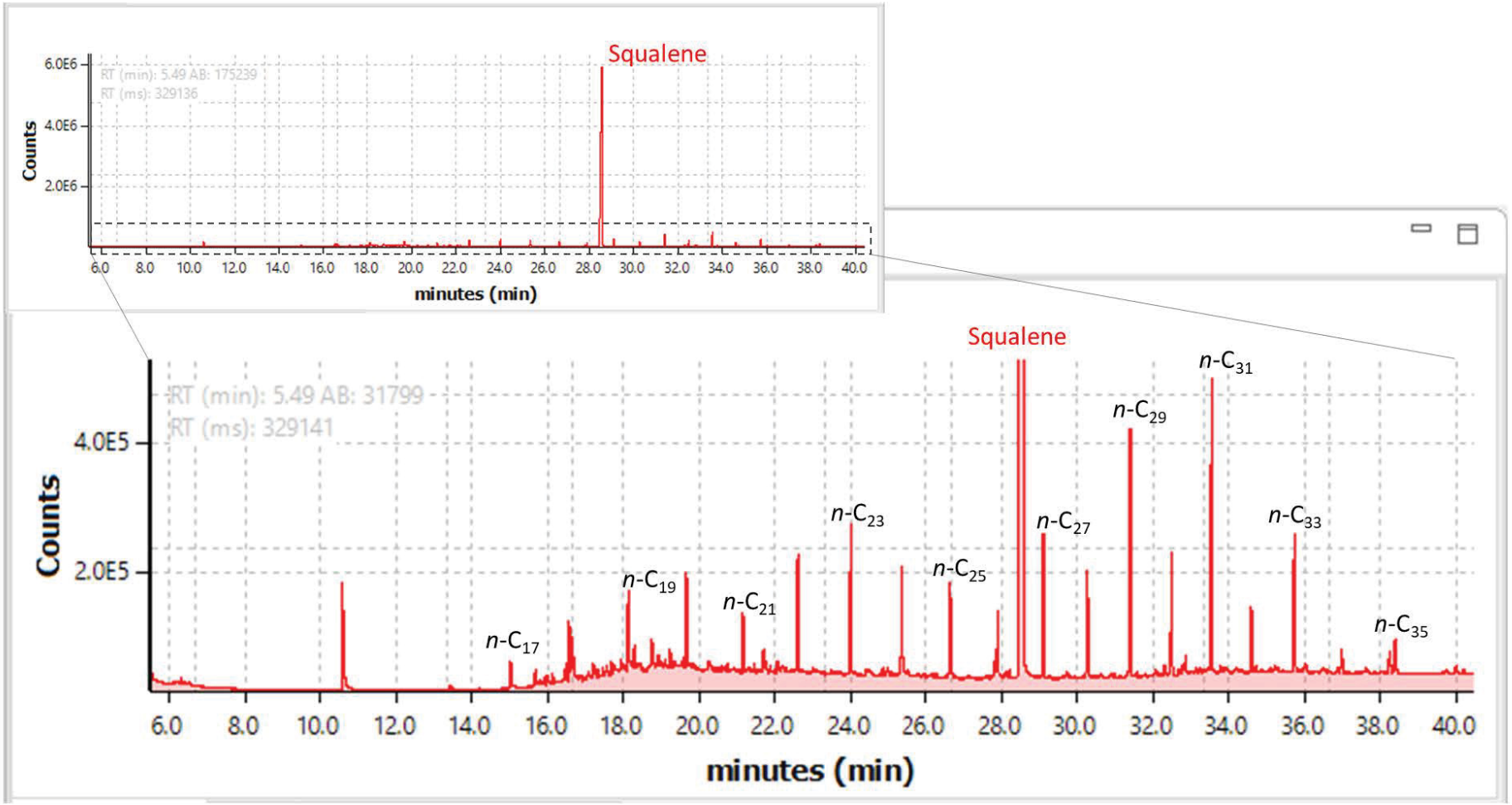

Fig. SM 1. Example of chromatogram (sample "34-36 cm") of the first apolar fraction (recovered with *n*-hexane), containing the *n*-alkanes.

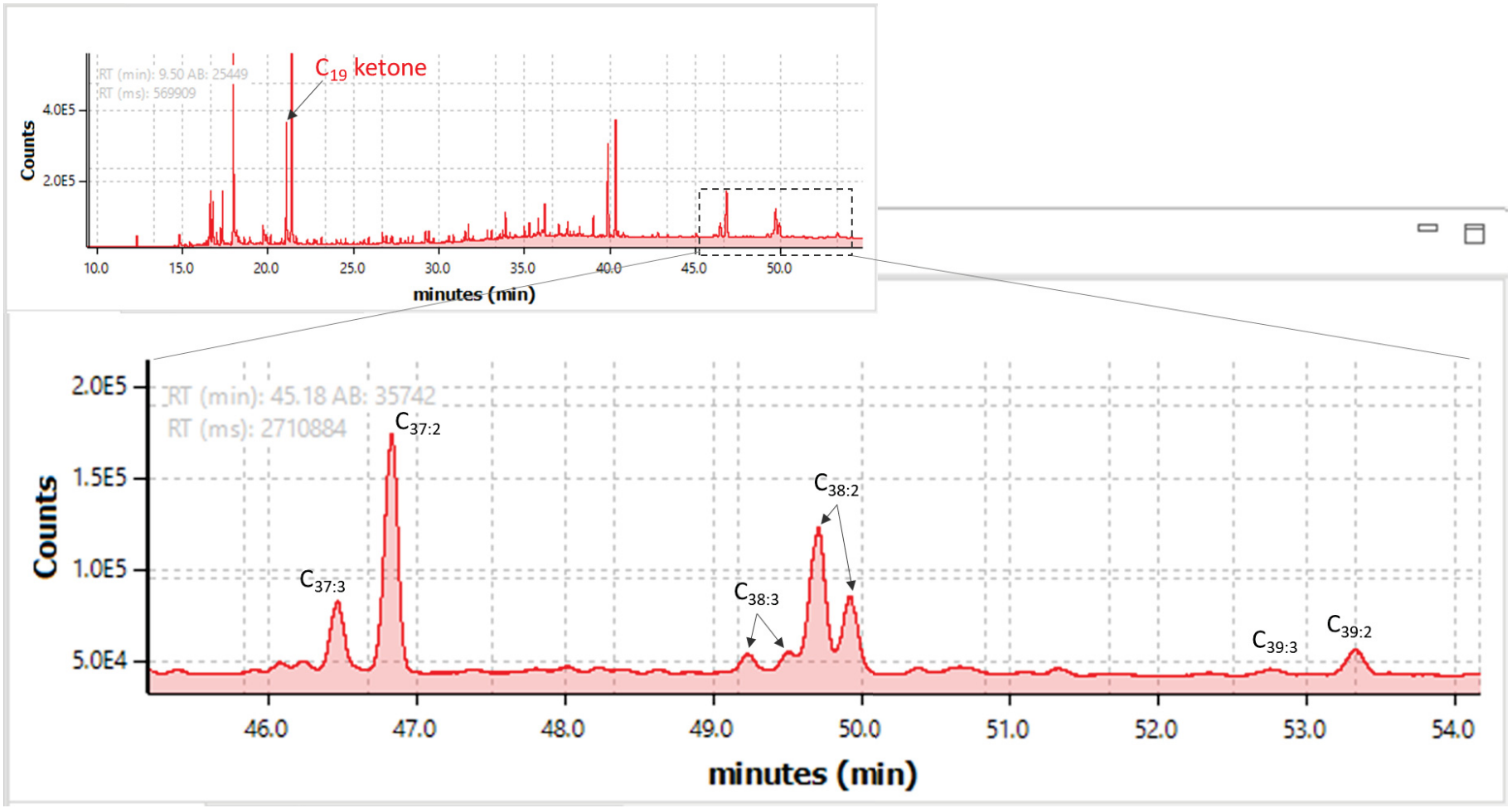

Fig. SM 2. Example of chromatogram (sample "34-36 cm") of the second apolar fraction (recovered with *n*-hexane:DCM (1:2 v:v)), containing the long-chain alkenones.

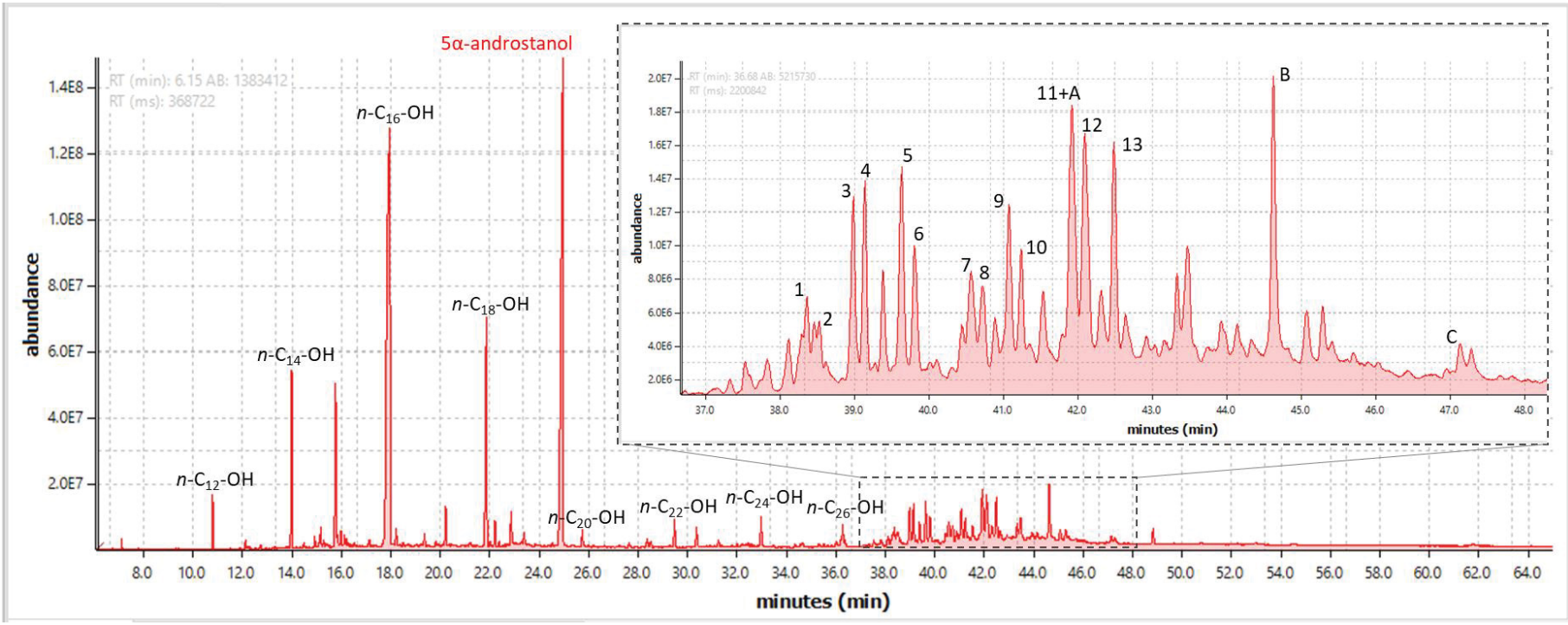

Fig. SM 3. Example of chromatogram (sample "34-36 cm") of the polar fraction (recovered with DCM:MeOH (1:1; v:v) and analysed via GC-MS), containing the *n*-alkanols, the steroids and the long-chain diols.
Identification of compounds: 1 = $27\Delta^{5,22E}$; 2 = $27\Delta^{22E}$; 3 = $27\Delta^{5}$; 4 = $27\Delta^{0}$; 5 = $28\Delta^{5,22E}$; 6 = $28\Delta^{22E}$; 7 = $28\Delta^{5}$; 8 = $28\Delta^{0}$; 9 = $29\Delta^{5,22E}$; 10 = $29\Delta^{22E}$; 11 = $29\Delta^{5}$; 12 = $29\Delta^{0}$; 13 = $30\Delta^{22E}$; A = C_{28}-diols; B = C_{30}-diols; C = C_{32}-diols.

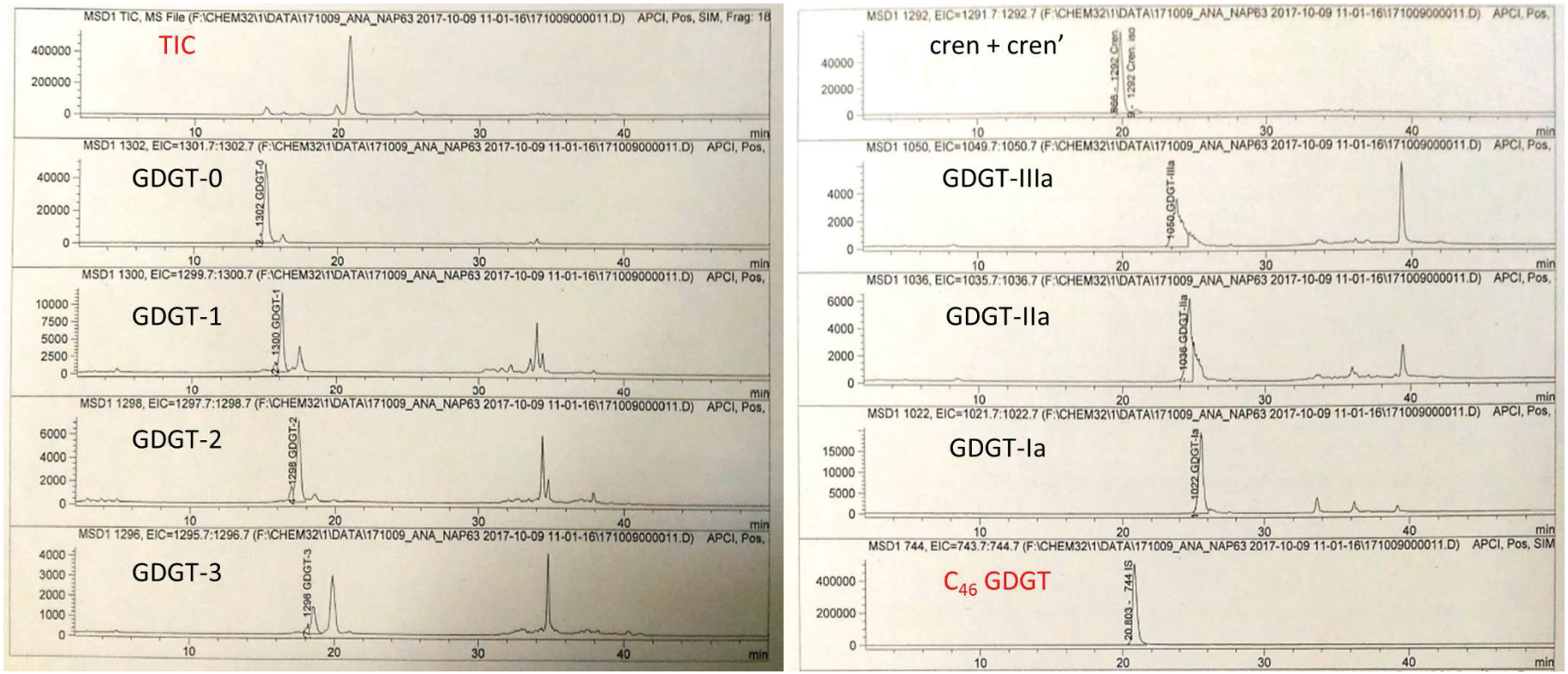

Fig. SM 4. Example of chromatogram (sample "34-36 cm") of the polar fraction (recovered with DCM:MeOH (1:1; v:v) and analysed via HPLC-MS), containing the GDGTs.

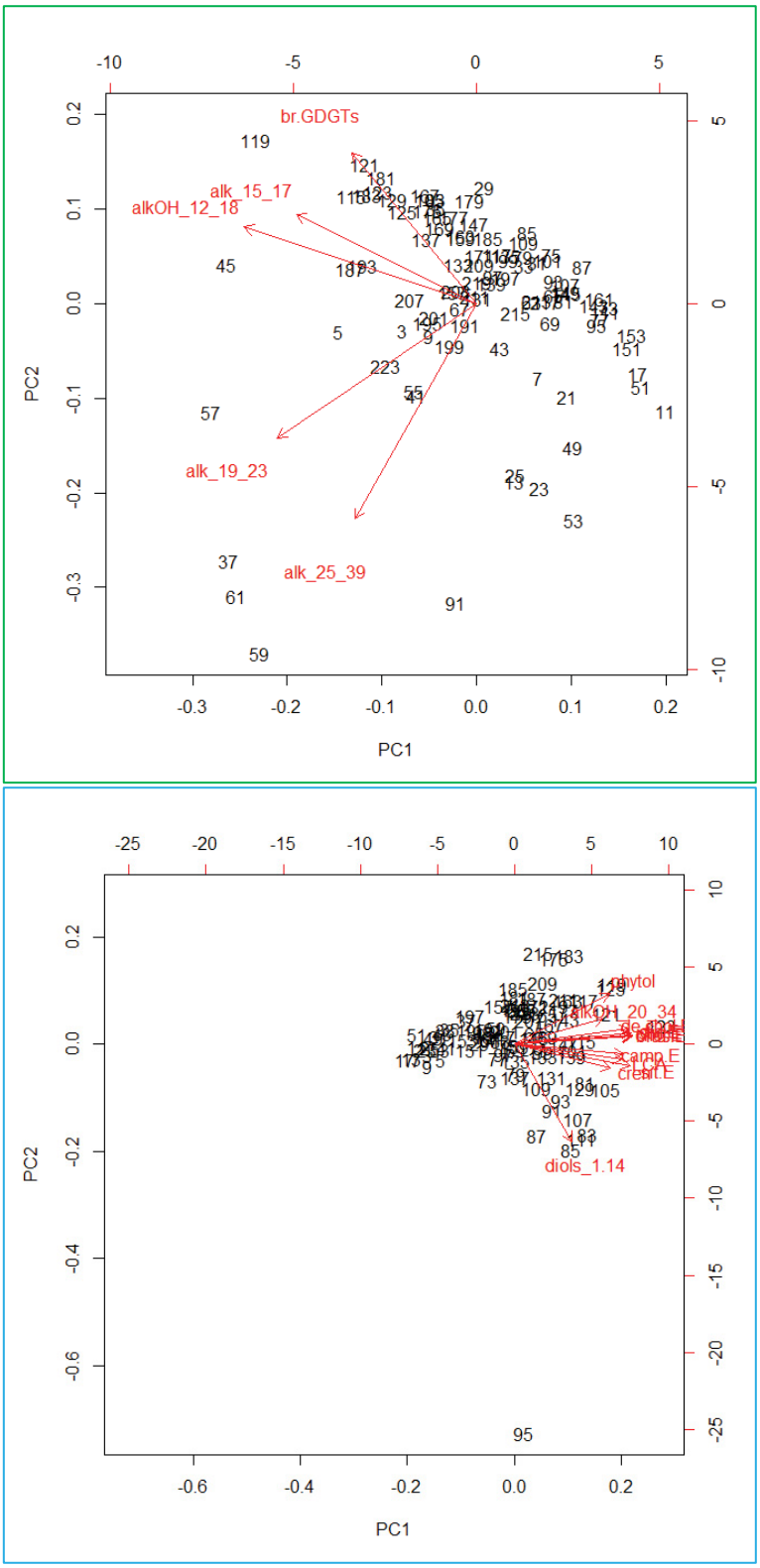

Fig. SM 5. Principal Component Analysis performed to select the organic proxy that best illustrates the organic matter (terrestrial = top; marine = bottom) variability.

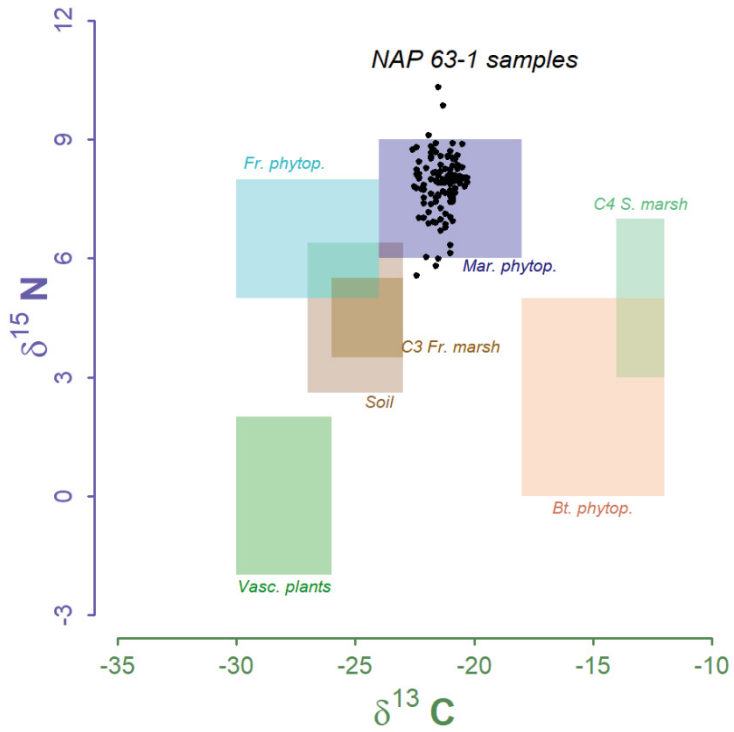

Fig. SM 6. Scatter plots of $\delta^{13}C$ versus $\delta^{15}N$, considering the ranges stablished by Bianchi and Canuel (2011) and the NAP 63-1 samples.

APÊNDICE 4 – DADOS BRUTOS DO CAPÍTULO 3

Impactos do aporte de material terrígeno e das mudanças oceanográficas durante o Pleistoceno Tardio e Holoceno na matéria orgânica sedimentar do oeste do Atlântico Sul

"*Impact of terrestrial material delivery and oceanographic changes during late Pleistocene and Holocene on the sedimentary organic matter from western South Atlantic*"

* Ana Lúcia L. Dauner, Gesine Mollenhauer, Márcia Caruso Bícego, Michel Michaelovitch de Mahiques, * César C. Martins

* Corresponding authors:
anadauner@gmail.com (A.L.L. Dauner)
ccmart@ufpr.br (C.C. Martins)

Table D 1. Dataset of bulk parameters, sedimentation rates (cm kyr^{-1}) and accumulation rates (ng cm^{-2} kyr^{-1}) of the apolar organic geochemical markers for core NAP 63-1: percentage of Total Organic Carbon (% TOC), percentage of Total Nitrogen (%TN), TOC/TN ratio, carbon isotope composition ($\delta^{13}C$), nitrogen isotope composition ($\delta^{15}N$) values, odd-numbered *n*-alkanes *n*-C_{15} to *n*-C_{17}, odd-numbered *n*-alkanes *n*-C_{19} to *n*-C_{23}, odd-numbered *n*-alkanes *n*-C_{25} to *n*-C_{39}, and long-chain alkenones (LCA).

Age [kyr BP]	Sedimentation rates	TOC [%]	TN [%]	TOC/TN	$\delta^{13}C$ [‰]	$\delta^{15}N$ [‰]	*n*-alkanes (*n*-C_{15} - *n*-C_{17})	*n*-alkanes (*n*-C_{19} - *n*-C_{23})	*n*-alkanes (*n*-C_{25} - *n*-C_{39})	LCA
1.518	---	0.692	0.068	10.15	-20.76	7.77	103	287	2180	421
2.448	2.151	0.540	0.097	5.59	-20.83	7.64	140	573	551	451
3.369	2.172	0.599	0.078	7.66	-20.80	8.01	242	489	1557	488
4.283	2.188	0.465	0.084	5.51	-21.16	8.25	35	339	742	341
5.240	2.090	0.423	0.099	4.28	-20.80	8.49	147	458	620	378
6.269	1.944	0.381	0.071	5.34	-21.30	7.68	17	229	367	280

7.441	1.706	0.377	0.063	5.99	-21.24	7.65	97	309	2289	255
8.160	2.782	0.350	0.066	5.32	-21.13	8.58	102	431	3513	357
8.901	2.699	0.219	0.052	4.25	-21.92	9.10	26	160	429	290
9.764	2.317	0.172	0.047	3.67	-22.40	7.78	63	87	379	259
10.630	2.309	0.175	0.044	4.01	-21.53	10.33	69	180	1348	272
11.426	2.513	0.316	0.050	6.31	-21.34	9.86	26	244	3343	331
12.506	1.852	0.390	0.061	6.42	-21.35	8.58	71	202	3340	339
13.490	2.033	0.399	0.071	5.61	-21.66	8.74	79	152	627	368
14.538	1.908	0.411	0.066	6.22	-21.32	7.99	18	106	1007	976
15.715	1.699	0.465	0.069	6.72	-21.49	7.61	11	165	516	468
16.832	1.791	0.418	0.076	5.47	-21.08	7.99	87	182	657	448
17.751	2.176	0.445	0.079	5.67	-20.96	8.13	31	204	720	460
18.702	2.103	0.435	0.077	5.66	-21.61	7.43	133	796	5306	546
19.595	2.240	0.427	0.074	5.75	-21.24	6.86	75	630	837	517
20.549	2.096	0.427	0.071	5.99	-20.83	7.76	78	662	1366	517
21.534	2.030	0.417	0.069	6.06	-20.83	7.96	20	475	776	401
22.241	2.829	0.449	0.055	8.14	-21.29	7.92	211	780	1138	714
22.951	2.817	0.495	0.082	6.06	-20.27	7.92	176	1178	2065	966
24.346	1.434	0.522	0.086	6.05	-20.99	8.70	49	295	1693	398
26.389	0.979	0.523	0.082	6.35	-20.72	8.61	7	202	368	396
28.422	0.984	0.530	0.081	6.58	-20.86	8.90	39	240	2674	420
29.266	2.370	0.521	0.083	6.26	-20.57	8.07	13	823	956	1161
30.025	2.635	0.563	0.085	6.60	-20.66	8.35	152	1156	1653	1305
30.823	2.506	0.582	0.091	6.42	-20.77	8.10	51	952	5612	1062
31.715	2.242	0.611	0.091	6.75	-20.46	8.30	222	601	5834	897
32.552	2.389	0.654	0.090	7.25	-20.59	7.90	46	211	991	985
33.321	2.601	0.810	0.074	10.98	-20.49	8.89	44	171	842	1258
34.184	2.317	0.633	0.088	7.20	-20.31	8.04	110	281	1151	1068

34.963	2.567	0.608	0.088	6.92	-20.86	8.52	69	214	862	1107
35.816	2.345	0.522	0.075	6.95	-20.39	8.03	60	70	482	753
36.677	2.323	0.467	0.074	6.30	-21.10	8.56	80	63	508	839
37.259	3.436	0.433	0.077	5.62	-20.88	8.34	88	93	705	1092
37.935	2.959	0.518	0.072	7.18	-20.69	8.26	29	75	556	956
38.547	3.268	0.557	0.086	6.44	-20.90	7.99	40	99	523	1196
39.014	4.283	0.658	0.089	7.40	-20.99	6.33	32	100	1070	1775
39.454	4.545	0.618	0.091	6.79	-20.93	6.95	98	154	1408	1797
39.975	3.839	0.581	0.086	6.79	-20.98	8.24	67	106	907	1411
40.479	3.968	0.455	0.071	6.44	-20.62	7.93	19	107	537	1284
40.948	4.264	0.461	0.070	6.59	-20.87	7.56	27	107	564	1228
41.452	3.968	0.469	0.068	6.93	-20.95	7.56	63	280	5516	1122
41.944	4.065	0.550	0.072	7.65	-20.87	7.49	45	157	626	1300
42.446	3.984	0.479	0.067	7.18	-20.86	7.52	32	166	679	1313
42.982	3.731	0.424	0.068	6.22	-20.62	7.99	138	120	946	1232
43.421	4.556	0.541	0.074	7.31	-21.16	7.91	85	153	951	1751
43.819	5.025	0.563	0.080	7.01	-20.41	7.82	70	106	891	1843
44.257	4.566	0.486	0.076	6.36	-21.36	7.26	150	156	747	1346
44.674	4.796	0.519	0.061	8.56	-21.14	8.08	145	133	888	1787
45.054	5.263	0.493	0.065	7.59	-21.22	6.77	11	120	821	1572
45.462	4.902	0.466	0.065	7.16	-21.61	8.90	114	171	705	1438
45.909	4.474	0.442	0.069	6.45	-21.36	8.19	17	87	675	1457
46.318	4.890	0.462	0.068	6.75	-21.63	8.17	154	213	786	1652
46.774	4.386	0.521	0.071	7.35	-20.99	7.43	121	234	721	1581
47.221	4.474	0.538	0.072	7.51	-21.03	7.71	144	178	872	1721
47.653	4.630	0.524	0.072	7.28	-21.15	7.12	228	328	974	2018
48.114	4.338	0.585	0.063	9.27	-20.94	7.42	153	246	980	2083
48.539	4.706	0.539	0.078	6.93	-20.90	8.53	114	330	1213	2682

48.989	4.444	0.593	0.084	7.04	-21.02	7.88	204	266	954	2063
49.449	4.348	0.508	0.072	7.05	-21.04	7.05	475	746	16263	1659
49.866	4.796	0.524	0.077	6.85	-21.37	8.35	285	224	1167	1781
50.348	4.149	0.533	0.072	7.41	-21.83	8.66	31	312	751	1285
50.815	4.283	0.475	0.072	6.62	-21.45	7.91	159	271	702	1263
51.395	3.448	0.440	0.074	5.95	-21.80	8.00	180	178	597	1047
51.962	3.527	0.477	0.055	8.74	-22.12	7.85	191	256	629	918
52.505	3.683	0.506	0.065	7.84	-21.58	6.89	86	236	681	1019
53.042	3.724	0.478	0.073	6.59	-22.07	7.38	68	193	859	1146
53.574	3.759	0.474	0.069	6.87	-21.36	6.98	44	136	597	887
54.228	3.058	0.506	0.062	8.22	-21.77	7.63	118	107	497	753
54.868	3.125	0.491	0.072	6.85	-21.55	8.08	173	121	654	939
55.517	3.082	0.388	0.069	5.62	-21.44	7.91	42	105	570	685
56.217	2.857	0.402	0.054	7.44	-21.51	7.56	51	177	498	567
56.902	2.920	0.489	0.065	7.55	-21.90	7.17	58	101	508	555
57.527	3.200	0.412	0.069	5.94	-21.03	6.12	332	107	569	669
58.147	3.226	0.472	0.073	6.42	-21.75	8.66	206	156	1500	696
58.752	3.306	0.431	0.071	6.09	-21.92	7.16	176	161	822	782
59.327	3.478	0.453	0.058	7.83	-21.58	7.53	54	107	633	746
59.853	3.802	0.449	0.087	5.16	-21.58	7.95	62	253	890	1093
60.396	3.683	0.474	0.091	5.23	-21.77	8.57	140	164	755	840
60.918	3.831	0.438	0.084	5.21	-21.63	8.69	227	183	955	1030
61.474	3.597	0.452	0.088	5.16	-21.68	6.91	211	215	841	884
62.051	3.466	0.479	0.088	5.46	-21.81	7.37	77	197	836	880
62.574	3.824	0.470	0.089	5.31	-21.48	5.98	115	162	1162	1008
63.129	3.604	0.481	0.089	5.42	-22.39	8.81	201	133	859	918
63.697	3.521	0.486	0.090	5.39	-21.80	8.83	150	132	1041	1257
64.252	3.604	0.469	0.089	5.28	-21.79	8.51	187	120	711	783

64.830	3.460	0.478	0.093	5.17	-21.73	8.15	172	195	863	872
65.374	3.676	0.499	0.087	5.77	-21.94	6.87	115	200	979	1021
65.906	3.759	0.486	0.086	5.64	-21.44	6.69	78	171	894	849
66.430	3.817	0.492	0.088	5.57	-22.10	7.02	165	521	1048	963
67.007	3.466	0.472	0.084	5.64	-22.43	5.57	113	539	1188	1022
67.580	3.490	0.484	0.088	5.50	-21.96	8.27	96	482	917	857
68.139	3.578	0.417	0.087	4.77	-22.20	7.75	126	504	899	651
68.833	2.882	0.415	0.081	5.13	-22.41	8.24	139	452	863	533
69.568	2.721	0.445	0.085	5.25	-21.76	8.57	112	232	648	644
70.238	2.985	0.474	0.086	5.54	-21.61	5.81	71	482	924	899
70.882	3.106	0.496	0.088	5.65	-22.43	8.12	118	521	950	1019
71.521	3.130	0.480	0.088	5.46	-21.15	7.95	118	346	919	1014
72.234	2.805	0.460	0.088	5.21	-22.60	8.75	147	372	937	1087
72.934	2.857	0.509	0.090	5.68	-22.32	8.43	142	496	981	1065
73.575	3.120	0.535	0.090	5.91	-22.29	8.04	102	321	856	1036
74.259	2.924	0.544	0.091	6.01	-22.14	7.53	33	361	965	1228
74.936	2.954	0.493	0.090	5.47	-22.00	6.03	61	285	843	1038
75.603	3.000	0.516	0.092	5.63	-22.47	7.82	41	252	979	1142
76.269	3.000	0.476	0.085	5.57	-22.35	8.13	86	199	1005	889
76.936	3.000	0.461	0.089	5.19	-22.30	7.02	100	267	1201	989
77.603	3.000	0.488	0.089	5.51	-22.06	7.72	151	289	947	935
78.269	3.000	0.454	0.088	5.18	-22.29	8.02	32	804	1062	930

Table D 2. Dataset of the accumulation rates (ng cm^{-2} kyr^{-1}) of the polar organic geochemical markers for core NAP 63-1: crenarchaeol, branched GDGTs (brGDGTs), even-numbered *n*-alkanols *n*-C_{12}-OH to *n*-C_{18}-OH, even-numbered *n*-alkanols *n*-C_{20}-OH to *n*-C_{34}-OH, phytol, dehydrocholesterol ($27\Delta^{5,22E}$), cholesterol ($27\Delta^{5}$), brassicasterol ($28\Delta^{5,22E}$), campesterol ($28\Delta^{5}$), stigmasterol ($29\Delta^{5,22E}$), sitosterol ($29\Delta^{5}$), dinosterol ($30\Delta^{22E}$), and long-chain diols (C_{28}1,14 + C_{30}1,14).

Age [kyr BP]	cren	brGDGTs	*n*-alkanols (*n*-C_{12}-OH-*n*-C_{18}-OH)	*n*-alkanols (*n*-C_{20}-OH-*n*-C_{34}-OH)	phytol	$27\Delta^{5,22E}$	$27\Delta^{5}$	$28\Delta^{5,22E}$	$28\Delta^{5}$	$29\Delta^{5,22E}$	$29\Delta^{5}$	$30\Delta^{22}$	long-chain diols
2.448	306.9	68.2	97.7	6.1	1.04	1.02	2.87	1.99	1.45	1.53	2.56	2.24	0.036
3.369	346.7	65.8	104.7	8.4	1.15	1.45	2.99	2.50	2.06	2.01	3.35	2.62	0.053
4.283	242.6	56.4	71.1	4.6	0.73	0.83	2.29	1.69	1.23	1.25	2.09	1.60	0.037
5.240	218.9	51.8	100.5	11.2	1.02	0.85	2.74	2.00	1.94	1.55	2.70	2.11	0.098
6.269	232.2	40.2	15.8	6.0	0.93	0.94	2.15	2.15	0.97	1.42	1.99	1.65	0.025
7.441	179.6	31.2	63.9	6.2	0.58	0.61	2.13	1.43	1.25	1.20	2.20	1.65	0.044
8.901	145.5	46.5	35.8	5.8	0.30	0.37	2.18	1.13	0.88	0.96	1.73	1.27	0.034
10.630	180.6	47.3	54.9	9.7	0.73	0.83	5.17	1.61	1.13	1.09	2.35	1.75	0.055
11.426	252.8	88.3	26.3	7.0	1.05	0.99	3.05	2.23	1.51	1.44	2.70	2.07	0.038
12.506	158.5	74.7	41.5	17.1	1.01	0.91	2.71	2.06	2.26	1.56	3.06	2.26	0.076
14.538	433.5	155.4	77.2	23.0	1.82	1.61	5.55	4.03	3.12	2.92	5.39	3.48	0.062
15.715	215.2	103.0	75.0	10.2	1.03	1.45	2.99	2.76	2.04	2.06	3.77	3.81	0.020
16.832	164.9	97.6	57.5	13.6	1.52	1.25	3.14	3.37	2.65	2.39	4.57	3.54	0.043
17.751	214.8	122.7	120.4	11.2	1.68	1.41	3.26	3.69	2.63	2.64	5.51	3.53	0.025
18.702	225.3	112.4	100.5	21.0	2.03	1.69	3.99	4.15	3.17	2.89	5.67	4.44	0.057
20.549	180.6	89.4	73.8	13.5	1.19	1.46	3.63	3.63	2.60	2.34	4.14	3.12	0.078
21.534	208.4	96.6	61.7	10.6	1.07	1.63	3.66	3.36	2.07	2.01	3.47	3.77	0.030
22.241	220.8	116.8	134.6	22.2	2.33	2.26	5.07	5.13	3.52	3.45	6.30	5.18	0.130
24.346	105.7	53.9	35.0	11.2	1.46	1.23	3.12	3.09	1.51	1.79	3.82	2.68	0.074
26.389	109.6	44.6	37.6	5.8	1.19	1.01	2.02	2.28	1.04	1.28	2.66	2.01	0.022
28.422	118.7	37.3	40.7	16.3	1.16	1.32	3.09	3.12	2.49	2.04	4.05	2.86	0.102
29.266	323.9	111.5	70.9	16.9	2.41	3.40	6.79	8.47	3.56	5.50	6.61	7.07	0.064
30.025	337.4	105.2	120.0	24.1	3.19	3.40	7.41	8.00	5.58	5.18	10.60	7.68	0.202

30.823	365.3	109.2	85.5	16.3	2.94	2.14	4.89	5.52	3.63	3.82	7.29	6.57	0.077
31.715	207.2	63.3	111.2	17.4	2.16	2.38	4.96	5.67	3.47	4.36	7.75	6.00	0.119
32.552	401.4	99.7	56.2	13.3	2.40	2.58	5.63	5.89	3.10	4.47	8.01	6.46	0.084
33.321	348.7	98.0	49.0	23.7	2.50	3.20	7.05	7.71	4.11	5.74	10.29	9.46	0.126
34.184	328.3	82.1	85.8	13.8	2.44	2.11	4.71	5.31	3.42	3.62	6.90	6.59	0.085
34.963	328.3	82.5	47.7	19.0	1.84	2.72	6.03	6.88	4.77	5.04	8.68	8.54	0.117
36.677	274.2	66.9	34.7	15.6	1.83	2.43	5.16	5.56	3.40	3.52	6.98	5.59	0.202
37.259	465.5	101.9	44.6	10.3	1.65	3.75	6.93	6.76	3.85	3.84	6.34	6.53	0.062
37.935	252.0	63.4	59.3	17.6	2.47	2.74	6.05	6.01	3.43	3.67	7.60	5.62	0.186
38.547	299.0	84.8	94.2	13.7	2.30	2.89	5.94	6.53	6.73	4.56	8.21	7.02	0.180
39.014	408.4	96.8	52.2	26.9	3.63	4.08	9.31	10.34	7.66	6.60	12.43	10.65	0.311
39.454	623.4	149.4	75.2	22.1	3.76	3.62	7.87	9.26	7.24	6.68	13.78	11.23	0.378
39.975	470.3	126.1	49.2	29.0	2.01	3.32	7.80	8.81	6.83	6.56	13.61	11.29	0.403
40.479	484.4	105.9	44.3	13.7	1.98	2.71	5.75	7.55	5.52	5.50	12.64	9.55	0.284
41.452	395.8	80.2	43.0	24.5	2.87	2.96	7.91	8.33	5.33	5.67	12.54	10.36	0.348
41.944	507.8	95.3	55.3	12.4	3.25	3.82	8.15	9.86	5.17	5.94	12.54	10.56	0.287
42.446	474.8	83.1	35.0	17.1	0.73	1.91	4.54	5.81	6.29	3.28	14.11	2.24	1.007
42.982	316.1	72.9	80.1	23.8	1.80	2.61	5.85	6.71	3.89	3.67	6.70	6.56	0.142
43.421	458.4	106.2	62.4	19.0	2.43	2.79	7.17	8.38	5.49	5.27	10.44	9.69	0.100
43.819	576.1	110.8	42.9	16.2	3.32	3.64	7.66	10.29	6.30	5.91	13.76	11.62	0.106
44.674	524.6	109.1	98.6	33.2	2.66	4.42	9.54	10.53	7.56	8.16	15.52	13.81	0.285
45.054	439.0	103.4	55.6	30.5	2.45	3.26	8.51	9.69	7.51	6.84	12.90	11.68	0.354
45.462	550.2	113.9	37.9	12.2	1.83	2.77	6.51	7.29	5.09	5.76	10.90	10.42	0.140
45.909	456.2	82.2	44.5	37.4	2.86	3.46	7.90	8.29	10.47	5.51	11.71	11.75	0.434
46.774	402.7	94.7	162.7	33.8	3.04	4.75	8.87	9.76	6.31	6.47	13.60	11.65	0.205
47.221	474.9	100.5	51.2	24.5	4.67	4.58	9.15	10.40	6.18	6.15	12.57	11.11	0.122
47.653	659.6	123.1	160.9	23.8	5.74	5.12	10.65	11.13	6.42	7.03	13.76	12.74	0.094
48.114	842.8	139.2	108.3	20.9	5.23	5.08	9.20	11.50	6.21	6.52	12.74	11.20	0.092

48.539	582.3	156.5	88.6	46.6	4.21	6.28	11.61	14.37	8.58	8.71	16.65	16.25	0.230
48.989	603.3	113.8	77.3	28.2	5.91	4.34	8.95	12.28	6.59	7.36	13.82	13.31	0.127
49.866	710.8	114.0	57.7	18.7	3.00	4.60	8.49	10.69	6.09	6.22	11.93	9.91	0.211
50.348	472.5	91.1	96.7	32.7	3.30	3.39	7.64	8.30	4.83	4.92	10.54	8.88	0.292
50.815	567.6	86.5	73.7	19.9	3.63	3.47	7.03	7.39	4.89	4.95	9.36	8.85	0.187
51.395	484.7	85.0	45.9	15.6	3.05	2.84	6.31	6.38	3.65	4.12	8.23	7.33	0.169
51.962	431.4	83.0	90.9	15.5	2.72	2.70	5.96	6.23	4.78	4.37	8.54	7.97	0.206
52.505	435.2	83.0	82.8	25.4	4.40	4.20	9.08	9.01	5.74	6.45	12.28	11.03	0.309
53.574	402.3	86.4	35.7	28.6	5.00	4.10	7.97	8.89	6.16	6.12	10.84	10.68	0.252
54.228	301.8	65.7	46.8	13.4	4.07	3.67	6.20	7.10	8.90	4.92	10.08	7.47	0.173
54.868	451.6	89.2	75.1	23.9	2.79	4.57	8.33	9.75	6.25	6.39	12.34	10.39	0.177
55.517	275.9	77.4	66.0	20.5	3.35	3.47	6.97	7.40	4.69	4.30	8.62	7.52	0.135
56.217	263.6	67.9	17.6	6.5	1.38	2.46	4.50	5.20	4.13	3.13	5.96	4.53	0.065
56.902	263.3	63.9	23.7	8.6	1.52	1.97	4.07	4.60	2.75	3.02	5.99	4.67	0.045
58.147	301.9	74.8	70.8	28.1	2.83	2.25	5.67	5.88	3.55	3.91	7.82	6.32	0.080
58.752	376.1	89.3	76.3	28.8	1.91	2.49	6.14	6.48	5.19	4.47	8.56	7.62	0.136
59.327	337.9	88.5	29.5	11.4	2.01	2.42	5.03	5.52	3.93	3.98	7.07	6.10	0.059
59.853	431.5	127.2	80.3	42.8	4.66	3.36	8.13	8.17	6.86	5.86	11.90	10.06	0.180
60.396	416.7	96.9	101.7	31.1	3.25	3.69	7.75	7.80	5.80	5.30	9.71	8.76	0.139
60.918	569.8	117.0	61.1	16.0	3.65	3.99	7.19	8.52	5.88	5.79	10.99	8.62	0.091
61.474	354.3	97.5	66.6	26.4	2.28	3.45	7.60	8.31	6.95	5.99	10.83	8.74	0.135
62.051	320.6	102.2	84.6	23.5	3.20	3.59	7.46	7.87	5.53	5.24	9.82	8.47	0.100
63.129	323.8	92.0	92.4	40.8	4.98	3.28	7.44	8.16	5.94	5.41	9.93	10.58	0.116
63.697	367.7	112.0	76.1	40.0	2.84	3.70	8.02	8.72	7.15	6.09	11.22	10.80	0.130
64.252	366.6	108.3	60.6	18.0	3.31	2.79	6.48	6.35	5.56	4.56	9.13	7.98	0.084
64.830	276.3	116.2	112.6	20.9	3.65	2.89	5.89	6.77	5.35	4.33	8.88	7.11	0.071
65.374	306.2	108.5	145.7	43.1	5.26	3.63	8.63	9.25	6.75	6.68	9.81	10.07	0.149
65.906	302.2	116.9	71.0	20.0	3.98	2.70	5.73	6.94	4.72	4.62	8.30	7.49	0.063

66.430	323.0	109.9	98.3	36.3	3.78	2.55	6.20	7.56	5.70	4.71	10.61	7.77	0.109
67.580	234.2	102.8	51.8	15.4	2.44	2.12	5.03	5.80	4.30	3.80	7.37	5.71	0.078
68.139	229.8	109.1	109.0	16.5	2.19	1.84	4.78	5.03	4.53	3.33	6.40	4.76	0.079
68.833	179.7	75.0	86.0	26.4	1.37	1.82	4.64	4.48	3.83	3.10	6.13	4.65	0.086
69.568	225.3	88.6	60.5	14.8	2.74	1.79	4.07	4.64	3.78	3.05	5.89	4.42	0.056
70.238	215.2	82.0	85.4	27.0	3.10	2.82	6.12	6.82	5.27	4.66	8.93	6.99	0.114
70.882	354.5	104.9	59.6	18.6	2.82	2.66	5.08	6.07	6.06	4.10	6.41	6.12	0.094
71.521	316.8	96.1	71.2	26.3	3.49	2.78	5.80	6.84	5.19	5.03	8.99	7.42	0.106
72.934	337.3	101.9	73.4	32.4	2.65	2.90	6.46	7.41	5.34	5.24	8.97	8.29	0.119
73.575	361.1	120.6	48.3	26.1	5.06	3.26	6.24	8.18	5.96	5.32	10.31	8.54	0.106
74.259	393.6	113.8	74.8	31.8	4.19	4.32	7.36	9.61	6.35	6.24	11.27	9.06	0.142
74.936	343.4	109.9	33.7	18.0	3.50	3.12	5.49	7.20	4.39	4.91	7.53	7.22	0.077
75.603	271.5	93.8	68.1	33.5	5.27	3.16	6.59	7.50	5.22	5.54	8.17	8.27	0.091
76.269	353.7	100.2	32.9	16.2	2.53	2.48	4.80	6.06	4.60	4.51	7.99	6.59	0.087
76.936	362.8	111.5	58.8	35.0	3.54	3.54	6.60	8.21	7.01	6.44	11.10	9.65	0.132
78.269	343.5	120.6	78.7	30.4	2.96	3.06	6.10	6.84	5.35	5.63	7.85	7.65	0.119